MATERIAL REMOVAL MECHANISM AND SURFACE INTEGRITY OF WROUGHT AND SLM-ED TI6AL4V ALLOYS IN ULTRA-HIGH-SPEED MACHINING

JIANG QINGHONG

PhD

The Hong Kong Polytechnic University

2024

The Hong Kong Polytechnic University

Department of Mechanical Engineering

Material Removal Mechanism and Surface Integrity of Wrought and SLM-ed Ti6Al4V Alloys in Ultra-high-speed Machining

Jiang Qinghong

A thesis submitted in partial fulfillment of

the requirements for the degree of

Doctor of Philosophy

August 2023

Certificate of Originality

I hereby declare that this thesis is my own work and that, to the best of my knowledge and belief, it reproduces no material previously published or written, nor material that has been accepted for the award of any other degree or diploma, except where due acknowledgement has been made in the text.

JIANG QINGHONG

Abstract

Titanium alloy (Ti-alloy) is a preeminent structural material with remarkable mechanical properties such as high specific strength, excellent corrosion resistance, and ideal biocompatibility. It has been extensively applied in various industries including aviation and aerospace, navigation, automotive, and biomedical industries. The conventional manufacturing and processing of high-performance Ti-alloy parts, however, encounter many technological bottlenecks and limitations, such as low productivity, difficulty in fabricating complex structures, high material wastage, and high production cost.

Recently, selective laser melting (SLM) has emerged as an advanced additive manufacturing technique for rapid, integrated, and lightweight manufacturing of Ti-alloy parts. Nevertheless, the SLM-manufactured (SLM-ed) Ti-alloy parts suffer from the trade-off dilemma between strength and ductility due to the internal defects and the non-equilibrium microstructure induced by high cooling rate and large temperature gradient during the solidification process. Moreover, the inherent inferior surface quality of SLM-ed parts limits their applications in critical areas. Therefore, surface machining is imperative for achieving high surface integrity of SLM-ed Ti-alloy parts.

However, Ti-alloy is known as a typical difficult-to-machine material, characterized by high specific strength, low thermal conductivity, high chemical reactivity, and low elastic modulus. Consequently, high machining force, elevated machining temperature, rapid tool wear, and compromised surface integrity tend to arise in the conventional machining of Ti-alloy. Furthermore, SLM-ed Ti-alloy exhibits completely different microstructures and properties compared to its wrought counterpart. These alterations not only affect machinability but also introduce additional challenges in the machining process.

Ultra-high-speed machining (UHSM) is a potential technique to address the machining challenges associated with Ti-alloy, given its capacity to enhance both surface integrity and machining efficiency. However, the dynamic responses and deformation behaviors of materials at ultra-high strain rates differ significantly from those at low strain rates. This leads to distinct material removal mechanisms in UHSM, which remains inadequately explored. Furthermore, there is limited research on the variation of microstructure evolution and surface integrity with machining speed in the machining of Ti-alloy. Additionally, the influence of different microstructures in SLM-ed and wrought Ti-alloys on their machinability also requires thorough study and analysis.

In tandem with these, this study starts with the SLM manufacturing of Ti6Al4V to fabricate strong and ductile Ti6Al4V by tailoring process parameters and microstructures. Subsequently, single-point-scratching (SPS) experiments and finite element simulations are conducted together to reveal the material removal and deformation mechanisms of both wrought and SLM-ed Ti6Al4V alloys, covering the spectrum from conventional speed machining (CSM) to ultra-high-speed machining (UHSM). Furthermore, the surface integrity of Ti6Al4V alloys in ultra-high-speed grinding (UHSG) is systematically investigated.

The first part of this thesis reports the investigations on the densification behaviors, defect formation mechanisms, microstructure evolution, and mechanical properties of SLM-ed Ti6Al4V at different energy densities. The densification map and process map of SLM-ed Ti6Al4V were developed to support the fabrication of near fully dense parts. The microstructure analysis revealed a progressive transformation with the decrease in energy density: from coarse α+β lamellar, ultrafine α+β lamellar, and to fully α' microstructure. The remarkable tensile strength combining high strength and ductility (Tensile strength: 1,390 MPa; elongation: 9.66%) was achieved at energy density of 76 J/mm^3 due to the high densification level and ultrafine microstructures. This study further revealed the fracture mechanisms and established the process-structure-property relationship of SLM-ed Ti6Al4V. These findings provide guidance for realizing the fabrication of strong and ductile Ti6Al4V by SLM.

The second part focuses on the material removal mechanisms of wrought coarse-grained Ti6Al4V under low-speed to ultra-high-speed conditions based on a developed SPS system. The material removal mechanisms were investigated in terms of surface creation, subsurface deformation, and chip formation. Multiscale characterization combining TKD, FIB, and STEM techniques was employed to investigate the microstructure evolution at the speed ranging from 20 to 220 m/s. The results indicated that material pile-up was suppressed at higher machining speeds due to the inhibition of plastic deformation. A deep machining-deformed zone (MDZ), consisting of a dynamic recrystallization zone (DRXZ) and a plastic deformation zone (PDZ), was induced at 20 m/s. The depth of PDZ was considerably reduced at higher machining speed and was absent at 220 m/s. Moreover, under ultra-high strain rate deformation, dislocation slip was inhibited, resulting in a transition of deformation mechanism from dislocation-mediated deformation (DMD) to twinning-mediated deformation (TMD). Consequently, a deformation-induced twin zone (DITZ) was generated in the topmost layer, in which a distinct microstructure characterized by ultrafine grain embedding nanotwins (UGENTs) was induced. Additionally, the segmented chips transitioned to the fragmented chips with the increasing machining speed. This study enhances the understanding of material removal and deformation mechanisms at ultra-high strain rates.

The third part delves into the material removal mechanisms of SLM-ed Ti6Al4V based on part 2. SLM-ed Ti6Al4V exhibited a decline pile-up ratio as the machining speed increased. However, the higher brittleness of SLM-ed Ti6Al4V resulted in less material accumulation on the edges of scratches. Additionally, the MDZ exhibited "skin effect" with an increase in machining speed, but it was shallower in SLM-ed Ti6Al4V compared with that in wrought Ti6Al4V under same speed conditions. As the strain rate increased, the deformation mechanism of SLM-ed Ti6Al4V also transitioned from DMD to TMD to coordinate the deformation. The multiple-fold twins were induced in the UGENTs, and the formation mechanism was revealed by multiscale characterizations and analyses. Regarding the chip formation, wrought Ti6Al4V exhibited a higher sensitivity to strain rate compared to SLM-ed Ti6Al4V. This can be attributed to different chip formation mechanisms. The segmented chips were formed as the phase transformation activated the adiabatic shear bands (ASBs) in wrought

Ti6Al4V, while the relative slip along the lath boundaries triggered the segmented chips in SLM-ed Ti6Al4V.

In the last part, a UHSG system was developed to achieve high-efficiency and high-quality machining. A series of grinding experiments of both wrought and SLM-ed Ti6Al4V alloys with the linear grinding speed ranging from 60 to 250 m/s were conducted. The surface integrity of the machined samples was systematically analyzed by considering both surface and subsurface characteristics. The results verified the material removal mechanisms elucidated in previous chapters and demonstrated the potential of UHSG in improving surface integrity. Meanwhile, the grinding forces of both materials at different grinding speeds were measured to evaluate their machinability. The effects of strain rate and microstructures on the deformation mechanism and machinability were elucidated based on the systematic investigations.

This thesis presents an original study on the material removal/deformation mechanisms and surface integrity of wrought and SLM-ed Ti6Al4V alloys in UHSM by applying multiscale characterizations. These findings not only provide a scientific and theoretical basis but also offer instructive insights into the manufacturing and processing of high-performance Ti-alloy parts.

Publications During the PhD Study Period

[1] **Qinghong Jiang**, Shuai Li, Sai Guo, Mingwang Fu, Bi Zhang. Comparative study on the process-structure-property relationships of TiC/Ti6Al4V and Ti6Al4V by selective laser melting. **Journal of Mechanical Sciences**, 2022.

[2] **Qinghong Jiang**, Shuai Li, Cong Zhou, Bi Zhang, Yongkang Zhang. Effects of laser shock peening on the ultra-high cycle fatigue performance of additively manufactured Ti6Al4V alloy. **Optics & Laser Technology**, 2021.

[3] **Qinghong Jiang**, Binbin He, Shuai Li, Cong Zhou, Mingwang Fu, Bi Zhang. Achieving hierarchically ultrafine grain embedding nanotwins structure in coarse-grained Ti-alloy at high strain rate deformation. (Under review).

[4] **Qinghong Jiang**, Shuai Li, Hao Liu, Mingwang Fu, Bi Zhang. Material removal mechanism of additively manufactured Ti6Al4V titanium alloy in ultra-high-speed machining. (Under review).

[5] **Qinghong Jiang**, Mingwang Fu, Bi Zhang. Ultra-high-speed grinding of wrought and additively manufactured Ti6Al4V alloy. (To be submitted).

[6] Shuai Li, **Qinghong Jiang**, Sai Guo, Bi Zhang, Cong Zhou. Effect of spattering on formation mechanisms of metal matrix composites in laser powder bed fusion. **Journal of Materials Processing Technology**, 2021.

[7] Shuai Li, Bi Zhang, **Qinghong Jiang**, Huili Han, Jiale Wen, Cong Zhou. Formation characteristics of nickel-based diamond abrasive segment by selective laser melting. **Optics and Laser Technology**, 2021.

[8] Sai Guo, Jianqiu Zhang, **Qinghong Jiang**, Bi Zhang. Surface integrity in high-speed grinding of Al6061T6 alloy. **CIRP Annals - Manufacturing Technology**, 2022.

[9] Sai Guo, Wei Du, **Qinghong Jiang**, Bi Zhang. Surface Integrity of Ultrasonically-Assisted Milled Ti6Al4V Alloy Manufactured by Selective Laser Melting. **China Journal of Mechanical Engineering**, 2021.

Conferences paper

[1] **Qinghong Jiang**, Mingwang Fu, Bi Zhang, "High-performance fabrication of titanium matrix composites by selective laser melting", The 16th CJUMP (China-Japan International Conference on Ultra-Precision Machining Process), November 19-21, 2021.

[2] **Qinghong Jiang**, Mingwang Fu, Bi Zhang, "Effect of grinding speed on the material removal mechanism and subsurface damage of Ti-alloy", Guangdong Province Postgraduates Academic Form, November 26-28, 2022.

Acknowledgements

The journey to pursue a PhD degree has been a journey of growth, learning, and self-discovery. I am truly grateful for the incredible people who have accompanied me along the way.

First and foremost, I extend my heartfelt gratitude to my supervisors, Prof. Bi Zhang at The Southern University of Science and Technology (SUSTech) and Prof. Mingwang Fu at The Hong Kong Polytechnic University (PolyU), whose unwavering dedication, expert guidance, and valuable insights have not only played a pivotal role in my research, but also have shaped me into a rigorous, discerning, and persistent researcher. I wish to extend my deepest gratitude to the Collaborative PhD Program between PolyU and SUSTech for granting me this invaluable opportunity for me to conduct the PhD research at both esteemed universities.

I must also acknowledge the financial support I received from Shenzhen Science and Technology Innovation Commission for the project numbered JSGG20210420091802007, Shenzhen Key Laboratory of Cross-Scale Manufacturing Mechanics under ZDSYS20200810171201007, and the project of GRF No. 15228621, ZE1W and 1-CD4H from PolyU.

I would like to express my appreciation to all my fellow labmates and colleagues from the research groups of Prof. Zhang and Prof. Fu for their generous support and encouragement throughout the course of my endeavors.

Last but not least, my heartfelt appreciation goes to my cherished family and Ms. Yue WANG for their boundless patience, unwavering understanding, and constant encouragement throughout my journey. Their steadfast support and affection provide me with the courage and confidence to surmount all challenges.

Table of Contents

List of Figures

List of Tables

List of Abbreviations

Abbreviations	Explanations
SLM	Selective laser melting
SLM-ed	SLM-manufactured
Ti-alloy	Titanium alloy
UHSM	Ultra-high-speed machining
SPS	Single-point-scratching
CSM	Conventional speed machining
FIB	Focus ion beam
STEM	Scanning transmission electron microscopy
MDZ	Machining-deformed zone
DRXZ	Dynamic recrystallization zone
PDZ	Plastic deformation zone
DITZ	Deformation-induced twin zone
UGENTs	Ultrafine grain embedding nanotwins
EBSD	Electron Backscatter Diffraction
TKD	Transmission Kikuchi Diffraction
AM	Additive manufacturing
EBM	Electron beam melting
LENS	Laser engineering net shape
UHSG	Ultra-high-speed grinding
PBF	Powder bed fusion
DMLS	Direct metal laser sintering
SL	Sheet lamination
UAM	Ultrasonic additive manufacturing
BJ	Binder jetting
DED	Directed energy deposition
EBAM	Electron beam additive manufacturing

(Continued)

Abbreviations	Explanations
WAAM	Wire and arc additive manufacturing
μ-SLM	Micro SLM
TRS	Tensile residual stress
CRS	Compressive residual stress
LAM	Laser-assisted machining
UAM	Ultrasonic-assisted machining
CM	Cryogenic machining
CDRX	Continuous dynamic recrystallization
GND	Geometrical necessary dislocation
LAGBs	Low angle grain boundaries
HAGBs	High angle grain boundaries
HCP	Hexagonal close packed
SPD	Severe plastic deformation
SFE	Stacking fault energy
SSD	Subsurface damage
HSM	High speed machining
ASB	Adiabatic shear band
JC	Johnson-Cook
SHPB	Split Hopkinson pressure bars
LSCM	Laser scanning confocal microscopy
CFRP	Carbon fiber reinforced plastics
CBN	Cubic boron nitride
UDTDM	Ultra-depth three-dimensional microscopy
WEDM	Wire electro discharge machine
OM	Optical microscopy
RD	Relative density
IPF	Inverse pole figures

(Continued)

Abbreviations	**Explanations**
BOR	Burgers orientation relationship
UTS	Ultimate tensile strength
HIP	Hot isostatic pressing
SAED	Selected area electron diffraction
HRTEM	High-resolution TEM
FFT	Fast Fourier transform
IQ	Image quality
KAM	Kernel average misorientation
HDDs	High-density dislocations
PSZ	Primary shear zone
SDZ	Second deformation zone
DMD	Dislocation mediated deformation
TMD	Twinning mediated deformation
ntGRT	Nano-twinning induced grain refinement
ntDRX)	Nanotwinning-assisted dynamic recrystallization
DART	Deformation-activated recrystallization twin
DDRX	Discontinuous dynamic recrystallization
DTs	Dislocation tangles
GRZ	Grain refinement zone
MD	Molecular dynamics

Chapter 1 Introduction

1.1 Research Background and Identified Research Problems

Ti-alloy is considered one of the most crucial structural and functional metal materials due to its exceptional combined properties of high specific strength, extraordinary corrosion resistance, and ideal biocompatibility. It has been increasingly utilized across various critical industries such as aviation, aerospace, navigation, automobile, military, biomedical industries, as well as some premium sports equipment and consumer electronics (Li *et al.* 2023; Niinomi 2019; Pushp *et al.* 2022). Nevertheless, the expensive raw materials and processing costs of Ti-alloy limit its applications to the aforementioned high-end fields, constraining its large-scale promotion.

The manufacture and processing of high-performance parts not only fulfill the increasing demands of contemporary engineering but also drive innovation, optimize resource utilization, and promote sustainable development, thereby providing advanced solutions for various application domains. However, the conventional manufacturing of a Ti-alloy part usually involves lengthy cycles and complex processes, requiring various equipment for casting, forging, heat treatment, and milling. This invariably leads to substantial material wastage, heightened energy consumption, and pronounced environmental pollution. Meanwhile, conventional manufacturing struggles to accommodate the rapid updates and improvements of products, making it challenging to achieve large-scale production of intricate parts.

Recently, the emerging additive manufacturing (AM) technology has attracted considerable attention due to its tremendous potential in realizing the manufacture of high-performance parts (Dilberoglu *et al.* 2017; Li *et al.* 2023). Unlike the conventional top-down paradigm in subtractive manufacturing methods, a part is manufactured layer by layer in a bottom-up manner in AM (Tofail *et al.* 2018). Over the past few decades, various AM techniques have emerged, and the range of materials that can be utilized in AM techniques is constantly expanding. Currently, many polymers, metals, ceramics, as well as composites materials can be additively manufactured (Bourell *et al.* 2017; Srivastava *et al.* 2022).

The adoption of metal AM techniques has gained considerable traction across diverse industries due to their established process chains and inherent benefits in producing high-value parts (Armstrong *et al.* 2022). In the case of Ti-alloy, AM techniques such as selective laser melting (SLM), electron beam melting (EBM), and laser engineering net shape (LENS) have garnered significant attention and utilization. Among these methods, SLM stands out as the most promising one, primarily attributed to its capability to manufacture high-strength parts with intricate geometries and exceptional precision (Nguyen *et al.* 2022).

Despite the numerous advantages of SLM, challenges persist in the SLM manufacturing of Ti-alloy. SLM is a complex process that is governed by numerous process parameters. Internal defects such as pores, lack of fusion, and cracks tend to arise if improper parameters are applied (Zhang *et al.* 2017). Meanwhile, non-equilibrium microstructures are usually obtained during the rapid solidification process under high cooling rates and temperature gradients. As a result, the SLM manufactured (SLM-ed) titanium ally parts usually exhibit high strength but low ductility, falling into the so-called strength-ductility trade-off dilemma.

Extensive efforts have been devoted to breaking through this dilemma so as to manufacture strong and ductile parts. For instance, post-treatment tehcniques, such as heat treatment and hot isostatic pressing (HIP), are commonly employed on the as-built Ti-alloy parts to tailor the microstructure and control the porosity, respectively (Lu and Zhuo 2023; Zhang *et al.* 2023). However, these post-treatment procedures substantially prolong the machining cycle and increase associated costs.

The microstructure evolution and defect formation in SLM-ed Ti-alloy are highly connected to the input, distribution, and consumption of laser energy. Hence, it is possible to tailor the resultant microstructures in-situ and mitigate the formation of defects by controlling the laser energy density. Previous researches indicate that excessive energy input tends to induce the keyhole porosity, while the lack-of fusion porosity is easily produced under insufficient energy input conditions. Therefore, high relative density parts can only be manufactured within the corresponding optimized processing window (Han *et al.* 2017; Meng *et al.* 2022). Additionally, novel microstructures such as ultra-fine α+β, or hierarchical α/α′ have been demonstrated to enhance material strength while maintaining a high ductility level (Cao *et al.* 2022; Xu *et al.* 2017). Nevertheless, the in-situ tailoring and the underlying mechanisms still require systematic investigations.

Furthermore, another significant challenge associated with SLM-ed Ti-alloy is the issue of rough surface. The inherent layer-by-layer building process in SLM results in a “stair effect”, leading to a noticeable increase of surface roughness, particularly on inclined surfaces or when a large layer thickness is applied (Mele *et al.* 2021). Meanwhile, the presence of attached powders, balling phenomenon, and spattered materials also has detrimental effects on the resultant surface roughness (Kuntoğlu *et al.* 2023). Generally, an as-built SLM-ed Ti6Al4V alloy part exhibits an average surface roughness (Ra) ranging from 5 μm to 40 μm (Pal *et al.* 2020), which is unacceptable, particularly for applications demanding a high surface finish. Therefore, surface machining is necessary to eliminate the defects in the surface layer of SLM-ed Ti-alloy parts (Malakizadi *et al.* 2022).

However, Ti-alloy is recognized as a typical difficult-to-machine material due to its low machinability. The difficulty in machining Ti-alloy originates primarily from its unique mechanical properties, characterized by high specific strength, low thermal conductivity, high chemical reactivity, and low elastic modulus (Oke *et al.* 2020; Pramanik and Littlefair 2015). This combination of material properties results in high machining forces, elevated machining temperatures, accelerated tool wear, as well as severe plastic deformation during the machining process (Pramanik 2014). Consequently, these factors collectively contribute to the compromised surface integrity.

Considerable endeavors have been undertaken by researchers to surmount the obstacles associated with machining Ti-alloys. These include the development of brand new cutting tools (Komanduri and Reed Jr 1983), the optimization of machining parameters (Yang and Liu 2015), the application of advanced cooling methods (Liu *et al.* 2013), as well as the exploration of non-traditional machining processes (Muthuramalingam *et al.* 2021; Niu *et al.* 2023). However, during the practical processing of Ti-alloys, it is usually necessary to sacrifice efficiency to improve processing quality, resulting in a trade-off of efficiency and quality. The ongoing challenge is to enhance machining quality while simultaneously maintaining high machining efficiency.

Additionally, compared with the coarse-grained conventional Ti6Al4V, SLM-ed Ti6Al4V exhibits finer microstructures due to the inherent large temperature gradient and high cooling rate during the SLM process. This distinction gives rise to unique mechanical properties and material dynamic responses when subjected to machining loading. For instance, SLM-ed Ti6Al4V demonstrates increased anisotropy, strength, and hardness, but lower ductility (Li *et al.* 2022). As a consequence, the machining characteristics of SLM-ed Ti6Al4V notably differ from those of conventionally wrought Ti6Al4V. This introduces additional machining challenges such as the larger cutting forces, higher temperatures, and accelerated tool wear (Zhang *et al.* 2023). Therefore, the machining process parameters that have been established for conventionally wrought Ti6Al4V cannot be directly applied to SLM-ed Ti6Al4V. It is necessary to make appropriate adjustments to accommodate the distinctive machining characteristics of SLM-ed Ti6Al4V.

To address the machining problems encountered in conventional machining methods. Advanced machining techniques have been developed and explored. Among these, the ultra-high-speed machining (UHSM) has emerged as a promising and innovative technique. UHSM offers notable benefits compared with conventional machining, including improved machining efficiency, enhanced machining quality, diminished tool wear, as well as mitigated subsurface damage (SSD) (Shi *et al.* 2017; Sun *et al.* 2019). Therefore, UHSM holds substantial potential for machining materials that are conventionally difficult to machine.

In comparison to conventional machining, UHSM achieves considerably higher machining linear velocities. However, there is currently n no standardized definition for UHSM, as the speed range is a relative concept that depends on the machining processes and the materials being machined. Generally, the grinding process is optimized for achieving very high linear velocities, and it is deemed to enter the UHSM region when the grinding speed exceeds 150 m/s.

UHSM is a complex process governed by multiple factors, including strain rate effect, size effect, and thermal effect. In UHSM, material is removed under ultra-high strain rates, and the material removal mechanism maybe completely different due to the alterations of material deformation behaviour and material response. From a microscale aspect, material deformation is highly dependent on dislocation motion, and dislocation kinetics are significantly influenced by strain rate. It is demonstrated that dislocations alone can no longer relieve mechanical loads when the strain rate reaching certain limiting conditions. In such scenarios, new deformation mechanisms such as twinning become the dominant factor (Zepeda-Ruiz *et al.* 2017). Meanwhile, the material's dynamic properties are intimately connected to the strain rate. As the strain rate increases, the flow stress significantly increases, while the fracture strain significantly decreases (Hu *et al.* 2020). Therefore, a ductile material can behave like a brittle material under very high strain rate conditions (Wang *et al.* 2015).

From a kinematic perspective, the increasing linear velocity substantially diminishes the maximum undeformed chip thickness, demonstrating a distinct size effect in ultra-high-speed grinding (UHSG) (Backer *et al.* 1952). As a result, the grinding force in UHSG tends to decrease, leading to a reduction in plastic deformation, thereby enhancing the machining quality.

Regarding the thermal effect, Salomon predicted that when the machining speed surpassed a critical threshold, the machining temperature tended to decrease with further increasing in machining speed. However, existing detection methods are unable to directly measure the temperature distribution within the machining zones under UHSM conditions. Theoretically, the machining heat in UHSM tends to be predominantly concentrated in a superficial layer due to insufficient time for heat to diffuse into the workpiece (Guo *et al.* 2022). Meanwhile, a significant portion of the heat generated during the cutting process is dissipated by the rapidly moving chips.

Undoubtedly, the material removal and deformation mechanisms of Ti-alloy are highly correlated with machining loading and are completely different under UHSM conditions. However, no systematic research in this field has been reported. Meanwhile, the mechanisms behind surface creation, microstructure evolution, and chip formation under extremely high strain rates remain unclear. In light of this, comprehensive investigations are required to understand the transitions in material removal mechanisms and surface integrity as strain rate machining conditions increase. These investigations will offer a theoretical foundation and practical guidance for achieving high-efficiency and high-quality machining of Ti-alloy by UHSM.

1.2 Research Objectives and Significance

To achieve the SLM manufacture of strong and ductile Ti6Al4V, this study conducted systematic examinations and characterizations to uncover the densification behaviors, defect formation mechanisms, microstructure evolution, and mechanical properties of SLM-ed Ti6Al4V at different energy densities.

Furthermore, this study carried out single point scratching (SPS) experiments to investigate the material removal mechanisms of both wrought and SLM-ed Ti6Al4V at speeds ranging from 20 to 220 m/s. The analysis of the material removal mechanism involved comprehensive examinations on surface generation, subsurface deformation, and chip formation. Multiscale characterizations and analyses were achieved through the integration of advanced techniques, including focus ion beam (FIB), scanning transmission electron microscopy (STEM), electron backscatter diffraction (EBSD), and transmission Kikuchi diffraction (TKD).

Additionally, an UHSG system was developed to realize high-efficiency and high-quality machining of Ti-alloys. The surface quality across conventional to ultra-high-speed regions was examined and compared by considering both surface characteristics and subsurface microstructures. The machinability of wrought and SLM-ed Ti6Al4V was systematically compared and analyzed. The objectives of the study are as follows:

(1) Uncovering densification behaviors, defect formation and microstructure evolution mechanisms to enable the manufacture of SLM-ed Ti6Al4V with superior tensile properties;

(2) Revealing the material removal and deformation mechanisms of Ti6Al4V alloys in UHSM, and elucidating their transition mechanisms with the increasing machining speed;

(3) Unveiling the influence of microstructures on the machinability of wrought and SLM-ed Ti6Al4V alloys;

(4) Examining the effects of grinding speed on the surface integrity of Ti6Al4V alloys and establishing an optimized UHSG process for these alloys.

This study focuses on the material removal mechanisms and surface integrity of Ti6Al4V alloys in ultra-high-speed machining. Comprehensive investigations into both mechanism and process were carried out based on the developed SPS and UHSG systems. By utilizing multiscale characterization techniques, this study attempts to systematically analyze and reveal the machining characteristics of Ti-alloy under various speed conditions. Notably, the study not only provides theoretical guidance for the ultra-high-speed machining of Ti-alloys but also offers advanced solutions for achieving high-efficiency and high-quality machining of difficult-to-machine materials.

1.3 Thesis Structure

This thesis consists of eight chapters and follows a coherent and well-structured organization. Chapter 1 introduces the research background, outlines the research problems, defines the research objectives, and highlights the significance of the study.

Chapter 2 provides a comprehensive literature review on critical topics relevant to this thesis. This encompasses the current state of additive manufacturing of Ti-alloy, the challenges faced in conventional machining of Ti-alloy, an overview of microstructure evolution during the machining of Ti-alloy, and an introduction to UHSM and its potential in machining difficult-to-machine materials.

Chapter 3 outlines the research methodologies utilized in this thesis and presents the research framework of the study. Additionally, this chapter emphasizes the logical structure of the thesis and the interrelationships among the different chapters.

Chapter 4 commences with a systematic investigation into process optimization, aiming to reveal the densification behaviors and the mechanism of defect formation in SLM-ed Ti6Al4V. This involves the development of densification maps and process maps for SLM-ed Ti6Al4V. Subsequently, systematic characterizations were conducted to analyze the microstructure evolution of samples manufactured using different process parameters. Furthermore, the tensile properties and fracture characteristics were analyzed. In this context, a comprehensive analysis was conducted to elucidate the intricate process-structure-property relationship of SLM-ed Ti6Al4V.

Chapter 5 delves into the investigation of material removal and deformation mechanisms of wrought Ti6Al4V in UHSM, while shedding light on their transitions as the strain rate increases. This chapter introduces the developed SPS system designed for ultra-high-speed scratch. A series of SPS experiments under different machining speeds were conducted to analyze the material removal mechanisms from multiple perspectives, including surface creation, subsurface deformation, and chip formation.

Chapter 6 focuses on the material removal and deformation mechanisms of SLM-ed Ti6Al4V based on the theoretical foundation and research methods established in Chapter 5. Systematic examinations including surface morphology/profile, subsurface microstructure evolution, as well as chip formation characteristics were performed through multiscale characterizations. Additionally, an extensive and thorough comparison was conducted to evaluate the distinctions in material removal and deformation mechanisms between conventionally wrought and SLM-ed Ti6Al4V.

Chapter 7 details the development of a UHSG system aimed at achieving high-efficiency and high-quality machining of Ti-alloys. A series of grinding experiments were conducted on both wrought and SLM-ed Ti6Al4V alloys, covering a range of grinding linear speeds spanning from 60 to 250 m/s. This chapter predominantly focuses on the investigations of surface integrity considering both surface and subsurface characteristics. The examination of deformation mechanisms across various machining speed ranges and their subsequent impacts on surface integrity was undertaken. Moreover, an evaluation and comparative analysis of the machinability of both wrought and SLM-ed Ti6Al4V were conducted in this Chapter.

In Chapter 8, the comprehensive conclusions of this thesis are presented, and suggestions for future research directions are also provided.

Chapter 2 Literature Review

2.1 Additive Manufacturing of Ti-alloy

2.1.1 Introduction of Ti-alloy

Ti-alloy is the most primarily structural and functional metal material due to its high specific strength, exceptional corrosion resistance, and ideal biocompatibility (Guerra-Yánez *et al.* 2023; Zhao *et al.* 2022). It has been increasingly applied in many critical industries such as aviation and aerospace, navigation, automotive and biomedical industries (**Fig. 2.1**). Particularly, the aviation and aerospace industries consume about 80% Ti-alloy production because of the high payoff of weight reduction. Additionally, Ti-alloy is mainly used for the manufacture of key engine parts and load-bearing parts attributed to its advantages in mechanical properties (Cui *et al.* 2011).

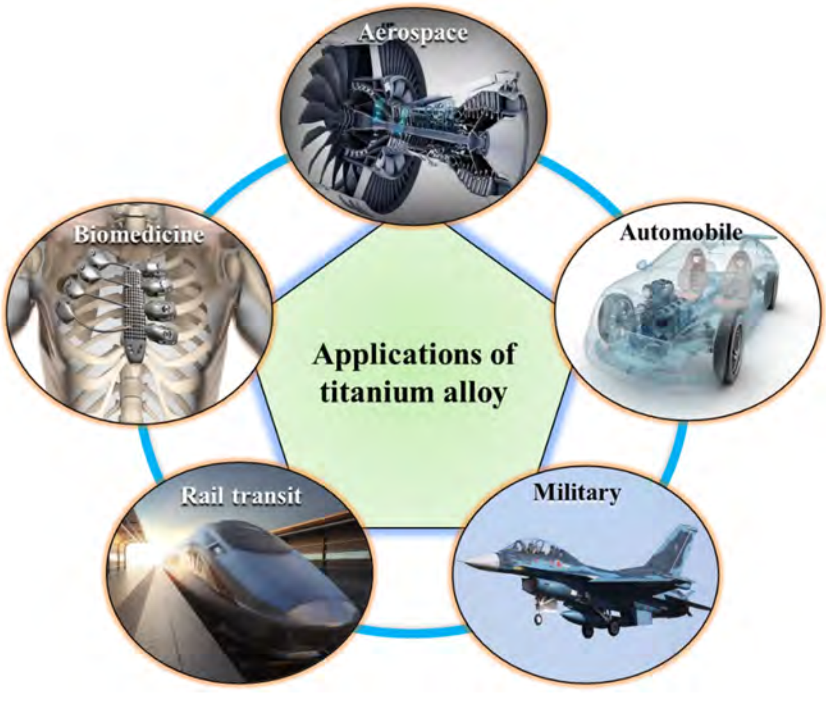

Fig. 2.1 Critical applications of Ti-alloy.

However, Ti-alloy is a typical hard-to-machining material due to its high strength, low thermal conductivity and high chemical reactivity, which causes severe tool wear and inferior surface integrity that in turn results in a low material remove rate (Jamil *et al.* 2022; Liang *et al.* 2019; Naskar *et al.* 2020; Pramanik and Littlefair 2015).

Furthermore, the manufacturing of Ti-alloy is often associated with a high buy-to-fly ratio that leads to senseless material waste. These factors in turn significantly increase the cost of Ti-alloy parts, restricting them from further extending.

2.1.2 Introduction of Additive Manufacturing Processes for Ti-alloy

Additive manufacturing (AM) refers to the techniques building a near net shape products by joining materials layer by layer from 3D model data directly. The extensive AM techniques with a wide range of processing materials covering polymers, metals, ceramics and biomaterials, have emerged over the past 30 years since the first rapid prototyping machine (SLA-1) was developed by Hull in 1983 (Gibson *et al.* 2015).

Among numerous AM processes, metal AM techniques have been extensively applied in various industries due to their high maturity and advantages in manufacturing of structural and functional parts (Durai Murugan *et al.* 2022). As shown in **Fig. 2.2**, the metal AM processes are divided into four categories in term of the basic AM principles, including powder bed fusion (PBF: SLM, EBM, DMLS), sheet lamination (SL: UAM), binder jetting (BJ), directed energy deposition (DED: EBAM, WAAM, LENS). **Table 2.1** systematically compares the advantages and limitations of the four metal AM categories. Although different metal AM processes might have differences in heat sources, feedstocks, procedures, parameters and applications, the foundational manufacturing mechanism is to control the input of local energy or binding agent to achieve the consolidation of raw materials layer upon layer.

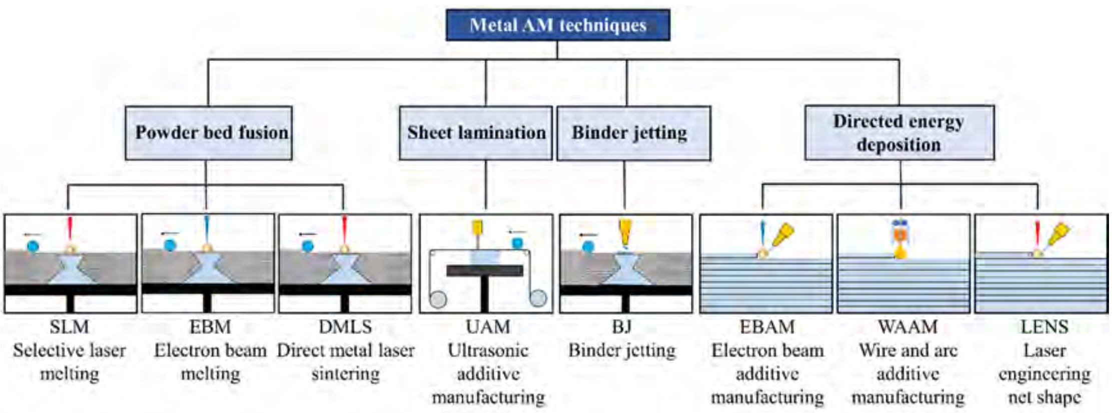

Fig. 2.2 Classification of metal AM processes.

SLM, as one of the most prosperous metal AM techniques, has particularly captivated considerable researchers in industry and academia owing to its ability in manufacturing high strength parts with complex features and high precision (Sefene 2022). Meanwhile, it has been adapted to manufacture a wide range of metals including ferrous alloys, aluminum alloys, Ti-alloys, and nickel-based alloys. Particularly for Ti-alloys, SLM has gradually converted to a mainstream manufacturing technique with a series of successful application cases conducted in critical fields (Olakanmi *et al.* 2015). Various advantages of SLM on the fabrication of Ti-alloy are summarized as follows:

(1) Rapid manufacturing without molds: Unlike with more traditional subtractive manufacturing techniques, it is no longer necessary to design and manufacture specific molds for different parts in SLM. Meanwhile, SLM is a single-step process, which greatly reduces the time and cost, and makes SLM a perfect way for rapid prototyping;

(2) Integrated manufacturing of complex parts: In an SLM process, parts are built layer upon layer. This particular mechanism breaks the limitation of geometric complexity, thereby allowing SLM to manufacture parts that are beyond the capacity of traditional methods.

(3) Lightweight design and manufacturing: The design freedom of SLM allows for adapting the design to the requirements to achieve optimal compatibility. Particularly, by combining with the advanced topology optimization technology, lighter parts with desired properties can be designed and manufactured, which significantly reduces the waste of materials and carbon emissions.

(4) High material utilization: In the conventional process, a blank is first generated by a forming process, followed by the subtractive manufacturing such as turning, milling, or grinding to manufacture a Ti-alloy part, in which enormous material waste is inevitable due to the very high buy-to-fly ratio. While the SLM process can manufacture the near net shape parts with minimum material waste, the SLM manufactured (SLM-ed) parts can be applied to service directly or after removing small machining allowance.

(5) Refined grain: Compared with conventional fabrication methods, the SLM process has a much higher cooling rate (10^3~10^6 k/s), resulting in substantial grain refinement, which finally contributes to the superior mechanical properties.

Table 2.1 Advantages and limitations of four metal AM categories. Advantages and limitations of four metal AM categories.

Process	Advantages	Limitations
PBF	High precision Complex feature High surface finish High mechanical properties	Single material Low deposition rate High thermal residual stress
SL	Internal Features High deposition rate Embedded part Low thermal residual stress	Material waste Additional cutting operation
BJ	Low cost High deposition rate	Poor accuracies Poor surface finish Poor mechanical properties Furnace cycles requirement
DED	Multi-materials Functionally graded parts Repairing and refurbishing damaged part	Poor resolution Poor surface finish High thermal residual stress

2.1.3 Challenges in SLM of Ti-alloy

As shown in **Fig. 2.3**, SLM is a complex physical process coupling multiple fields including temperature, flow and transformation field. In an SLM process, a concentrated laser beam with a high-energy-density scans and melts the powder material at a high speed, leading to high cooling rate and high temperature gradient in the highly localized melt pool. As a result, a dynamic molten pool is induced, in which Marangoni convection, vaporization of elements with low melting point and gradient surface tension result in a violent disturbance. In addition, the temperature field also governs the complex phase transformations that are influenced by the repeated melting-solidification-remelting process. Multiple fields interrelate and interact in an SLM process, which pose enormous challenges to manipulating the molten pool's dynamics and the final quality of manufactured parts.

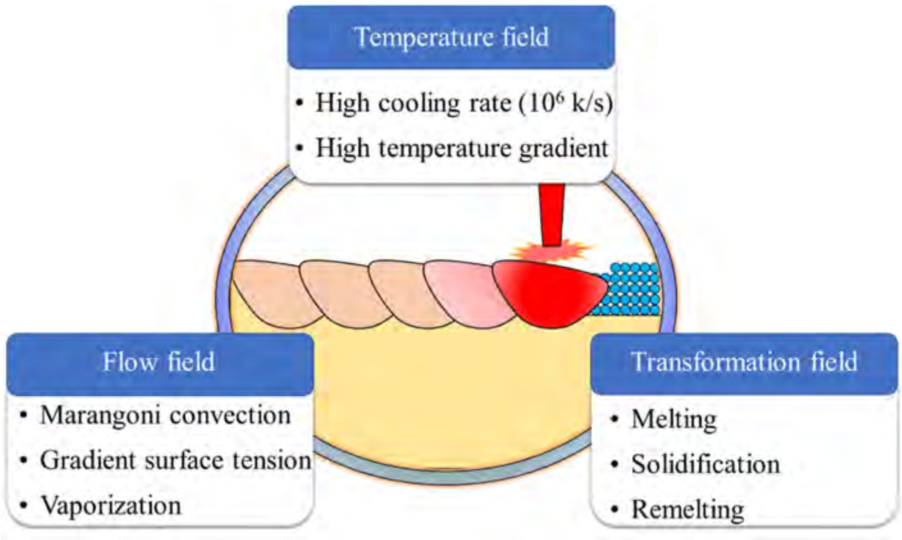

Fig. 2.3 Multiple fields in an SLM process.

One of the significant causes that limits the promotion of SLM-ed Ti-alloy is surface quality. Generally, an as-built SLM-ed Ti6Al4V alloy part has an average surface roughness (Ra) ranging from 6 μm to 40 μm, which is unacceptable in critical structural and functional parts since a rough surface is detrimental to mechanical properties.

The surface finish of SLM-ed Ti6Al4V in the as-built condition is governed by various factors, including process and material parameters, orientation and location, and machines (Chen *et al.* 2018; Mele *et al.* 2021). The poor side surface roughness is often attributed to the "stair effect" that is an unavoidable consequence of the lase-wise building process, which significantly increases the surface roughness, particularly in an inclined surface when a larger layer thickness is applied. Meanwhile, the attached powders in partially melted condition and the balling phenomenon adversely affect the side surface roughness, while a coarse top surface is usually associated with rippled structures between adjacent tracks, balling, and spattered materials.

Parameter optimization is significant to control surface finish and accuracy, although many researches have been conducted to investigate the effects of process parameters on surface characteristics of SLM-ed Ti6Al4V (Hopkinson and Mumtaz ; Pal *et al.* 2020). It is difficult to obtain an ideal surface finish by adjusting parameters due to the special manufacturing nature in SLM. Recently, micro SLM (μ-SLM) technique (Fu *et al.* 2020; Wei *et al.* 2022) has been applied to increase the fabrication resolution by scaling down the laser spot size, but surface roughness is still about several microns.

Meanwhile, In an SLM process, the high energy density of a laser beam introduces a large temperature gradient when scanning at a high speed, which results in a non-uniform solidification, thus inducing tensile residual stress (TRS) in the near-surface layers (Fang *et al.* 2020; Liu *et al.* 2016; Van Belle *et al.* 2013). The TRS accumulates with an increase in part size, which may not only lead to part warpage, deformation, or even cracking during the fabrication process (Thijs *et al.* 2010; Yadroitsev and Yadroitsava 2015), but reduce the service performance (particularly fatigue and stress corrosion resistance) of parts (Waqar *et al.* 2022).

Additionally, internal defects such as pores, cracks, and lack of fusion, are easily induced during the complex SLM process (Gong *et al.* 2014; Zhang *et al.* 2017). Particularly, the defects distributed near the surface are easily induced due to the sudden starting, stopping, or turnaround of laser beam (Khairallah *et al.* 2020). Therefore, surface machining is necessary to improve the surface finish, induce compressive residual stress (CRS), as well as remove the defects in the surface layer.

2.1.4 Strength-ductility Trade-off Dilemma in SLM-ed Ti6Al4V

In structural applications, the simultaneous achievement of high strength to resist external loads and adequate ductility to accommodate deformation and prevent brittle fracture is of utmost importance. This delicate balance between strength and ductility assumes critical significance in industries like aerospace, automotive, and biomedical, where materials must exhibit exceptional mechanical strength alongside sufficient ductility to withstand dynamic loading and challenging service conditions (Han *et al.*

2023).

However, a common phenomenon known as the strength-ductility trade-off exists in many materials (Du *et al.* 2023; Gao *et al.* 2020). This trade-off manifests as an inverse relationship between strength and ductility. The pursuit of increased strength often results in a reduction in ductility, because strengthening mechanisms such as grain refinement, phase transformation, and solid solution strengthening can enhance the material's strength, but restrict the movement of dislocations that responsible for ductile deformation, leading to reduced ductility. Conversely, facilitating plastic deformation often leads to a reduction in strength (Guo *et al.* 2020).

The strength-ductility trade-off is widely encountered in SLM-ed Ti6Al4V. One of the key factors contributing to this trade-off is the presence of porosity in SLM-ed Ti6Al4V. The formation of pores or voids during the SLM process can act as stress concentrators, leading to premature failures. Pore size, distribution, and interconnectivity significantly influence the material's ductility, as they can initiate crack propagation and limit plastic deformation (Stef *et al.* 2018).

Another factor is the specific microstructure produced in SLM-ed Ti6Al4V. The exceedingly high cooling rate encountered during the SLM process surpasses the critical cooling rate of 410 K/s necessary for the martensitic transformation (β→α') in Ti-6Al-4V. As a consequence, SLM-ed Ti-6Al-4V predominantly exhibits acicular α' martensite rather than the equilibrium α and β phases (Kobryn and Semiatin 2001). The presence of acicular α' martensite in SLM-ed Ti6Al4V contributes to enhanced strength by impeding dislocation motion. However, this microstructural feature also leads to strain localization and imposes limitations on plastic deformation, ultimately resulting in a reduction in ductility.

The presence of residual stresses in SLM-ed Ti6Al4V also impacts the strength-ductility trade-off. The rapid heating and cooling rates during the SLM process result in the generation of significant residual stresses within the material. These stresses can influence crack initiation and propagation, reduce ductility and promote brittle fracture (Chen *et al.* 2019).

2.2 Conventional Machining Methods of Ti-alloy

2.2.1 Machining Methods and Challenges of Wrought Ti-alloy

Ti-alloy is known as an expensive material compared to other metals. This not only arises from the cumbersome fabrication processes, but the difficulties encountered in its mechanical machining. Presently, despite the popularizing and utilizing of Ti-alloy in many industries, Ti-alloy still suffers from poor machinability since it is a typical difficult-to-machine material. As shown in **Fig. 2.4**, The challenge of machining Ti-alloy is associated with its mechanical and physical properties (Niknam *et al.* 2014).

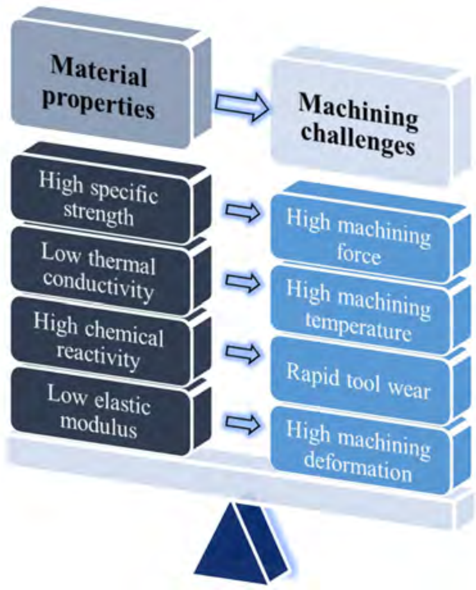

Fig. 2.4 Machining challenges of Ti-alloy and the corresponding material properties that cause these challenges.

Inherently, Ti-alloy has high specific strength, high work-hardening ability, and can maintain strength and hardness at elevated temperature, which result in high cutting force during the machining process. Meanwhile, the high temperature in machining of Ti-alloy is also a big challenge, which is associated with the low thermal conductivity and specific heat of Ti-alloy. For instance, the thermal conductivity of Ti6Al4V is 7.5 W/mK, which is much lower than that of steel (45 W/mK), copper (398 W/mK), aluminum (235 W/mK). Therefore, the machining heat cannot be dissipated through chips and workpiece during the machining process, the local overheating might cause surface burning or even cracking of the machined surface and severe tool wear. Meanwhile, many commonly used tool materials are chemically reactive to Ti-alloy due to its inherent high chemical affinity, which also accelerates the tool wear. And the springback phenomenon is also severe in the machining of Ti-alloy due to its low elastic modulus, which also aggravates the workpiece deformation and tool vibration.

Besides, the segmented chips are easily produced during the machining of Ti-alloy due to the particular physical properties. The formation of periodic cracks and adiabatic shear bands are two prevailing theories to explain the occurrence of segmented chips (Siju *et al.* 2022; Sun *et al.* 2014). Sun et.al (Sun *et al.* 2009) demonstrated that the frequency of cyclic cutting force was equal to that of the chip segmentation, thus such segmented chips were highly related to the dynamic cyclical cutting force (Jung *et al.* 2020). And the fluctuating cutting force is believed to result in a rough machined surface, chatter, and rapid tool breakage (Pramanik 2014).

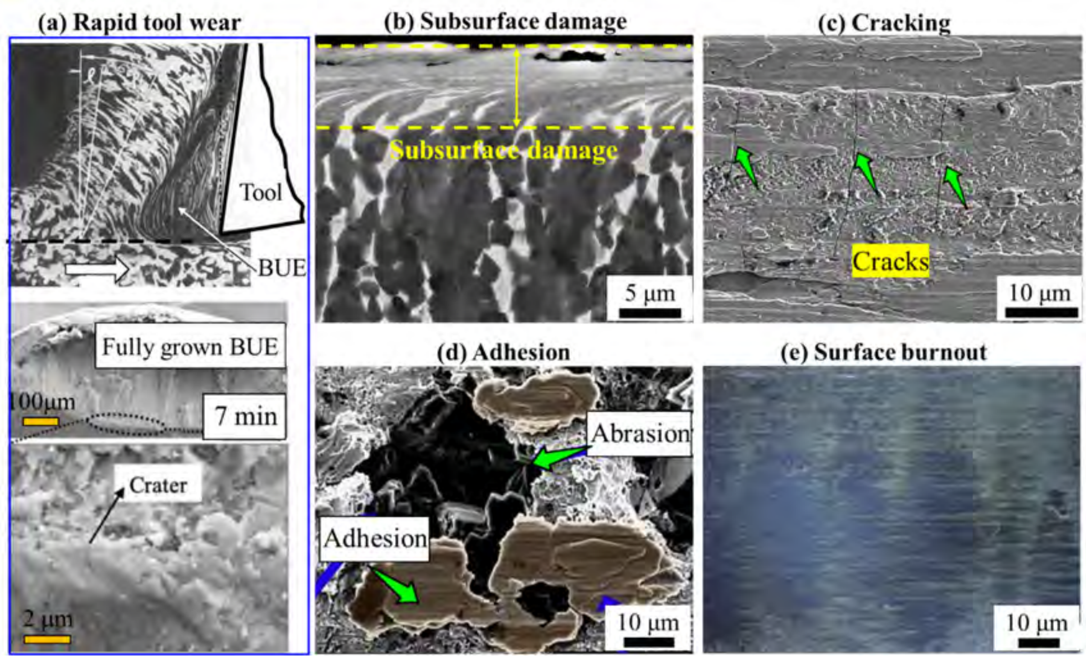

Fig. 2.5 Typical challenges in conventional machining of Ti-alloy: (a) Rapid tool wear (Mishra *et al.* 2021); (b) Subsurface damage; (c) Cracking (d) Adhesion ; (e) Surface burnout.

To overcome the machining difficulties of Ti-alloy, research efforts such as parameter optimization, developing new tool materials or design, improving cooling and lubrication systems have been extensively conducted. Meanwhile, advanced hybrid machining methods including laser-assisted machining (LAM), ultrasonic-assisted machining (UAM), and cryogenic machining (CM) have been extensively reported to machine Ti-alloy (Agrawal *et al.* 2021; Kalantari *et al.* 2021; Zhang *et al.* 2020). However, these methods are difficult to achieve high-quality and high-efficiency machining of Ti-alloy, and have not been widely applied in industry.

2.2.2 Machinability of Additively Manufactured Ti-alloy

Machinability is a concept widely employed in the fields of manufacturing and engineering to denote the difficulty level of machining or shaping a material through diverse machining processes, including cutting, drilling, milling, turning, or grinding. However, the machinability of a material is similar to the palatability of wine–easily appreciated but not readily measured in quantitative terms (Trent and Wright 2000). This is primarily due to the multitude of factors associated with the cutting process itself, including cutting tool, machining environment, and machining method, which can significantly influence the machinability of an alloy. Additionally, the inherent properties of the workpiece material, such as strength, ductility, and thermal conductivity, are also partially linked to its machinability.

Generally, cutting force, tool wear/tool life, surface integrity, material removal rate, and chip formation are the major criteria to evaluate the machinability of a material. Understanding the machinability of materials is significant for the selection of machining process and parameters, which is a prerequisite for improving machining efficiency, controlling machining cost and quality. As shown in **Fig. 2.5**, SLM-ed Ti6Al4V has distinctly different properties compared with its wrought counterpart due to the specific fabrication process. These changed material properties may significantly influence the machinability, resulting in new machining challenges. The detail comparison is as follows:

Intrinsically, SLM-ed Ti6Al4V has peculiar microstructures due to the inherent large temperature gradient and high cooling rate (10^3~10^6 k/s) during the SLM process. Acicular α' or lamellar α+β microstructure with ultrafine size are two typical microstructures of SLM-ed Ti6Al4V. In contrast, wrought Ti6Al4V usually exhibits equiaxed grains with grain size of micrometers to more than ten micrometers. Such a huge difference in microstructure leads to different material properties. From the previous studies, the as-built Ti6Al4V specimens by SLM usually exhibited a high strength but low ductility. The tensile strength of as-built SLM-ed Ti6Al4V can reach 1200-1300 MPa, while the elongation usually lower than 8%. For wrought Ti6Al4V, the tensile strength of usually ranges from 900 to 950 MPa, but superior ductility ups to 18% can be realized (Lewandowski and Seifi 2016; Xu *et al.* 2017). Meanwhile, SLM-ed Ti6Al4V also exhibits a higher hardness thanks to its refined microstructure (SLM-ed Ti6Al4V: 350~425 HV, wrought Ti6Al4V: 300~350 HV) (Al-Rubaie *et al.* 2020). Unlike to the isotropic wrought material, the SLM-ed Ti6Al4V shows high anisotropy caused by the layered manufacture principle. The typical columnar prior β grains distributed along the building direction tend to be produced due to the epitaxial growth, which induces strong anisotropy in microstructure and mechanical properties. Additionally, in an SLM process, the high energy density of a laser beam introduces a large temperature gradient when scanning at a high speed, which results in a non-uniform solidification, thus inducing tensile residual stresses (TRS) in the near-surface (Xiao *et al.* 2020).

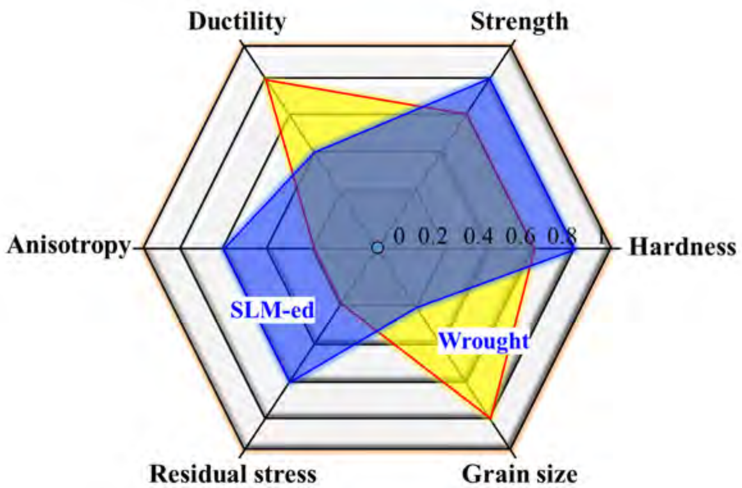

Fig. 2.6 Property comparison between SLM-ed and wrought Ti6Al4V.

Recently, increased number of researches regarding the machining of SLM-ed Ti-alloy have been published (Li *et al.* 2022; Malakizadi *et al.* 2022). Polishetty et al.

(Polishetty *et al.* 2017) compared the cutting force and surface finish of wrought and SLM-ed Ti6Al4V in turning process, it was found that the cutting force of SLM-ed Ti6Al4V was significantly higher than that of the wrought counterpart due to the higher strength of SLM-ed Ti6Al4V. Al-Rubaie et al. (Al-Rubaie *et al.* 2020) also investigated the machinability of wrought and SLM-ed Ti6Al4V in terms of surface roughness, cutting forces, tool wear, and chip morphology in toroidal milling. The SLM-ed Ti6Al4V was also reported to have higher cutting force and more severe flank wear, but low surface roughness. Meanwhile, they suggested that no significant changes in the chip morphology based on the visual analysis.

In addition to surface characteristics, the SLM-ed Ti-alloy shows completely different behaviors in terms of subsurface damage. In Giovanna's (Rotella *et al.* 2018) research, the wrought Ti-alloy exhibited superior surface finish, but larger plastic deformation layer. Meanwhile, Ni et al. (Ni *et al.* 2020) investigated the machining anisotropy of SLM-ed Ti-alloy, and the results indicated that the anisotropy of microstructure and mechanical properties resulted in high degree of anisotropic cutting force, surface morphology and surface roughness.

Overall, the SLM-Ti-alloy shows significantly different machinability compared to its wrought counterpart due to the peculiar microstructure and mechanical properties. The inherent refine microstructure improves the mechanical properties such as hardness, yield and ultimate strength of SLM-Ti-alloy, which is beneficial to improve the service performance, but also introduces more machining challenges. The recent studies have demonstrated that higher cutting force, cutting temperature, and more severe tool wear could be induced in the machining of SLM-Ti-alloy. However, the material removal mechanism, microstructure evolution and subsurface damage in the machining of SLM-Ti-alloy are still need systematic investigation. These knowledge and insight would provide scientific and practical guidance for the selection of machining parameters of SLM-Ti-alloy.

2.3 Microstructure Evolution in Machining of Ti-alloy

During a machining process, the microstructures in the machining influenced layer regarding grain size/orientation phase structures, and dislocation/twin are completely changed due to severe plastic deformation induced by large strain, high strain rate and temperature (Wu *et al.* 2023). As a result, the material physical and mechanical properties such as hardness, strength, and ductility undergo corresponding alterations, which finally influence the service performance and life of the machined parts. Understanding the complex microstructural changes is crucial for achieving desired performance of machined parts.

2.3.1 Grain Refinement

Grain refinement is a critical process for strengthening metals by reduction in size of the grains inside a material (Luqman *et al.* 2023). The commonly applied approaches for achieving grain refinement can be divided into four categories: vibration and stirring during solidification, induction of rapid solidification, addition of grain refiner and severe plastic deformation (Ren-Guo Guan 2017). During a conventional machining process, severe plastic deformation is induced by the interaction between workpiece material and cutting tool. Consequently, the microstructures in the subsurface of machined parts are substantially refined, and a gradient microstructure layer tends to be generated (Liao *et al.* 2019).

In the upmost layer of the machining influenced zone in Ti-alloy, a white layer, appearing as a white color under optical light microscopy, is commonly encountered. Chou et al. (Chou and Evans 1999) indicated that the white contrast of this layer was caused by its increased resistance to etchants compared with the bulk material, while Akcan et al. (Akcan *et al.* 2002) believed the phenomenon was ascribed to the scattering of light from the ultra-fine grains in the white layer.

White layer is widely observed in various machining processes such as turning (Zhang *et al.* 2021), milling (Brown *et al.* 2022), grinding (Rasmussen *et al.* 2017), electrical discharge machining (George *et al.* 2022). The formation of white layer is primarily attributed to two mechanisms: phase transformation and ultrafine grain structure (Griffiths 1987). Velásquez et al. (Velásquez *et al.* 2010) investigated the subsurface microstructure of Ti6Al4V alloy during orthogonal cutting condition, it is revealed that the grain structure in the white layer cannot be identified by SEM due to the significant grain refinement. Through the TEM observation, Brown et al. (Brown *et al.* 2019) revealed that the white layer induced during the milling of Ti6Al4V alloy was comprised of ultrafine equiaxed grains, characterized by an average diameter of less than 200 nanometers. However, no evidence of an $\alpha \rightarrow \beta$ phase transformation was identified. Moreover, the average grain size in the white layer of Ti6Al4V alloy can be effectively reduced to below 100 nm under high-speed milling (Xu *et al.* 2019).

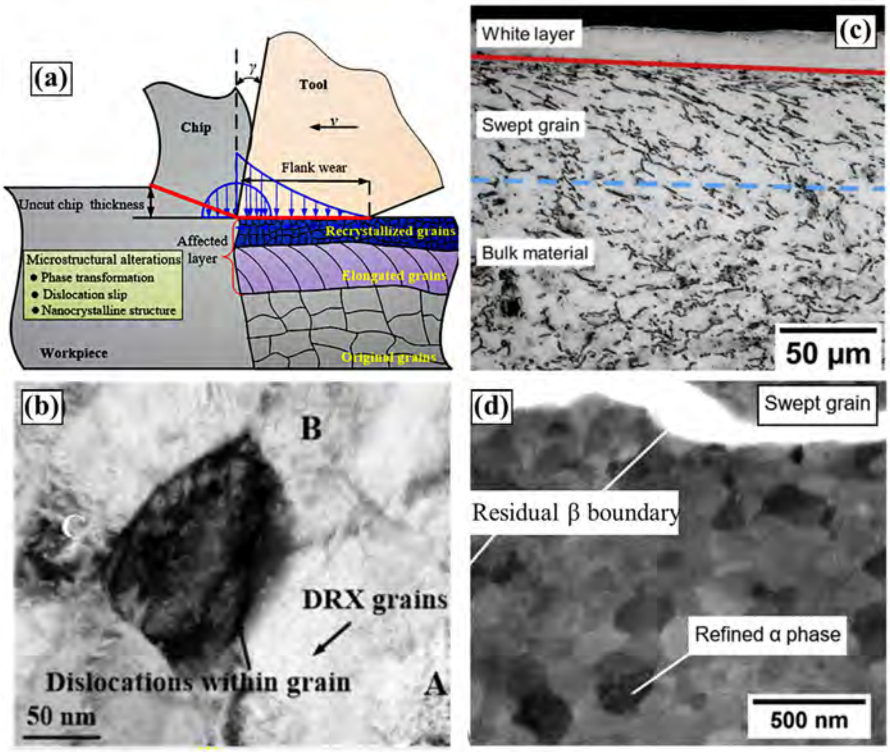

Fig. 2.7 (a) Subsurface microstructure alteration in the cutting of titanium ally; (b) TEM observation of the DRX grains in the white layer (Xu *et al.* 2019); (c) Optical micrograph showing a typical machining-induced white layers in Ti6Al4V; (d) Cross-sectional backscattered electron SEM image reveals the ultrafine grains in the white layer (Brown *et al.* 2019).

The formation of ultrafine grain structures of Ti6Al4V alloy induced by machining processes is indicated following the continuous dynamic recrystallization (CDRX) mechanism (Xu *et al.* 2019). The CDRX process is induced by the high geometrical necessary dislocation (GND) densities and dislocation cell structures. Under the influence of thermomechanical effect, dislocation migrated from the cell interior to the cell boundaries and pile-up at the low angle grain boundaries (LAGBs). The LAGBs transformed to high angle grain boundaries (HAGBs) by continuously consuming dislocation, leading to the final grain refinement. The DRX process is activated upon reaching the threshold of temperature and strain conditions. In contrast to the heat treatment process, the duration time of the thermomechanical impact is much shorter, which effectively limits the grain growth process, thereby promoting the formation of ultrafine grain structures by the DRX process.

2.3.2 Deformation twinning

Twinning is one of the important mechanisms of plastic deformation in metallic materials, which significantly influences the mechanical properties of metal materials. Extensive studies have demonstrated that the induction of twin structures is favor to enhancing material strength, balancing strength and ductility, as well as improving fatigue and irradiation resistances (Li *et al.* 2018; Li *et al.* 2023).

From a crystallographic perspective, twins refer to two crystals or two parts of a crystal that establish a mirror-symmetric orientation relationship along a shared plane (Li *et al.* 2023). Generally, twins can be categorized into three primary classifications based on varying formation mechanisms: (i) Growth twin: formed during the grain growth process in the fabrication processes; (ii) Annealing twin: formed by nucleation and growth during material annealing (iii) Deformation twin: formed in the plastic deformation process by the application of mechanical loading.

Ti6Al4V is a typical α+β Ti-alloy, in which the α-Ti is the main phase with higher volume fraction (Usually large than 90%). Therefore, the deformation behavior is primarily dependent on the α-Ti. α-Ti is a typical hexagonal close packed (HCP) structure with limited independent slip systems, hence the deformation twins are prone to occur during severe plastic deformation (SPD) process (Coghe *et al.* 2012). Simultaneously, deformation twins are also frequently observed in the β-Ti due to its low stacking fault energy (Bertrand *et al.* 2011).

Crocker et.al (Crocker and Bevis 1970) presented fifteen possible deformation twinning modes in titanium by theoretical analysis of the crystallography. However, the commonly observed twins in titanium mainly include: $\{10\bar{1}2\}$, $\{11\bar{2}1\}$, $\{11\bar{2}2\}$, $\{10\bar{1}1\}$ (Wang *et al.* 2015). Among these, $\{10\bar{1}2\}$ and $\{11\bar{2}1\}$ belong to tension twins, while $\{11\bar{2}2\}$ and $\{10\bar{1}1\}$ are the compression twins. The activation of different types of twins is highly connected to the deformation conditions such as strain, strain rate, and temperature. In the quasi-static plastic deformation at ambient temperature,, it is revealed that $\{10\bar{1}2\}$, $\{11\bar{2}1\}$, $\{11\bar{2}2\}$ are popular twin types (Rosi 1957), while $\{10\bar{1}1\}$ twin tends to be activated at high strain rate and high temperature deformation conditions because of the reduction of critical resolved shear stress for $\{10\bar{1}1\}$ twin. For instance, Zhong et.al (Zhong *et al.* 2018) found that the $\{10-11\}$ twinning system was the dominant twinning mode in the additively manufactured Ti6Al4V. Furthermore, $\{10-11\}$ twin is commonly observed in the subsurface of Ti6Al4V machined by high-speed machining (Wang and Liu 2016).

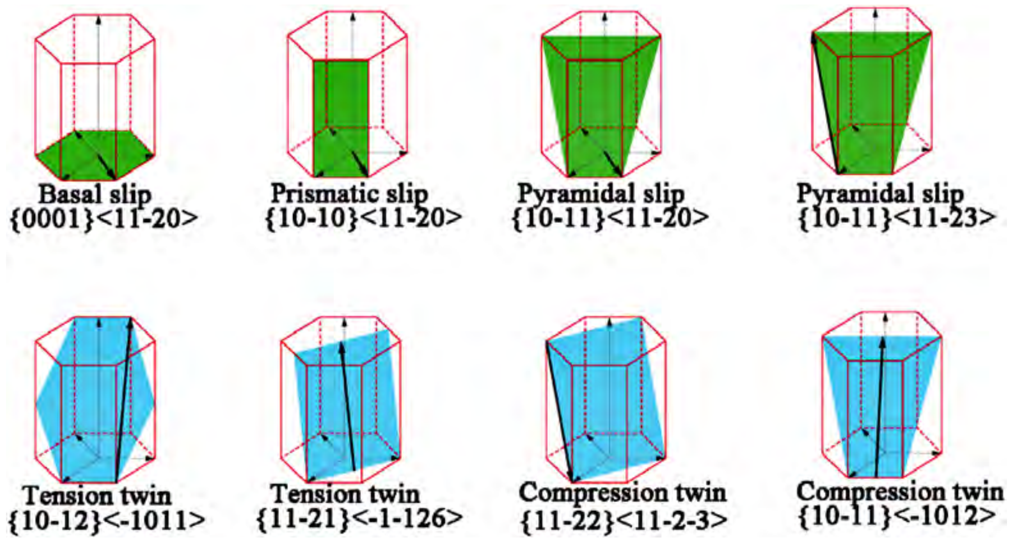

Fig. 2.8 Typical slip systems and twinning modes in Ti alloys (Zhong *et al.* 2018).

2.3.2 Transition Between Dislocation Slip and Deformation Twinning

Dislocation slip and deformation twinning are two primary plastic deformation mechanisms in metallic materials. They interact and compete with each other to coordinate plastic deformation. Nevertheless, in specific scenarios, the dominant role transits between these two mechanisms (Qi *et al.* 2022). The transition between dislocation slip and deformation twinning is governing by numerous factors including strain rate, temperature, stacking fault energy (SFE), grain size, etc.

Deformation strain rate and temperature are considered as the most primary influence factors on deformation modes. In conventional HCP metals, higher strain rates and/or lower temperatures are effective to promote the deformation twinning (Wang *et al.* 2015). Nicolò Maria et.al (Nicolò Maria *et al.* 2023) investigated the micromechanical behavior of pure magnesium under varying strain rates and temperature conditions, and the results indicated that for T≤423 K, the deformation was dominant by twinning within the entire range of applied strain rates. However, at T>423 K, the deformation twins were not observed at the strain rate below 10 s^{-1}, and instead, prismatic dislocations became the dominant mechanism due to the reduction in the critical resolved shear stress of non-basal slip. For $\dot{\varepsilon}$ >10 s^{-1}, the slip to twin transitions took place as the dislocation slip could not match the high deformation rate.

Additionally, SFE plays a significant role in the deformation behavior of crystalline materials. In materials with high SFE, the lower energy barriers and easier cross-slip make dislocation slip the dominant mechanism for accommodating plastic deformation (Mills and Neeraj 2001). For instance, deformation twins are difficult to be produced in aluminum with high SFE even under shock-loaded at low temperature (Gray 1988). In contrast, the twinning tendency is much higher in materials with low SFE. Deformation twins are abundant in many low SFE metals like copper and steel (Qiao *et al.* 2024; Tian *et al.* 2022).

Furthermore, grain size also influences the competition between dislocation slip and deformation twinning. It has been demonstrated that deformation twinning was significantly inhibited in copper alloys as the grain size decreased to sub-micrometer level (Zhu *et al.* 2013). This phenomenon is ascribed to the fact that the activation stress of twin boundaries increases more rapidly with decreasing grain size compared to the activation stress of dislocation slip. Similar effect was identified in titanium, Sun et.al (Sun *et al.* 2013) concluded that the deformation twinning propensity constantly decreased as the grain size decreased from several microns to 50 nm.

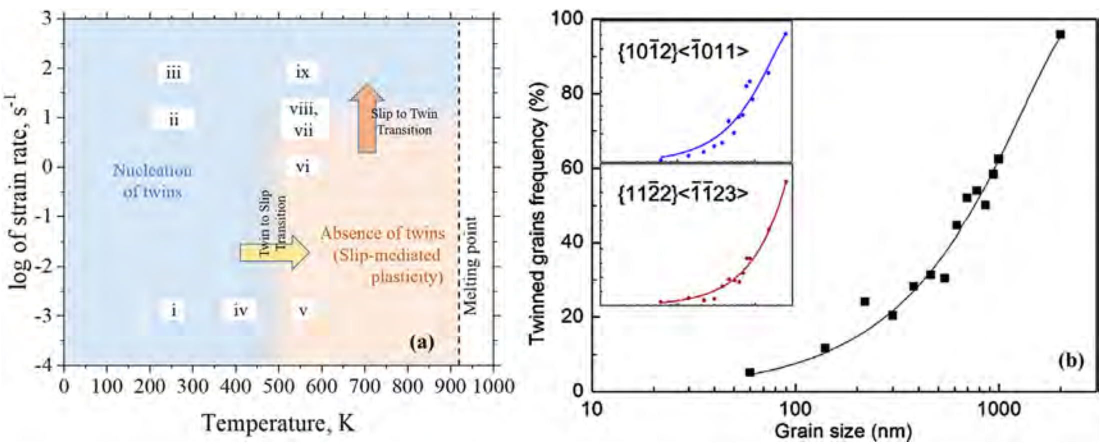

Fig. 2.9 (a) Dislocation/twinning transition map in magnesium across various temperature and strain rate (Nicolò Maria *et al.* 2023); (b) Grain size effect on the twinning frequency in titanium (Sun *et al.* 2013).

2.4 Ultra-high-speed Machining Process

2.4.1 Definition of Ultra-high-speed Machining

Improving productivity and quality and cutting costs are eternal pursues of machining process. To achieve these goals, high performance machining techniques have been pursued by both academia and industries. Ultra-high-speed machining (UHSM) has attracted much attention in recent years, because it not only has enormous advantages in improving machining efficiency and accuracy, reducing tool wear, but can inhibit the subsurface damage in manufactured parts (Chen *et al.* 2015; Shi *et al.* 2017; Sun *et al.* 2019).

Machining methods can be divided into three classes in terms of the speed ranges, namely conventional speed machining (CSM), high speed machining (HSM), and Ultra-high-speed machining (UHSM). Nevertheless, there is no unified and definitive standard for defining these three speed ranges. **Fig. 2.10** shows different definitions of speed ranges. In 1931, Salomon was granted a German patent about HSM, he first proposed the concept of HSM and the hypothesis of cutting-temperature versus speed relationships based on a series of experiment. The curve indicated that there is a turning point, that is, when the cutting speed exceeds this turning point, the cutting temperature will drop rapidly. Nevertheless, the existence of Salomon curve is not been verified and still being debated as open questions. Icks (Tuffentsammer and Icks 1982) suggested that HSM was within the speed range of 1000-10000 m/min and depended on the machining processes. And Schulz (Schulz and Moriwaki 1992) defined different high speed ranges for several materials in 1994.

Schnieider proposed a fixed classification in three areas of cutting speed: CSM: ≤500 m/min; HSM: 500-10000 m/min; UHSM: ≥ 10000 m/min. In 1998, Tonshoff et.al (Tönshoff *et al.* 1998) suggested that HSM can be defined as machining at cutting speeds with an essential overstepping of conventional speeds. While Denkena et.al (Denkena *et al.* 2007) recommended a material specific definition of HSM range by considering the mechanical and thermodynamic properties of machined material in 2007. Wang et.al (Wang *et al.* 2015) gave a classification method base on chip formation: HSM: Adiabatic shearing band (ASB) formation; UHSM: fragmented chip formation.

Apparently, it is difficult to define the boundaries of CSM, HSM, and UHSM by specific speed ranges. The speed range is a relative concept, which is not only depends on multiple factors such as machining processes and machined materials, but changes with the development of machining processes (Arndt 1973).

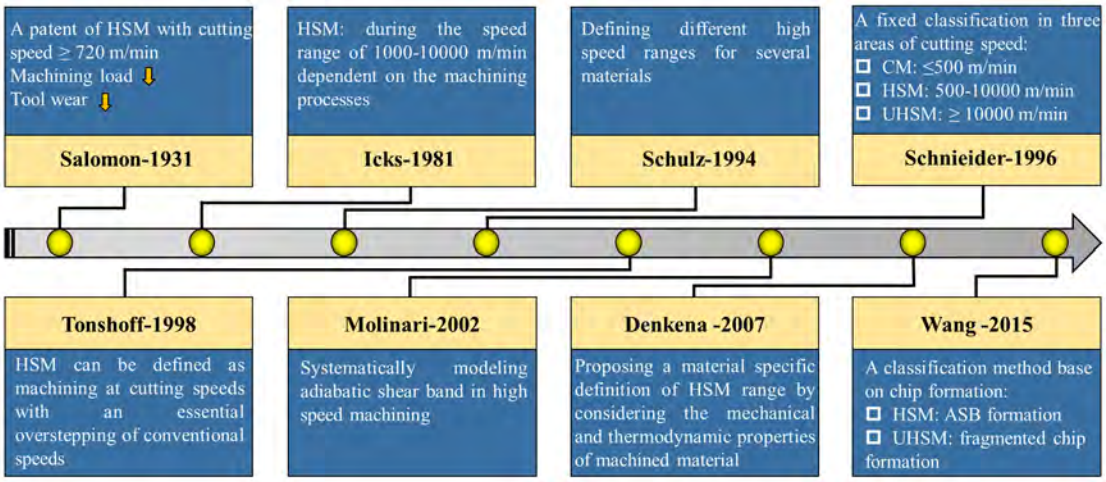

Fig. 2.10 Different definitions of speed ranges.

2.4.2 Material Removal Mechanisms in UHSM

With the rapid development of machine tool, the machining speed constantly increases. The UHSM is a complex physical process accompanying with large strain, high strain rate and high temperature in a local deformation region (Wang *et al.* 2021). The material removal mechanisms during the UHSM may completely different from that during the conventional machining because of the alterations of material deformation behaviour and material response. Therefore, investigations of material dynamic response and material deformation behaviour are necessary to understand the material removal mechanisms in UHSM.

2.4.2.1 Material dynamic response in UHSM

As shown in **Fig. 2.11**, material responses can be divided into static response, quasi-static response, and dynamic response according to different strain rate. For instance, creep test is generally considered as a static process due to its very low strain rate, while tensile/compression tests fall into quasi-static process. And conventional cutting and grinding belong to dynamic process because of their increased strain rate. For UHSM, the strain rate is higher than 10^7 s^{-1}, and materials have been demonstrated with distinctive mechanical properties under such high strain rate.

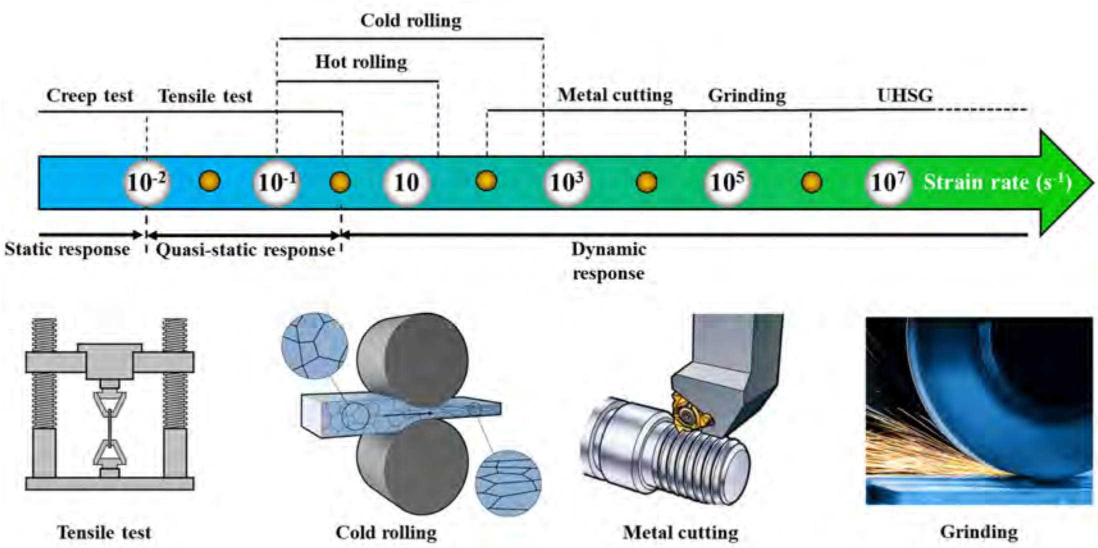

Fig. 2.11 Material response classifications and corresponding applications.

The flow stress-strain response is demonstrated to be strongly dependent on the loading conditions such as strain rate and stress state (Lee *et al.* 2007). Hu et al. (Hu *et al.* 2020) investigated the mechanical behaviours of Ti6Al4V over a wide range of strain rates. The results indicated that the initial failure strain decreased with increasing strain rate, while higher work-hardening rate was observed at higher strain rate.

As the increase of loading rate, both the tensile strength σ_b and yield strength σ_s tend to increase, but the increase rate of σ_s is higher than that of σ_b. As a result, the yield-to-tensile ratio (σ_s/σ_b) is infinitely close to 1 at very high loading rate (Wang *et al.* 2015). In this case, the material plasticity significantly decreases, and the material may fracture without apparent plastic deformation. Accordingly, the ductile materials exhibit similar dynamic response with brittle materials. As shown in **Fig. 2.12b**, Wang et al. (Wang *et al.* 2015) elaborated the mechanical response of materials under different strain rate, and the ductile material experienced severe plastic deformation at low strain rate. Nevertheless, when the strain rate exceeded the critical value of ductile-to-brittle transition (Point E), the ductile material undergone a brittle fracture.

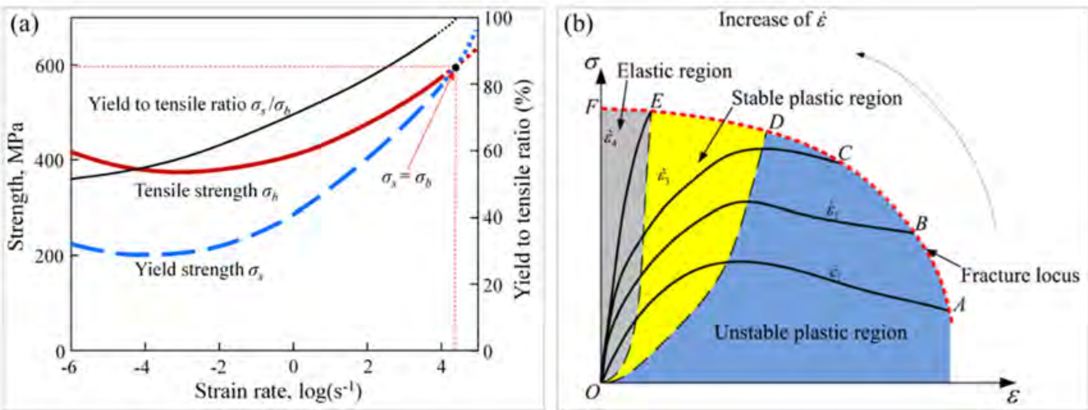

Fig. 2.12 (a) Material strength under different strain rate (Wang *et al.* 2015); (b) Mechanical response of materials under different strain rate (Wang *et al.* 2015).

As shown in **Fig 2.13**, Zhang et.al (Yang and Zhang 2019) investigated the effect of strain rate on Δσ (Difference between ultimate tensile strength and yield strength) by summarizing the experimental date from different researchers. They described the relationship between Δσ and strain rate by the following equation:

$$\Delta\sigma = k_0 - k_s \ln \dot{\varepsilon} \tag{2.1}$$

where k_0 is a material constant; k_s represents strain-rate sensitivity on material embrittlement, $\dot{\varepsilon}$ is strain rate. They divided materials into three types according to their strain-rate sensitivity, among which the type I materials with the highest k_s are the most susceptible to embrittlement at high strain-rates, while the type III materials are of the lowest k_s and the least susceptible to embrittlement. Particularly, Ti6Al4V with strain-rate sensitivities of 35.4 belongs to the type I, which is very sensitive to strain rates and susceptible to embrittlement at high strain-rates.

The establishment of material constitutive model is an effective method to investigate the material response during machining process. For conventional machining, the maximum strain rate is usually within 10^5 s^{-1}, Johnson-Cook (JC) constitutive model is the most commonly used model to describe material dynamic deformation within that strain rate range. Presently, mechanical test particularly split Hopkinson pressure bars (SHPB) test is widely applied to obtain the constitutive parameter. Although some high-velocity impact tests such as explosives, pulsed laser, exploding foil can be up to 10^7 s^{-1}, it is very difficult to precisely measure the constitutive parameters at very high strain rate (Edwards 2006). Therefore, the constitutive model suitable for describing material dynamic behaviours in UHSM is yet to be established, and this raises enormous challenges to the investigation of the deformation process in UHSM.

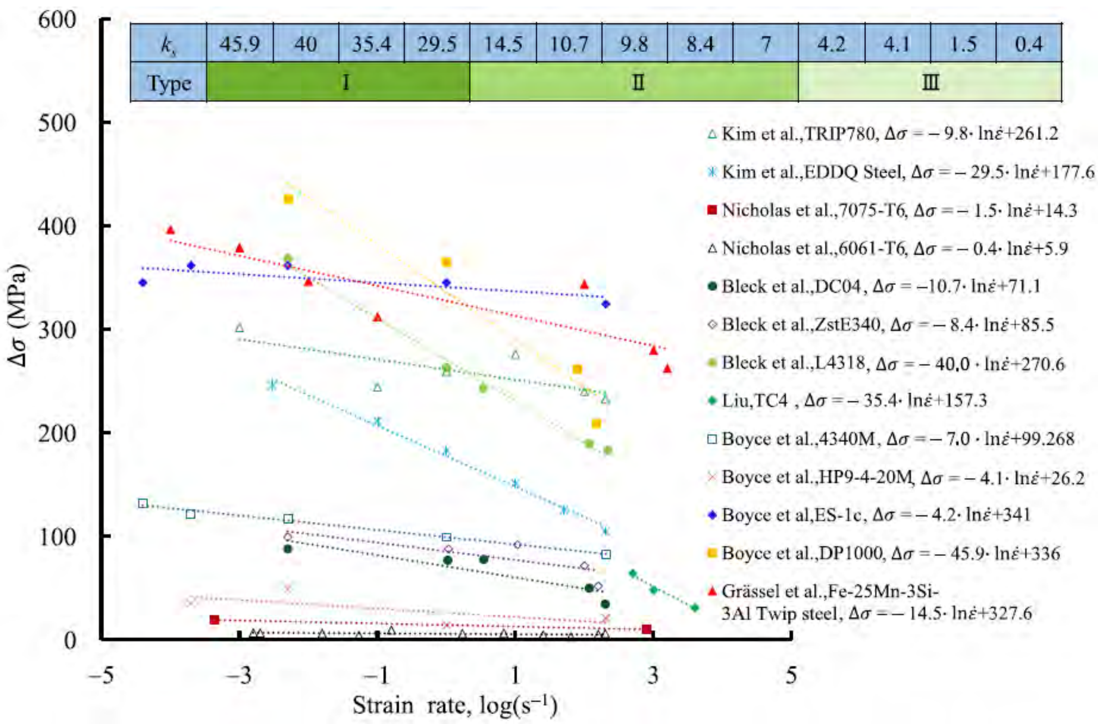

Fig. 2.13 Effects of strain rate on Δσ (Yang and Zhang 2019).

2.4.2.2 Ductile-to-brittle transition in UHSM

Material embrittlement phenomenon can be observed in many circumstances, and it can be induced by various conditions, including process related (Welding, high strain rate loading, and triaxial tensile stress loading) and environment related (Hydrogen, irradiation, corrosion, and low temperature) (Darnbrough *et al.* 2015; Stepanov *et al.* 2015; Xing *et al.* 2017). The material embrittlement in machining is intimately tied to the strain rate, particularly during UHSM where strain rate can reach up to 10^7 s^{-1}, making the material susceptible to embrittlement.

Zhou et al. (Zhou *et al.* 2003) suggested that the ductile materials were expected to behave like a brittle material during machining when the cutting speed v_c exceeded the plastic wave propagation speed v_p. They calculated the v_p of pure aluminum (A1199) and aluminum alloy (A5056), and found that the corresponding v_p were 200 m/s and 300 m/s respectively. Meanwhile, they conducted UHSM experiment on these two materials, and the results illustrated that the plastic flow was significantly inhibited at the grinding speed beyond v_p. Additionally, the results of surface roughness and hardness tests showed that the v_p was the breaking point, and better surface quality and less working hardening can be achieved as the machining speed higher than v_p.

$$v_p = \sqrt{\frac{1}{\rho}\frac{\partial \sigma_p}{\partial \varepsilon_p}} \tag{2.2}$$

Wang et al. (Wang *et al.* 2015) calculated the critical speed of ductile-to-brittle transition for 7075-T7451 aluminum alloy, and they suggested that the brittle regime machining of this material would be achieved when the machining speed was up to 70 m/s. They also conducted orthogonal cutting experiments of 7050-T7451aluminum alloy at a wide cutting speed range (0.83~133 m/s), and the results verified a transition of material removal mechanisms existed as the increase of strain rate.

These researches on critical condition of ductile-to-brittle transition are of great importance and are instructive for the UHSM of ductile materials. Nevertheless, the mechanical properties may change as the increase of loading rate, resulting in alteration of plastic wave propagation speed. Meanwhile, the material fracture and damage mode are also highly related to material microstructure, stress state, and internal defects. Therefore, the critical transition speed is hard to precisely predict the ductile-to-brittle transition behaviour.

In addition to the stress wave, Zhang et al. (Yang and Zhang 2019) analysed the underlying mechanism of strain rate induced material embrittlement from the aspect of dislocation kinetics. They pointed out that the dislocation movement strongly influenced the material embrittlement. Dislocations have sufficient time to overcome barriers during a plastic deformation process at a low strain rate. However, if a material is subject to loading at a very high strain-rate, dislocations do not have enough time to overcome the barriers, which results in dislocation pile-up, and eventually brittle fracture instead of plastic deformation. That is why a ductile material embrittled at an ultra-high train rate.

2.4.2.3 Material deformation behavior in UHSM

The material dynamic response determines the material deformation behavior, and the material deformation behavior strongly influences the final machining quality. The material removed undergoes severe plastic deformation during a machining process. As shown in **Fig. 2.14**, the material deformation in a metal cutting process is mainly distributed in three deformation zones, including primary deformation zone, secondary deformation zone, and tertiary deformation zone. The primary plastic or shear deformation occurs in the primary deformation zone, while plastic deformation due to the friction between the chip and the tool takes place in the secondary deformation zone. Also, frictional rubbing occurs between the workpiece and the tool flank face.

During machining, the material is removed in the form of chips with different morphologies and shapes, depending on the workpiece material and process parameters. The chip formation has attracted intense scientific interest because it reflects the material removal mechanisms. For conventional machining of Ti-alloy, the segmented chips are easily produced due to particular physical properties. Presently, the formation of periodic cracks and ASBs are two prevailing theories to explain the occurrence of segmented chips (Siju *et al.* 2022; Sun *et al.* 2014). However, different chips and chip formation process are involved as the increase of machining speed due to the completely different material dynamic response.

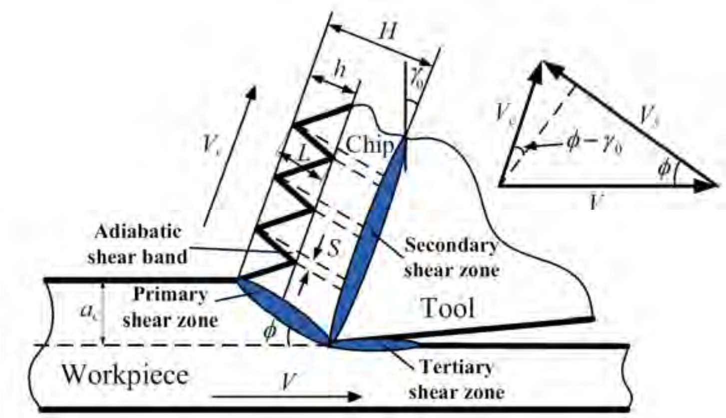

Fig. 2.14 Schematic diagram of metal cutting.

As shown in **Fig. 2.15**, Wang et.al (Wang and Liu 2015) investigated the evolution of chip morphology of Ti6Al4V at different cutting speeds by both simulation and experiment. The results indicated that higher degree of serrated characteristic tend to occur at higher cutting speed (Chip serrated degree: *G* (Given by Eq, 2.3, H and h are defined in Fig. 2.14)), and the chip morphology was transformed from serrated to fragmented at 2500 m/min. This phenomenon was also been observed in Gay et al' study (Sutter and List 2013), the cutting speed plays a dominant role on the chip formation. As the cutting speed increases, the shear frequency of the chip formation linearly increases, smaller serrated elements are formed, and such elements tend to be separated when the cutting speed exceeds a critical value. The fragmented chips were formed at speed of 45 m/s under depth-of-cut of 0.1 mm, while the critical speed decreased to 35.6 m/s when the depth-of-cut of 0.25 mm was applied.

$$G = \frac{H-h}{H} \tag{2.3}$$

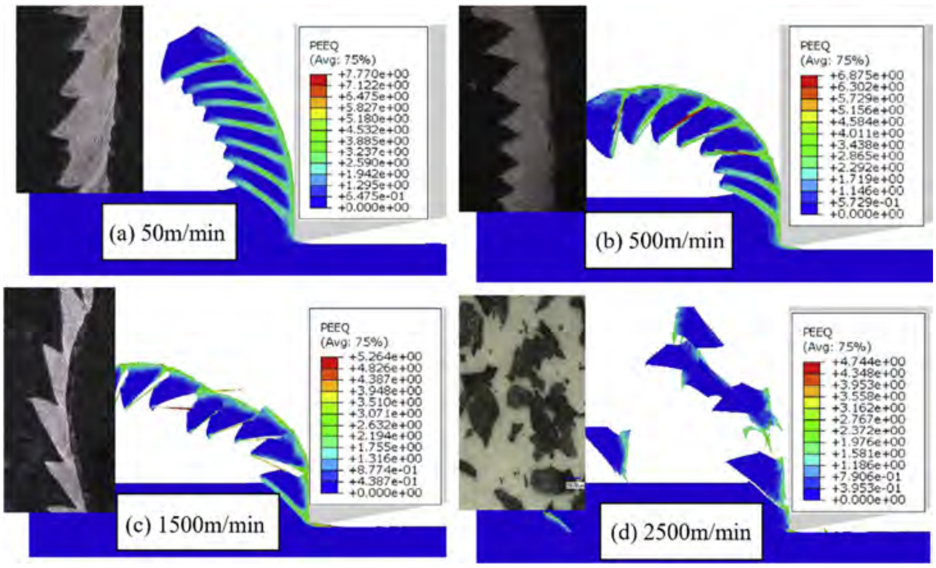

Fig. 2.15 Evolution of chip morphologies of Ti6Al4V at different cutting speeds (Wang and Liu 2015).

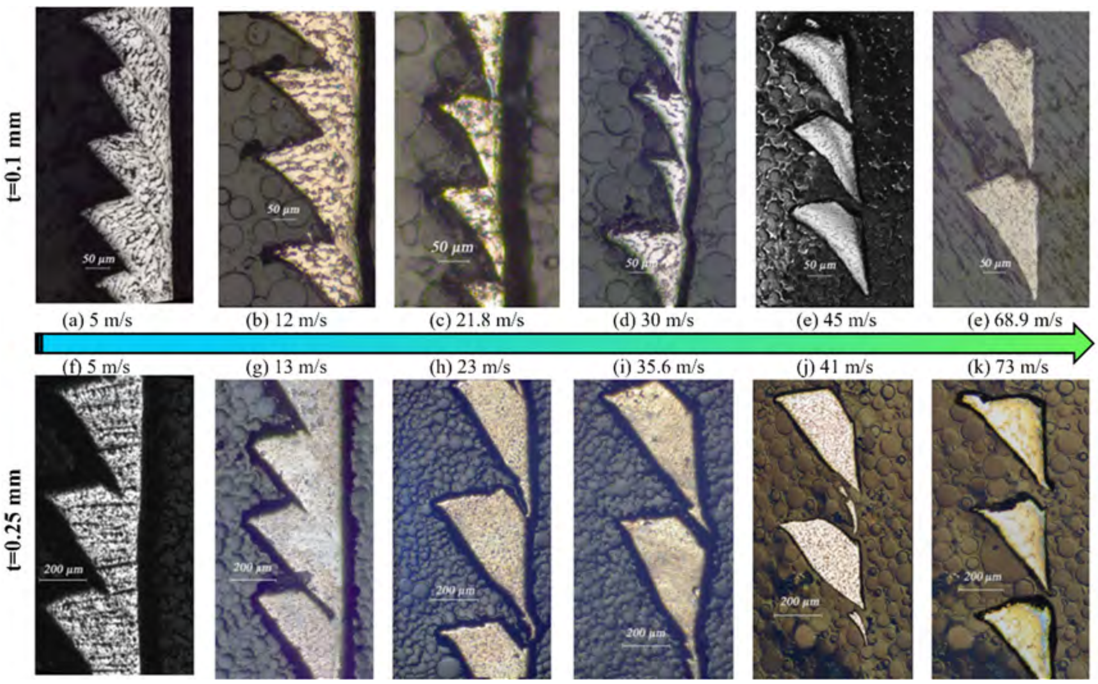

Fig. 2.16 Chip morphologies of Ti6Al4V at different cutting speeds with two depth-of-cut: (a)-(e) t=0.1mm; (f)-(k) t=0.25 mm (Guy and Gary 2013).

2.4.3 Subsurface Damage in UHSM

During a machining process, subsurface damage such as metamorphic layer, and cracks are easily introduced, which significantly degrades the service performance of a part (Aramcharoen *et al.* 2008; Wang C *et al.* 2016). However, most researchers focus more on surface characteristics and ignore the MDZ, which can lead to misleading results sometimes. According to Zhang's experimental results, even for parts without any observable damage, severe MDZ could be existed in their subsurface (Bi *et al.* 1988; Zhang and Howes 1994). UHSM, as an advanced manufacturing technique, has huge potential to control MDZ by increasing strain rate.

The damage distribution of engineering materials in UHSM process is governed by the "skin effect". In essence, the machining-induced MDZ is prone to distribute in the superficial layer of a workpiece machined at a high strain rate (Zhang and Yin 2019). In a review paper, Zhang et.al (Zhang and Yin 2019) revealed the effect of strain rate on the MDZ of brittle materials at different strain rates during machining. As shown in **Fig. 2.17**, the MDZ depth in the brittle materials decreased with increasing strain rate, which well depicts the "skin effect" of damage formation in terms of strain rate. Additionally, a theoretical equation was concluded to quantitatively describe the relationship between MDZ and strain rate according to the best fitting line in **Fig. 2.17**:

$$\delta = \mathrm{k} \cdot \left(\frac{d\varepsilon}{dt}\right)^{-0.34} \tag{2.4}$$

where k is a constant (k=1531 in **Fig. 2.17**).

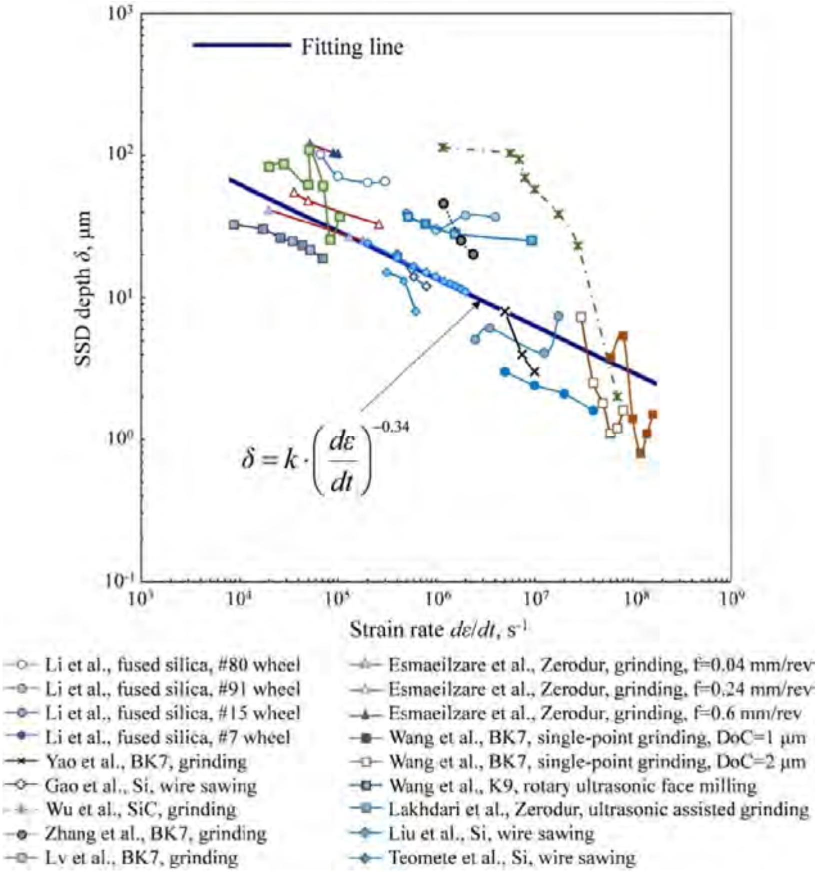

Fig. 2.17 MDZ depth of the hard and brittle materials at different strain rates in machining (Zhang and Yin 2019).

In addition to hard and brittle materials, the “skin effect” of MDZ was also identified in metallic materials such as In-718 (Pawade *et al.* 2008), D2 tool steels (Kishawy and Elbestawi 2001), nickel-based ME16 superalloys (Veldhuis *et al.* 2010). Guo et al. (Guo *et al.* 2022) investigated the MDZ distribution of Al6061T6 alloy at a linear grinding speed of 30.4~307.0 m/s, and the results revealed that the dynamic recrystallization zone (DRXZ) significantly decreased from 2.1 μm at 30.4 m/s to 0.4 μm at 307.0 m/s, manifesting a distinct damage skin effect.

Zhang et.al analysed the underlying mechanisms of the “skin effect” based on the principles of dislocation kinetics and crack initiation and propagation. They indicated that the dislocations tended to be attracted to the free surface by image force in a loading process, which resulted in higher dislocation density in the skin layer of the material than that in the deeper layers. Particularly, dislocation density should have a larger gradient at a higher strain rate. Under such condition, dislocation entanglement first takes place in the skin layer, followed by crack nucleation and propagation. As a result, the distribution of MDZ follows the “skin effect” at a high strain rate.

From the energy point of view, material damage is a way to relax energy, and the damage tends to propagate to where the energy requirement is the lowest for its formation according to the minimum energy principle. Since the free surface has the lowest energy for damage formation compared to other locations within the material, damage tends to propagate towards the free surface (Zhang and Yin 2019). However, the “skin effect” of MDZ is collectively controlled by numerous factors such as strain rate, dislocation movement, stress distribution, and material properties, thus its internal mechanisms are very complicated and are not fully understood.

Chapter 3 Research Methodology

3.1 Research Framework

To address the challenges in manufacturing and processing of high-performance Ti-alloy parts, this study systematically investigated the SLM manufacturing and UHSM of Ti-alloys. The thesis framework is illustrated in **Fig. 3.1**. Despite the various advantages that SLM offers for the manufacturing of Ti-alloy, SLM-ed Ti6Al4V parts still encounter a trade-off dilemma between strength and ductility. Furthermore, the intrinsic coarse surface and poor surface accuracy of SLM-ed Ti6Al4V parts cannot meet the high requirement of surface quality in some critical applications. Therefore, surface machining is necessary for the critical surface of SLM-ed Ti6Al4V parts.

However, Ti6Al4V alloy is known as a typical difficult-to-machine material due to its low machinability and poor surface integrity. Conventional machining methods struggle to achieve high-efficiency and high-quality machining of Ti6Al4V alloy. UHSM offers advantages in achieving high-efficiency machining while ensuring high machining quality. Nevertheless, the mechanisms that govern the material removal and deformation in the UHSM of Ti6Al4V alloy remain unclear. Additionally, the impact of the unique microstructure of SLM-ed Ti6Al4V on machining characteristics at different machining speeds has not been thoroughly explored.

To address the aforementioned critical problems, this thesis is structured into four parts for in-depth investigations. The first part focuses on the SLM manufacturing of Ti6Al4V alloy and involves systematic examinations and characterizations regarding processes, structures, and properties. Firstly, this study starts with the development of densification map and process map for SLM-ed Ti6Al4V based on process optimization studies, thus providing guidance for the parameter selection of SLM-ed Ti6Al4V. Subsequently, the study systematically unveils the microstructure evolution and defect formation mechanisms at varying energy densities. Moreover, an exploration of the tensile properties and fracture mechanisms of SLM-ed Ti6Al4V is carried out. Lastly, building on the comprehensive findings, an in-depth analysis of process-structure-property relationships is undertaken, providing a pathway for the SLM manufacturing of strong and ductile Ti6Al4V alloy.

The second part is devoted to investigate the material removal and deformation mechanisms of coarse-grained wrought Ti6Al4V. To facilitate the mechanism study, an experiment system is designed and developed to achieve extremely high-speed SPS. A series of SPS experiments at speeds ranging from 20 to 220 m/s are performed, and the material removal mechanisms under different strain rate conditions are revealed by considering surface creation, subsurface deformation, and chip formation.

For the surface creation, the 3D surface morphology is captured using a laser scanning confocal microscopy (LSCM), and the pile-up ratio is quantitatively analyzed via the MULTI-FILE ANALYSIS software. Furthermore, the subsurface microstructures are systematically investigated. Both cross-sectional and longitudinal section TEM lamellae are extracted by FIB to examine the global distribution of machining deformation zone (MDZ) and the subsurface microstructure evolution. Advanced STEM and TKD techniques are combined to characterize the micro-scale and nano-scale features across a wide range of strain rate machining conditions. Additionally, to examine the transitions of chip formation mechanisms from low-speed to ultra-high-speed machining, both the chip morphology and the corresponding sectional microstructure evolution are detected. Lastly, for deeper insights into the deformation mechanism and microstructure evolution, FEM simulations for single-point grinding are conducted to evaluate the strain rate/strain/temperature distributions under different speed conditions.

Building upon the foundational theories and research methodologies established in the second part, the third part delves into the material removal and deformation mechanisms of SLM-ed Ti6Al4V. Due to pronounced discrepancies in microstructure and mechanical properties, SLM-ed Ti6Al4V exhibits different machining characteristics compared with its wrought counterpart. These discrepancies induce notable variations in the material removal mechanism. In light of this, in addition to systematic investigations that involve the analysis of surface morphology, profile, subsurface microstructure evolution, and chip formation characteristics, a comprehensive comparison is performed to evaluate the differences in material removal and deformation mechanisms between the wrought and SLM-ed Ti6Al4V.

The material removal mechanisms of both wrought and SLM-ed Ti6Al4V are investigated and elucidated by SPS studies. However, the SPS technique can not directly applied to the processing of industrial components. To verified the universality of UHSM theories and promote the application of UHSM, the fourth section focuses on the UHSG of Ti-alloy. Here, a UHSG system, equipped with a high-speed hydrostatic bearing motorized spindle and a carbon fiber reinforced plastics (CFRP) matrix CBN grinding wheel, is developed to achieve UHSG machining with a maximum linear speed reaching up to 250 m/s. A comprehensive analysis of the surface integrity encompassing both surface and subsurface of the machined specimens is performed. Meanwhile, detailed explorations are undertaken to investigate the transition of dominant deformation mechanisms across various speed regions and their effects on surface integrity. Finally, a systematic evaluation and comparison of the machinability of both wrought and SLM-ed Ti6Al4V is provided.

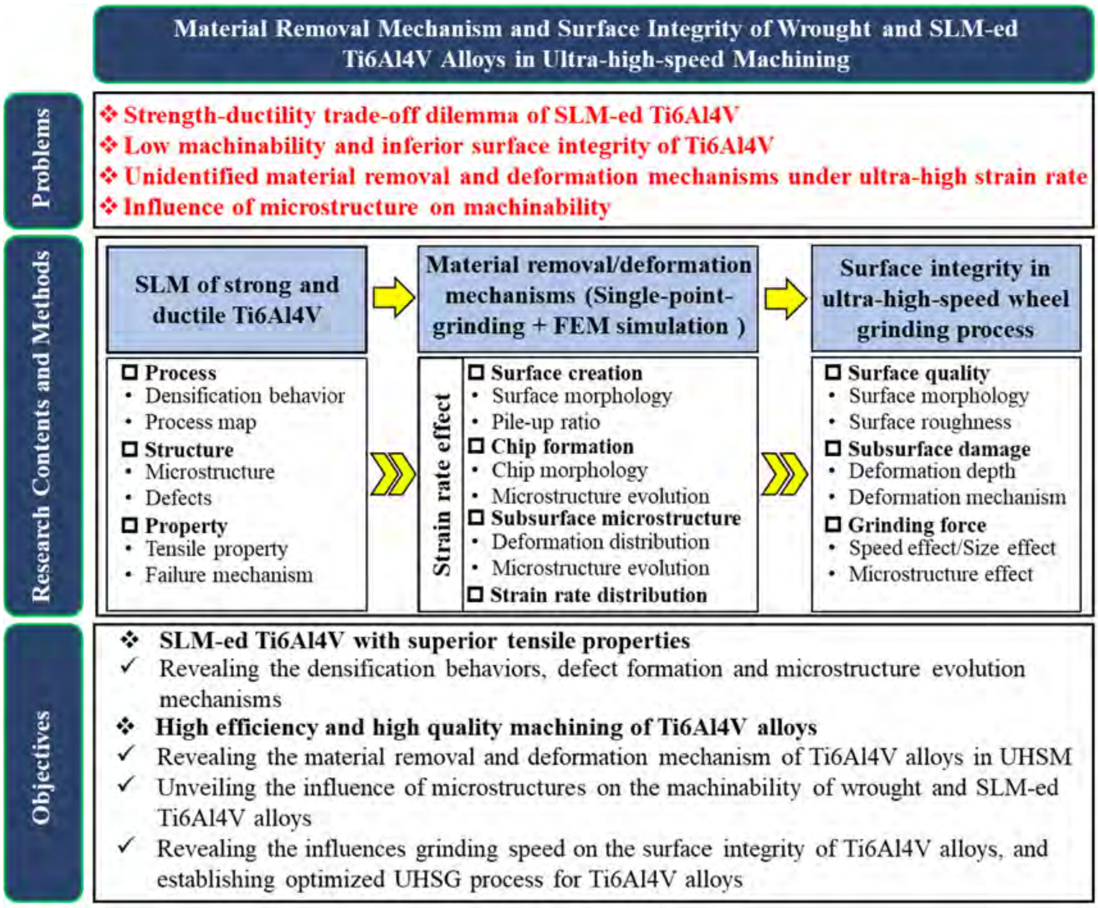

Fig. 3.1 Framework of the thesis.

3.2 Material Characterization Methods

In this thesis, advanced characterization tools such as SEM, EBSD, TKD, FIB, and STEM are combined to achieve multiscale characterization. These approaches enable the extraction of vital information ranging from the surface (3D morphology, surface roughness, 2D profile) to the subsurface (grain size/distribution, phase structure, dislocation/stacking fault, nanocrystalline/nano-twin). Through the comprehensive utilization of tools, a detailed analysis is formulated concerning defect formation, microstructure evolution, and material deformation mechanisms.

Fig. 3.2 Characterization equipments: (a) Scanning electron microscopy (SEM); (b) X-ray diffraction (XRD); (c) Transmission electron microscopy (TEM); (d) Ultra-depth three-dimensional microscopy (UDTDM); (e) Focus ion beam system (FIB); (f) Wire electro discharge machine (WEDM).

3.3 Research Originality and Significance

This thesis provides an original study on the SLM manufacturing and UHSM processing of high-performance Ti-alloy parts. The originality and significance of this thesis can be identified as follows:

(1) Achieving the manufacture of strong and ductile SLM-ed Ti6Al4V by in-situ tailoring process to generate ultrafine $\alpha+\beta$ lamellar microstructure;

(2) Establishing an SPS system capable of achieving a linear scratch speed of 220 m/s. Discovering an UGENTs at ultra-high strain rates and proposing its formation mechanism;

(3) Revealing the transition from dislocation-mediated deformation to twinning-mediated deformation induced by ultra-high strain rate. Elucidating the “skin effect” of machining-deformed zone with increasing machining speed;

The outcomes of this study make a significant contribution to enhancing the comprehensive scientific understanding of the material removal and deformation mechanisms of Ti6Al4V alloy under ultra-high strain rates. Additionally, this study provides innovative solutions for the manufacturing and processing of high-performance Ti-alloy parts.

Chapter 4 Selective Laser Melting of High-performance Ti6Al4V Alloy

4.1 Introduction

Selective laser melting (SLM) has emerged as a highly successful additive manufacturing technique, garnering significant attention from both industrial and academic researchers due to its capability to produce high added value products with complex features and exceptional strength. Notably, the application of SLM in the manufacturing of Ti6Al4V has garnered substantial interest due to its high demand and immense potential.

Nevertheless, SLM is a highly intricate physical process that involves the interaction of many complex phenomena, including high-energy laser radiation, rapid powder material melting, intense melt flow, rapid solidification, and intricate phase transformations. Meanwhile, the SLM process is governed by numerous process parameters. Consequently, improper process parameter selection can lead to the occurrence of internal defects such as pores, lack of fusion, and cracks. Additionally, the solidification process characterized by high cooling rates and significant temperature gradients often results in the formation of a non-equilibrium acicular martensitic microstructure. These defects and non-equilibrium microstructure are considered significant factors contributing to the strength-ductility trade-off dilemma encountered in SLM-ed Ti6Al4V parts (Xuan 2023).

The “holy grail” of metal selective laser melting is to manufacture high-performance near net shape parts. To address the strength-ductility trade-off dilemma encountered in the SLM manufacture of Ti6Al4V parts, the post-treatment methods such as heat treatment and hot isostatic pressing are usually applied to tailor the microstructure and control the porosity, respectively. However, these supplementary steps introduce additional time and cost considerations. This raises an intriguing question: is it possible to achieve both high strength and ductility in Ti6Al4V through SLM without the need for subsequent post-treatments?

Previous researches have demonstrated that proper selection of process parameters can effectively prevent the occurrence of defects and enable production of dense parts by using the SLM technique. Moreover, by modifying the thermal profile through the adjustment of process parameters, it is possible to decompose the α' martensite into an ultrafine lamellar α+β microstructure. This particular microstructure exhibits a substantial enhancement in plasticity while simultaneously retaining a high level of strength (Xu *et al.* 2015; Xu *et al.* 2017). However, there is a need for systematic investigations to understand the microstructure evolution, and its correlation with SLM parameters, as well as the underlying fracture mechanism.

Tailoring process parameters and microstructure is a feasible approach to improve the mechanical properties, thereby enabling the manufacture of strong and ductile SLM-ed parts. In this regard, this chapter starts with a systematic investigation on the process optimization to unveil the densification behaviors and the defect formation mechanism of SLM-ed Ti6Al4V. The densification maps and process maps of SLM-ed Ti6Al4V are developed. Subsequently, systematic characterizations are conducted to analyze the microstructure evolution of samples manufactured by different process parameters. The results indicate that the SLM-ed Ti6Al4V exhibits typical coarse columnar grains with inside ultrafine lamellar microstructures. A progressive transformation of the microstructures occurs as the energy density decreases: from coarse α+β lamellar to ultrafine α+β lamellar, and finally to a fully α' microstructure.

Additionally, the tensile properties of the SLM-ed Ti6Al4V specimens are analyzed. The remarkable tensile strength combining high strength and ductility (tensile strength: 1,390 MPa; elongation: 9.66%) of SLM-ed Ti6Al4V is achieved at energy density 76 J/mm^3, which is mainly attributed to the high densification level and ultrafine microstructures. Fracture analyses further reveal that the failure of SLM-ed Ti6Al4V occurs due to the nucleation and coalescence of micro-voids at the interface of the lamellar α and β phases.

This study contributes to the establishment of the process-structure-property relationships through a systematic investigation of the densification behavior, microstructure evolution, and property alterations in SLM-ed Ti6Al4V. Therefore, it offers a promising pathway toward the high-performance manufacturing of Ti6Al4V alloy.

4.2 Experimental Procedures and Methodology

4.2.1 Feedstock Powder and SLM Parameters

Ti6Al4V powders from Oerlikon were used to manufacture SLM specimens. **Fig. 4.1a** shows SEM morphology and size distribution of the powders of an average powder size of 16.72 μm. An SLM equipment (SLM®125HL, SLM Solutions, Germany) was adopted to manufacture Ti6Al4V specimens in the experiment. The SLM machine is schematically illustrated in **Fig. 4.1b**, which is equipped with a 400 W fiber laser with a spot diameter of 64 μm. The SLM fabrication process was conducted in an argon atmosphere with an oxygen content less than 400 ppm, and the substrate was preheated and maintained at 200 °C to reduce the temperature gradient. The 67° rotary scanning strategy was adopted for all fabrication, the schematic representation of the scanning strategy is shown in **Fig. 4.2b**.

In the present study, cubic samples with a size of 8×8×8 mm were manufactured to determine the densification and process map. The parameter setting is summarized in **Table 4.1**, the hatch spacing and layer thickness were set at 80 μm and 30 μm, respectively. The laser power ranged from 130 to 250 W, while the scanning speed changed from 300 to 1,500 mm/s. The volume energy density (E_d) was calculated by Eq. (4.1):

$$E_d = \frac{P}{vdt} \tag{4.1}$$

Table 4.1 Processing parameters used to manufacture the cubic samples.

Process parameter	Value				
Laser power P (W)	130	160	190	220	250
Scanning speed *v* (mm/s)	300	600	900	1,200	1,500
Hatch spacing *d* (μm)	80				
Layer thickness *t* (μm)	30				

Fig. 4.1 (a) SEM image of Ti6Al4V powders and the corresponding size distribution; (b) The SLM equipment applied in this study; (c) Schematic arrangement of the SLM system.

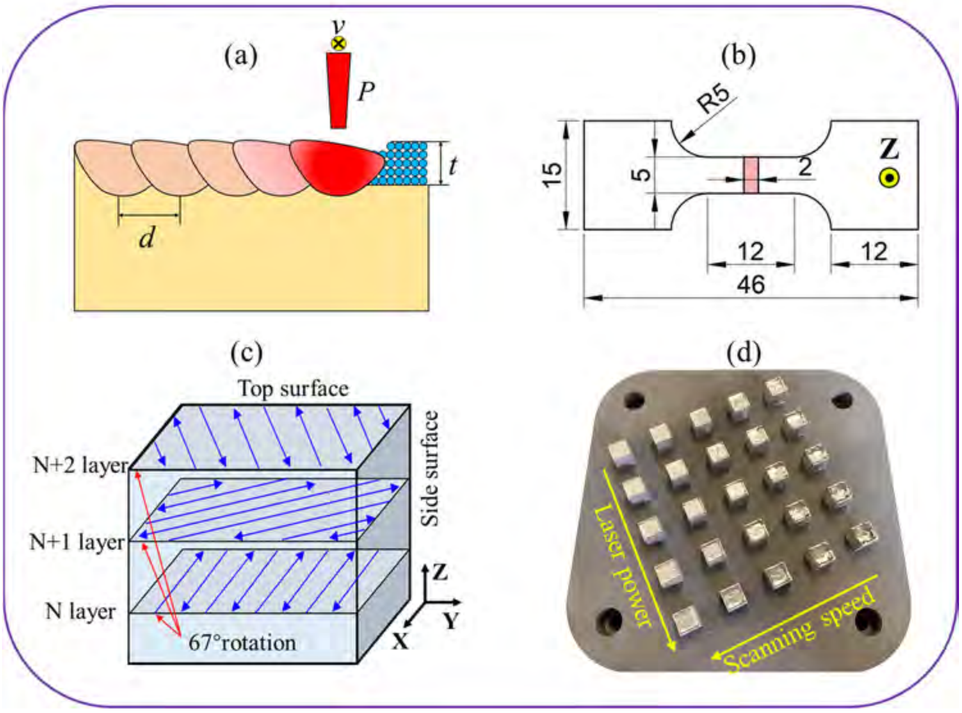

Fig. 4.2 (a) Schematic representation of the process parameters; (b) Dimensional drawing of the tensile specimen (all dimensions are in mm); (c) Schematic representation of the scanning strategy; (d) Manufactured cubic samples.

4.2.2 Material Characterization Methods

The SLM-ed cubic samples were cut from the substrate by wire cut machine and polished before further characterization. The Archimedes method was applied to measuring the relative density (RD). To determine the phase constitution, X-ray diffraction (XRD) was conducted with Cu Kα radiation at a scanning speed of 5 °/min (working voltage 45 kV, working current 200 mA). The etched samples ($HF:HNO_3:H_2O=1:2.5:50$) were detected by the optical microscopy (OM), while the microstructure analyses were also performed by scanning electron microscopy (SEM) and transmission electron microscopy (TEM). The grain characteristics and crystallographic orientation were further investigated by electron backscatter diffractometry (EBSD). Samples for EBSD were prepared by vibration polishing. The tensile test at room temperature was conducted on a universal testing machine equipped with a laser extensometer at a tensile speed of 0.5 mm/min. **Fig. 4.2b** shows the size and shape of tensile specimens and the specimens were manufactured to the final size by surface machining (Z direction refers to the building direction).

4.3 Densification Behavior and Parameter Optimization

The SLM is a complex physical process involving numerous parameters. The defects would be easily induced if inappropriate parameters are applied, resulting in a considerable reduction of the mechanical properties of a manufactured part. Thus, it is necessary to investigate the densification behavior to guide the parameter selection for industrial applications. Energy density (E_d) is regarded as a crucial parameter to control the manufacturing quality of an SLM-ed part, thus the densification behavior at different E_d was systematically investigated by determining the densification maps and characterizing the cross-sectional morphology.

4.3.1 Densification Map and Defects

Figure. 4.3a shows the densification map of the SLM-ed Ti6Al4V samples, which can be divided into three regions according to the densification levels. The samples manufactured in region I exhibited an optimal densification level. Particularly, the maximum RD (99.7%) was achieved when the applied E_d was around 65 J/mm^3. The high densification in region I was attributed to the low defect rate, and the defect-free cross-section morphology is shown in **Figs. 4.3, b** and **c**. But small pores (≤50 μm) started to appear in region I with the increase of E_d (**Fig. 4.3d**). Region II was the window with a scanning speed of 600 mm/s, and the RD of samples in this region had a pronounced drop due to the introduction of a large number of medium pores (50-100 μm, **Fig. 4.3e**), which indicated that the scanning speed had significant effects on the RD of the SLM-ed parts. Moreover, large pores (≥100 μm, **Fig. 4.3f**) were introduced in region III in which the E_d exceeded 175 J/mm^3. Particularly, the samples manufactured in this region exhibited severe depression in the center area of the top surface due to the excessive heat input (**Fig. 4.2d**).

In addition, according to the fitting curves in **Fig. 4.3a**, when the applied E_d exceeded the optimum threshold, the RD decreased continuously with the increase of E_d due to the introduction of larger pores. However, a reverse tendency was observed when the E_d exceeded 180 J/mm^3. In order to clarify the underling mechanism, the cross sections of these samples were also detected. As shown in **Fig. 4.4**, although the large pores were caused by the excessive energy, the subsurface layers nearby the top surface were pore-free. This is because severe surface bulge was accumulated under the enormous heat input as the increase of sample height, resulting in a failure of powder spreading. Thus the top surface was subjected to direct laser re-melting, and the pores in the subsurface layers were effectively removed (Karimi *et al.* 2021). Moreover, the depth of the pore-free layers increased with the increase of laser power, which explained the upward tendency of the RD.

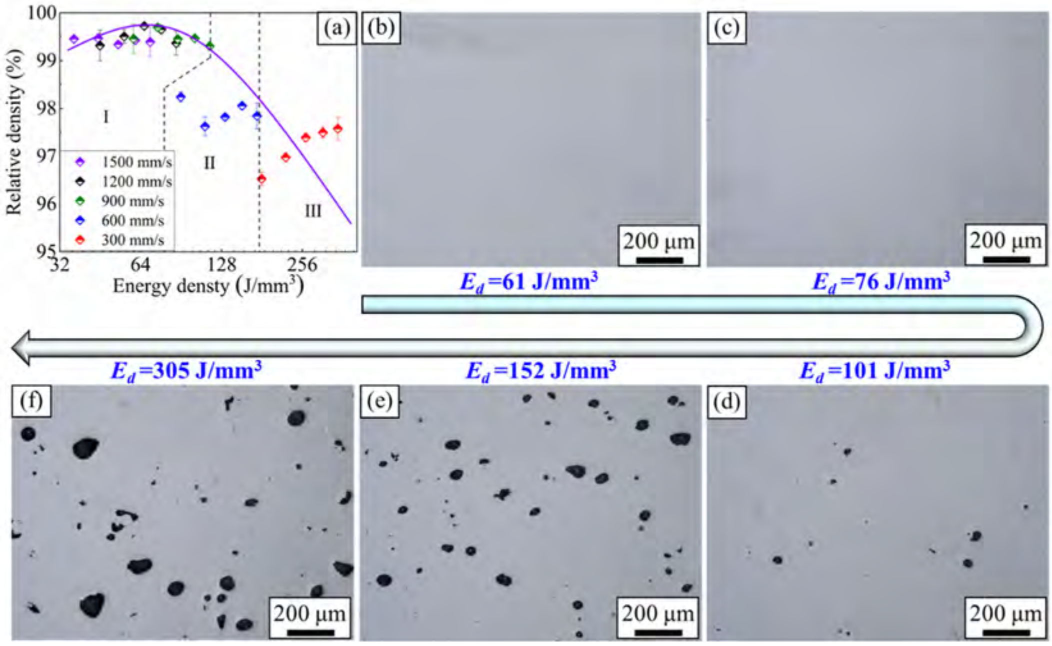

Fig. 4.3 (a) Densification map of SLM-ed Ti6Al4V; Optical images of cross sections after polishing: (b) 61 J/mm^3; (c) 76 J/mm^3; (d) 101 J/mm^3; (e) 152 J/mm^3; (f) 305 J/mm^3.

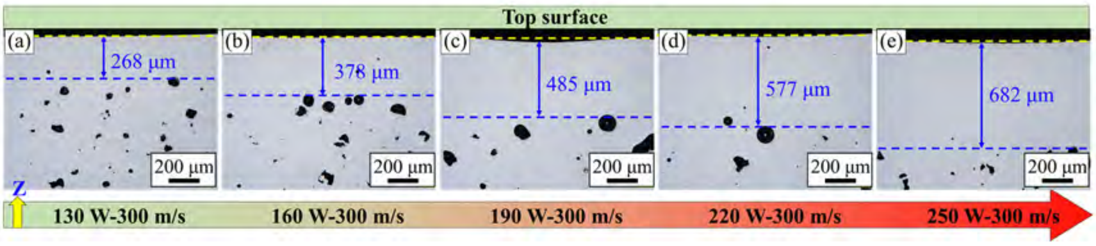

Fig. 4.4 Pore-free surface layer at scanning speed of 300 m/s: (a) 130 W; (b) 160 W; (c) 100 W; (d) 220 W; (e) 250 W.

4.3.2 Pore Defect Formation Mechanism

The keyhole-induced pore formation process is schematically illustrated in **Fig. 4.5**. The low-melting point elements evaporate easily when a laser beam with an excessive energy is applied, resulting in an exponential rise of the recoil pressure in a local zone (The recoil pressure P_{Recoil} can be calculated by Eq. (4.2). A keyhole-shaped depression zone is produced under the effect of the recoil pressure (Zhao *et al.* 2020). The keyhole traps a large number of rays due to the multiple reflections, and absorbs massive energy. This will lead to higher temperature and lower viscosity in the keyhole boundary, and keep the keyhole open at this moment. Meanwhile, a strong flow (as indicated by the green arrow) also exists under the influences of the recoil pressure and Marangoni effect. A protrusion zone is therefore introduced on top of the keyhole tail. As the laser beam moves forward, the protrusion zone collapses rapidly to the opposite (Bayat *et al.* 2019). As a result, the gas in the keyhole tail has no time to escape, and eventually, pores are formed as the melting material solidified along solidification front with most pores located at the bottom or middle of the molten pool.

$$P_{Recoli} = 0.54\left[P_0 \exp\left(\frac{\Delta H_{lv}}{R \bullet T_{Boil}}\left(1 - \frac{T_{Boil}}{T}\right)\right)\right] \tag{4.2}$$

here, P_0 is the ambient pressure; R is gas constant; ΔH_{lv} is latent heat of evaporation material; and T_{Boil} is the boiling temperature.

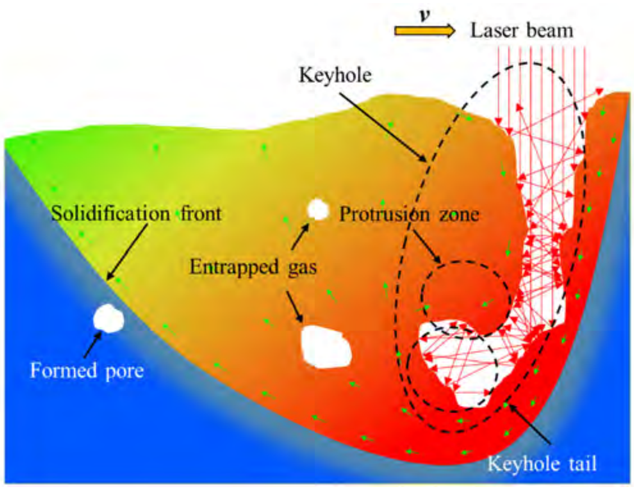

Fig. 4.5 Schematics of keyhole-induced pore formation process.

4.3.3 Process Map and Metallographic Structure

Process map and metallographic structures were combined to investigate the effects of process parameters on the manufacturing quality. As illustrated in **Fig. 4.6a**, the three regions in the densification map of the SLM-ed Ti6Al4V can also be projected on its process map. Particularly, Region I was regarded as the optimum process window, in which all the manufactured samples exhibited a high RD, and a large proportion of this region can yield samples with an optimum RD higher than 99.5%. As shown in **Figs. 4.6, b** and **c**, the metallographic structures of the samples manufactured in region I were typical prior β columnar grains. The boundaries of columnar grains were jagged and discontinuous because of the mismatch between successive layers induced by the 67° scan rotation strategy. Meanwhile, as the energy input increased, the width of the columnar grains increased due to a larger heat affected zone (**Figs. 4.6, d-f**).

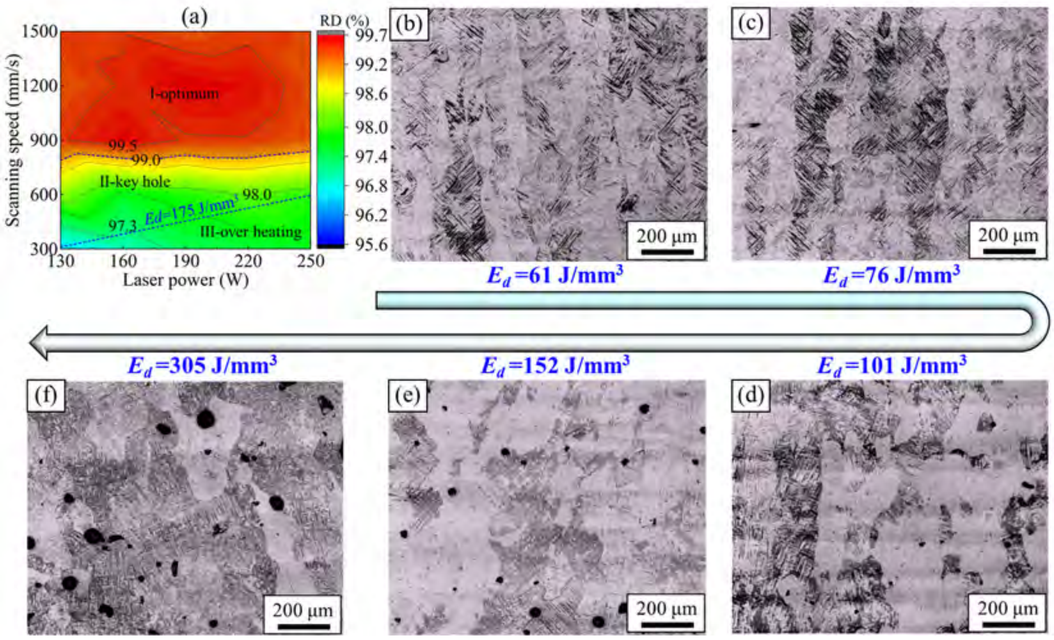

Fig. 4.6 (a) Process map of SLM-ed Ti6Al4V; Optical images of cross sections after etching: (b) 61 J/mm^3; (c) 76 J/mm^3; (d) 101 J/mm^3; (e) 152 J/mm^3; (f) 305 J/mm^3.

The representative 3D metallographic structures are assembled and displayed in **Fig. 4.7**. It is evident that the side surfaces of the SLM-ed Ti6Al4V exhibited typical columnar prior β grains penetrating multiple layers due to the epitaxial growth (Kumar *et al.* 2018). While the top cross-section showed a rhombic-shaped grid morphology with the corner angle equal to 67°, and the side length of the rhombus was around 80 μm that was consistent with the hatching spacing, implying that the morphology was the direct reflection of the scanning strategy.

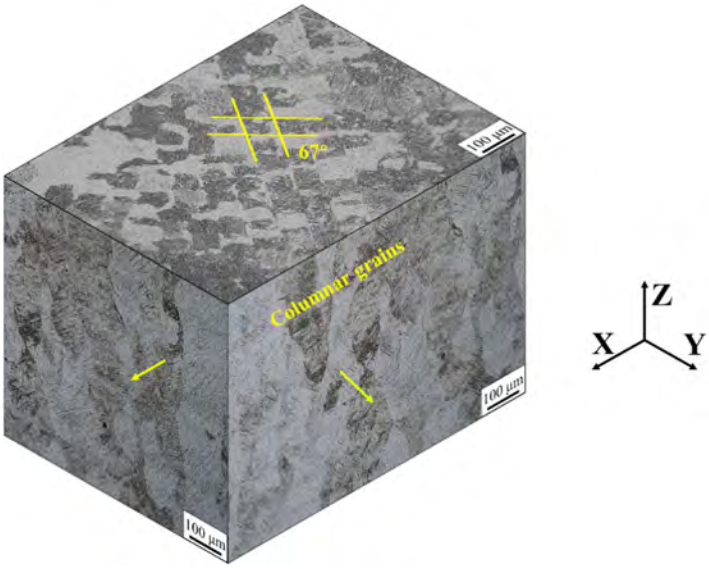

Fig. 4.7 Representative 3D metallographic structure of SLM-ed Ti6Al4V (Manufactured at 76 J/mm^3).

4.4 Microstructure Evolution

The microstructure of SLM-ed Ti6Al4V is completely different from the conventional counterpart. The much higher cooling rate in an SLM process allows it to yield remarkably refined microstructures. Meanwhile, adjusting process parameters can precisely control the local heat input, thus tailoring the microstructure. Therefore, systematic investigations were conducted to reveal the microstructure evolution at different E_d.

4.4.1 X-ray Diffraction Detection

XRD patterns of the SLM-ed Ti6Al4V at different E_d are shown in **Fig. 4.8**. The noticeable diffraction peaks of hexagonal close-packed (α'/α) Ti were identified at 2θ=35.4°, 38.6°, 40.5°, 53.3°, 63.9° in all the SLM-ed Ti6Al4V samples. Meanwhile, the diffraction peak of β-Ti was detected at 2θ=39.5° in the SLM-ed Ti6Al4V manufactured at E_d higher than 76 J/mm^3, which implied that the presence of a small amount of β phases. The diffraction peak intensity of β-Ti decreased as the decrease of E_d, implying that the reduction of β-Ti content. Particularly, as the E_d reduced to 61 J/mm^3, the diffraction peak of β-Ti was not observed.

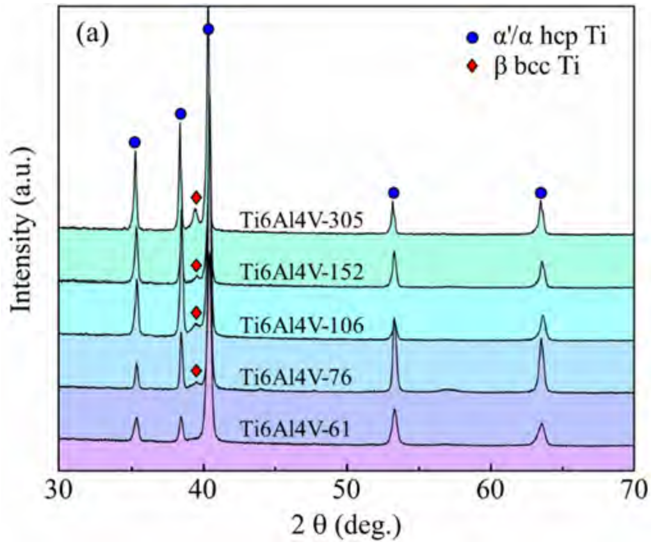

Fig. 4.8 XRD patterns of SLM-ed Ti6Al4V manufactured at different E_d.

4.4.2 Microstructure Characterization

Figure 4.9 shows the SEM images (BSE mode) of the SLM-ed Ti6Al4V manufactured at different E_d. The observed microstructures were in agreement with the results of the XRD detection. The lamellar α+β structures containing α-laths and retained β phases in between were obtained at high E_d (≥76 J/mm^3, **Figs. 4.9, b-e)**, while the fully martensitic α' microstructure was observed when the E_d was reduced to 61 J/mm^3 (**Fig. 4.9f**). Notably, the grain size was significantly refined with the decrease of E_d. To quantitatively evaluate the grain refinement effect, the thickness of α'/α phase was counted by the Nano Measurer. As depicted in **Fig. 4.9a**, the martensite thickness was reduced linearly from 537 nm in sample manufactured at E_d of 305 J/mm^3 to 201 nm in sample manufactured at E_d of 61 J/mm^3.

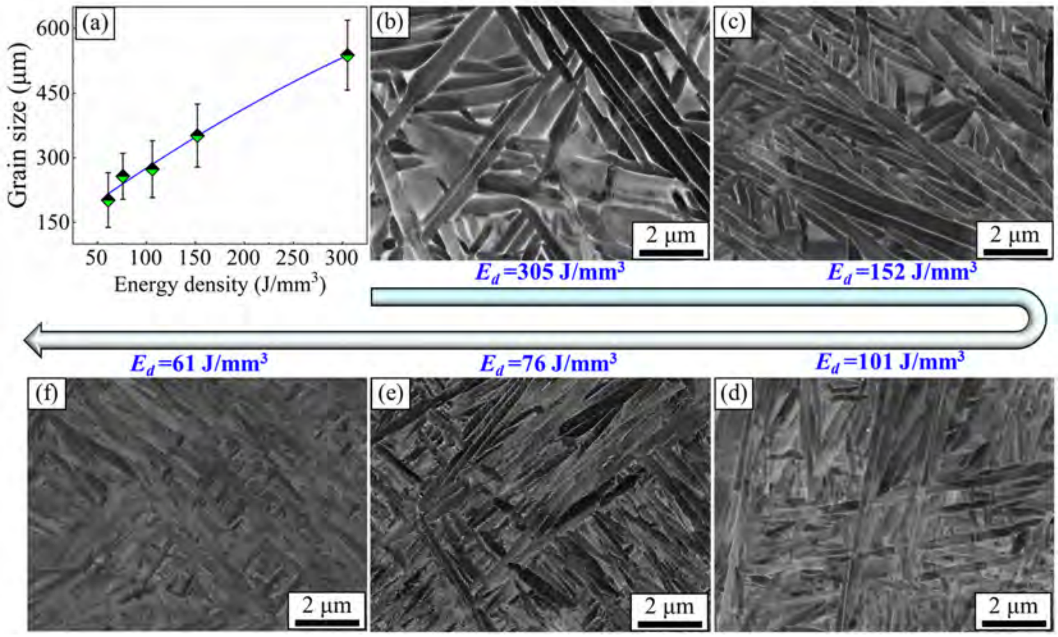

Fig. 4.9 (a) Dependency of grain size of matrix and reinforcement on E_d; (b)-(f) SEM images of SLM-ed Ti6Al4V.

EBSD analyses were conducted on the samples manufactured at E_d of 76 J/mm^3 to further investigate the grain and phase structures. As shown in the inverse pole figures (IPF) (**Figs. 4.10, a** and **d)**, the columnar prior β grain boundaries (Marked with the black dashed lines) were discernible in both X-Y and X-Z views of the SLM-ed Ti6Al4V, which was in agreement with the metallographic observation. The lath shaped martensites confined within the columnar grains were regularly arranged, because the martensites phase developed from the parent β phase follow the Burgers orientation relationship (BOR) ($\{0001\}_\alpha//\{110\}_\beta$, $<11\bar{2}0>_\alpha//<111>_\beta$) under the rapid cooling rate (Antonysamy *et al.* 2013). It can be seen that different α martensite variants were staggered with each one shared a specific orientation (**Figs. 4.10, b** and **e**). The phase maps are shown in **Fig. 4.10, c** and **f**. The statistic results of the phase map show that the β phase accounted for 1.6 % and 1.9 % of the scanned area in the top and side surfaces, respectively. But the detected β phase showed a discontinuous state due to the limitation of resolution in EBSD (Wang and Chou 2018).

The grain boundary map of the SLM-ed Ti6Al4V is shown in **Fig. 4.10g** (Corresponding to the IPF image in **Fig. 4.10b**). **Fig. 4.10h** displays the grain size (Lamellar thickness of martensite) distribution. The grain size of the α phase in the SLM-ed Ti6Al4V ranged from 0 to 800 nm, and the average grain size was 282 nm, which is very approximate to the result in **Fig. 4.9a**. **Fig. 4.10i** shows the misorientation angle distributions. The proportion of low-angle grain boundaries (LAGB: ≤15°) accounted for 24.3% in the SLM-ed Ti6Al4V.

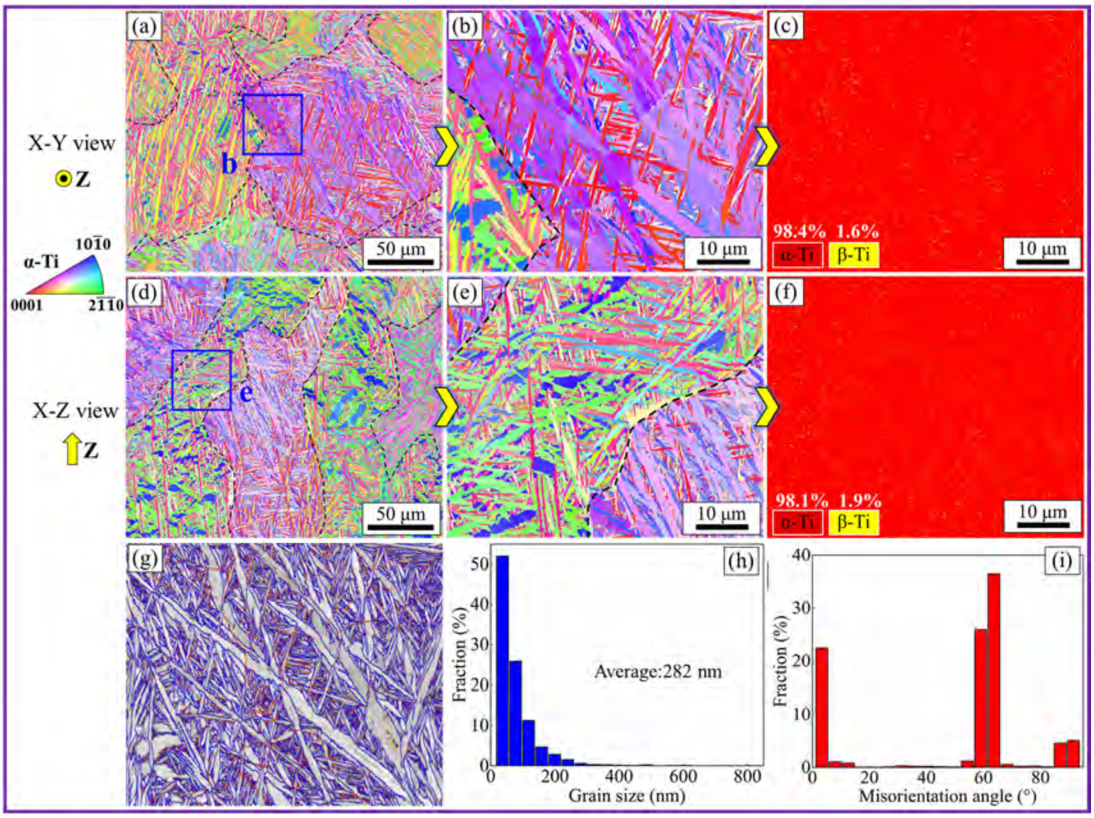

Fig. 4.10 EBSD analysis of SLM-ed Ti6Al4V. X-Y view: (a) IPF; (b) IPF of box b in (a); (c) phase map of (b). X-Z view: (d) IPF; (e) IPF of box e in (d); (f) phase map of (e); (g) grain boundary maps of (b); (h) grain size distribution of (g); (i) misorientation angle distribution of (g).

To investigated the phase transformation during to solidification process, the parent grain reconstruction was conducted by using the MTEX toolbox. According to the BOR of ($\{0001\}_{\alpha}//\{110\}_{\beta}$, $<11\bar{2}0>_{\alpha}//<111>_{\beta}$), the parent grain maps were reconstructed from the resulting child phase. As shown in **Fig. 4.11**, the reconstructed β-orientation maps of SLM-ed Ti6Al4V are corresponding to the EBSD results in **Figs. 4.10, a** and **d**. The thick reconstructed β grains in X-Z view were penetrated multiple layers, and one parent β grain precipitated different α martensite variants, which is matched with the observation of metallographic structures in **Fig. 4.6**.

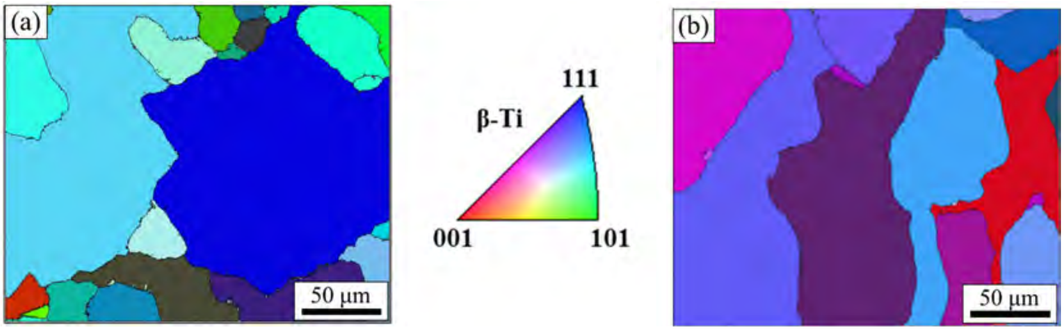

Fig. 4.11 Reconstructed β-orientation map: (a) X-Y view (Corresponding to Fig. 4.10a); (b) X-Z view (Corresponding to Fig. 4.10d).

4.5 Tensile Properties and Fracture Mechanism

4.5.1 Tensile Properties

Figure 4.12 exhibits the stress-strain curves of SLM-ed Ti6Al4V manufactured under different process parameters. The corresponding yield strength, ultimate tensile strength (UTS), and elongation are summarized in **Table 4.2**. The SLM-ed Ti6Al4V-76 exhibited an outstanding mechanical property by combining UTS of 1,390.52 MPa and elongation of 9.66%, which was much superior to that of the SLM-ed Ti6Al4V specimens in the previous studies. Meanwhile, the Ti6Al4V-101 also achieved excellent tensile properties (UTS: 1,361.41 MPa, elongation: 7.62%), whereas the Ti6Al4V-152 showed an inferior tensile property (UTS: 1,248.33 MPa, elongation: 5.46%) compared with Ti6Al4V-101 and Ti6Al4V-76.

Table 4.2 Results of tensile tests: $\sigma_{0.2}$-yield strength; σ_u-ultimate tensile strength; δ-elongation. (The suffix number in specimen name represents the applied E_d).

Specimen	$\sigma_{0.2}$ (MPa)	σ_u (MPa)	δ (%)
Ti6Al4V-152	1095.95±10.34	1248.33±13.88	5.46±1.08
Ti6Al4V-101	1209.17±7.26	1361.41±6.67	7.62±0.92
Ti6Al4V-76	1259.44±13.63	1390.52±17.74	9.66±0.20

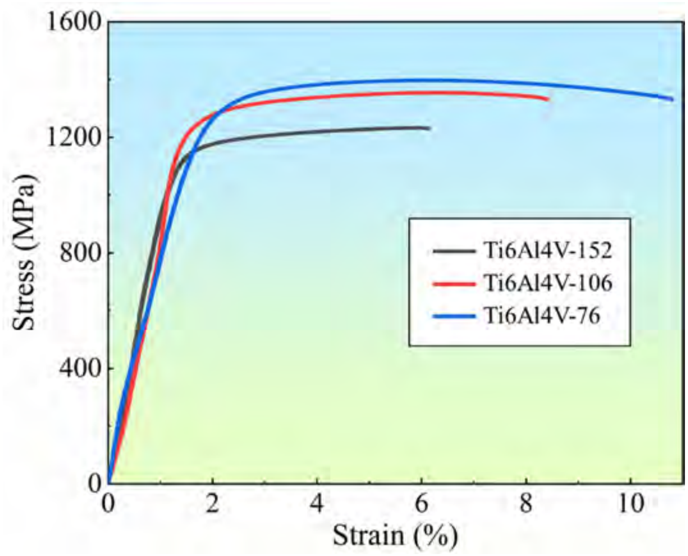

Fig. 4.12 Stress-strain curves of SLM-ed Ti6Al4V

Figure 4.13 compares the tensile properties of the as-built SLM-ed Ti6Al4V specimens in this study and the as-built counterparts from recent references. From the previous studies, the as-built Ti6Al4V specimens by SLM usually exhibited a high tensile strength but low elongation (below 8%) due to the inherently brittle α′ martensite and the induced defects (Singla *et al.* 2021; Zhang *et al.* 2017). Consequently, the post-treatments with high costs such as heat treatment and HIP are regarded as a necessary process to improve the material ductility, however, at the expense of strength reduction, falling into the so-called strength-ductility trade-off dilemma (Liu *et al.* 2019). The SLM-ed Ti6Al4V specimens in this study show excellent tensile properties, particularly the Ti6Al4V-76, which achieves high tensile strength (1,390 MPa) while maintaining high elongation (9.66%) simultaneously.

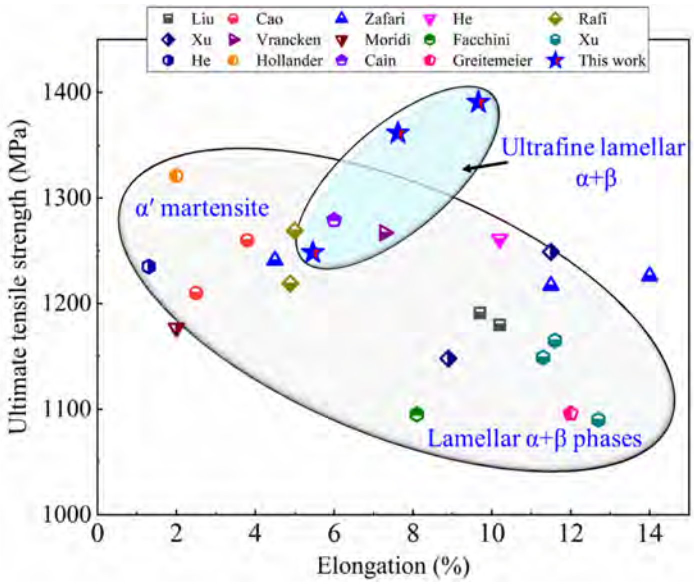

Fig. 4.13 Comparison of tensile properties of the as-built SLM-ed Ti6Al4V in this study and the as-built counterparts from recent references (Cain *et al.* 2015; Cao *et al.* 2017; Facchini *et al.* 2010; Greitemeier *et al.* 2016; He *et al.* 2018; He *et al.* 2019; Hollander *et al.* 2006; Liu *et al.* 2019; Moridi *et al.* 2019; Rafi *et al.* 2013; Vrancken *et al.* 2012; Xu *et al.* 2017; Xu *et al.* 2015; Zafari *et al.* 2018).

4.5.2 Fracture Mechanism

To investigate the underlying fracture mechanism, the fracture surfaces were analyzed. **Fig. 4.14** displays the SEM fracture morphologies, and the insets are the corresponding macroscopic images after fracture. From the macroscopic morphologies, the fracture surfaces were oriented along with the direction of maximum shear stress in the SLM-ed Ti6Al4V specimens. Meanwhile, slight necking could be observed in the Ti6Al4V-152 and Ti6Al4V-101, while distinct necking appeared in the Ti6Al4V-76. As shown in **Fig. 4.14a**, noticeable pore defects surrounding with tearing ridges existed in the fracture surface of the Ti6Al4V-152, demonstrating that cracks tended to initiate and rapidly propagate from the pore defects during the loading process. Thus, the inferior mechanical strength of the Ti6Al4V-152 was highly related to its lower RD (98.05%). By contrast, pore defects were barely observed in the Ti6Al4V-101 and Ti6Al4V-76 due to their high RD. The high magnification images revealed a dimple morphology in all the specimens, and the dimple size increased with an increasing plasticity in the Ti6Al4V-152 to Ti6Al4V-76, implying an elevated ductility.

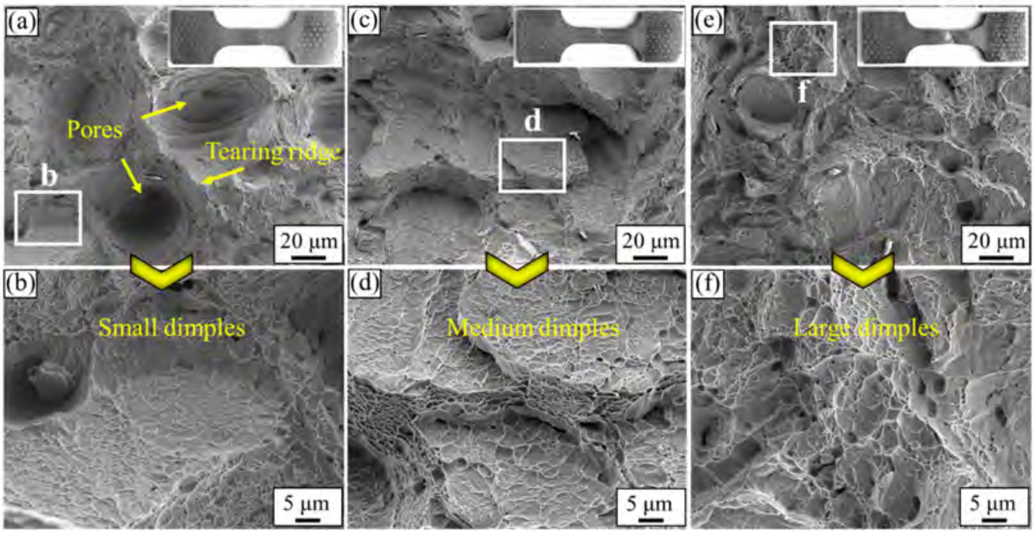

Fig. 4.14 SEM fracture morphologies of SLM-ed Ti6Al4V: (a)-(b) Ti6Al4V-152; (c)-(d) Ti6Al4V-101; (e)-(f) Ti6Al4V-76.

To further investigate the deformation and damage evolution mechanisms, the longitudinal sections of the fracture surface were cut and observed. As displayed in **Figs. 4.15, a-c**, the macroscopic fracture surfaces exhibited an increasing slant angle from Ti6Al4V-152 to Ti6Al4V-76. **Figs. 4.15, d-f** display the microcracks closing to the fracture surface, most observed cracks propagated along with the direction of the maximum shear stress, except one crack shown in **Fig. 4.15d** that was aligned with the loading direction. In order to reveal the initiation of cracks, the longitudinal sections were etched and observed. As shown in **Figs. 4.15, g-i**, under the external loading, the micro-voids tended to nucleate at the interface of the lamellar α and β aligning 45° with respect to the loading direction, and then coalesced along the α-laths, resulting in the initiation and propagation of cracks.

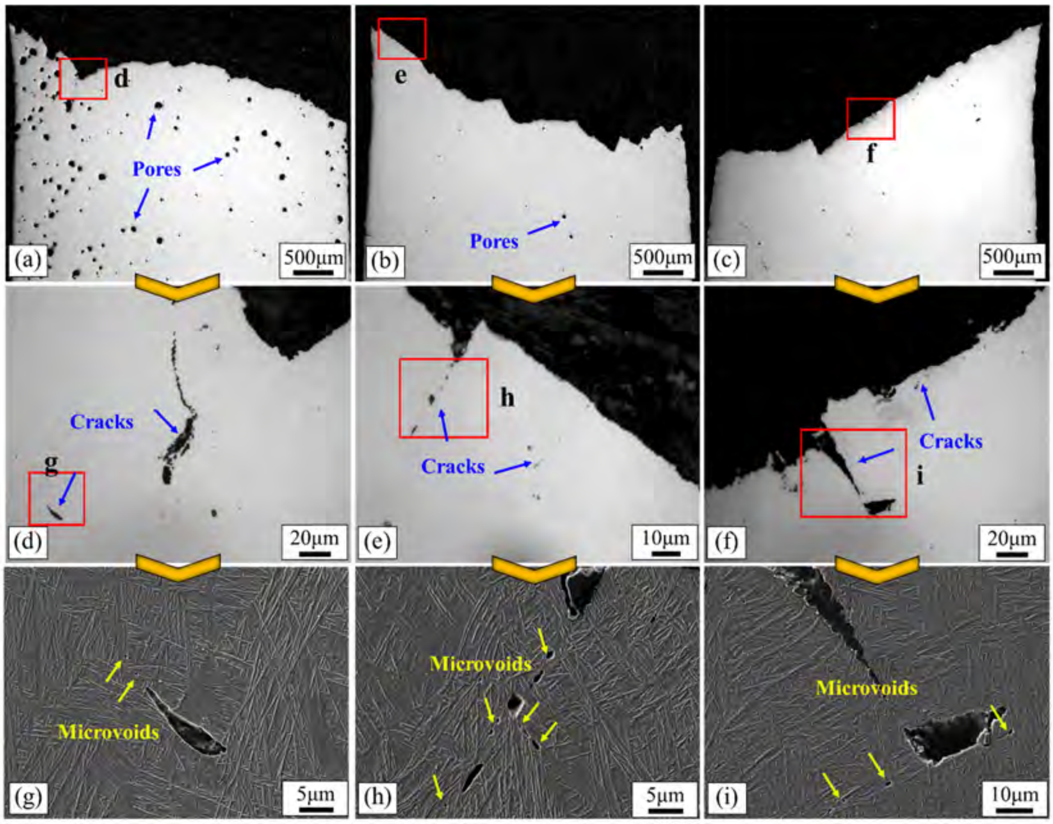

Fig. 4.15 Longitudinal sections of fracture surface: (a)-(c) Ti6Al4V-152 to Ti6Al4V-76; (g)-(i) enlarged views of d, e, f; (g)-(i) enlarged views of g, h, i (after etching).

4.6 Conclusions

In this study, high-performance Ti6Al4V was manufactured by the SLM technique, and systematic characterizations and analyses were conducted to reveal the process-structure-property relationship. The main findings are drawn as follows:

(1) Densification map and process map were obtained based on the process optimization, providing guidance for the parameter selection of SLM-ed Ti6Al4V. The optimized process window was around 65 J/mm^3, defect-free Ti6Al4V parts can be manufactured in this process window;

(2) The metallographic structure of the SLM-ed Ti6Al4V exhibited typical prior β columnar grains with lamellar α/β or fully martensitic α' microstructure distributed inside, depending on the applied E_d, the fully martensitic α' microstructure was produced when the E_d decresded to 61 J/mm^3;

(3) The microstructures of the SLM-ed Ti6Al4V were refined with the decrease of E_d

due to the higher cooling rate. An ultrafine lamellar α+β microstructure with an average α-lath thickness of 282 nm was obtained at the E_d of 76 J/mm^3;

(4) The strong and ductile Ti6Al4V specimens with the tensile strength of 1,390 MPa and the elongation of 9.66% were manufactured, mainly attributed to the high densification level and ultrafine microstructure. The fracture analyses indicates that the failure of the SLM-ed Ti6Al4V results from the nucleation and coalescence of microvoids at the interface of the lamellar α and β phases.

Chapter 5 Material Removal Mechanisms of Wrought Ti6Al4V in Single-point-scratching

5.1 Introduction

Ti-alloy's exceptional mechanical properties make it a paramount structural material. Its application in critical areas, such as aviation, aerospace, navigation, automotive, and biomedical industries, significantly enhances the service performance of essential components, thereby driving technological advancement. Conversely, with the continuous advancement of manufacturing and processing technologies, Ti-alloy is expected to unleash greater potential, further expanding its application prospect. Nevertheless, Ti-alloy is known as a typical difficult-to-machine material. The inherent difficulties in machining Ti-alloy stem from its specific material characteristics, including high specific strength, low thermal conductivity, high chemical reactivity, and low elastic modulus. Conventional machining techniques encounter substantial challenges, including high machining forces, elevated temperatures, rapid tool wear, and compromised surface integrity, when dealing with Ti-alloy.

Achieving high-efficiency, high-quality, and minimizing damage machining of parts applied in critical applications is an enduring pursuit shared by the engineering and academic communities. Despite considerable efforts made by researchers to overcome the challenges associated with machining Ti-alloy, such as the development of specialized cutting tools, optimization of machining parameters, implementation of effective cooling strategies, and exploration of non-traditional machining processes, it remains a challenge to simultaneously enhance and maintain a balance between machining quality and efficiency in the machining of Ti-alloy.

Ultra-high-speed machining (UHSM) has emerged as a promising and innovative approach in the field, it offers substantial advantages in terms of elevated machining efficiency, enhanced machining quality, and diminished tool wear. Moreover, UHSM exhibits great potential in mitigating subsurface damage induced during the processing process. However, despite its merits, the material removal and deformation involved in the intricate UHSM process subjected to extremely high strain rates still lacks a comprehensive understanding. Meanwhile, extensive investigations are expected to comprehensively explore the intricate characteristics encompassing microstructure evolution, grain refinement mechanisms, dislocation motion, and twin formation mechanisms in the UHSM of Ti-alloy.

In light of this, the present study aims to investigate the material removal and deformation mechanisms of wrought Ti6Al4V in UHSM regions, and their transitions as the strain rate increases. A single-point-scratching (SPS) system was designed and developed to achieve ultra-high-speed scratch. Based on which, a series of SPS experiments with machining speeds ranging from 20 to 220 m/s were conducted. The material removal mechanisms were analyzed in terms of surface creation, subsurface deformation, and chip formation by applying multiscale characterization combing FIB, STEM, and TKD.

5.2 Experimental Procedures and Methodology

5.2.1 Workpiece Material and Experimental Setup

Wrought Ti6Al4V with equiaxed grains (average grain size: 14.7 μm) was selected as the workpiece material, the corresponding EBSD detection and its grain size distribution are shown in **Fig. 5.1**. The SPS experiments were conducted in a grinding machine (QuestGT27, Hardinge) equipped with a high-speed hydrostatic bearing motorized spindle (Maximum speed: 60,000 rpm, from TDM SA in Switzerland). The experimental setup is schematically illustrated in **Fig. 5.2f**, the conical single-point diamond tool (Tip radius: 30 μm, cone angle: 120°) was mounted on a carbon fiber reinforced plastic (CFRP) wheel with lightweight, high strength, and high damping characteristics. Subsequently, the CFRP wheel was assembled onto the high-speed spindle to realize ultra-high-speed scratch.

The workpieces with dimensions of 10×10×3 mm were fixed on a workpiece wheel using paraffin wax, and the surface damage of those workpieces were removed by on-process grinding and polishing (Abrasive papers from #180 to #3000 and polishing cloth were tailored and affixed on another titanium wheel to realize on-process grinding and polishing).

Eight SPS trials with grinding linear speed velocity varying from 20 to 220 m/s were carried out. The speed ratio of grinding linear speed to feed speed was fixed to produce equally spaced single scratches without repeated machining. The machining parameters of Ti-alloy in SPS are listed in **Table 5.1**. Before each trial, a fresh single-point grinding tool was substituted, and on-process dynamic balance was conducted to guarantee dynamic balancing performance (**Fig. 5.2c**). A sample holder with carbon tape was arranged above the sample to collect flying chips (**Fig. 5.2d**).

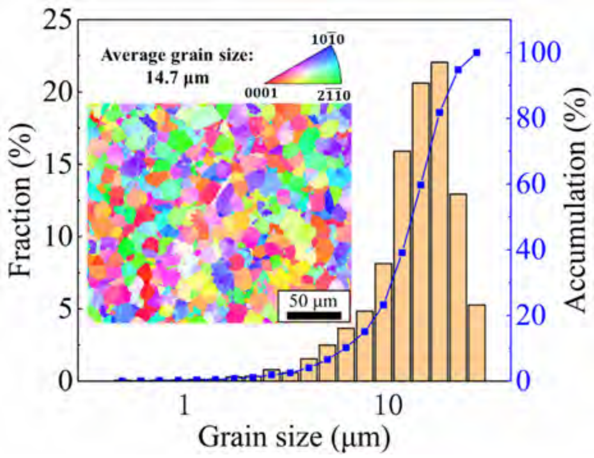

Fig. 5.1 EBSD detection of Ti6Al4V material and its grain size distribution.

Table 5.1 Machining parameter of Ti-alloy in single-point-scratching

Trials	**Spindle speed (rpm)**	**Grinding linear speed v_s (m/s)**	**Feed speed v_f (mm/min)**	**Depth-of-cut (μm)**
1	3474	20	313	2.5
2	10423	60	938	
3	17371	100	1563	
4	24320	140	2188	
5	27794	160	2500	
6	31268	180	2813	
7	34742	200	3125	
8	38217	220	3438	

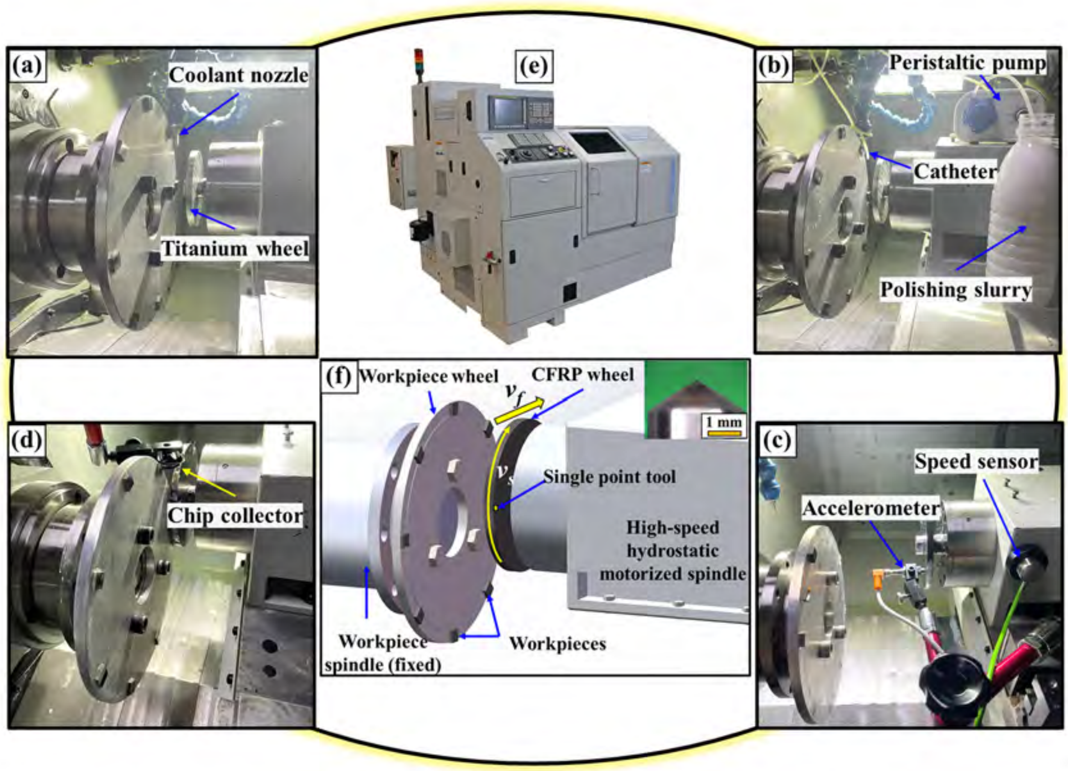

Fig. 5.2 Experimental setups: (a) Sample grinding; (b) Sample polishing; (c) Dynamic balance; (d) Single-point-scratching; (e) Hardinge machine tool; (f) Schematic diagram of single-point-scratching.

5.2.2 Material Characterization Methods

The surface morphology was detected by laser scanning confocal microscopy (LSCM) and scanning electron microscopy (SEM, Merlin, Zeiss, Germany), and the cross-sectional profile of scratches was analyzed by the MULTI-FILE ANALYSIS software. In order to unveil the distribution and evolution of the subsurface microstructure, it is essential to expose the subsurface layer for observation. The conventional approach involves sectioning the sample and subsequently performing grinding, polishing, and etching to prepare the sample for analysis. Nonetheless, the bulk sample prepared through the conventional method offers only restricted insights. Furthermore, the sample preparation procedure often introduces additional damage and compromises the original features resulting from the machining process. In this regard, subsurface samples of the scratches were prepared by the FIB milling (Helios 600i), and detected by a transmission electron microscopy (Talos F200X G2).

5.3 Surface Morphology and Profile of Wrought Ti6Al4V at Different Grinding Speeds

Figure 5.3 shows the typical 3D surface morphology and the corresponding cross-sectional profile of scratches with machining speed ranging from 20 to 220 m/s. For the scratches machined at lower speeds (≤100 m/s), high and discontinuous pile-ups were formed on both sides of the scratches due to severe plastic deformation. The pile-up became more uniform and continuous with the increasing machining speed, and the volume of the pile-up significantly decreased. Additionally, small grooves were observed in the bottom of the machined scratches at lower speed, which may result from the adhered materials in the tooltip. Nevertheless, such grooves vanished in the high-speed region, indicating an inhibitory effect on severe plastic deformation.

The pile-up ratio R_p is induced to quantitatively evaluate the pile-up effect (R_p is defined by Eq. (5.1)). **Fig. 5.4** shows the influence of machining speed on the pile-up ratio, consistent with the surface morphology observation, the scratches machined at low speeds exhibited a high pile-up ratio due to the material accumulation on the sides of scratches, particularly, the pile-up ratio reached 84.4% at a grinding speed of 20 m/s. Notably, the pile-up ratio almost linearly decreases as the machining speed increases.

$$R_p = \frac{A_1 + A_2}{B} \tag{5.1}$$

here, A_1, A_2, B represent the corresponding areas in Fig. 5.4.

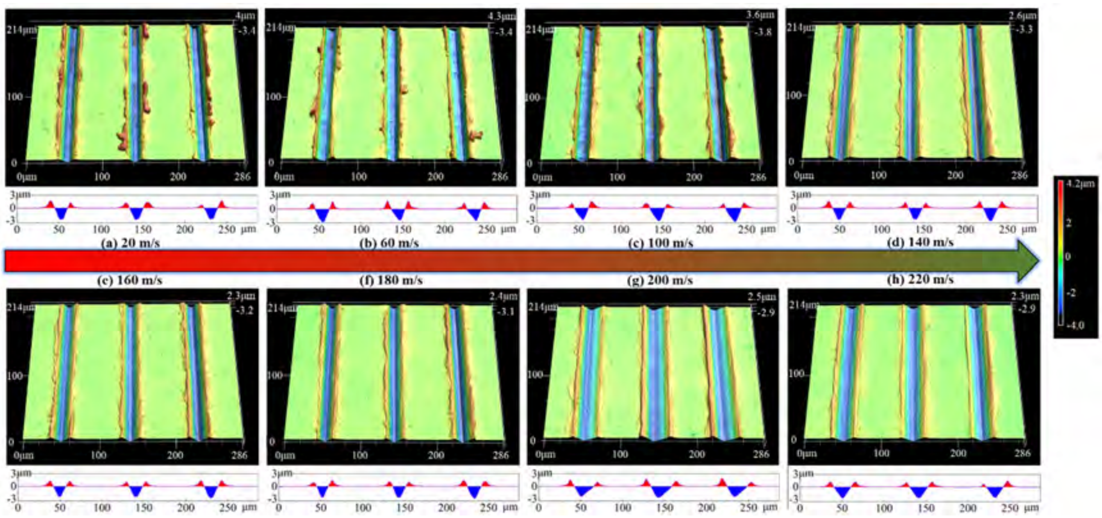

Fig. 5.3 3D surface morphology and the corresponding cross-sectional profiles of

scratches machined at different machining speeds.

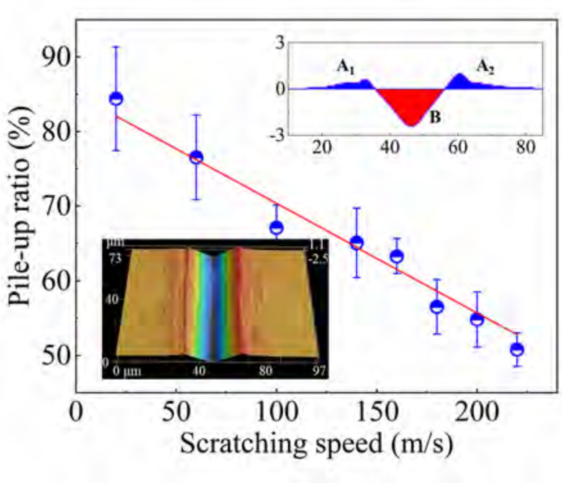

Fig. 5.4 Speed effect on the pile-up ratio.

5.4 Subsurface Deformation Mechanisms of Wrought Ti6Al4V at Different Grinding Speeds

5.4.1 Plastic Deformation Distribution

To investigate the subsurface plastic deformation in Ti6Al4V induced by machining, it is necessary to first characterize the subsurface microstructure of as-polished Ti6Al4V. As shown in **Fig. 5.5a**, the subsurface of as-polished Ti6Al4V shows clean and undeformed microstructures, indicating the original damage of the buck material was effectively removed by the material preparation process. In Ti6Al4V alloy, the Al element is the main stabilizer for the α phase, while the V element is the main stabilizer for the β phase. Accordingly, the α phase is Al-rich but V-deficient, but the β phase is V-rich but Al-deficient. Therefore, the distribution of the two phases is evident in the Al and V elemental maps shown in **Figs. 5.5, b** and **c**, respectively. **Fig. 5.5e** reveals the β phase in Ti6Al4V, the inset further identifies the SAED pattern of the β phase. **Fig. 5.5f** displays the original dislocation structures in Ti6Al4V prior to machining, it can be identified that the dislocations are randomly distributed in the undeformed grains.

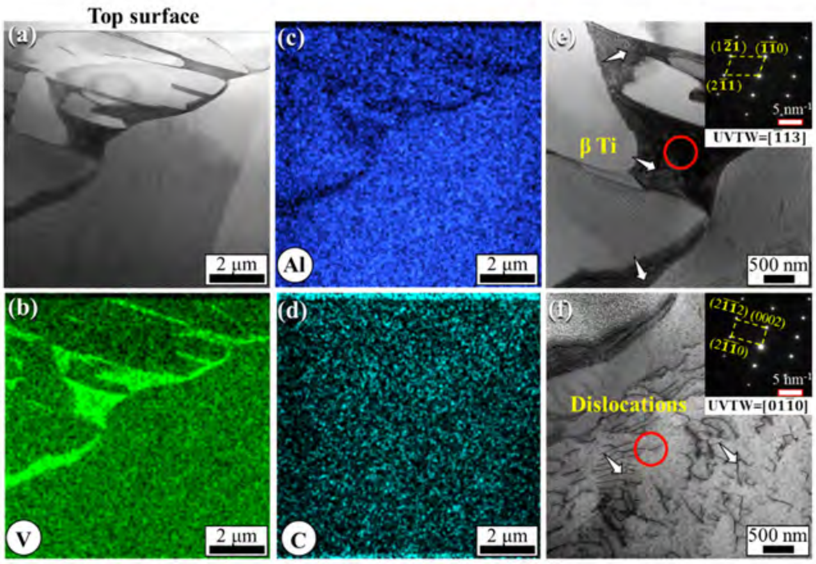

Fig. 5.5 TEM characterization of the subsurface microstructure in as-polished Ti6Al4V: (a) TEM image showing the subsurface cross-section; (b) V element map; (c) Al element map; (d) C element map; (e) β Ti; (f) Original dislocation structure. (The insets are the SAED pattern taking from the area marked by the corresponding red cycle).

Figure 5.6a shows the surface morphology of the scratch machined at 20 m/s, a C layer was coated on the sampling surface before the FIB processing to protect the surface from the extra damage by ion-bombardment (**Fig. 5.6b**). **Fig. 5.6d** exhibits the TEM image of the global cross-sectional of scratch, a machining-deformed zone (MDZ) with a thickness of ~5 µm can be observed. Meanwhile, high pile-ups existed on both sides of the scratch, which is consistent with the results in Section 5.3. The distribution of α and β phases can be recognized in the Al and V maps in **Figs. 5.6, e** and **f**, respectively. As shown in the V map, plentiful precipitations of the β phase were observed in the near-surface, indicating phase transformation was induced during the machining process. Additionally, **Fig. 5.6g** shows the remained C protective layer on the top surface.

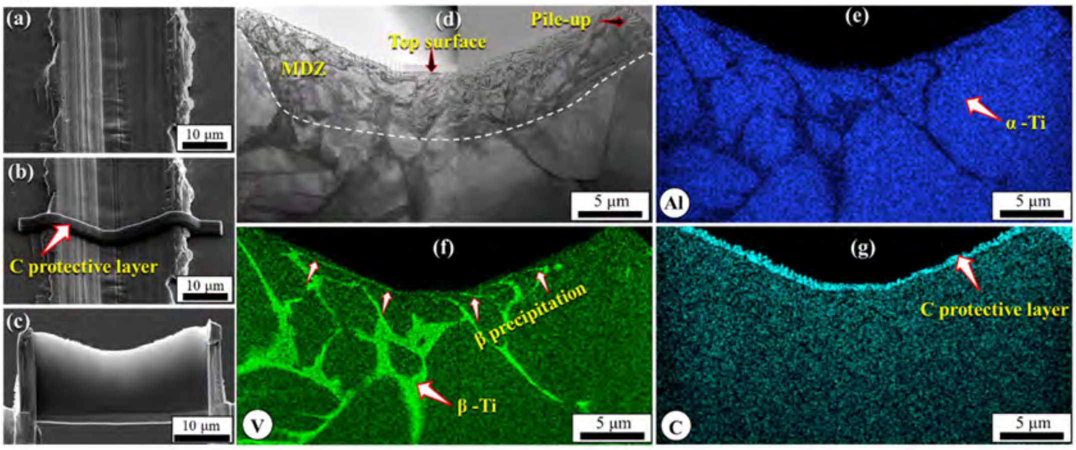

Fig. 5.6 (a-c) Cross-sectional TEM sample preparation by FIB (20 m/s): (a) Surface morphology of scratch; (b) Lift out location of cross-section sample; (c) SEM micrograph of lifted lamella; (d-g) STEM image and corresponding EDS maps: (d) STEM image showing the global cross-section; (e) Al element map; (f) V element map; (g) C element map.

In comparison, the MDZ in the cross-section of the scratch machined at 220 m/s shows a significant reduction (**Fig. 5.7d**). The thickness of MDZ at 220 m/s declined to around 1 μm, which was decreased by 80% compared to that at 20 m/s, implying a conspicuous "skin effect" of MDZ. Nevertheless, there are no distinctive β precipitations in the subsurface of the scratch machined at the ultra-high-speed. Moreover, the subsurface microstructures at low and high machining speeds also show a noticeable difference, which is intimately connected to the deformation mechanism, this will be elucidated in detail in the following.

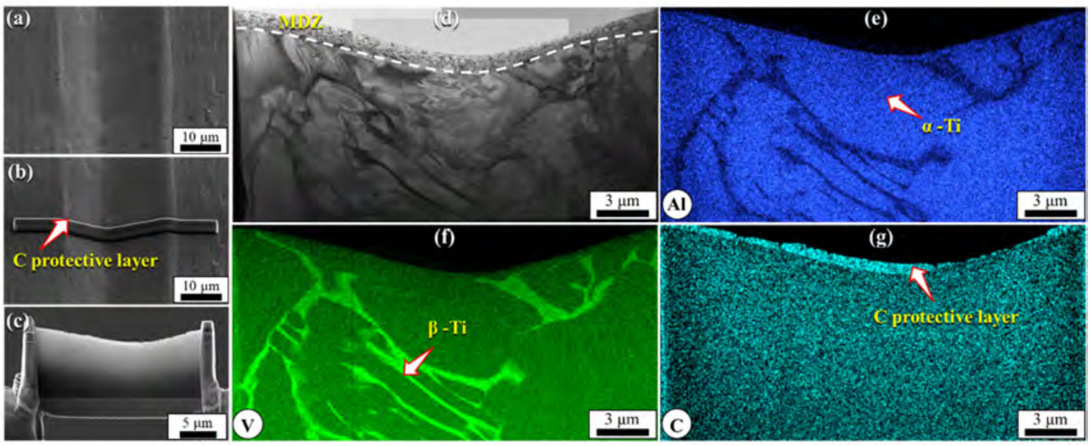

Fig. 5.7 (a-c) Cross-sectional TEM sample preparation by FIB (220 m/s): (a) Surface

morphology of scratch; (b) Lift out location of cross-section sample; (c) SEM micrograph of lifted lamella; (d-g) STEM image and corresponding EDS maps: (d) STEM image showing the global cross-section; (e) Al element map; (f) V element map; (g) C element map.

The EDS and SAED pattern analyses were combined with the STEM morphology to systematically investigate the alteration of microstructures and phases at both low and ultra-high machining speeds. As shown in **Fig. 5.8**, the MDZ in three typical regions, including the bottom, side wall, and pile-up of the scratch (20 m/s), are particularly considered. **Fig. 5.8a** shows the MDZ in the bottom region of the scratch. The laminar β precipitations in nanoscale tend to be induced in the near-surface due to the intense thermos-mechanical effect. Meanwhile, highly refined DRX grains were detected in this layer. As the distance from the ground surface increased, deformed grains elongating along the horizontal direction were produced.

As for the MDZ in the side wall of the scratch, **Figs. 5.8, d-f** display the grain morphology in this region. A distinctive recrystallization layer with a thickness of ~230 nm was observed in the near-surface, the DRX grains surrounded by multiple stacking faults were refined to nanocrystals with an average diameter size of 30~80 nm. At the depth beneath 230 nm, the grains were highly elongated along the direction of the side wall due to the extrusion force of the tooltip. When it comes to the pile-up region, a crack was detected along the boundary of pile-up and matrix where it was influenced by a severe shear impact (**Fig. 5.8g**). A shear band was recognized along the direction of crack propagation, in which severely broken grains were revealed (**Fig. 5.8i**). Besides, nanoscale β precipitation was also detected along the near-surface of the pile-up (**Fig. 5.8h**).

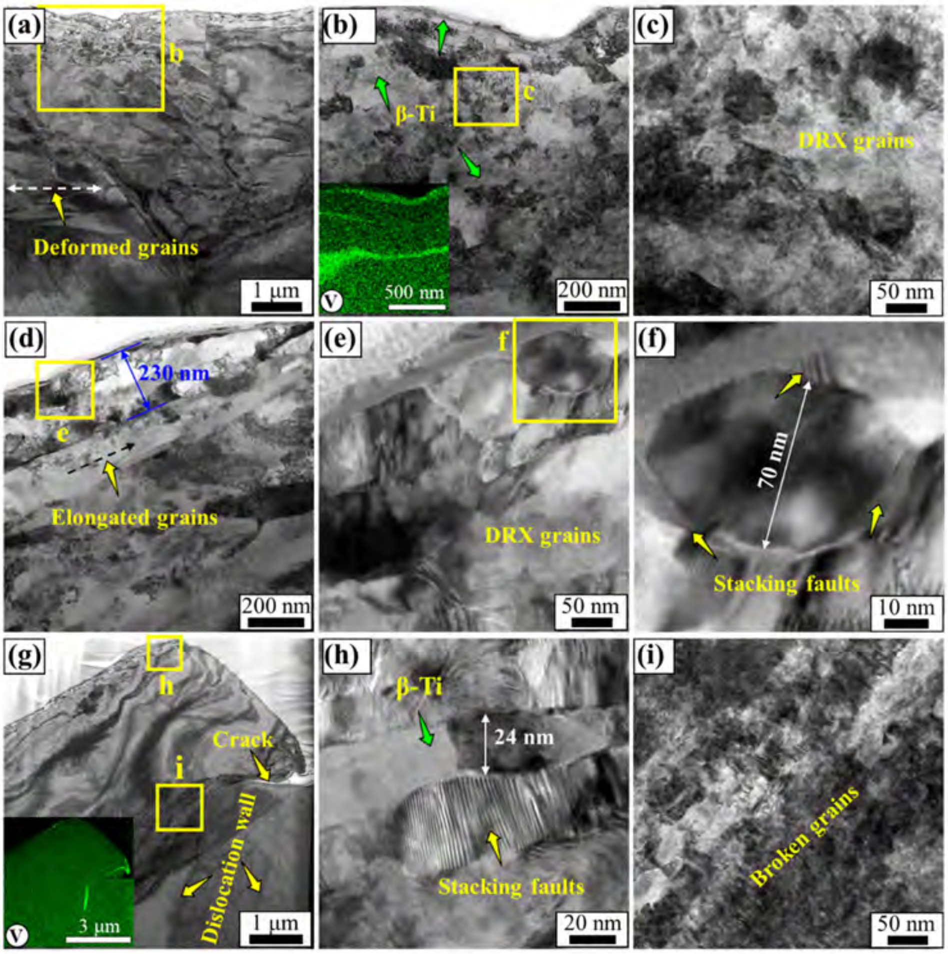

Fig. 5.8 STEM characterization of MDZ at 20 m/s: (a)-(c) Bottom of the scratch; (d)-(f) Side wall of the scratch; (g)-(i) Plie-up of scratch. The insets display the corresponding V map.

Figure 5.9 presents the detailed MDZ of scratch machined under the ultra-high-speed condition (220 m/s). As opposed to low machining speed, no DRX layer was observed in the subsurface layer. Instead, nanoscale twins became the dominant structure in the MDZ. As shown in **Fig. 5.9a**, a deformation-induced twin zone (DITZ) was detected, in which nanoscale twin structures were distributed inside, and a twin collision was observed in the enlarged view (**Fig. 5.9c**). A bulky β-Ti was located in the subsurface of the bottom of the scratch, and it can be inferred that this β-Ti was the original phase. However, contrary to the counterpart of 20 m/s, no laminar β precipitations were detected in the near-surface layer, which implies that the deformation-induced α→β transformation was inhibited in UHSM.

The microstructures in the side wall region are displayed in **Figs. 5.9, d-f**. A distinctive boundary separated the MDZ from the matrix material, and the undeformed single crystal structures were identified beneath the boundary (**Fig. 5.9e**). The twins in the MDZ were distributed along the 45° direction with respect to the surface direction of the side wall, that is, the direction of the maximum shear force. Another interesting observation is that the deformed β-Ti exhibited a pinning effect on the growth of twins by constraining them in one side of a β-Ti (**Figs. 5.9, e** and **f**). A similar pinning effect can be identified in the plie-up of scratch (**Fig. 5.9i**). Additionally, although the grains beneath the MDZ had no distinctive plastic deformation, the dislocation structures were rearranged and dislocation walls were formed under the influence of stress (**Fig. 5.9h**).

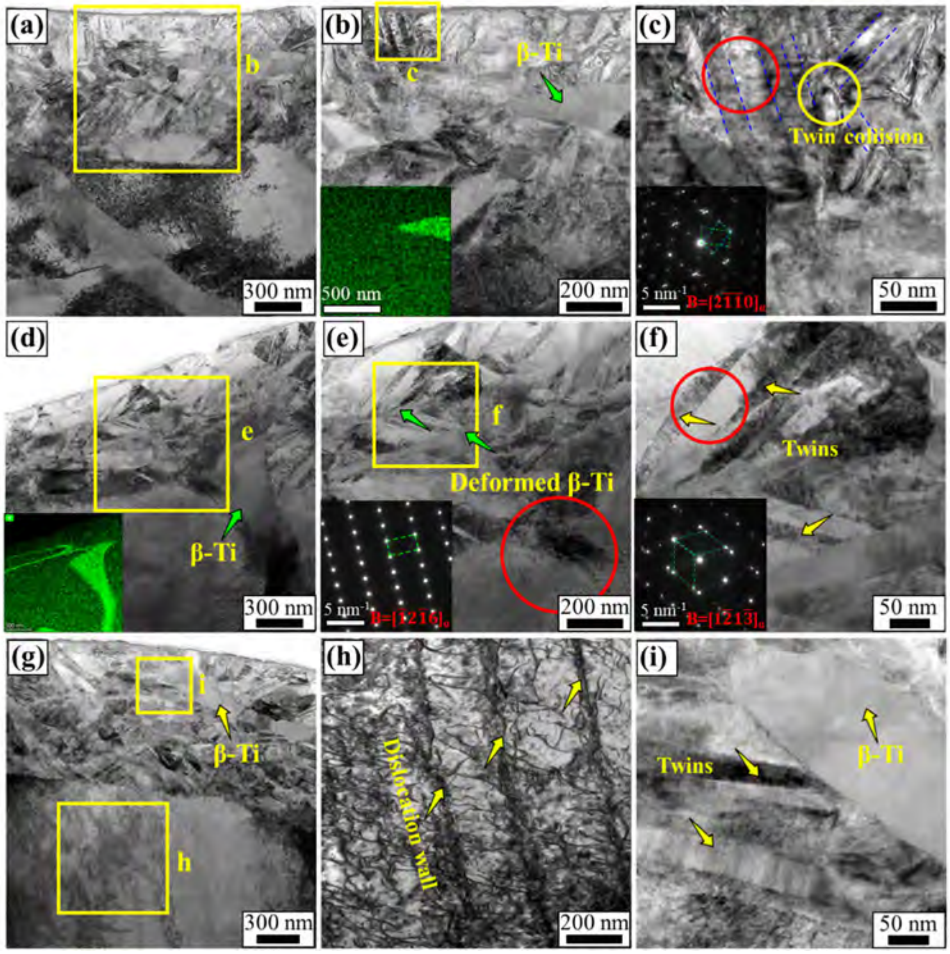

Fig. 5.9 STEM characterization of MDZ at 220 m/s: (a)-(c) Bottom of the scratch; (d)-(f) Side wall of the scratch; (g)-(i) Plie-up of scratch. The insets display the corresponding V map or SAED pattern (All SAED patterns were taken from the area marked by the corresponding red cycle).

To calibrate the twin type and investigate its distribution and morphology, the details were further investigated. **Fig. 5.10a** shows the STEM image of twins in the MDZ, and the related dark field image is displayed in **Fig. 5.10b**. According to the SAED pattern in **Fig. 5.10c**, the twin system was determined as the compression $\{0\bar{1}11\}$twin. Meanwhile, the twin structure was uniformly distributed in the whole MDZ with the parallel twin clusters filling in the polygon nanoscale grains (**Fig. 5.10d**). The high-resolution TEM (HRTEM) image of twins is shown in **Fig. 5.10e**. it is revealed that the twin thickness was around 15 nm, and the inset in **Fig. 5.10e** was the Fast Fourier Transform (FFT) image, which further verified the $\{0\bar{1}11\}$ twin system. Additionally, the twin interface was further highlighted in the inverse FFT image (**Fig. 5.10f**), the included angle between the plane $(1\bar{1}01)_T$ and the twin plane $(0\bar{1}11)$ was 64°.

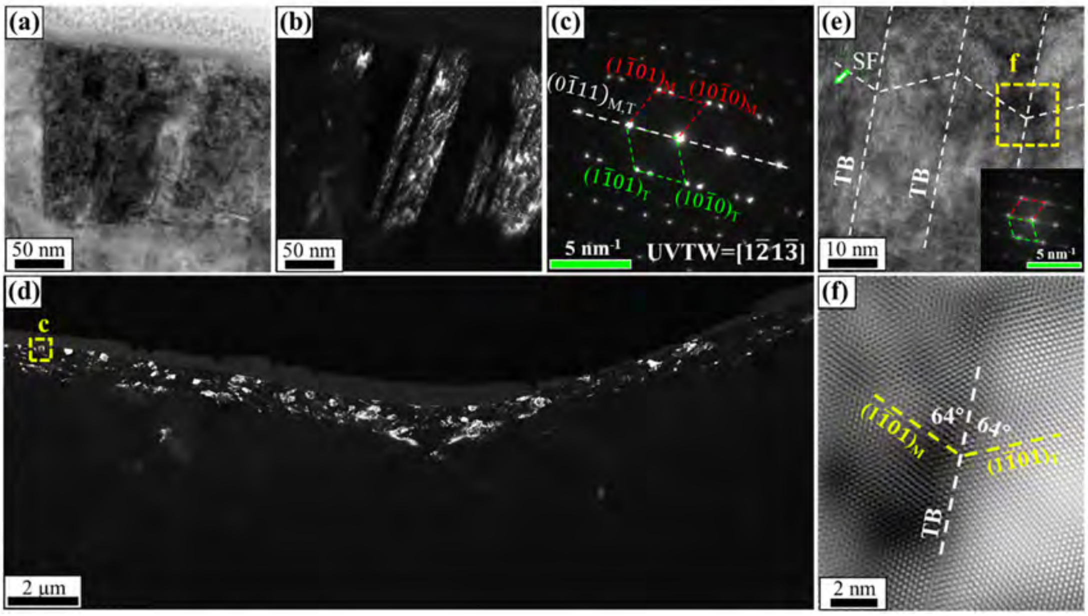

Fig. 5.10 (a) STEM images of twin in MDZ; (b) Dark field images of twins; (c) SAED pattern of twins in (a); (d) Dark field images of twins in MDZ; (e) HRTEM image; (f) Inverse FFT of f in (e).

The cross-sectional TEM samples were further tested by the TKD technique to gain insights into the deformation mechanism. As shown in image quality (IQ) maps (**Figs. 5.11, a** and **e**), the MDZ shows a significant decline in thickness from 20 to 220 m/s, which is consistent with the results of TEM observation. **Fig. 5.11b** depicts the inverse pole figure (IPF) map corresponding to **Fig. 5.11a**, the severely refined DRX grains with distinctive misorientation were distributed in the near-surface. By combining the grain boundary map (**Fig. 5.11c**), the elongated grains beneath the DRX grains were demonstrated to be separated by high angle grain boundaries (HAGBs), and extensive low angle grain boundaries (LAGBs) were observed within the elongated grains. In contrast, the plastic deformation was constricted in a very thin layer near to top surface, while the grains at the deeper region seldom detected HAGBs and LAGBs.

The kernel average misorientation (KAM) maps reveal the local average misorientation angle. Notably, areas with elevated KAM angles were consistently aligned with the MDZ at both 20 m/s and 220 m/s. This suggests that a high degree of strain and high density of dislocations were distributed within the related regions. In addition, the interface of α/β revealed the high KAM angle due to the local strain distributed there.

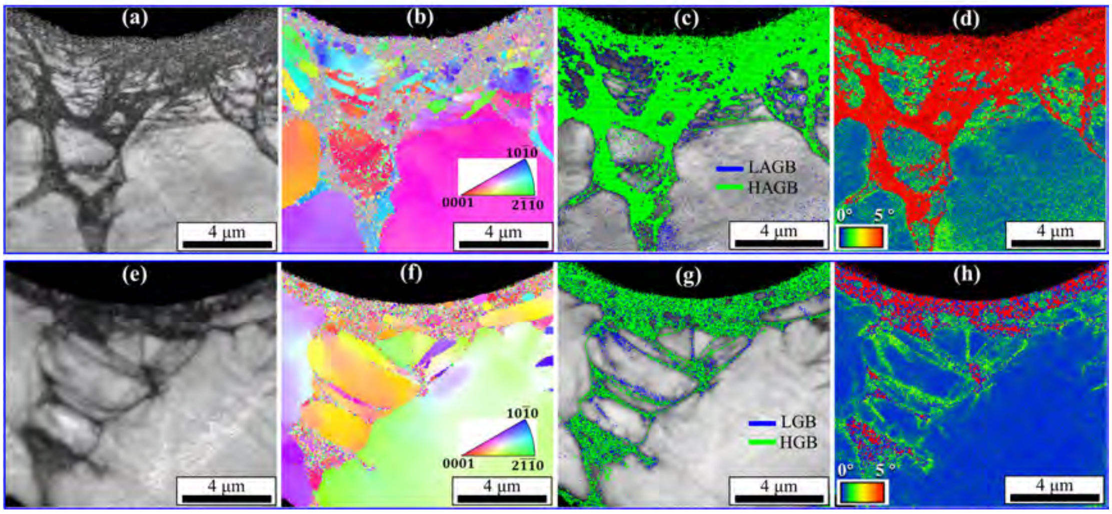

Fig. 5.11 TKD characterization of cross-sectional TEM sample: 20 m/s (a) IQ map; (b) IPF map; (c) Grain boundary map; (d) KAM map; 220 m/s (e) IQ map; (f) IPF map; (g) Grain boundary map; (h) KAM map.

5.4.2 Subsurface Deformation Mechanisms

As revealed in the preceding section, distinct MDZs were produced in the SPS of Ti-alloy at conventional and ultra-high-speed machining speeds. Accordingly, the subsurface deformation mechanism changes as the machining speed increases. To delve deeper into the detailed deformation mechanisms and their transitions from conventional speed to ultra-high-speed, the longitudinal sections of scratches machined at different were characterized by FIB+TEM.

As shown in **Fig. 5.12a**, gradient microstructures were induced in the subsurface at 20 m/s, the MDZ can be divided into two zones in terms of the different microstructures. The zone near to the top surface was the dynamic recrystallization zone (DRXZ) filled with equiaxed DRX grains in nanoscale, and the thickness of DRXZ was around 700 nm (**Figs. 5.12, c** and **d**). The zone beneath the DRXZ was defined as the plastic deformation zone (PDZ), in which grains were elongated along the machining direction. The SAED pattern reveals the boundaries between the elongated grains were HAGBs (**Fig. 5.12g)**. Furthermore, it was discernible that the elongated grains were limited within the original β phase.

Given that the stress was gradually attenuated from the machining surface to the subsurface, a transition layer was identified between the DRXZ and PDZ. In this transition layer, the primary microstructures consisted of dislocation cells and subgrains, as evident in **Figs. 5.12, e** and **f**. Additionally, the grains in the matrix beneath the PDZ exhibited no discernible plastic deformation. However, high-density dislocations (HDDs) and dislocation walls were generated within these grains due to the dislocation slip and rearrangement activities (**Fig. 5.12h**).

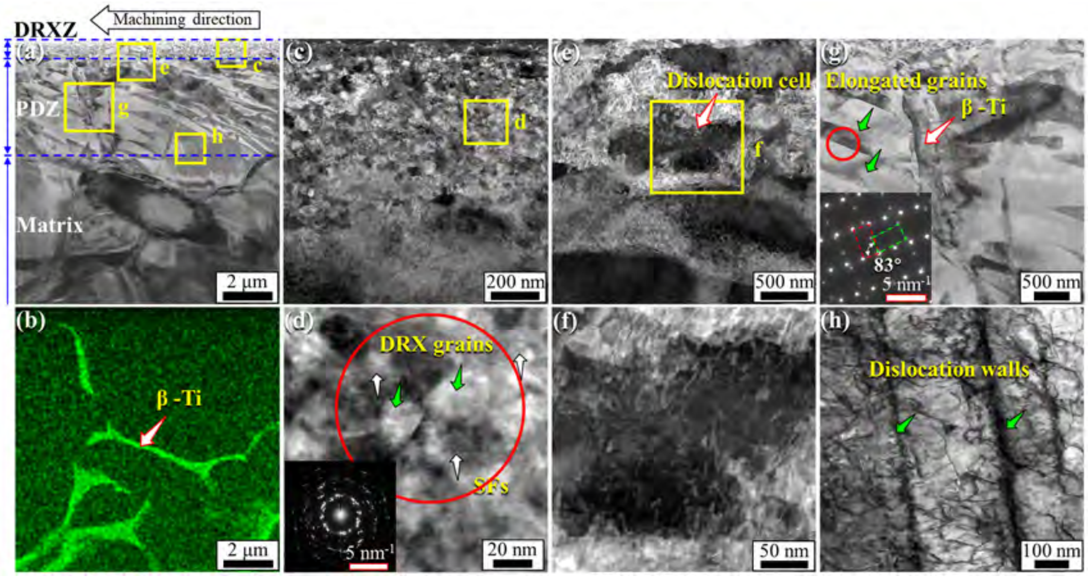

Fig. 5.12 MDZ of longitudinal section at 20 m/s: (a) MDZ distribution; (b) V element map; (c) DRX grains in DRXZ; (d) Enlarged view of d; (e) Dislocation cell; (f) Enlarged view of h; (g) Elongated grains in PDZ; (h) Dislocation walls in matrix.

As the machining speed increases to 160 m/s, the depth of MDZ was decreased to ~2 μm. Meanwhile, the deformation mechanism was significantly changed. Instead of the DRXZ, a DITZ with a thickness of ~650 μm was induced in the topmost layer (**Figs. 5.13, a** and **c**). The twin structure of $\{0\bar{1}11\}$ was calibrated by the SAED pattern obtained from zone axis of $[2\bar{1}\bar{1}0]$ (**Fig. 5.13e**). Meanwhile, the twin collision phenomenon was observed in some polygon nanoscale grains in the near-surface with a higher stress gradient (**Fig. 5.13f**). The HRTEM image of enlarged twins is shown in **Fig. 5.13g**, with the FFT pattern further identifying the twin mode (**Fig. 5.13h**).

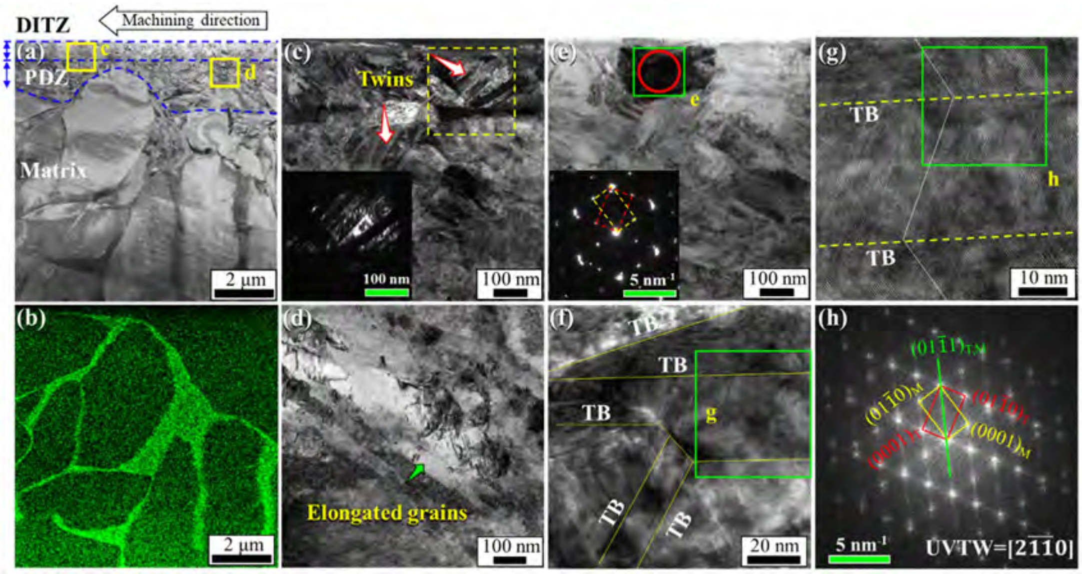

Fig. 5.13 MDZ of longitudinal section at 160 m/s: (a) MDZ distribution; (b) V element map; (c) Parallel twins in DITZ; (d) Elongated grains in PDZ; (e) STEM image of twin structure in near-surface; (f) Enlarged view of e; (g) HRTEM image of twins; (h) FFT of h.

As shown in **Fig. 5.14a**, the PDZ was absent in the subsurface when the machining speed was up to 220 m/s, demonstrating an effective inhibitory effect of ultra-high strain rate on plastic deformation. A uniform DITZ with a distinctive boundary with the matrix can be observed in the near-surface. Furthermore, a unique microstructure characterized by ultrafine grain embedding nanotwins (UGENTs) structure was identified in the DITZ. A typical UGENTs grain is displayed in **Fig. 5.14e**, it is evident that multidirectional parallel nanoscale twin systems were distributed within a polygonal ultrafine grain (Diameter: 100~200 nm) in the DITZ. Combining the STEM and dark field images, it can be observed that the twin structures, distributed in three directions with a mutual angle of 60°, intersect with each other, and these three kinds of twins were calibrated as the $\{0\bar{1}11\}$ compression twin (**Figs. 5.14, e-h**).

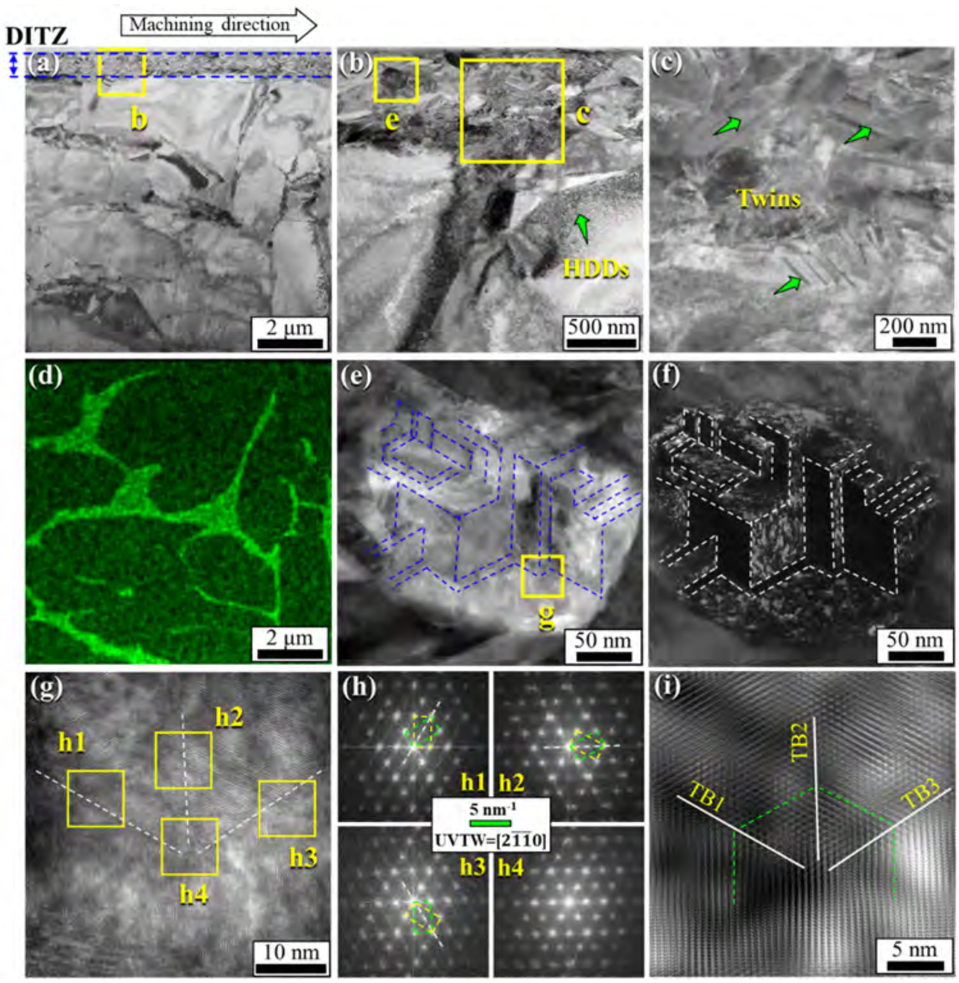

Fig. 5.14 MDZ of longitudinal section at 220 m/s: (a) MDZ distribution; (b) Enlarged view of microstructure in the near-surface; (c) Twins in DITZ; (d) V element map; (e) Enlarged STEM image of e in (b); (f) Dark field image corresponding to (e); (g) HRTEM image of g in (e); (h) FFT images corresponding to the boxes in (g); (i) Inverse FFT of h4 in (g).

5.5 Chip Formation Mechanisms of Wrought Ti6Al4V at Different Grinding Speeds

5.5.1 Chip Morphology Evolution

Figure 5.15 shows the chip morphologies at different machining speeds. The long segmented chips with a feature length of up to 275 µm were observed at the lowest machining speed of 20 m/s (**Fig. 5.15a**). This chip morphology is similar to that of chips observed in the conventional machining speed (Sutter and List 2013). **Fig. 5.15b**

presents the enlarged free surface in **Fig. 5.15a**. The shear surfaces of two primary shearing bands (PSBs) are visible, and it is evident that multiple secondary shearing bands existed in between the PSBs.

With an increase in machining speed, the shear frequency linearly increases. Accordingly, shorter segmented chips were produced due to the ASB effect, leading to a substantial reduction in chip feature size (**Figs. 5.15, c** and **d**). When the machining speed is increased to 140 m/s, the chip feature length decreased to scale of tens of microns. Furthermore, the formation of fragmented chips occurs due to the separation of segmented chips from ASBs as the machining speed ups to 200 m/s (**Fig. 5.15h**).

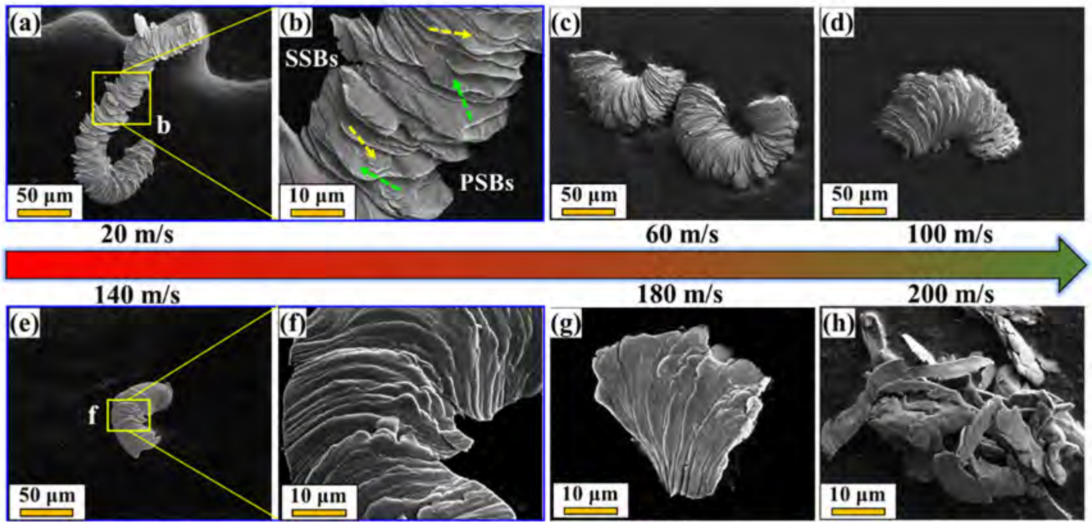

Fig. 5.15 Chip morphologies of Ti6Al4V at different machining speeds: (a) 20 m/s; (b) Enlarged view of box b; (c) 60 m/s; (d) 100 m/s; (e) 140 m/s; (f) Enlarged view of box f; (g) 180 m/s; (g) 200 m/s.

5.5.2 Chip Microstructure Evolution

To investigate the deformation mechanism, TEM samples perpendicular to the shear direction were lifted out from chips by FIB. **Fig. 5.16** displays the longitudinal section characterization of the chip produced at 60 m/s. From the global view of the extracted section (**Fig. 5.16b**), the chip experienced severe plastic deformation under the localized shear and friction, the microstructure was significantly refined to nanocrystalline. Notably, the intensification of plastic deformation exacerbated grain refinement from the free surface to the tool/chip interface.

It can be observed that abundant nanoscale streamlined lamellar β-Ti were induced by severe plastic deformation (V map in **Fig. 5.16b**). Notably, the occurrence of the ASBs coincided with the boundary of lamellar β-Ti. In the area near the free surface, cracks were observed along the ASB between two segmentations. It is noteworthy that these cracks partially propagated into the chip from the free surface, but did not extend throughout the entire chip section. This implies that the cracks were originated from the free surface rather than the region near the tooltip.

Additionally, the microstructures in different regions of the chip section show noticeable distinction. In the upper part of the chip section, the primary microstructure was equiaxed DRX grains with a diameter of 80~90 nm. However, the microstructure in the area near to free surface was coarse elongated grains due to less plastic deformation (**Fig. 5.16c**). Meanwhile, the O enrichment was detected along the cracks due to the newly formed surface (**Fig. 5.16c**). As depicted in **Fig. 5.16d**, the ASB was magnified for further observation. It is revealed that the prevailing microstructure within the ASB was composed of lamellar β-Ti with a thickness around 25 nm, indicating that the distinctive β transformation was induced in the ASB by thermomechanical effect.

In the middle part of the chip section, the microstructure was characterized by highly elongated α-Ti grains distributed in between lamellar β-Ti, and the original β-Ti was heavily deformed due to the severe shear effect (**Fig. 5.16e**). As for the microstructure in the area near the tool/chip interface, the nanoscale lamellar grains were elongated along the interface direction under the action of friction.

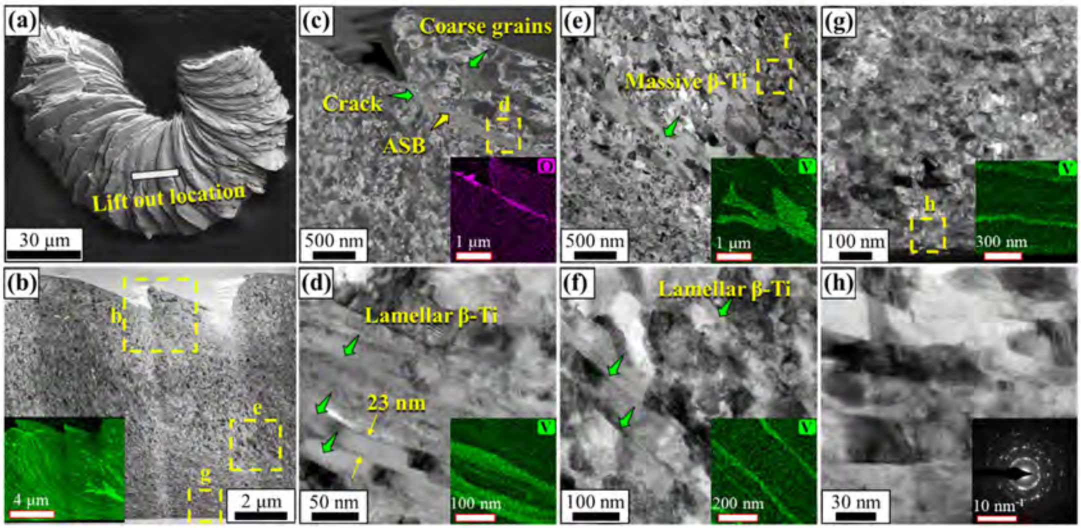

Fig. 5.16 Longitudinal section characterization of the chip produced at 60 m/s: (a) Lift out location of TEM sample; (b) Microstructure across the whole section; (c) Microstructure near the free surface of the chip section; (d) Enlarged view showing the ASB; (e) Microstructure in the middle part of the chip section; (f) Enlarged view of f in (e); (g) Microstructure near the tool/chip interface; (h) Enlarged view of h in (g).

Figure. 5.17 presents the longitudinal section characterization of the chip produced at 180 m/s. The chip thickness was significantly reduced as the machining speed increased, it decreased from 8~10 μm at 20 m/s to 3~4 μm at 180 m/s. Notably, the cracks induced by the ASBs propagated deeper into the chip section in comparison to those observed in the chip produced at 20 m/s (**Figs. 5.17, d, h, i)**. Consequently, the longer chips are prone to detach into shorter chips composing fewer segments.

For segments within the chip generated at 180 m/s, it is observed that the free surface of segments tended to rotate towards the previously produced segment (**Fig. 5.17d**). This phenomenon contradicts the behavior observed at lower machining speeds. The reason for this disparity is that the newly produced segment in shorter chips tends to rotate with the previous segment, which does not have sufficient time to escape due to the high-speed and severe friction effects of the tool's rake surface. In contrast, the free surface of segments typically rotates along the opposite direction due to the crimp of long chips at lower machining speeds (Calamaz *et al.* 2008).

Additionally, thin compression segments were observed in the area near the free surface of the chip section, and these segments were identified as the β phase (Fig. 5.17g). It can be deduced that the β transformation was induced by the severe compression from the uncut material. As a result, cracks tended to initiate and propagate along the boundaries of such β segments, resulting in the formation of thin compression segments (**Figs. 5.17, e** and **g**).

To identify the orientation relationship of lamellar β and α phase, HRTEM was also obtained (**Fig. 5.17k**). From the FFT pattern taken from the phase interface, the β-Ti still followed the typical Burges relationship of $\{0001\}_{\alpha}//\{110\}_{\beta}$, $<11\bar{2}0>_{\alpha}//<111>_{\beta}$ with α-Ti even at such a high strain rate (**Fig. 5.17l**). Moreover, although the chips were subjected to high temperature similar to the chip produced at low machining speeds, a few twins were detected due to the high strain rate (**Fig. 5.17f**).

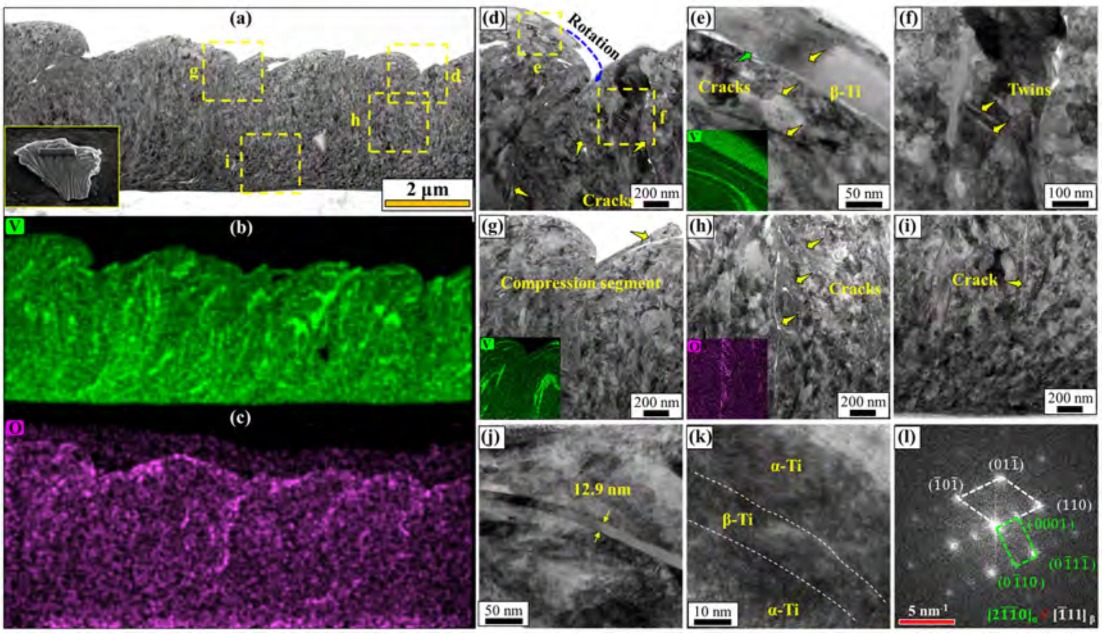

Fig. 5.17 Longitudinal section characterization of chip produced at 180 m/s: (a) Microstructure across the whole section (the inset shows the lift out location of TEM sample); (b) V map of the whole section; (c) O map of the whole section; (d) Enlarged view of d in (a); (e) Enlarged view of e in (d); (f) Enlarged view of f in (d); (g) Enlarged view of g in (a); (h) Enlarged view of h in (a); (i) Enlarged view of i in (a); (j) nanoscale streamlined lamellar β-Ti; (k) HRTEM of α/β interface; (l) FFT pattern of α/β interface.

5.6 Finite element simulation of SPS

A single-point grinding FEM was established with DEFORM-2D, and the machining temperature, strain, and strain-rate fields at different machining speeds were obtained to further understand the deformation mechanism and microstructure evolution. **Fig. 5.18** depicts the 2D geometrical model and the set-up conditions. To simplify the model, a plane strain model coupling thermomechanical analysis was developed under the orthogonal cutting condition. The workpiece material was meshed using isoparametric quadrilateral elements and modeled as elastic-viscoplastic. Meanwhile, the tool is regarded as rigid in this study.

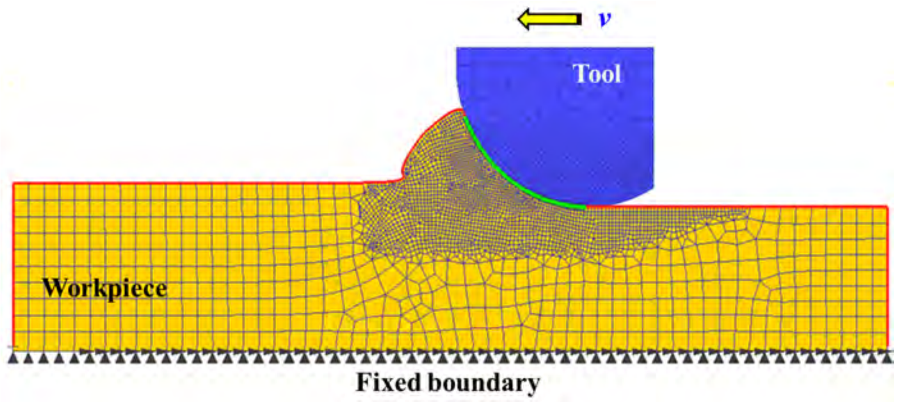

Fig. 5.18 Geometrical model and the set-up conditions.

The model was established based on the Johnson-Cook (JC) material constitutive model.

$$\sigma=\left[A+B(\varepsilon)^{n}\right]\left[1+C\ln\left(\frac{\dot{\varepsilon}}{\dot{\varepsilon}_0}\right)\right]\left[1-\left(\frac{T-T_{room}}{T_{melt}-T_{room}}\right)^{m}\right] \tag{5.2}$$

where σ is the equivalent flow stress; ε, $\dot{\varepsilon}$, $\dot{\varepsilon}_0$ represent the plastic strain, strain rate, and reference strain-rate, respectively; T_{room} and T_{melt} refer to room temperature and melting point; *A*, *B*, *C*, *n*, *m* are material constants. There parameters are summarized in **Table 5.2**. The shear failure criterion is given by Eq (5.3):

$$\varepsilon_f=\left[D_1+D_2\exp(-D_3\gamma)\right]\left[1+D_4\ln\left(\frac{\dot{\varepsilon}}{\dot{\varepsilon}_0}\right)\right]\left[1+D_5\left(\frac{T-T_{room}}{T_{melt}-T_{room}}\right)\right] \tag{5.3}$$

where γ is the stress triaxiality D_1, D_2, D_3, D_4, D_5 are the corresponding material parameters with the specific values are listed in **Table 5.3**.

Table 5.2 Material parameters for the Johnson-Cook model (Johnson and Cook 1985)

***A* (Mpa)**	***B* (Mpa)**	***C***	***n***	***m***	ε_0	T_{melt} **(°C)**	T_{room} **(°C)**
724	683	0.035	0.47	1	1	24	1560

Table 5.3 Johnson-Cook failure parameters of Ti6Al4V (Sun and Guo 2009)

D_1	D_2	D_3	D_4	D_5
-0.009	0.25	-0.5	0.014	3.87

Figure 5.19 illustrates a comparison of the distribution of strain rate, strain, and temperature during the machining process at cutting speeds ranging from 20 to 220 m/s. It is clear that the shear localization in the primary shear zone (PSZ) was significantly strengthened as the machining speed increased. The strain rate field, strain field, and temperature field were confined to a narrower band at higher machining speeds.

The majority of plastic work done in the deformation zone was translated to heat, which leads to a temperature rise. However, at higher strain rate, the material experienced rapid deformation without sufficient time for heat dissipation, resulting in a phenomenon known as adiabatic heating. This adiabatic heating, combined with the softening effects caused by elevated temperatures, contributes to the localization of plastic strain within a narrow region referred to as the adiabatic shear band (ASB). The ASB became the predominant zone for further plastic flow, leading to a concentration of deformation and eventual fracture (la Monaca *et al.* 2022; Yang *et al.* 2020).

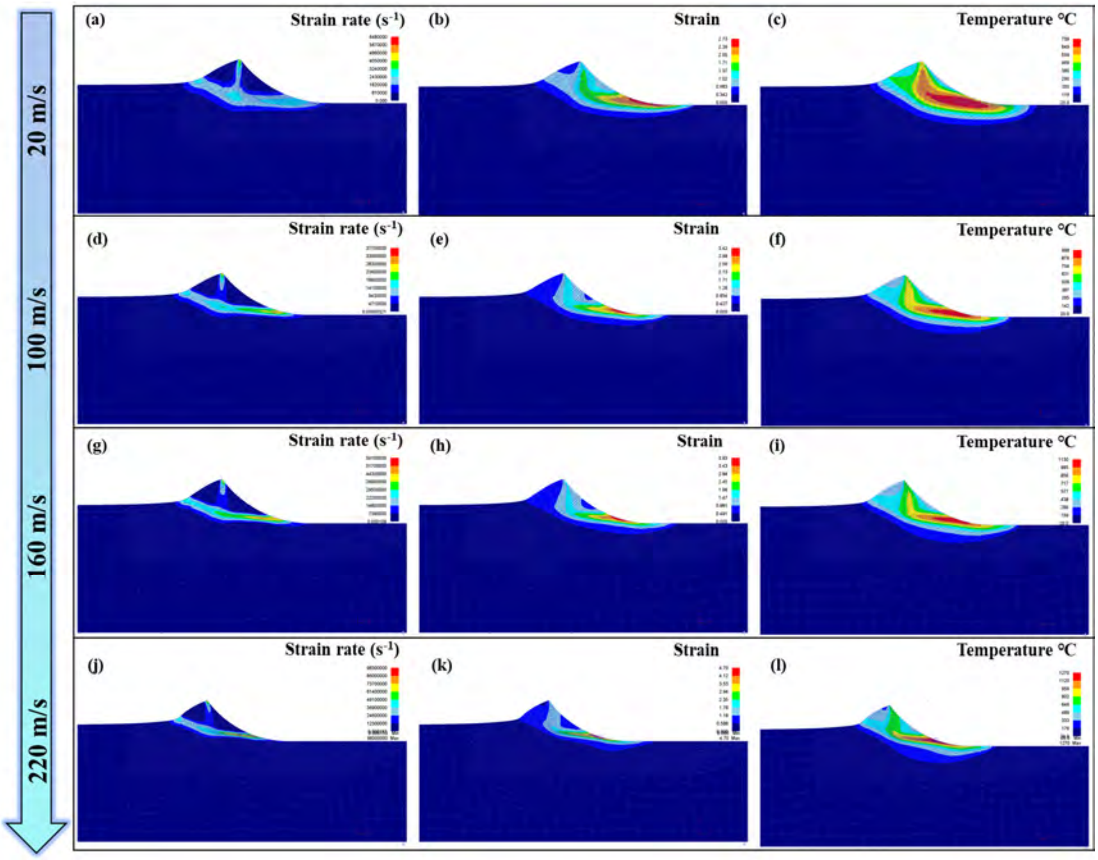

Fig. 5.19 Finite element simulation results. (a-c) Strain rate field, strain field, and temperature field at 20 m/s; (d-f) Strain rate field, strain field, and temperature field at 100 m/s; (g-i) Strain rate field, strain field, and temperature field at 160 m/s; (j-l) Strain rate field, strain field, and temperature field at 220 m/s.

As shown in **Fig 5.20a**, the material flow field revealed the presence of a stagnation point in the cutting boundary near the tooltip. In the second deformation zone (SDZ), the material located below the stagnation point exhibited a downstream flow along the tool surface, resulting in compression and integration with a portion of the machining surface. Conversely, the material situated above the stagnation point displayed an upstream flow, leading to the formation of chips. To quantitatively assess the distribution of strain rate, strain, and temperature at different speeds. The corresponding data along the depth direction starting from the stagnation point was extracted and analyzed.

As depicted in **Fig. 5.20b**, the maximum strain rate occurred in the middle region of ASB rather than the tool/chip contact boundary. Notably, as the machining speed increased from 20 m/s to 220 m/s, the amplitude of the strain rate exhibited a significant increase from 3.64×10^6 s^{-1} to 6.96×10^7 s^{-1}. Notably, the strain rate displayed a steeper descent gradient along the depth direction. Additionally, both the temperature and strain were confined in the superficial layer, which explains the reduced depth of MDZ in the subsurface of machined samples under ultra-high-speed conditions (**Figs. 5.20, c** and **d**).

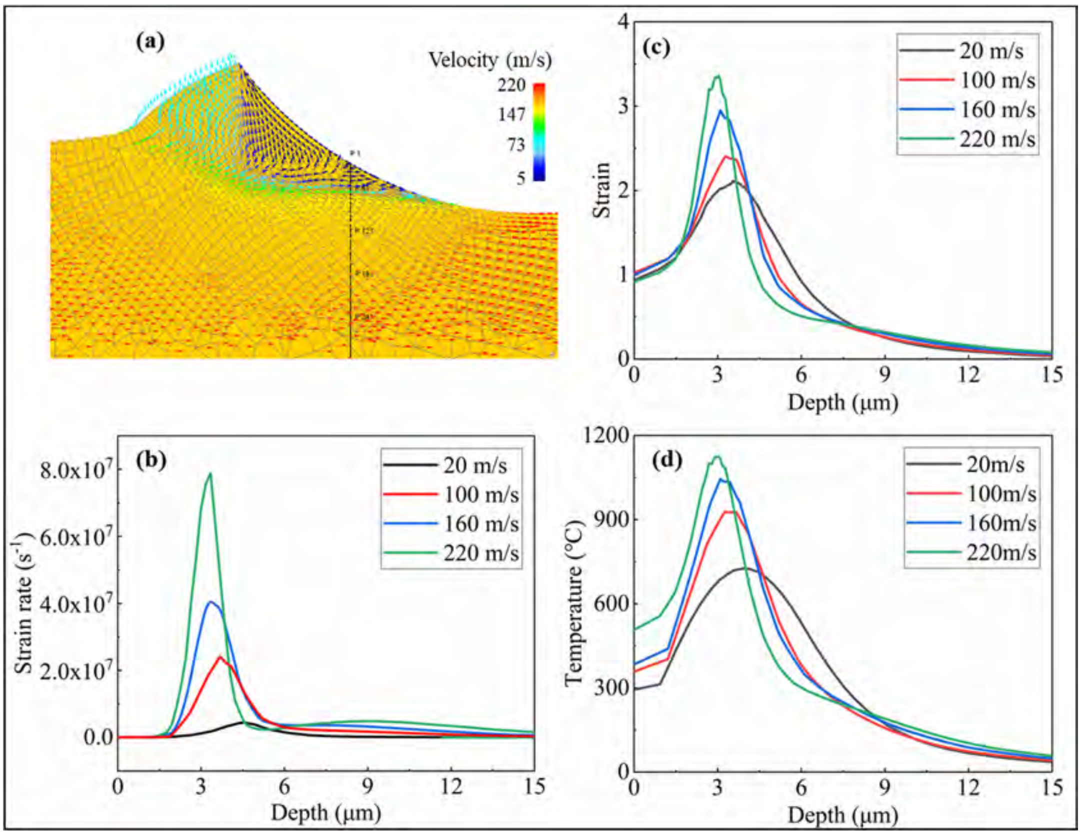

Fig. 5.20 Finite element simulation results: (a) Velocity field at 220 m/s; (b) Strain rate distribution along the depth direction from the tooltip; (c) Strain distribution along the depth direction from the tooltip; (d) Strain rate distribution along the depth direction from the tooltip.

5.7 Discussion

The strain rate effect widely exists in the material deformation and machining processes, which influences the material deformation behaviors by governing the material responses. Material responses can be divided into static response, quasi-static response, and dynamic response according to different strain rate ($\dot{\varepsilon}$). For instance, creep test is generally considered as a static process due to its very low strain rate ($\dot{\varepsilon}<10^{-2}$ s^{-1}), and tensile/compression tests fall into quasi-static process ($10^{-2}<\dot{\varepsilon}<10^{2}$ s^{-1}), while conventional machining such as cutting and milling belong to dynamic process because of the increased strain rate ($10^3<\dot{\varepsilon}<10^5$ s^{-1}). In the macro-scale, material responses including flow stress, strain hardening, and fracture behavior fluctuate dramatically under different strain rates. While in the micro-scale, material responses are primarily determined by dislocation motion, deformation twinning, and phase transformation, which also vary with strain rates.

The strain rate effect has been extensively investigated in the static or quasi-static regions. Recently, with advancements in experimental and simulation techniques, searchers have shifted their focus to the dynamic response region. However, the strain rate effect at a very high level such as ups to 10^7 s^{-1} is rarely reported. This study conducted systematic SPS of Ti6Al4V across a range of speeds, from 20 to 220 m/s. The comprehensive characterization in terms of machined surface, subsurface, and chips was performed. This study attempts to analyze the strain rate effect on the transformation of material removal mechanism, damage mode, and microstructure evolution during the machining of Ti6Al4V.

5.7.1 Surface Creation of Wrought Ti6Al4V with Increasing Machining Speed

From the aspect of the machined surface, distinctive pile-ups were distributed on two sides of the scratch machined at a lower speed, exhibiting a high pile-up ratio. This indicates severe material flowing was produced by the plowing effect of the tooltip. As the machining speed increases, the pile-up ratio decreased due to the higher degree of work-hardening at higher strain rates, this is also supported by previous researches. Hu et al. (Hu *et al.* 2020) investigated the mechanical behaviours of Ti6Al4V under various strain rates, the results indicated that the initial failure strain decreased with the increase of strain rate, while higher work-hardening rate was observed at higher strain rate.

The formation of severe pile-ups is detrimental to the high-efficiency and high-quality machining. This is because it demands extra energy consumption to remove them or results in surface defects if they persist on the machined surface. In this regard, the cutting effect and material removal rate are increased at higher strain rates since the plastic flow of material is effectively inhibited.

5.7.2 Subsurface Microstructure Evolution of Wrought Ti6Al4V with Increasing Machining Speed

The investigation of MDZ in the subsurface of machined parts has received increasing attention due to its substantial influences on the part service performance such as wear and fatigue resistance (Li *et al.* 2021; Liao *et al.* 2021; Wang *et al.* 2021). The microstructure evolution is demonstrated highly dependent on strain rate according to the comprehensive analyses of subsurface microstructure at different machining speeds.

Figure 5.21 schematically illustrates the subsurface microstructure evolution under low and ultra-high strain rates. The region with detectable deformation at grain scale was defined as the MDZ. The wrought Ti6Al4V machined at low strain rates exhibited a deep MDZ characterized by gradient microstructures from the top surface to the subsurface. The MDZ can be divided into two zones, namely DRXZ and PDZ, depending on their respective microstructure features.

Although no grain deformation was observed beneath the MDZ due to the attenuation of stress along the depth direction, scattered dislocation walls were formed through dislocation rearrangement. As it moves towards the surface, distinct grain deformation was visible in PDZ. The initial grains were elongated under the shear effect, and LAGBs were formed as the high-density dislocation pile-up along the dislocation walls. With further deformation, some LAGBs transformed into HAGBs by continuously absorbing dislocations (Liu *et al.* 2020). Therefore, the elongated grains with refined feature sizes were formed in PDZ. Additionally, abundant LAGBs remained within the elongated grains, indicating high-density dislocation pile-up and subgrains existed in the PDZ.

The topmost was the DRXZ characterized by significantly refined nanocrystalline, such grains were mainly induced by the DRX mechanism under the combined effects of high strain rate and high temperature. The new recrystallization nuclei tended to form along the boundary of elongated grains as the increase of dislocation density, and the nuclei continue to grow driven by the stored energy associated with the dislocations or sub-boundaries (Huang and Logé 2016). Finally, the equiaxed DRX grains at nanoscale were generated under the short-duration thermomechanical effect.

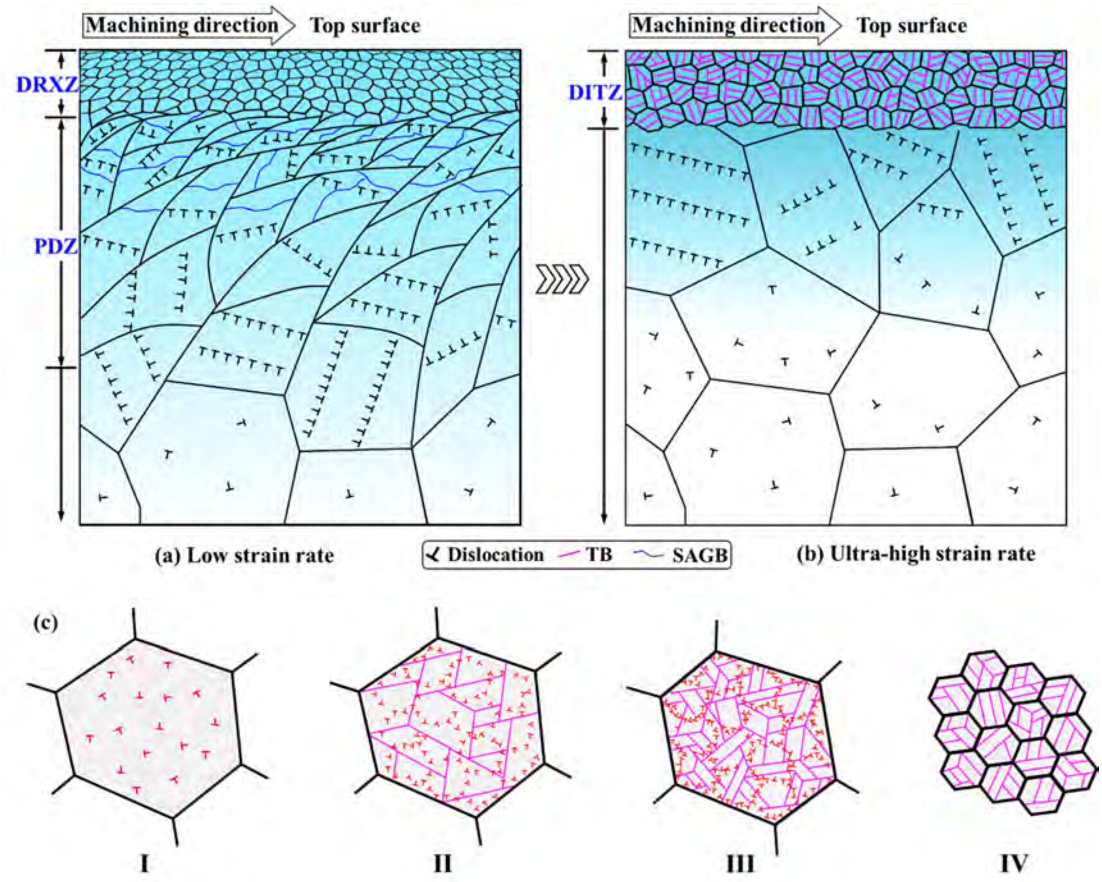

Fig. 5.21 Schematic of subsurface microstructural evolution: (a) Low strain rate; (b) Ultra-high strain rate; (c) Schematic drawing showing the evolution sequence of UGENT structure.

As the strain rate increased, the MDZ was effectively reduced due to a significant decline of PDZ. Particularly, the PDZ vanished when the strain rate reached the ultra-high region. The inhibition effect was highly associated with strain-rate hardening, the ductile material experienced severe plastic deformation at low strain rates. Nevertheless, the plastic deformation was significantly suppressed at increasing strain rate, when the strain rate exceeded the critical value of ductile-to-brittle transition, the ductile material underwent a brittle fracture (Wang *et al.* 2015). As a result, the subsurface deformation was confined to a shallower region, exhibiting a "skin effect" of MDZ.

Moreover, the deformation mechanism significantly changes under higher strain rate conditions. In conventional metal deformation processes, plastic deformation is primarily regulated by the dislocation slip, with mechanical twinning serving as a supplemental mechanism since it demands larger critical stress than dislocation slip (Pan *et al.* 2021). However, an increased contribution of twinning to plastic deformation has been widely observed in some extreme deformation conditions such as low temperature (Ye *et al.* 2021), high strain rate (George 2012; Rida *et al.* 2020), and ultrafine grain size (Chen *et al.* 2003).

In particular, strain rate has a significant influence on the formation of deformation twins. For instance, it is difficult to achieve twinned grains in high-SFE metals, but a novel twinning mechanism of pure aluminum under a high strain rate compression was reported (Liu *et al.* 2022). Additionally, twinning is a highly favored deformation mechanism under shock loading. Metals that do not twin through conventional deformation at ambient temperature can generate twins under shock loading conditions (Mogilevsky and Newman 1983).

This study revealed a transition of the subsurface deformation mechanism from dislocation slip to mechanical twinning as the strain rate increases. At low strain rates, the dominant mechanism was dislocation-mediated deformation (DMD) and mechanical twinning was absent. As the strain rate increased, the activation of slip systems was retarded (Dai and Song 2022), and the twinning-mediated deformation (TMD) mechanism tended to be induced in the DITZ at the topmost of the subsurface. In the deeper layer, the PDZ associated with dislocation slip was generated to coordinate deformation. As the strain rate further increased (220 m/s), the TMD transited to the dominant deformation mechanism. The molecular dynamics simulation research (Zepeda-Ruiz *et al.* 2017) can be a useful reference to understand the transition. The simulation results suggested that the dislocation slip could not relieve the mechanical loading when the strain rate was up to a critical strain rate (5.56×10^{8} s^{-1}) in the compression deformation of tantalum, the deformation twinning took over as the dominant mechanism for dynamic response.

Compared with mechanical twinning, dislocation slip is predominantly influenced by thermal activation and necessitates adequate time to surmount energy barriers, thus dislocation slip is favored at high temperatures. Deformation twinning is a sudden re-orientation process of the crystal lattice, which is much more pronounced under high strain rate conditions (Tang *et al.* 2022). Material deformation in machining is a complex process accompanied by high strain rates and high temperatures. From the microstructure evolution, it can be concluded that strain rate plays a predominant role in material deformation. Particularly at ultra-high strain rate loading, the dislocation slip is inhibited and the deformation twinning is activated and serves as the predominant deformation mechanism.

A new deformation mechanism at ultra-high strain rates led to a completely different microstructure. Under the ultra-high strain rate conditions, a novel microstructure called UGENTs was induced. A new microstructure evolution mechanism of UGENTs was proposed and schematized in **Fig. 5.21c**. High density $\{0\bar{1}11\}$ compression nanotwins nucleated and grow in different pyramidal slip planes as the dislocation slip was inhibited at ultra-high strain rate, the coalescence and intersection of nanotwins significantly altered the grain orientation, which in turn increased the probability of dislocation slip. Consequently, dislocation accumulation was promoted, which created a favorable environment for the formation of LAGBs and eventually HAGBs. As a result, a distinct microstructure characterized by ultra-fine grains containing nanotwins was formed.

Nanotwin-induced grain refinement at high strain rates has been reported in previous studies, the refinement process was designated as nanotwinning-assisted dynamic recrystallization (ntDRX) and deformation-activated recrystallization twin (DART) (Liu *et al.* 2022; Tiamiyu *et al.* 2022). For ntDRX, the deformation twins induced by high strain rate impact in copper promoted the formation of nanoscale DRX grains (Tiamiyu *et al.* 2022). While twin boundaries were observed inside the micro-scale DRX grains formed by high strain rate impact of single-crystal high-purity Al at a cryogenic temperature (Liu *et al.* 2022). It should be noted that the nano-grains induced by ntDRX were typical defect-free DRX grains, but the ultra-fine grains produced in this study contain multiple nanotwins inside, such unique microstructure has been demonstrated possessing enhanced strength and ductility (Zhu *et al.* 2012). Meanwhile, the deformation twin, induced by DART mechanism, was mainly promoted by the migration of the noncoherent boundary and occurred at a very low-density level.

5.7.3 Chip Formation mechanisms of Wrought Ti6Al4V with Increasing Machining Speed

The investigation of chip formation during a machining process is critical for a better understanding of the material removal mechanisms. As the machining speed increased, the long-segmented chips produced at low machining speed (20 m/s) were transited to much smaller segmented chips, and microscale fragmented chips were eventually formed when the machining speed reached 200 m/s.

The transition to fragmented chips was attributed to the evolution of ASB, the ASB refers to a narrow zone characterized by highly localized shear deformation, which was governed by multiple factors including thermal softening, strain rate hardening, and strain hardening (Yan *et al.* 2021). The onset of ASB was closely linked to high strain rates, as several materials, including Ti-alloys (Ma *et al.* 2017), aluminum alloys (Wu *et al.* 2018), and stainless steels (Gu *et al.* 2016), tended to form ASBs when the machining speed exceeded a critical value.

At higher strain rates, the heat induced by plastic deformation was constrained in a narrow band, the material in this band was easy to deform due to the thermal softening, promoting the shear instability and the formation and development of ASB. The fully matured shear bands at high strain rates were believed to lead to the formation of fragmented chips (Ye *et al.* 2017). The material in ASB had completely different mechanical properties such as hardness, strength, and toughness compared with the surrounding material (Wan *et al.* 2012). As a result, cracks tended to initiate and propagate along the ASB as the deformation progresses, eventually leading to the separation between adjacent segmented chips and the formation of fragmented chips.

The microstructure characteristics of formed chips can provide valuable insight into the thermal and mechanical loads during machining, as well as the underlying deformation mechanisms. Conventionally, plastic deformation was mainly restricted in the ASB while the material outside the ASB remained barely deformed, and the phase transformation, DRX, or twinning serving to consume the deformation energy were usually detected inside the ASB (Ye *et al.* 2013; Zhang *et al.* 2014).

However, in this study, the nanoscale DRX grains were the dominant microstructure in the whole chip section, and distinct phase transformation was also observed outside the ASBs. This noticeable difference was attributed to more severe plastic deformation induced by the large negative rake angle (-60°). As the negative rake angle of the tool increased, the compression effect was further amplified, leading to a greater temperature rise (Opoz and Chen 2016). This increase in temperature, in turn, stimulated the initiation and growth of DRX in elongated grains outside the ASBs. Meanwhile, the nanoscale β-Ti lamellae were found to be intercalated among the DRX grains and distributed along the direction of shear deformation. A higher density of these lamellae was observed in regions closer to the ASB and tool/ship contact interface due to the higher temperature.

As the strain rate increased to an ultra-high level, a transition from segmented chips to fragmented chips tended to be triggered. Meanwhile, the microstructure also showed different characteristics. The DRX grains were still the primary microstructure in the chip section but with a smaller size (~35 nm) due to the time limitation for grain growth under ultra-high strain rates. Contrary to the machined surface, twin structure was seldomly observed in the chip section. The formation of twins was impeded by two critical factors: the stress release process that occurred during the separation of adjacent chips (Ye *et al.* 2017), and the elevated temperature within the chips (Abukhshim *et al.* 2006), the former degraded the critical stress condition necessary for twin formation, while the latter boosted the DRX process, which competes with twin formation.

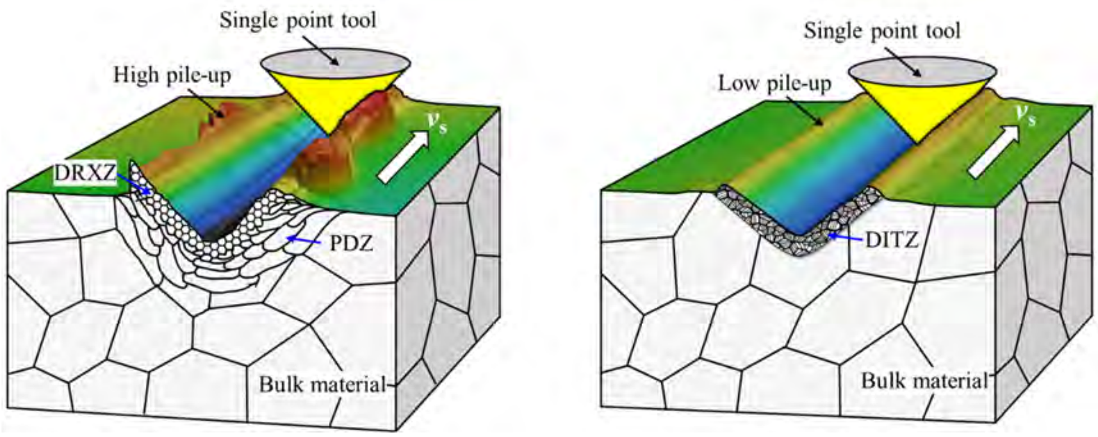

Fig. 5.22 Schematic drawing of machining process and the MDZ distribution in the cross-section under low and ultra-high strain rates.

5.8 Conclusions

In this study, an SPS experimental system was developed, and based on this, a series of SPS experiments were conducted ranging from 20 to 220 m/s to investigate the strain rate effect from low to ultra-high regions in the machining of Ti6Al4V alloy. The underlying material removal and deformation mechanisms at different machining speeds were revealed by applying a multiscale characterization method combining TKD, FIB, and STEM techniques. For the first time, this study revealed a novel UGENTs microstructure and its formation mechanism under ultra-high strain rate conditions. The main findings are drawn as follows:

(1) Higher machining speed can improve machining removal rate and machining quality by inhibiting the pile-up effect;

(2) At low machining speeds, a deep MDZ was induced in the machined subsurface. The MDZ can be divided into DRXZ and PDZ according to the alterations in microstructure. The DRXZ was characterized by nanoscale DRX grains, while the PDZ comprised elongated grains;

(3) The MDZ showed a distinctive “skin effect” as the PDZ was significantly inhibited at higher machining speeds. When the machining speed reached 220 m/s, the PDZ disappeared. Meanwhile, the material deformation mechanism transited from DMD to TMD as the strain rate increased, and the TMD played the dominant role at ultra-

high strain rates as the dislocation slip was inhibited;

(4) A novel microstructure characterized by ultrafine grain embedding nanotwins was generated at an ultra-high strain rate, and a nano-twin predominant grain refinement process was proposed to describe the formation mechanism;

(5) The chip formation showed a strain rate dependence, as the segmented chips transitioned to fragmented chips with much smaller feature sizes and refined microstructure at high machining speeds.

Chapter 6 Material Removal Mechanisms of SLM-ed Ti6Al4V in Single-point-scratching

6.1 Introduction

The SLM technique presents an unparalleled opportunity for the efficient and rapid manufacturing of net-shaped parts with intricate geometries, surpassing the capabilities of conventional manufacturing methods. This innovative approach holds tremendous potential for the production of high added value Ti-alloy parts, offering unprecedented possibilities for advancement in the field. However, the inferior surface integrity of as-built SLM-ed parts makes it hard to meet the ever-increasing requirements in critical applications. Therefore, surface mechanical machining is necessary to guarantee the surface quality of SLM-ed parts.

UHSM has been demonstrated to possess the capability to achieve high machining quality in a highly efficient way in machining wrought Ti6Al4V. Nevertheless, SLM-ed Ti6Al4V has distinctively different microstructures and mechanical properties compared with wrought Ti6Al4V. During an SLM deposition process, SLM-ed Ti6Al4V experiences very high cooling rates and a large temperature gradient, resulting in refined acicular or lamellar microstructures, rather than the coarse equiaxed microstructure observed in wrought Ti6Al4V. The unique microstructure characteristics contribute to the enhancement of strength, hardness, and brittleness in as-built SLM-ed Ti6Al4V. Additionally, the surface layer of SLM-ed Ti6Al4V tends to exhibit high tensile residual stresses. Accordingly, these differences give rise to distinct machining characteristics of SLM-ed Ti6Al4V, and it is necessary to investigate the alterations of material removal and deformation mechanisms during the UHSM process.

Recent studies have explored the mechanical processing of additively manufactured metallic alloys (Khanna *et al.* 2021; Zhang *et al.* 2020). In the conventional machining of SLM-ed Ti6Al4V, higher cutting forces compared to wrought Ti6Al4V were reported due to its increased strength and hardness. Generally, the machined SLM-ed Ti6Al4V usually exhibits a better surface finish attributed to the lower ductility.

Nevertheless, it is crucial to recognize that microstructure, strain hardening, and machining deformation layer also play important roles in the machining of Ti6Al4V alloys. Previous studies have confirmed that SLM-ed Ti6Al4V exhibited distinct machining characteristics compared with wrought Ti6Al4V due to the discrepancies in microstructures, mechanical properties, and responses to machining loading. Consequently, the optimized machining process parameters for wrought materials must be suitably adjusted to cater to additively manufactured parts. Furthermore, the material removal behaviors of SLM-ed Ti6Al4V in the UHSM process have not been investigated, and the influence of ultra-high strain rate on the machining of SLM-ed Ti6Al4V remains unknown.

In this regard, this chapter focuses on the material removal and deformation mechanisms of SLM-ed Ti6Al4V theoretical foundation and research methodologies established in the UHSM of wrought Ti6Al4V. The material removal mechanisms were analyzed from the aspects of surface morphology/profile, subsurface deformation, and chip formation characteristics by applying multiscale characterization methods. Additionally, the influence of microstructure difference between wrought and SLM-ed Ti6Al4V on material removal and deformation mechanisms were compared and investigated.

6.2 Experimental Procedures and Methodology

6.2.1 Workpiece Material and Experimental Setup

The SLM-ed Ti6Al4V samples with a high relative density (99.7%) were manufactured by the optimized parameters (Laser power: 220 W; Scanning speed: 1200 mm/s; Hatch spacing: 80 μm; Layer thickness: 30 μm) (Jiang *et al.* 2023). The 67° scan rotation strategy was applied to manufactured 10×10×5 mm block samples layer upon layer (**Fig. 6.1a**). **Fig. 6.1b** reveals the representative 3D metallographic structure of the SLM-ed samples. The SLM-ed Ti6Al4V displayed typical columnar β grains on its side surfaces, while the upper surface exhibited a grid-like pattern. Ultrafine lamellar α+β microstructures were obtained (**Fig. 6.1d**), and the SLM-ed Ti6Al4V exhibited superior tensile properties (Tensile strength:1390 MPa; Elongation: 9.66%).

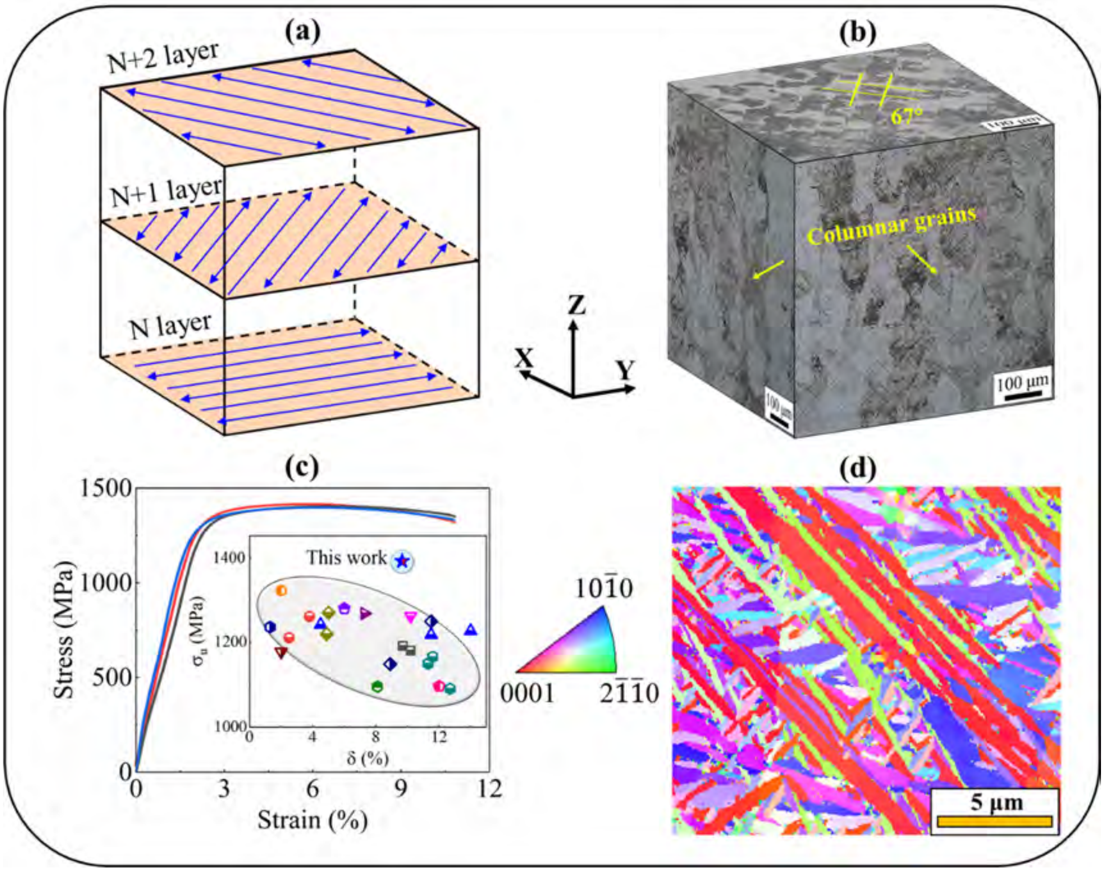

Fig. 6.1 (a) Scanning strategy for manufacturing Ti6Al4V by SLM; (b) 3D metallographic structure; (c) Stress-strain curves (The inset displays the tensile properties comparison with recent references); (d) EBSD analysis of the ultrafine lamellar α+β microstructures.

SLM-ed Ti6Al4V samples were affixed onto a titanium wheel using paraffin wax after cutting from the substrate by wire-cutting. On-process grinding and polishing were applied to remove the coarse surface layer. The SPS experiments were conducted using a Hardinge QuestGT27 grinding machine. This machine was equipped with a high-speed hydrostatic bearing motorized spindle capable of reaching a maximum speed of 60,000 rpm. **Figs. 6.2, b** and **c** depict the schematic diagram of the SPS system.

To attain exceptionally high machining speeds, a wheel made of carbon fiber reinforced plastic (CFRP) was utilized. The CFRP wheel exhibited several advantageous including lightweight construction, exceptional strength, and excellent damping properties. Its primary function was to securely hold the conical single point diamond tool, featuring a tip radius measuring 30 μm and a cone angle of 120°. Evenly spaced parallel single scratches were produced as the spindle rotates and feeds along the Y-axis (**Fig. 6.2d**). **Table 6.1** summaries the parameter design, eight SPS trials were performed, with the grinding linear speed velocity ranging from 20 to 220 m/s. Prior to each trial, a new single-point grinding tool was used, and an on-process dynamic balance was carried out to ensure proper dynamic balancing performance.

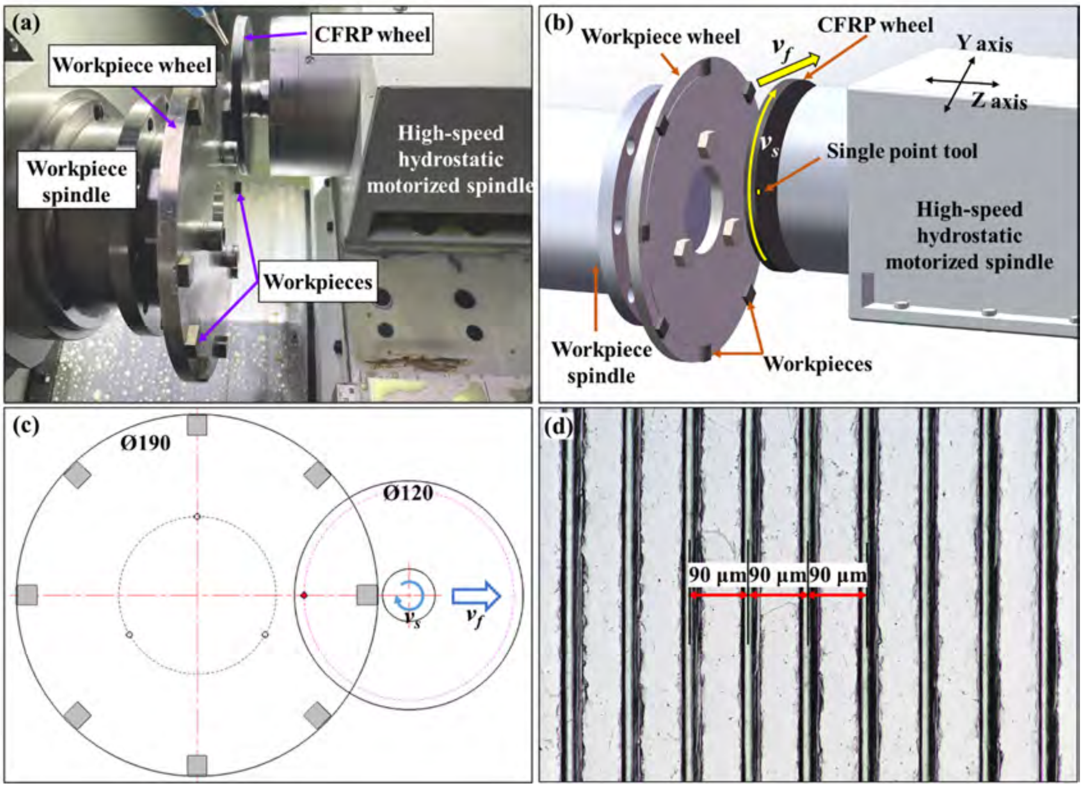

Fig. 6.2 Experimental setups: (a) Single-point-scratching setup; (b), (c) Schematic diagram of single-point-scratching; (d) Parallel single point scratches.

Table 6.1 Machining parameter of Ti-alloy in single-point-scratching.

Trials	**Spindle speed (rpm)**	**Scratching linear speed v_s (m/s)**	**Feed speed v_f (mm/min)**	**Depth-of-cut (μm)**
1	3474	20	313	2.5
2	10423	60	938	
3	17371	100	1563	
4	24320	140	2188	

Table 6.1 (Continued)

Trials	**Spindle speed (rpm)**	**Grinding linear speed v_s (m/s)**	**Feed speed v_f (mm/min)**	**Depth-of-cut (μm)**
5	27794	160	2500	2.5
6	31268	180	2813	
7	34742	200	3125	
8	38217	220	3438	

6.2.2 Material Characterization Methods

The machined scratches were analyzed in terms of surface and subsurface. The surface morphology was detected by laser scanning confocal microscopy (LSCM), and the cross-sectional profiles were analyzed by the MULTI-FILE ANALYSIS software. The focus ion beam (FIB: Helios 600i) and transmission electron microscopy (Talos F200X G2) techniques were combined to reveal the subsurface microstructures. The large cross-sectional TEM lamellae were extracted to investigate the global distribution of the subsurface microstructure, while the longitudinal section TEM lamellae were prepared to identify the deformation mechanism. **Fig. 6.3** shows the workflow for manufacturing TEM lamella by Fib, both longitudinal and cross-sectional samples were prepared to investigate the subsurface microstructure distribution and evolution.

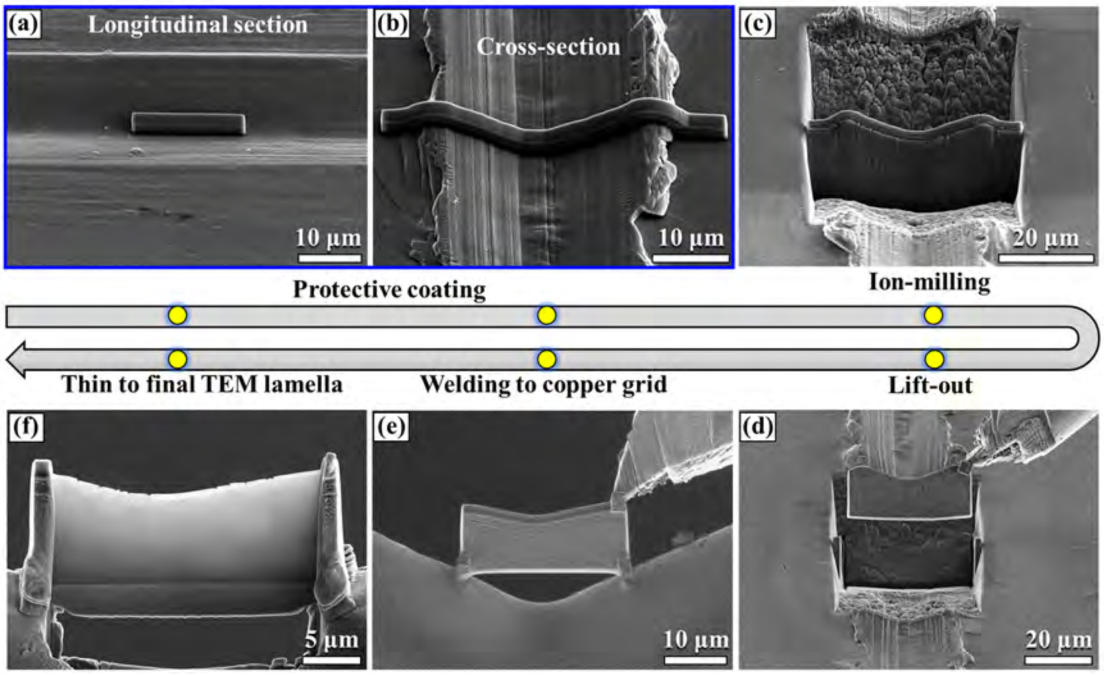

Fig. 6.3 Workflow for manufacturing TEM lamella by Fib: (a), (b) Coating carbon layer on the scratch surface to protect the interested surface layer; (c) Ion-milling to expose the interested subsurface area; (d) Lift-out the cross-sectional sample after U cut; (e) Welding the sample to copper grid for further thinning; (f) Repeat thinning with gradually decreasing current.

6.3. Results

6.3.1 Surface Morphology and Profile of SLM-ed Ti6Al4V at Different Machining Speeds

Figure 6.4 illustrates the typical 3D surface morphology and the corresponding average cross-sectional profiles of the scratches machined at low to ultra-high speeds. It can be observed that distinct material accumulations existed on both sides of single scratches machined at relatively low speeds. The pile-up was produced by the plastic deformation of workpiece material under the plowing effect of the tooltip. As the machining speed increased, the cutting effect was strengthened, and the material pile-up became less pronounced, leading to a higher material removal rate.

To quantitatively analyze the effect of machining speed on the pile-up phenomenon, the pile-up ratio was calculated based on the average cross-sectional profile. **Fig. 6.5** depicts the quantitative analysis results of the pile-up ratio as a function of machining speed. it is revealed that the pile-up ratio linearly decreased from 74.8% at 20 m/s to 51.6% at 220 m/s as the machining speed increased, which is consistent with the observation of 3D surface morphologies.

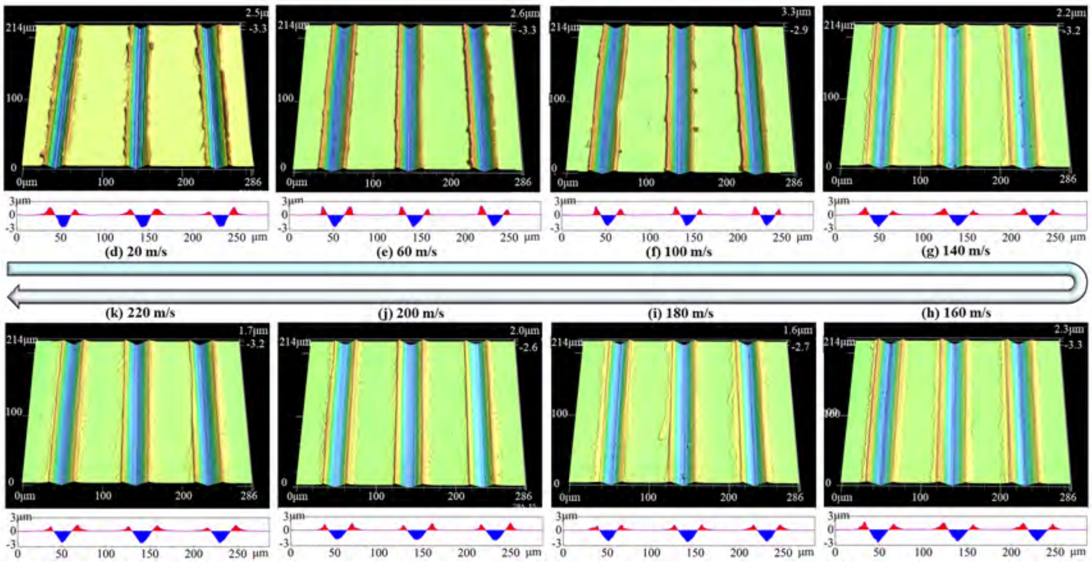

Fig. 6.4 3D surface morphology of scratches machined at different machining speeds and the corresponding cross-sectional profiles.

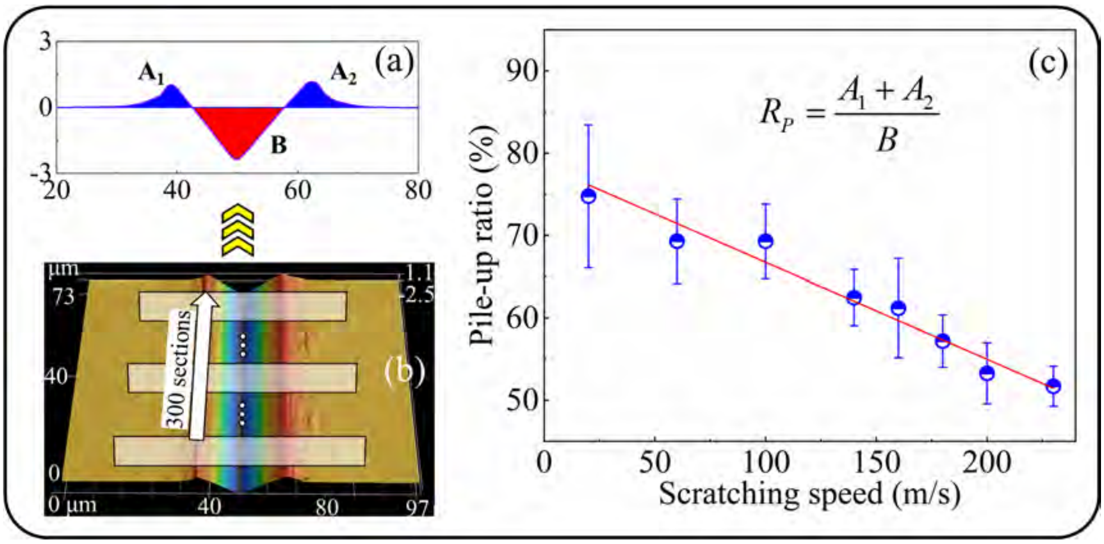

Fig. 6.5 (a) Average cross-sectional profile; (b) 300 sections are extracted to generate an average cross-sectional profile; (c) Speed effect on the pile-up ratio.

6.3.2 Subsurface Deformation Mechanisms of SLM-ed Ti6Al4V at Different Machining Speeds

Figure 6.6 shows the TEM images of the subsurface microstructure in polished SLM-ed Ti6Al4V. The parallel α martensite laths were the dominant microstructure distributed within the prior β grains (**Figs. 6.6, a** and **b**). Except the uniformly distributed dislocations inside the α laths, transformation twins were detected between some α laths (**Fig. 6.6c**). The internal twins were generated to accommodate the shape strain (Zhong *et al.* 2018). As shown in **Fig. 6.6d**, the twins were calibrated as {10−11} <−1012> twins. This twinning system is widely reported as the preferred twin in Ti6Al4V manufactured by laser AM techniques, which is attributed to the high cooling rates and thermal gradients during the solidification process (Pantawane *et al.* 2021). Additionally, the thickness of the twins varied from a dozen nanometers to more than one hundred nanometers due to the very different local stress conditions.

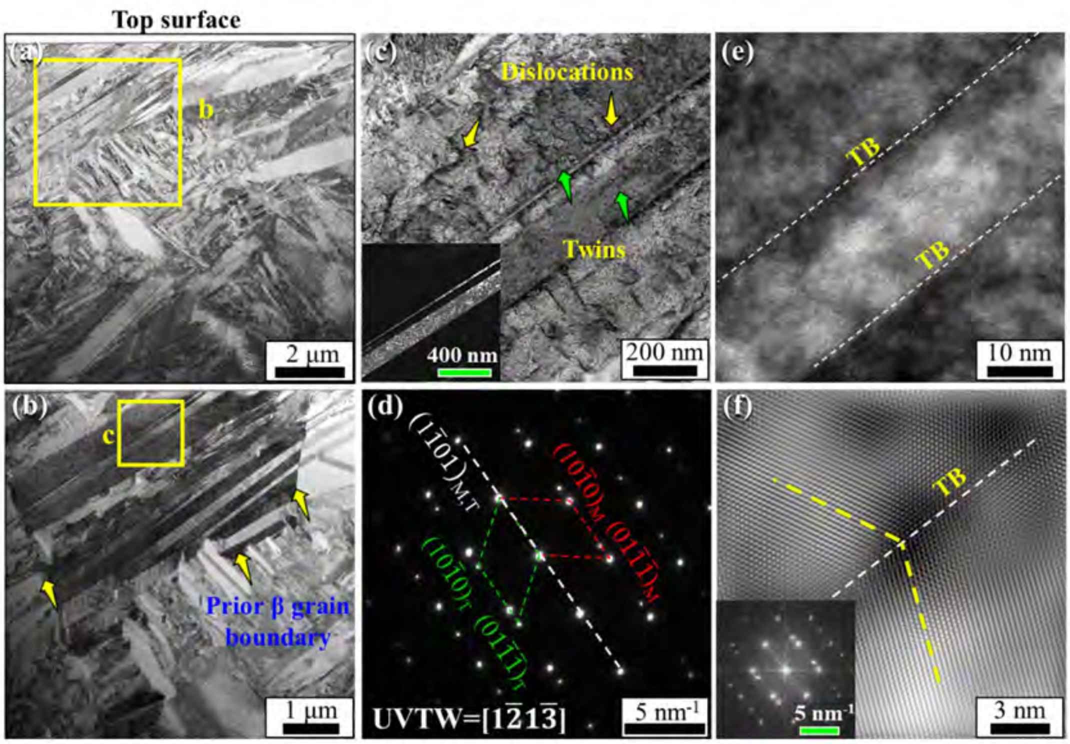

Fig. 6.6 (a) STEM image of the subsurface microstructure in as-polished Ti6Al4V; (b) Enlarge view of box b; (c) Twin and dislocation structures (The inset is the corresponding dark-field image); (d) Composite diffraction spots containing the matrix

and the twins; (e) HRTEM of the twin; (f) Inverse FFT of the twin interface.

Figure 6.7a displays the lift-out location of the cross-sectional sample machined at 20 m/s, it can be seen that the distinct pile-ups were distributed along the scratch edges. According to the global distribution of microstructure in the cross-section (**Fig. 6.7b**), a machining-deformed zone (MDZ) composed of severely deformed microstructures with an average thickness of around 2.8 μm was identified. The oxygen map indicates that oxygen enrichment occurred along the newly formed crack in the interface of pile-up and the matrix material (**Fig. 6.7c**), while the V element shows a uniform distribution (**Fig. 6.7d**). Three typical regions, including the scratch's bottom, side wall, and pile-up, were carefully analyzed to ascertain the microstructure alteration in MDZ. Right at the bottom of the machined scratch, gradient microstructures were formed under the intense compression impact from the tooltip (**Fig. 6.7e**). The topmost layer was full of dynamic recrystallization (DRX) grains with an average diameter of ~20 nm (**Fig. 6.7f**). Beneath the DRX layer, fine elongated grains feature with inside multiple substructures such as high-density dislocation tangles or slip bands were identified (**Fig. 6.7g)**.

As for the side wall of the scratch, the microstructure in the topmost layer was also revealed as DRX grains. At the deeper layer in MDZ, the microstructure was highly elongated grains with inside forest dislocations, those grains were elongated along the direction of the side wall under the extrusion force of the tooltip (**Figs 6.7, h-j)**. High material pile-up tended to be produced at conventional machining speed, and cracks were induced as the accumulated material was continuously pushed to the edges of the scratch. The material flow traces can be identified in the pile-up material and its contiguous areas with the matrix, indicating severe plastic deformation was produced (**Fig. 6.7k**). Additionally, the grains in the pile-up region were also highly elongated, but the surface layer in contact with the tooltip was full of DRX grains due to the high thermomechanical effect (**Figs. 6.7, l and m**).

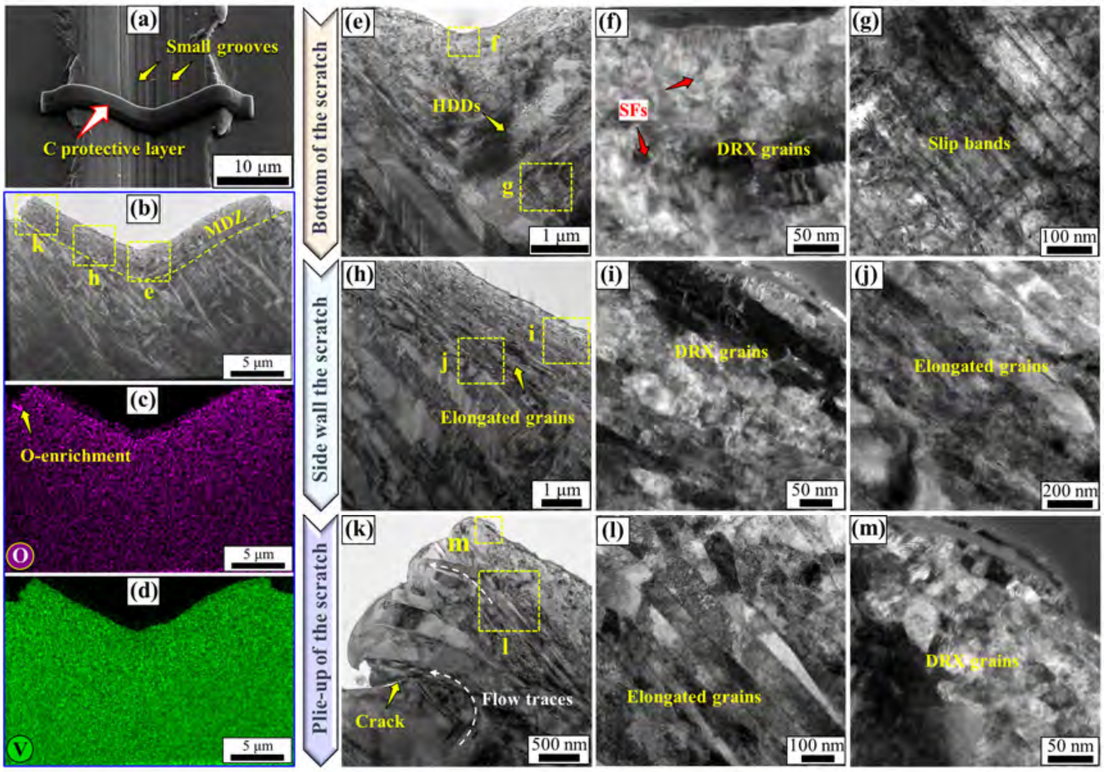

Fig. 6.7 Cross-sectional characterization of the scratch machined at 20 m/s. (a) Lift out location of cross-sectional sample; (b) STEM image of the global cross-section and the corresponding O and V maps; (c)-(e) Bottom of the scratch; (f)-(h) Side wall of the scratch; (i)-(k) Plie-up of scratch.

Figure 6.8 reveals the microstructure characterization of the scratch machined at 220 m/s from the cross-sectional view. The MDZ was substantially reduced to ~1 μm (**Fig. 6.8b**), which was decreased by 64% compared to that at 20 m/s. The subsurface shows a uniform distribution of V element (**Fig. 6.8d**), and no oxygen enrichment occurred in the surface layer (**Fig. 6.8c**). Meanwhile, distinct microstructures were observed in the MDZ. From the bottom of the scratch, the ultrafine grains with polygonal shape were identified (**Fig. 6.8e**), and it is evident that lens-like twins distributed within these grains. **Fig. 6.8f** exhibits the enlarged view and the inset shows the dark-field image of parallel twins.

The High-resolution TEM (HRTEM) image in **Fig. 6.8g** shows a twin boundary, and the inset FFT pattern identified the $\{0\bar{1}11\}$ twin. **Fig. 6.8h** shows the side wall of the scratch, a clear boundary between the MDZ and the matrix can be distinguished.

The enlarged view also reveals the ultrafine grains with embedding twins (UGENTs) structure. The edge area of the scratch produced at 220 m/s shows a lower pile-up compared to that of the scratch produced at 20 m/s (**Fig. 6.8k**). Ultrafine grains with a diameter size of 100~200 nm were observed in the MDZ. Substructures such as nanoscale twins and dislocations were identified inside the ultrafine grains (**Fig. 6.8l**). Additionally, it is evident that high-density dislocations (HDDs) were induced in the α laths in the matrix (**Fig. 6.8m**).

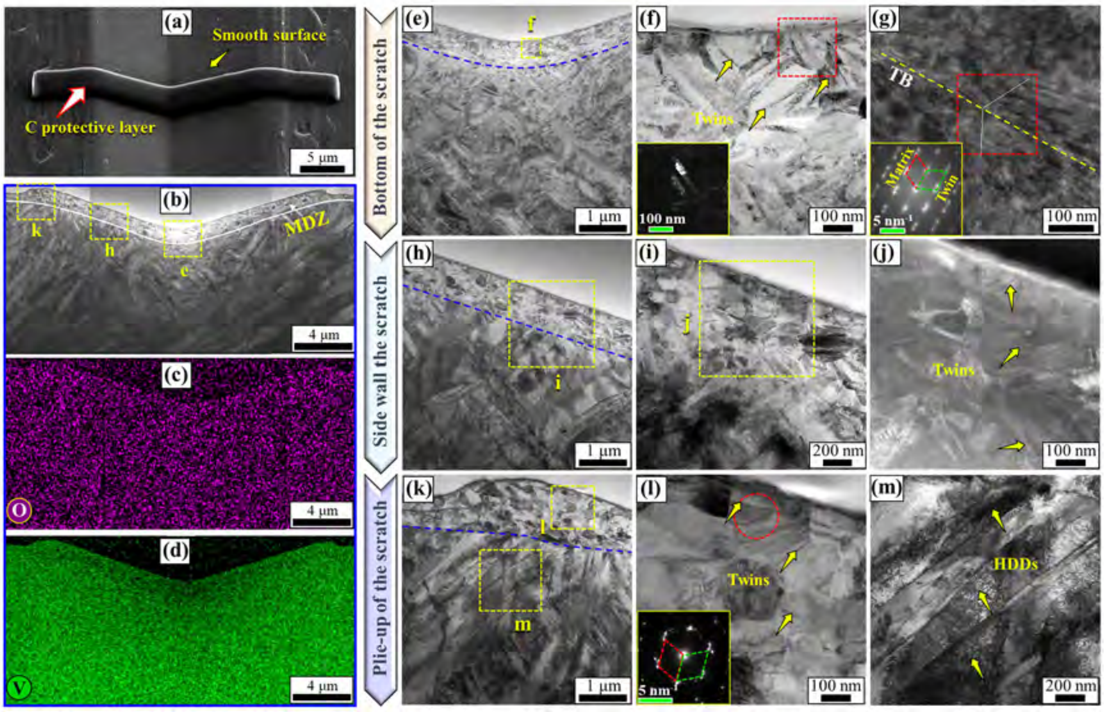

Fig. 6.8 Cross-sectional characterization of the scratch machined at 220 m/s (a) STEM image of the global cross-section and the corresponding V, O and C maps; (b)-(d) Bottom of the scratch; (e)-(g) Side wall of the scratch; (h)-(j) Plie-up of scratch.

The longitudinal TEM lamellae were further characterized to identify the underlying deformation mechanism. **Fig. 6.9a** displays the subsurface microstructure distribution of the longitudinal section at 20 m/s. The depth of the MDZ was around 2.8 μm, which is consistent with the observation from the cross-section view. According to the microstructure features, the MDZ can be divided into two distinct layers. The topmost layer is identified as the DRX zone (DRXZ), characterized by equiaxed nanocrystals. The dark-field image in **Fig. 6.9b** shows the uniform distribution of DRX grains in the top surface layer. The enlarged view reveals that the DRX grains were surrounded by multiple stacking faults (**Fig. 6.9d**), which suggests that they were formed through the continuous dynamic recrystallization (CDRX) mechanism (Huang and Logé 2016).

The deeper zone beneath DRXZ was termed the plastic deformation zone (PDZ) since the microstructure gradually transformed to elongated grains as the reduction of thermomechanical effect along the depth direction (**Figs. 6.9, g** and **h**). There was no definite boundary that existed between the DRX and PDZ because the stress and strain rate were progressively changed from the top surface to the subsurface. Instead, a transition layer was identified, in which ultrafine DRX grains nucleated and formed along the boundary of dislocation cells (**Fig. 6.9e**). It can be inferred that the DRX grains in the transition layer were produced following the discontinuous dynamic recrystallization (DDRX) mechanism (Zhong *et al.* 2020).

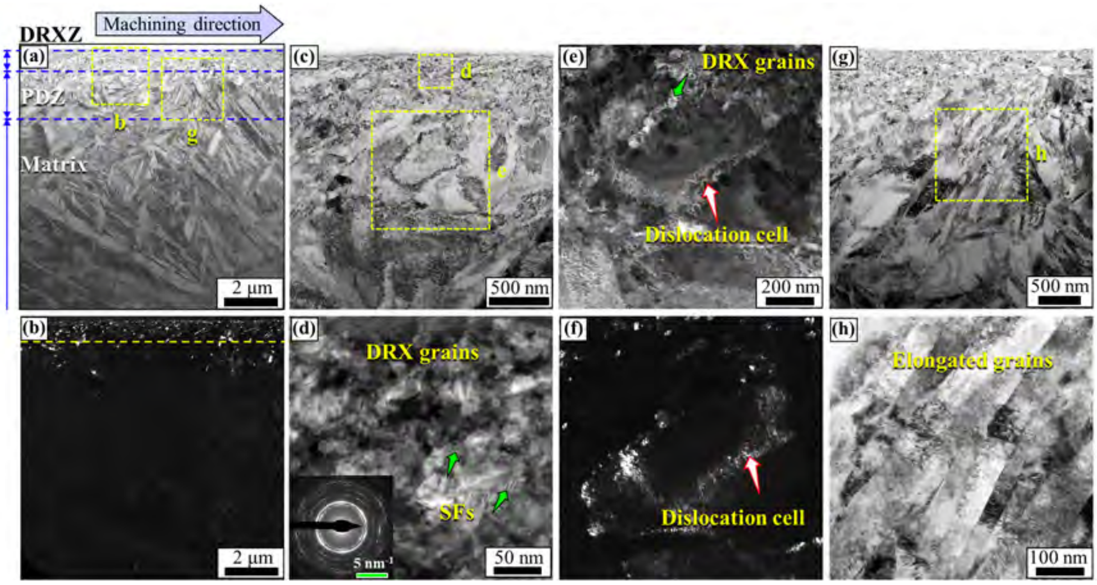

Fig. 6.9 Subsurface microstructure of longitudinal section at 20 m/s: (a) Plastic deformation distribution; (b) Dark-field image of the DRXZ; (c) MDZ in the near surface; (d) DRX grains in the top surface; (e) DDRX grains in the transition zone; (f) Dark-field image of (e); (g) Elongated grains in PDZ; (h) Enlarge view of h in (g).

As the machining speed increases, the time duration for deformation significantly decreases at higher strain rates, leading to alterations in the distribution and mechanism of plastic deformation. **Fig. 6.10a** shows the plastic deformation distribution of the scratch machined at 160 m/s. The depth of MDZ was decreased to 1.6 μm. Notably, the thickness of PDZ was decreased from 1.7 μm at 20 m/s to 0.9 μm at 160 m/s, indicating a noticeable inhibition effect on plastic deformation. As seen in **Fig. 6.10b**, elongated grains with dislocation tangles (DTs) were observed in the PDZ. Moreover, DRX grains were absent in the topmost layer, instead, the UGENTs were detected (**Figs. 6.10, d** and **g**). The HRTEM image (**Fig. 6.10h**) further reveals the presence of nano-scale twins within the polygonal UGENTs.

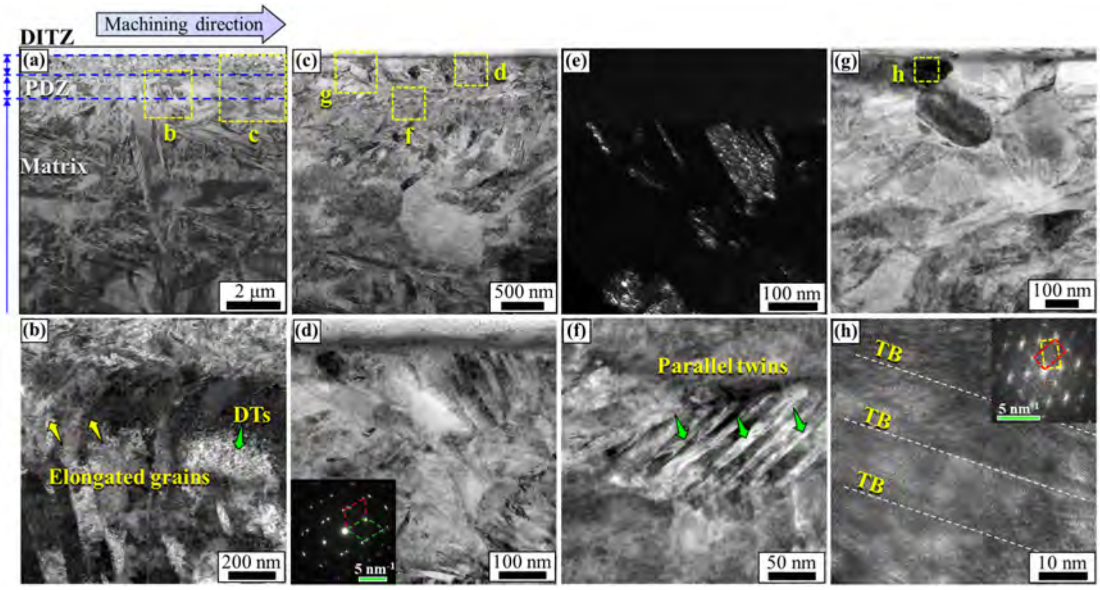

Fig. 6.10 Subsurface microstructure of longitudinal section at 160 m/s: (a) Plastic deformation distribution; (b) Microstructures in the PDZ; (c) MDZ in the near surface; (d) Nano-twins in the DITZ; (e) Dark-field image of (c); (f) Enlarged view showing parallel twins; (g) UGENTs in topmost layer; (h) HRTEM of nano-scale twins.

As shown in **Fig. 6.11a**, the MDZ of the scratch made at 220 m/s further decreased to 750 nm. Notably, the PDZ in the subsurface was absent, which suggests that the plastic deformation was significantly inhibited under the ultra-high strain rate condition. **Fig. 6.11b** displays the DITZ in the near-surface layer, it is evident that the UGENTs structure was induced, which is consistent with the results observed from the cross-sectional view. Upon closer examination of the enlarged view (**Fig. 6.11c**), a distinct UGENT structure is evident. Parallel lens-like $\{0\bar{1}11\}$ twins and dislocations presented within an ultrafine grain (**Figs. 6.11c-f**). Additionally, **Figs. 6.11g, h** show a typical

UGENT structure with intersected twins, indicating that the number of activated twin systems is also influenced by the grain orientation.

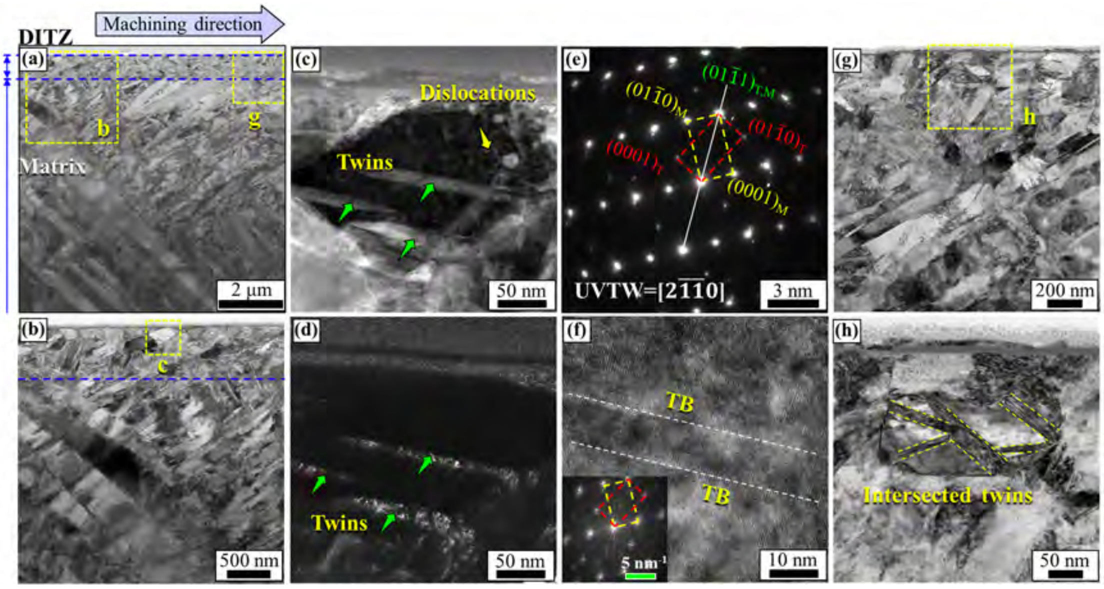

Fig. 6.11 Subsurface microstructure of longitudinal section at 220 m/s: (a) Plastic deformation distribution; (b) MDZ in the near surface; (c) Nano-twins in an ultrafine grain; (d) Dark-field image of (c); (e) SAED pattern of twins; (f) HRTEM of the twins; (g) Enlarge view of h in (a); (h) Enlarge view shows the intersected twins in an ultrafine grain.

Figure. 6.12a displays a polygonal nanograin (d<100nm) containing inside intersected twins. By examining the STEM morphology and the inset dark-field image, it can be observed that two sets of parallel nanoscale twins collided, forming V-shaped intersected twins. The HRTEM of the inside deformation twins was taken to reveal the twin collision mechanism. As depicted in **Fig. 6.12b**, five distinct twins were identified within the nanograin, denoted as T1 to T5. T1, T2, and T3 were paralleled and aligned on the left side, while T4 and T5 aligned on the right side. According to the inverse FFT images and FFT patterns (**Figs. 6.12, c-f**), the two sets of twins were identified as the $\{0\bar{1}11\}$ twins, and the twin boundaries were the typical coherent twin boundary.

Notably, three-fold twins formed due to the collision of multiple twinning systems. **Fig. 6.12g** reveals the intersecting area of T2 and T5. The local boundary between the two intersected twins was also demonstrated as a $\{0\bar{1}11\}$ coherent twin boundary (**Fig.**

6.12h), and the two ends of this twin boundaries jointed with TB1, TB3, and TB2, TB4 respectively, forming two three-fold twins. The upper three-fold twin comprised TB1, TB3, and TB5, with an included angle of 120°, while the lower one consisted of TB2, TB4, and TB5, with an included angle of 60°.

In contrast to the sequential twinning mechanism of multiple-fold deformation twins formed under low strain rate conditions (Zhang *et al.* 2017; Zhu *et al.* 2022). The remarkably high strain rate in this study facilitated the simultaneous activation of multiple twinning systems along $\{0\bar{1}11\}$ planes. As a consequence, the collision of two $\{0\bar{1}11\}$ twins led to the formation of three-fold twins. A similar microstructure was observed in the nanotwinned Ti-alloys through additive manufacturing characterized by very high cooling rates (Zhu *et al.* 2022).

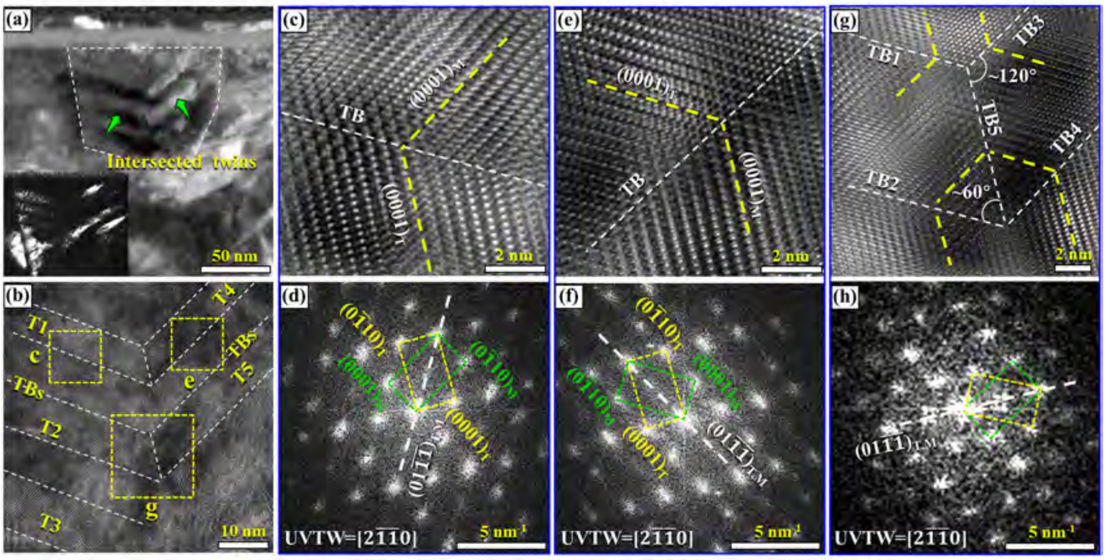

Fig. 6.12 Twin intersection of sample machined at 220 m/s: (a) Intersected twins in a nanograin (the inset is the dark-field image of twins); (b) HRTEM of the twins (Five twins were respectively designated with the numbers T1 to T5); (c) Inverse FFT of c in (b); (d) FFT pattern of (c); (e) Inverse FFT of e in (b); (f) FFT pattern of (e); (g) Inverse FFT of g in (b); (h) FFT pattern of (g). (The TBs are indicated by the white-colored dashed lines, whereas the basal planes are marked by yellow-colored dashed lines).

6.3.3 Chip Formation Characteristics of SLM-ed Ti6Al4V at Different Machining Speeds

Figure 6.13 shows the chip morphology of SLM-ed Ti6Al4V machined from low to ultra-high-speed conditions. Surprisingly, segmented chips were not produced in SPS of SLM-ed Ti6Al4V at 20 m/s as what was observed in the wrought Ti6Al4V. Instead, the long continuous chip (~1 mm) was generated, and corrugated deformation traces were observed on the free surface of the chip (**Figs. 6.13, a** and **b**). Theoretically, the higher brittleness associated with SLM-ed Ti6Al4V is anticipated to favor the formation of segmented chips. It can be inferred that the unexpected result may be attributed to a different chip formation mechanism, and this will be further investigated in the following section.

At a machining speed of 60 m/s, regular segmented chips were generated (**Figs. 6.13, c** and **d**), and the chip length decreased to approximately 300 μm. Similar to the SPS of wrought Ti6Al4V, the feature size of the chips decreased as the machining speed increases. Notably, the segment detachment occurred as the machining speed reached 220 m/s.

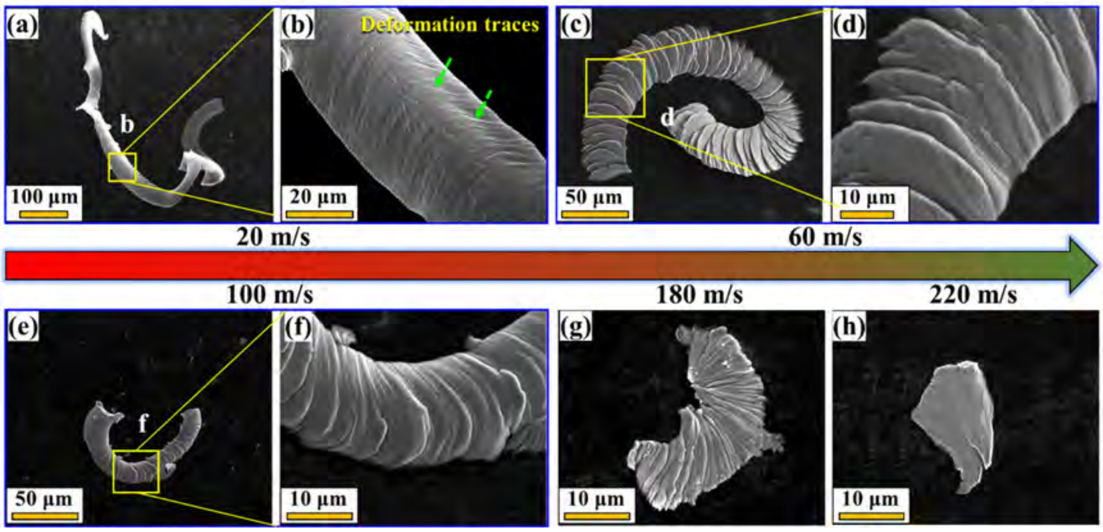

Fig. 6.13 Chip morphologies of SLM-ed Ti6Al4V generated at different machining speeds: (a) 20 m/s; (b) Enlarged view showing the deformation traces; (c) 60 m/s; (d) Enlarged view displaying the segments; (e) 100 m/s; (f) Enlarged view depicting the small segments; (g) 180 m/s; (h) 220 m/s.

To further investigate the underlying mechanism of chip formation, TEM samples of the chip section were prepared and detected. As depicted in **Fig. 6.14a**, no distinct segments and ASBs were observed from the chip section, which is consistent with the observation from the chip surface morphology. The O element distribution map reveals that both the free surface and the chip-tool contact surface exhibit O enrichment (**Fig. 6.14b**). Further examination uncovered the presence of microcracks beneath the corrugated deformation traces (**Fig. 6.14c**). Additionally, the primary microstructure observed in the upper part of the chip section was the deformed laminar structure with inside HDDs (**Fig. 6.14d**).

In the middle part of the chip section, a mixed microstructure comprising both deformed laths and a few DRX grains was produced due to the elevated temperature (**Fig. 6.14e**). As plastic deformation intensified in the area closer to the bottom part of the chip section, the mixed microstructure transited into highly elongated grains (**Fig. 6.14h**). Furthermore, nanoscale DRX grains with an average diameter of ~30 nm were generated in the lower region, and nanoscale laminar grains were induced in the chip-tool contact surface layer due to severe friction effect.

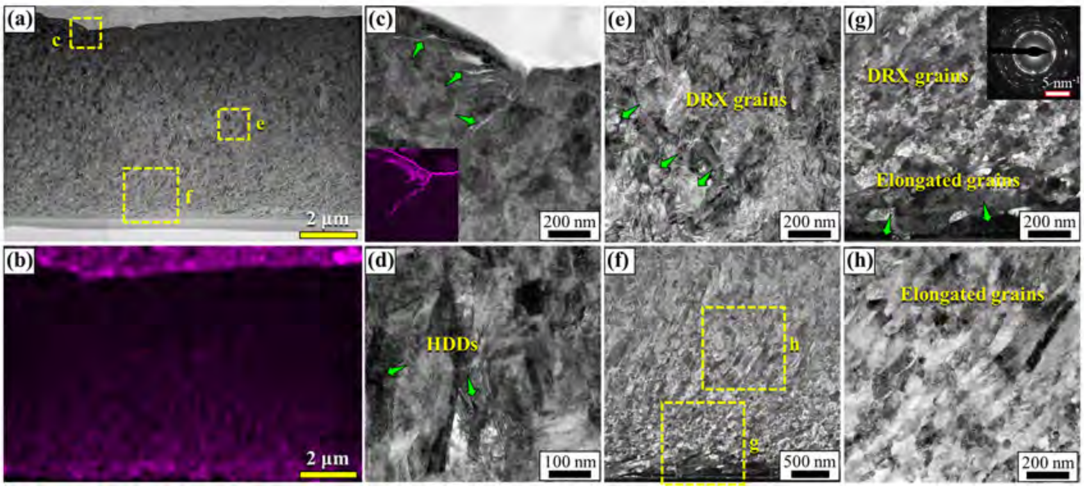

Fig. 6.14 Section characterization of chip produced at 20 m/s: (a) Microstructure distribution of the global chip section; (b) O element distribution map; (c) Enlarged view of the free surface area c in (a); (d) HDDs in deformed laminar; (e) Mixed microstructures containing laminar and DRX grains in the middle part of chip section; (f) Microstructures in the area near the contact interface of chip and tool; (g) Enlarged

view of g in (f); (h) Enlarged view of h in (f).

The segmented chips were generated as the machining speed increased to 60 m/s. the O element map (**Fig. 6.15b**) reveals that cracks between the adjacent segments were propagated to the middle part of the chip section, indicating the chip was partially segmented. The V element map (**Fig. 6.15c**) exhibits a uniform distribution, implying that no distinct phase transformation occurred. In the region near to the free surface, the microstructure mainly consisted of deformed laths with inside HDDs and dislocation tangles. Notably, small steps were observed in the free surface of segments (**Fig. 6.15d**), and the edges of steps were in alignment with the boundaries of laths. It can be inferred that the relative slip along the lath boundaries tended to be activated under the shear loading. These steps facilitated the initiation of cracks under the accumulation of stress and strain, ultimately contributing to the formation of segmented chips.

Figure 6.15e presents a typical shear region located between two segments, where a crack initiated from the free surface and propagated into the chip along the shear plane. Notably, an ultra-thin shear band with a thickness of approximately 16nm was observed. The microstructures near to the shear band were ultrafine laths and DRX grains, while no phase transformation was detected in the shear region (**Fig. 6.15f**). Additionally, as the intensity of plastic deformation increased, the microstructures underwent a transition from elongated laths in the middle part to DRX grains in the region near the tool/chip interface.

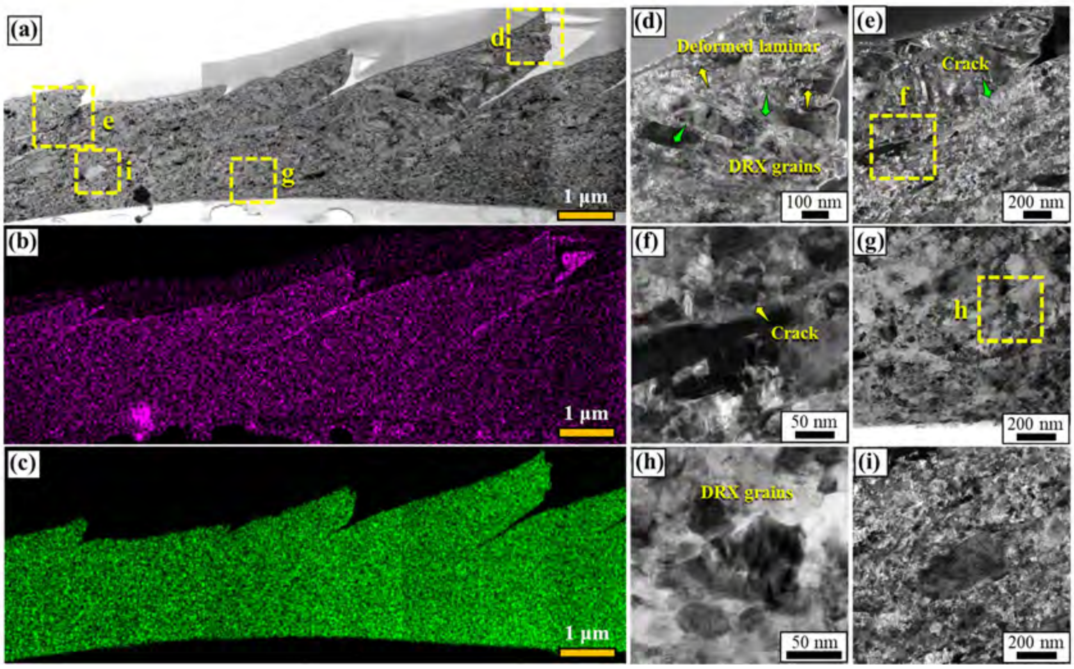

Fig. 6.15 Section characterization of chip produced at 60 m/s: (a) Microstructure distribution of the global chip section; (b) O element distribution map; (c) V element distribution map; (d) Microstructure near the free surface of the segment; (e) Microstructure in the shear region; (f) Ultra-thin shear band; (g) Microstructure in the bottom part of chip section; (h) Enlarged view showing the DRX grains; (i) Microstructure in the middle part of chip section.

Figure 6.16a presents the chip section produced at a machining speed of 200 m/s. Numerous cracks initiated from the free surface were generated in the upper part of the chip section (O map reveals the crack distribution). Similar to the wrought Ti6Al4V chips produced at ultra-high speed, the free surface of segments tended to rotate towards the previously produced segment due to the high-speed and severe friction effects. In **Fig. 6.16c**, cracks were observed propagating along the lath boundaries, and extensive SFs were induced ahead of the crack tip due to the stress concentration (**Fig. 6.16d**). Additionally, deformation twins were produced in the chip section (**Fig. 6.16e**), and DRX and elongated grains were distributed in the region near the tool/chip contact interface.

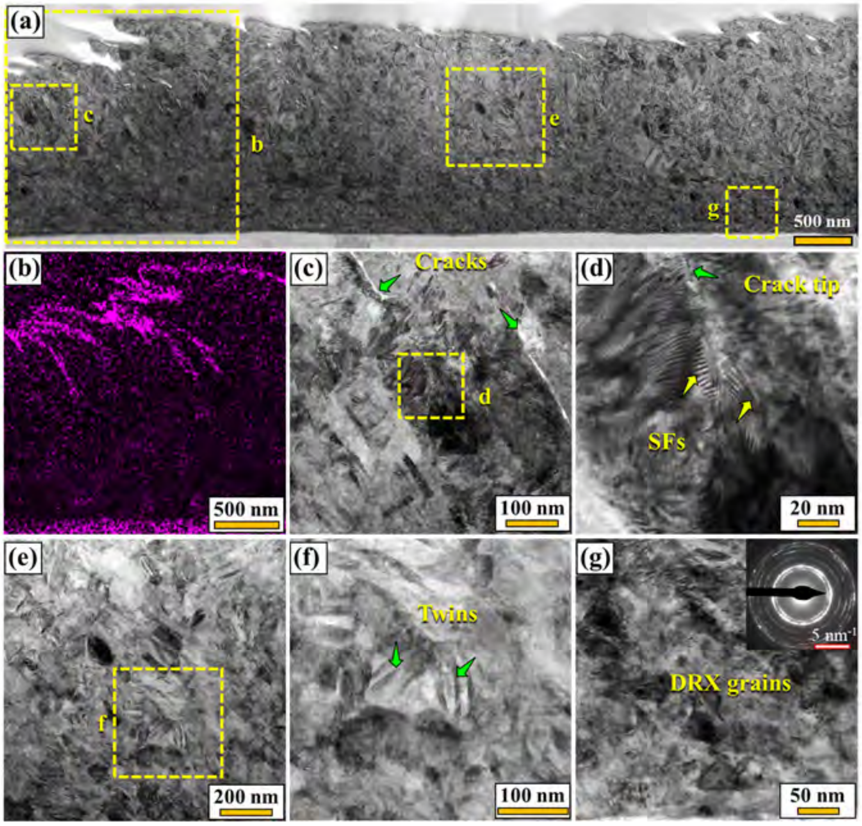

Fig. 6.16 Section characterization of chip produced at 200 m/s: (a) Microstructure distribution of the global chip section; (b) O element distribution map of area b in (a); (c) Cracks propagated along the lath boundaries; (d) Microstructure near to the crack tip; (e) Microstructure in the middle part of chip section; (f) Enlarged view showing deformation twins; (g) Microstructure in the bottom part of chip section.

6.4 Discussion

SLM-ed Ti6Al4V exhibits distinct microstructures and mechanical properties compared to its wrought counterpart, owing to the entirely different manufacturing paradigm. These differences impart SLM-ed Ti6Al4V with divergent machinability and material removal mechanisms (Ming *et al.* 2019). Previous research on mechanical machining of SLM-ed Ti6Al4V primarily focused on the cutting force, tool wear, surface finish, or macroscale structure alteration in conventional machining processes such as turning and milling (Khaliq *et al.* 2020; Le Coz *et al.* 2020; Li *et al.* 2022; Velásquez *et al.* 2010). Nevertheless, the alterations in machined subsurface and chips at the micro- and nano-scale remain unknown. Furthermore, the material removal mechanisms of SLM-ed Ti6Al4V in high-speed or ultra-high-speed regions have not been investigated.

This study presents a systematic and novel investigation into the material removal mechanisms of SLM-ed Ti6Al4V under varying strain rate conditions, ranging from low to ultra-high levels. By conducting comprehensive characterizations and analyses of the surface, subsurface, and chips at multiple scales, this study seeks to elucidate the relationship between strain rate and the transformation of material removal mechanisms and microstructure evolution during the machining of SLM-ed Ti6Al4V.

6.4.1 Subsurface Microstructure Modification of SLM-ed Ti6Al4V in SPS from Conventional to Ultra-high-speed

Surface finish is a commonly utilized metric for assessing machining quality. Nevertheless, it has been discovered that achieving a higher surface finish does not automatically guarantee an enhanced service performance. This is primarily due to the significant influence exerted by subsurface microstructure modification on mechanical properties, particularly fatigue and wear resistance (Javidi *et al.* 2008; la Monaca *et al.* 2021). A machining affected layer tends to be induced due to the intense thermomechanical effect during a machining process (Li *et al.* 2023). In the machining of wrought Ti6Al4V, severely refined microstructures are formed in the subsurface layer and complex phenomena including phase transformation, dynamic recrystallization, and grain deformation are involved (Li *et al.* 2022; Liang and Liu 2017). Moreover, the microstructure evolution of wrought Ti6Al4V is highly dependent on the strain rate. In light of this, systematic characterizations combining FIB and STEM were employed to investigate the subsurface microstructure modification of SLM-ed Ti6Al4V in SPS from conventional to ultra-high-speed.

Based on the experimental findings, the subsurface microstructural distribution of SLM-ed Ti6Al4V at both conventional and ultra-high-speed are schematically illustrated in **Fig. 6.17**. At low machining speeds, the subsurface of SLM-ed Ti6Al4V exhibited a deep MDZ, characterized by two distinct zones. The original SLM-ed Ti6Al4V in the matrix possessed a typical lamella structure, while the microstructures tended to be deformed and elongated along the direction of scratch, leading to the formation of PDZ. The PDZ possessed gradient grain structures, with finer laminar grains generated as the depth decreased due to intensified plastic deformation. Additionally, HDDs and substructures were induced in the elongated grains.

As moving to the DRXZ in the topmost region, abundant fine crystal nuclei nucleated along the boundaries of elongated grains under the combination effects of strain and elevated temperature. These nuclei underwent grain growth by consuming deformation stored energy and adsorbing dislocation, forming equiaxed DRX grains at a scale of nanometers following the DDRX mechanism (Liang *et al.* 2020; Wang *et al.* 2020).

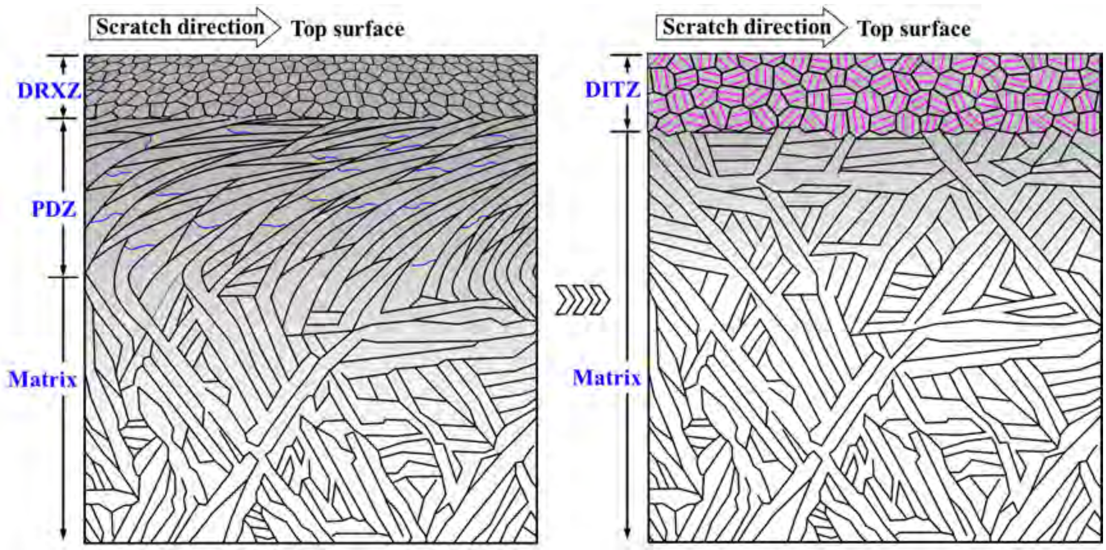

Fig. 6.17 Schematic of subsurface microstructural distribution: (a) Low strain rate; (b) Ultra-high strain rate.

6.4.2 Material Removal Mechanisms of SLM-ed Ti6Al4V

The material removal mechanisms of SLM-ed Ti6Al4V at various machining speeds were thoroughly examined, focusing on surface creation, subsurface deformation, and chip formation. According to the surface features, the material pile-up phenomenon was effectively inhibited as the machining speed increased, suggesting a decrease in plastic deformation under ultra-high-speed conditions. This is inextricably tied to the material’s distinct responses under varying strain rate conditions (Kuruc *et al.* 2022).

A ductile material exhibits significant plastic deformation under low strain rate loading conditions. However, as the strain rate increases, the extent of plastic deformation diminishes. Additionally, when the strain rate surpasses a critical value associated with the ductile-to-brittle transition, the ductile material undergoes brittle fracture (Wang *et al.* 2015; Zhou *et al.* 2003). Compared to wrought Ti6Al4V, SLM-ed Ti6Al4V exhibited a lower pile-up ratio particularly at the lower speed region due to the higher brittleness. Nevertheless, as the machining speed increased, the disparity in pile-up ratio diminished, indicating a reduction in the difference of brittleness under ultra-high strain rate conditions.

The reduction of plastic deformation levels at higher strain rates was further evidenced by examining subsurface deformation. With increasing machining speed, the plastic deformation layer caused by thermomechanical impact of the cutting tool notably diminished, and no PDZ was observed when the machining speed exceeded 220 m/s. Consequently, the overall MDZ in the subsurface exhibited a “skin effect” as the strain rate increased. In other words, the high strain rate machining resulted in a shallower deformation layer. This phenomenon resulted from the comprehensive effects of multiple factors, including stress/temperature field distribution and energy dissipation.

Firstly, at high strain rates, the stress/temperature fields tended to concentrate within a shallow layer, resulting in a smaller stress/temperature affected depth. This was due to the significantly shorter duration of the cutting tool’s action, which restricted the propagation of stress and heat to deeper regions through a faster stress unloading process. Additionally, the attenuation of stress waves increased linearly with their frequency. The higher frequency generated under high strain rates caused rapid attenuation, confining the stress field to the surface layer (Liu and Ahrens 1997; Oda *et al.* 1990). From the perspective of energy, the high-frequency shearing effect under high strain rate conditions induced more shear bands, leading to a larger number of cracks during the chip formation process. This, in turn, consumed a significant amount of impact energy and effectively inhibited the plastic deformation (Dong *et al.* 2020).

Figure 6.18 schematically illustrates the material removal processes of SLM-ed Ti6Al4V under different machining speed conditions. At low-speed machining (≤20 m/s), the chips were removed in a continuous mode instead of the segmented mode observed in wrought Ti6Al4V. The segmented chips were observed in SLM-ed Ti6Al4V at 60 m/s, implying that the segmented chips were prone to initiate in wrought Ti6Al4V under the same machining condition. This finding deviates from previous research results, which suggested that SLM-ed Ti6Al4V was more susceptible to adiabatic shearing and exhibited a higher tendency to form segmented chips (Kishawy *et al.* 2023; Shunmugavel *et al.* 2019). The presence of this discrepancy may be attributed to transformation in the material removal mechanisms in wrought and SLM-ed Ti6Al4V.

Based on the direct STEM characterization, it has been determined that the formation of segmented chips in wrought Ti6Al4V can be attributed to the activation of ASBs induced by phase transformations. In contrast, in SLM-ed Ti6Al4V, the initiation of segmented chips was linked to the relative slip along the lath boundaries. This transformation can be attributed to the distinctive laminar microstructures in SLM-ed Ti6Al4V, which exhibited higher resistance to deformation at elevated temperatures (Motoyama *et al.* 2021). As a result, higher stress was required to activate the shear localization behavior. Therefore, the occurrence of segmented chips took place at higher machining speeds in SLM-ed Ti6Al4V compared to wrought Ti6Al4V.

As the machining speed increased to high-speed regions, the phenomenon of shear localization became more pronounced. This was evident from the confinement of the primary shearing zone within a narrower band and a notable increase in segmented frequency. The segments tended to separate from each other, leading to the formation of fragmented chips and exhibiting a brittleness removal mode.

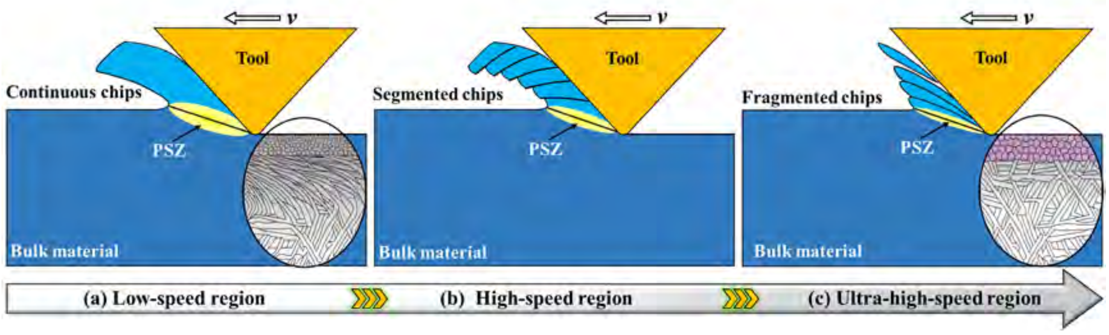

Fig. 6.18 Schematic of material removal process of SLM-ed Ti6Al4V under different machining speeds: (a) Low speed; (b) High speed; (b) Ultra-high speed.

6.4.3 Dislocation-mediated Deformation to Twin-mediated Deformation Transition

Plastic deformation in metals occurs to minimize the potential energy resulting from external loads. Two primary mechanisms contribute to this process: dislocation-mediated deformation and twin-mediated deformation (Qi *et al.* 2022). Generally, dislocation slip is considered the prominent mechanism, while twinning serves as the complimentary deformation mechanism (Sun *et al.* 2016; Vinogradov *et al.* 2016). However, these two mechanisms compete with each other, and their transition occurs under specific conditions. Comprehensive researches have revealed that various factors, including both extrinsic ones like deformation temperature, strain rate, and grain size, and intrinsic ones such as crystal orientation and stacking fault energy (SFE), significantly influence the shift from slip-dominated deformation to twinning (Cai *et al.* 2014; Meyers *et al.* 2001; Zhu *et al.* 2013).

In this study, the transition from dislocation slip to twinning was observed in ultra-high-speed regions. This phenomenon was intimately connected to the synergistic effect of deformation temperature and strain rate. Typically, under low strain rates, the critical shear stress for slip (σ_s) tended to decrease with rising temperature. This phenomenon can be attributed to the reduction in the shear modulus as the temperature increased. On the other hand, the critical stress required for twinning remained relatively unchanged despite the variations in temperature (Nicolò Maria *et al.* 2023). Therefore, in the low-speed machining region, the temperature was the dominant factor, and no deformation twins were detected at 20 m/s.

As the machining speed increased, the capacity of dislocations to alleviate deformation became inadequate, particularly in the superficial layer where the strain rate was very high. The evidence is that deformation twins were induced in the upmost layer in the subsurface of the sample machined at 160 m/s. When the machining speed reached 220 m/s, the PDZ in the subsurface almost vanished, and high-density twins were generated in the deformation layer, suggesting that deformation twinning emerges as the dominant mode of dynamic response in ultra-high strain rates.

Dislocation slip refers to the continuous and progressive movement of dislocations within a material. The average dislocation velocity (v) exhibits a direct correlation with the applied shear stress, as described by phenomenological Eq. (6.1) (Regazzoni *et al.* 1987):

$$v = C\tau^m \tag{6.1}$$

Here, C represents a constant, and the power law exponent, denoted by m, can vary depending on the applied stress. Notably, a consensus has emerged within the scientific community, identifying three regimes of the average dislocation velocity based on three different mechanisms governing plastic deformation. As depicted in **Fig. 6.19**, for low strain rate and stress level, the dislocation motion is governed by the thermal activation mechanism, and the m is considerably above m>1in this region (Hiratani and Nadgorny 2001). In region II, a drag force induced by the dislocation-phonon interactions that is proportional to the dislocation speed dominated dislocation motion. As a result, the velocity of dislocations is proportional to the applied stress (m=1) (Parameswaran *et al.* 2003). Notably, a non-linearity exists under high stress and strain rate conditions, the dislocation velocity asymptotically approaches the shear wave velocity due to the additional drag caused by the relativistic effect (Kim *et al.* 2020).

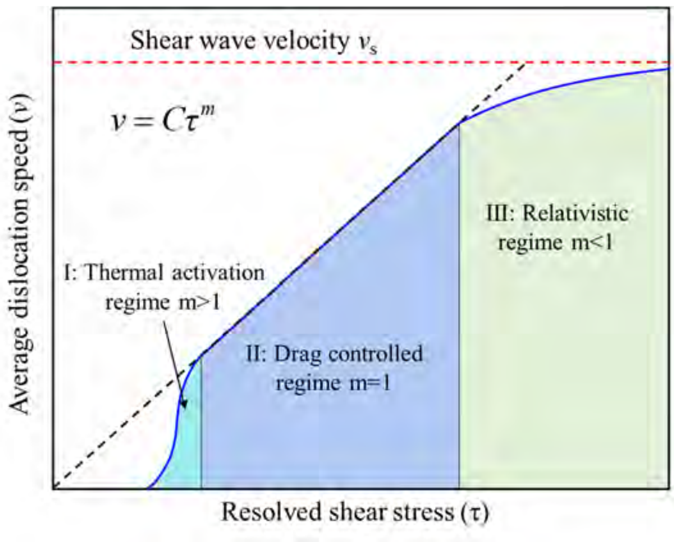

Fig. 6.19 Classical representation of the three regimes of the average dislocation

velocity: Region I-thermal activation regime m>1; Region II- Free glide regime m=1; Region III-Relativistic regime m<1. Figure adapted from (Regazzoni *et al.* 1987).

Experimental evidence for high-speed dislocation remains scarce due to technical challenges, and most investigations are based on theoretical models and computer simulations (Gurrutxaga–Lerma *et al.* 2021). Luis et.al (Zepeda-Ruiz *et al.* 2017) conducted molecular dynamics simulations to investigate the limits of metal plasticity, and the results demonstrated that the existence of transition from dislocation-mediated deformation to twin-mediated deformation under very high strain rate conditions.

On one hand, at a sufficiently high strain rate, the time scales become too short to facilitate dislocation activation (Gurrutxaga-Lerma *et al.* 2015). Conversely, twinning entails abrupt and discrete deformations along twin boundaries, making it become a possible deformation-mediated mechanism at ultra-high strain rates. Meanwhile, high work-hardening and drag force are generated with a material subjected to high strain rate loading, which impedes dislocation movement and leads to stress concentration. Consequently, high stress level facilitates the formation of deformation twins.

Regarding the deformation temperature, higher temperatures are generally unfavorable for the formation of twins, as the critical shear stress required for twinning (τ_t) tends to increase with temperature in most hcp metals. However, there is an exceptional type of twin known as {10−11} twin that exhibits a lower critical shear stress (τ_t) at elevated temperatures (Paton and Backofen 1970). This particular characteristic accounts for the presence of {10−11} twins in the matrix of the SLM-ed TiAl4V. Furthermore, it also accelerates the transition from slip-dominated deformation to twinning.

6.5 Conclusions

This study conducted systematic investigations on the material removal mechanisms of SLM-ed Ti6Al4V over a large speed range, spanning from 20 to 220 m/s. Multiscale characterization methods were combined to detect and analyze the surface creation, subsurface deformation, and chip formation to achieve a comprehensive understanding of the material removal process. The obtained results provide profound insights into the microstructure evolution and deformation mechanism of SLM-ed Ti6Al4V at different machining speeds, thus elucidating the transition of material removal mechanisms from low to ultra-high strain rates. The main findings are drawn as follows:

(1) The pile-up ratio of SLM-ed Ti6Al4V demonstrated a decreasing trend with increasing machining speed. However, in comparison to wrought Ti6Al4V, the higher brittleness of SLM-ed Ti6Al4V caused less material accumulation on the edges of scratches, particularly at low machining speeds;

(2) The depth of the MDZ in SLM-ed Ti6Al4V was closely correlated with the machining speed. Lower-speed machining induced a deeper MDZ due to severe plastic deformation, whereas the MDZ was considerably restricted in the superficial layer in the ultra-high-speed region, showing a distinctive “skin effect”;

(3) SLM-ed Ti6Al4V showed distinct material removal modes from low to ultra-high-speed regions. At low machining speeds (≤20 m/s), the material was removed in continuous chips. As the machining speed increased to 60 m/s, segmented chips started to form, and at the highest machining speed of 220 m/s, fragmented chips became evident.

(4) The formation of segmented chips was attributed to the activation of ASBs induced by phase transformation in wrought Ti6Al4V, while the formation of segmented chips in SLM-ed Ti6Al4V was primarily driven by the relative slip along the lath boundaries. This different chip formation mechanism leaded to a higher critical speed of segmented chips in SLM-ed Ti6Al4V.

(5) Under low strain rate conditions, the microstructure evolution in SLM-ed Ti6Al4V was predominantly governed by dislocation-mediated deformation. The primary microstructures observed from the top to the subsurface were Dynamic Recrystallization (DRX) and elongated grains. However, as the machining speed reached the ultra-high levels, a transition from dislocation slip to twinning was observed. Twinning-mediated deformation became the dominant mode at these

ultra-high strain rates, leading to the formation of a novel microstructure referred to as UGENTs.

Chapter 7 Surface Integrity of Ti6Al4V Alloys in Ultra-high-speed Grinding

7.1 Introduction

Ti-alloys are extensively utilized in critical applications owing to their exceptional combination of mechanical properties. Nonetheless, despite notable advancements and widespread adoption of Ti-alloys, the machining of these materials continues to pose significant challenges in industrial applications since they are classified as difficult-to-cut materials. Ti-alloys exhibit inferior machinability in comparison to other metals due to their inherent mechanical and material properties, such as low thermal conductivity, high chemical reactivity, and low elasticity modulus. These properties contribute to the challenges during the machining process, resulting in a high cutting temperature, substantial cutting force, and limited tool life, resulting in compromised surface integrity of the machined parts.

Particularly, surface integrity of a part plays a crucial role in determining its overall service performance. The surface integrity encompasses various key characteristics, including surface topography, microstructural alterations, and mechanical properties. Surface topography refers to the presence of surface defects and roughness. Microstructural alterations include phenomena such as plastic deformation, grain refinement, texture changes, and phase transformation. Lastly, mechanical properties such as microhardness and residual stress also play a crucial role in determining the surface integrity of a part. By examining and understanding these surface integrity characteristics, researchers and engineers can gain valuable insights into the quality, performance, and reliability of a part.

The preceding chapters have elucidated the material removal mechanisms of Ti-alloys at ultra-high strain rates, specifically focusing on surface creation, subsurface microstructure alteration, and chip formation in single-point grinding. It has been deduced that the behaviors of material removal and plastic deformation are closely interconnected with the strain rate conditions. Remarkably, the material removal rate can be significantly enhanced by restraining material pile-up during ultra-high strain rate deformation. Simultaneously, control over material plastic deformation within the subsurface layer can be achieved within the ultra-high strain rate range. Furthermore, ultra-high-speed scratching process can induce a hierarchically ultrafine grain embedding nanotwins (UGENTs) structure. These findings substantiate that ultra-high-speed machining presents itself as a promising approach for enhancing the surface integrity of Ti6Al4V alloy.

In this context, an ultra-high-speed grinding (UHSG) system was developed to achieve high-efficiency and high-quality machining of Ti-alloys. Based on this grinding system, a series of grinding experiments of wrought and SLM-ed Ti6Al4V alloys with grinding linear speeds ranging from 60 to 250 m/s were conducted. The surface integrity of the machined samples was systematically analyzed by considering both surface and subsurface characteristics. The transitions in deformation mechanisms corresponding to varying machining speeds and their consequential impacts on surface integrity were meticulously explored. Furthermore, an assessment and comparison of the machinability of both wrought and SLM-ed Ti6Al4V were performed.

7.2 Experimental Preparation

7.2.1 UHSG System Development and Experiment Parameter Design

The UHSG system was developed by integrating a high-speed hydrostatic bearing motorized spindle (maximum speed: 60,000 rpm) into a QuestGT27 grinding machine manufactured by Hardinge (**Fig. 7.1a)**. To facilitate UHSG, a specially designed grinding wheel was designed and developed. The grinding wheel utilized a carbon fiber reinforced plastics (CFRP) substrate and featured a vitrified bonded cubic boron nitride (CBN) abrasive layer with a wheel concentration of 175%. The dimensions of the grinding wheel were 118.0 mm in diameter, and 8.0 mm in thickness (Dimension drawing of the UHSG wheel is depicted in **Fig. 7.1c**), and it possessed a grain size of #120.

As shown in **Fig. 7.1b**, the workpieces were cut into plate samples with dimension of 10*10*3 mm. These samples were then securely affixed to the periphery of the workpiece wheel using paraffin wax. The workpiece spindle and the grinding wheel spindle rotated in the direction to realize higher grinding linear speeds. **Table 7.1** presents the experiment parameters for the UHSG processes of Ti6Al4V alloy, A total of eight trials were designed to investigate the influence of grinding speed on surface integrity. The grinding wheel speed varied between 40 m/s and 230 m/s, while the workpiece speed remained fixed at 20 m/s. Consequently, the grinding linear speed ranged from 60 to 250 m/s.

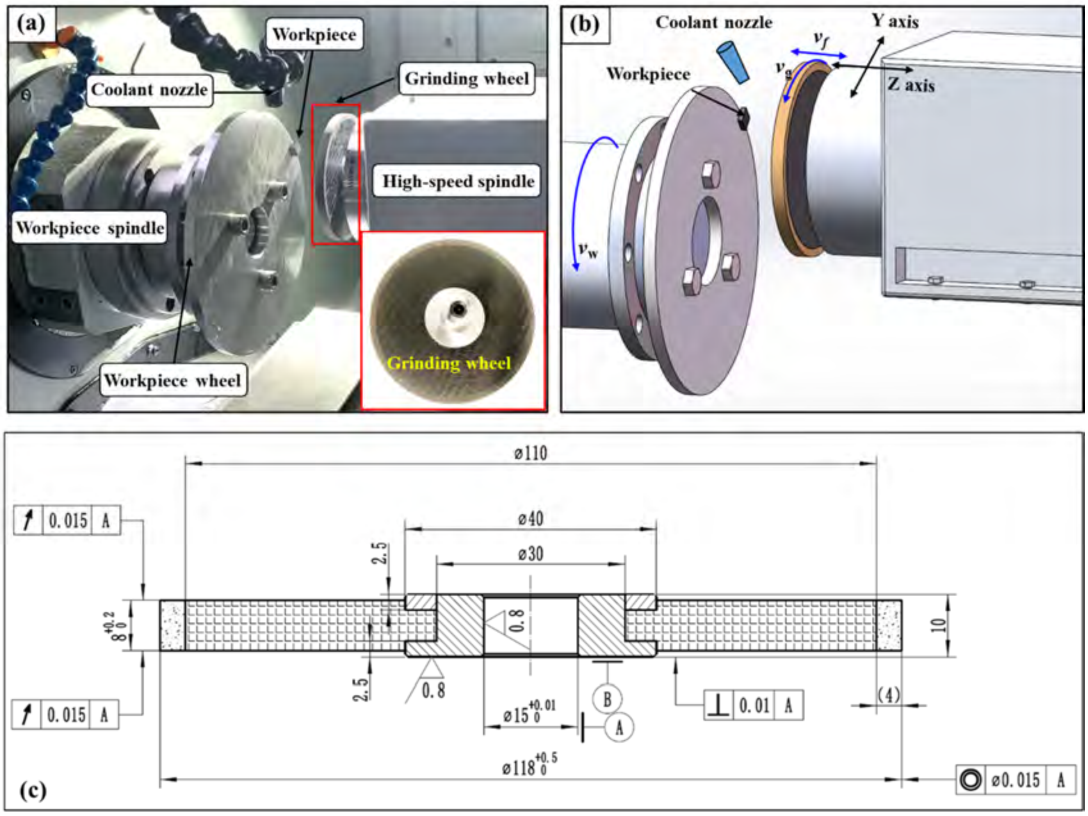

Fig. 7.1 (a) Experimental setup of ultra-high-speed grinding; (b) Schematic diagram of experimental setup; (c) Dimension drawing of the ultra-high-speed grinding wheel.

Table 7.1 Parameters for the UHSG processes of Ti6Al4V alloy.

Trials	**Speed of grinding wheel v_g (m/s)**	**Speed of workpiece wheel v_w (m/s)**	**Grinding depth a_p (μm)**	**Feed rate v_f (mm/min)**	**Grinding linear speed v (m/s)**
1	40	20	5	100	60
2	80				100
3	120				140
4	140				160
5	160				180
6	180				200
7	200				220
8	230				250

To ensure optimal machining performance, the UHSG wheel underwent truing, sharpening, and dynamic balance prior to each grinding trial (**Fig. 7.2**). Truing of the wheel involved a relative rolling action with a #80 diamond rolling wheel, with both the grinding wheel and the diamond rolling wheel rotating in the same direction at speeds of 10,000 rpm and 2,000 rpm, respectively. During the truing process, the grinding wheel spindle fed along the Z axis at a feed rate of 200 mm/min, with a truing depth of 0.5 μm per pass. Following truing, the grinding wheel was dressed using a SiC wheel, following the same procedure as truing. After truing and dressing, the grinding wheel was dynamically balanced using a BMT240M.2 dynamic balancing instrument manufactured by MPM in Germany. Furthermore, a water-based coolant was utilized throughout the grinding process.

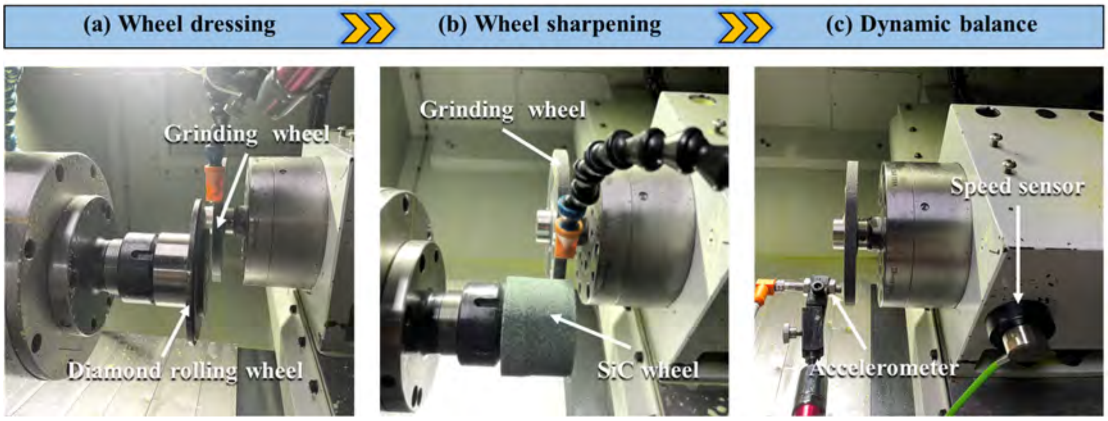

Fig. 7.2 (a) Grinding wheel dressing; (b) Grinding wheel sharping; (c) Dynamic balance.

7.2.2 Measurement and Material Characterizations

Systematic measurement and material characterizations were conducted to investigate the surface integrity of the machined samples. The machining surfaces were first detected by a white light interferometer (Taylor Hobson Talysurf CCI, USA) to obtain the 3D surface morphology and surface roughness, and the surface roughness was analyzed by a multi-file analysis software. Meanwhile, the detailed surface characteristics were also observed by SEM.

The machined samples were cut along the grinding direction to expose the cross-sectional subsurface, the cross-sections were ground with abrasive paper (#180, #600, #1000, #2000, #3000) and experienced a vibration polishing to remove the damage induced by material preparation. Following these steps, the prepared samples were analyzed by SEM in ABS mode to identify the plastic deformation layer in the subsurface. Additionally, the electron backscatter diffractometry (EBSD) technique was employed to investigate alterations in the grain scale, including grain orientation and size. For TEM analysis, cross-sectional samples were meticulously prepared using the focused ion beam (FIB) technique. The process for preparing TEM samples is depicted in **Fig. 7.3**. The TEM samples were thoroughly examined to unveil the deformation mechanism of Ti6Al4V alloys in UHSG.

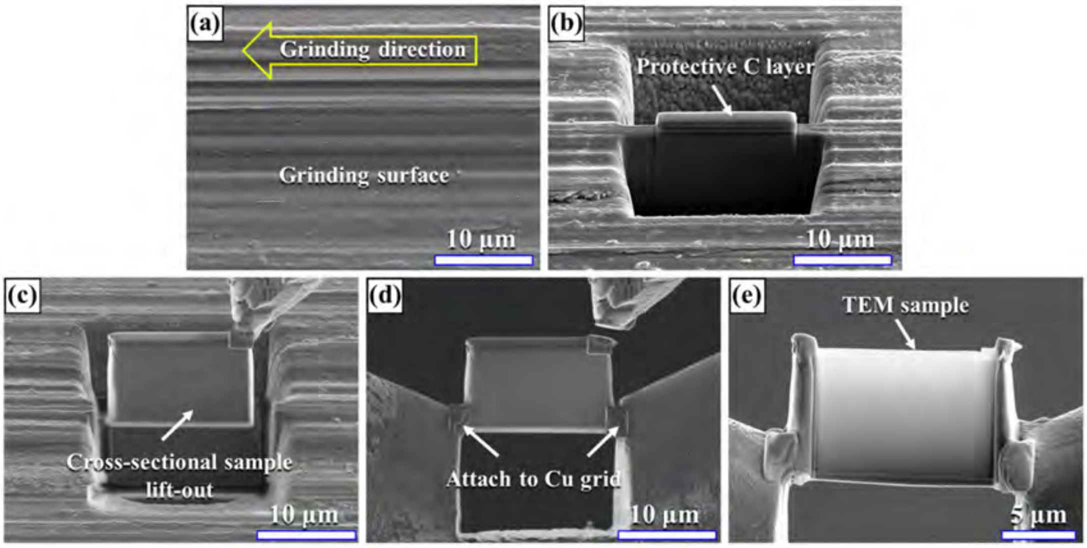

Fig. 7.3 TEM cross-sectional sample preparation: (a) Grinding surface; (b) Ion-milling trenches around the interested area; (c) Cross-sectional sample lift-out; (d) Attaching the lamella to a TEM grid; (e) FIB-thinned TEM lamella.

The grinding force was measured by a KISTER 9109A dynamometer equipped with a 5080A charge amplifier. The experimental setup for the grinding force test is shown in **Fig. 7.4a**, and its schematic diagram is depicted in **Fig. 7.4b**. To comprehensively investigate the mechanism of ultra-high-speed grinding of Ti-alloy and enhance its grindability, two sets of grinding force tests were meticulously designed and conducted. In the first set of experiments, the v_g/v_f ratio was fixed to maintain a specific maximum undeformed chip thickness to examine the strain rate effect during ultra-high-speed grinding. In the second set of experiments, the feed rate v_f was fixed at 100 mm/min while varying the grinding speed within the range of 20-200 m/s. This allowed for the investigation of the influence of the maximum undeformed chip thickness on the material removal mechanism, specifically focusing on the size effect. The detailed parameter settings are summarized in **Tables 7.2** and **7.3**.

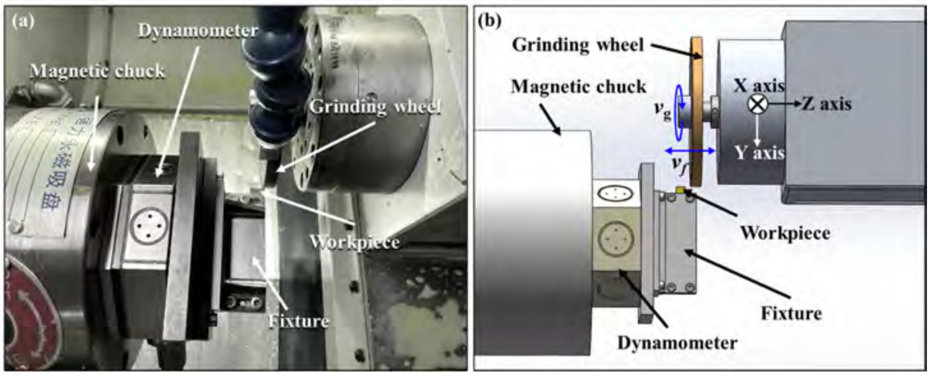

Fig. 7.4 (a) Experimental setup for grinding force test; (b) Schematic diagram of the experimental setup.

Table 7.2 Parameters for grinding force test at fixed feed rate v_f.

Trials	Speed of grinding wheel v_g (m/s)	Feed rate v_f (mm/min)	Grinding depth a_p (μm)
1	20		
2	60		
3	100		
4	140	100	5
5	160		
6	180		
7	200		

Table 7.3 Parameters for grinding force test at fixed v_g/v_f ratio.

Trials	Speed of grinding wheel v_g (m/s)	Feed rate v_f (mm/min)	Grinding depth a_p (μm)
1	20	20	
2	60	60	
3	100	100	
4	140	140	5
5	160	160	
6	180	180	
7	200	200	

7.3 Effects of Grinding Speed on the Surface Roughness and Morphology

7.3.1 Wrought Ti6Al4V

The morphology of the ground surface was determined by the intricate interactions between the abrasive grits and the workpiece surface. **Fig. 7.5** presents the SEM surface morphologies of wrought Ti6Al4V samples machined at various grinding speeds. Notably, the ground surface of the sample machined at a grinding speed of 60 m/s displayed prominent surface defects, including scale-like smearing and furrows (**Fig. 7.5a**). At lower grinding speeds, materials experienced significant side-flowing due to pushing and squeezing effects exerted by abrasive grits, resulting in their adherence to the ground surface and the subsequent formation of smearing defects (Zhou *et al.* 2017). Meanwhile, the tearing materials or chips could be redeposited to the ground surface by friction welding. In another scenario, the chips could also be adhered to the abrasive grits, causing the grits to function as blunt particles. Consequently, this leads to the formation of large furrows on the ground surface.

As the grinding speed increased, the extent of surface smearing gradually diminished, and it became less noticeable at grinding speeds reaching 160 m/s (**Fig. 7.5d**). Additionally, the grinding grooves remained visible in the ground surface produced at 160 to 180 m/s, while they tended to become smaller at higher grinding speeds, indicating an improvement in surface quality with increased grinding speed.

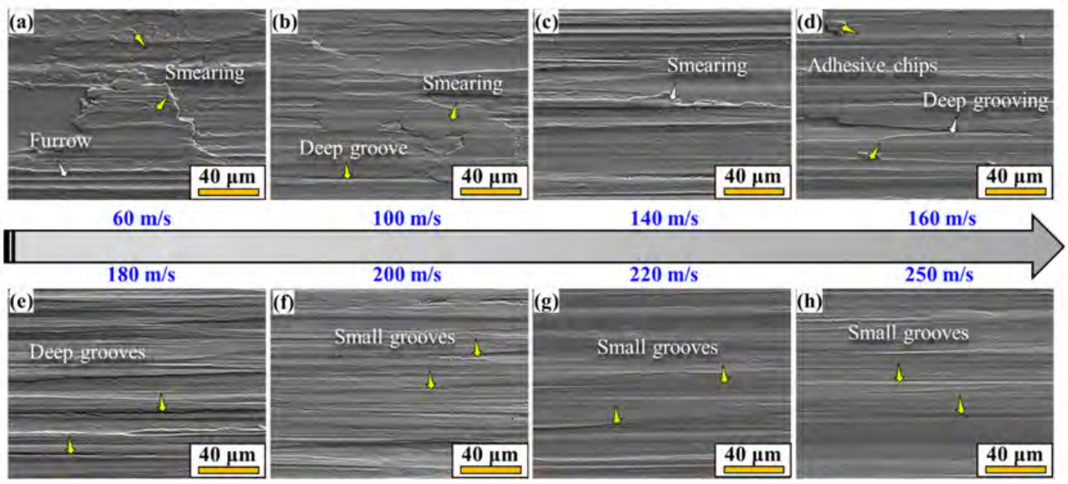

Fig. 7.5 SEM morphology of the wrought Ti6Al4V samples machined at various grinding speeds.

Figures 7.6, a-h illustrate the 3D surface topographies and corresponding average profiles. It is evident that as the grinding speed increased, there was a noticeable reduction in the size and quantity of surface defects. Additionally, the grinding streaks exhibited a diminishing trend, which aligns with the SEM morphology results. In order to quantitatively assess the impact of grinding speed on surface roughness, roughness parameters such as Ra and Rz were extracted from the 3D surface topographies. **Fig. 7.6i** demonstrates that both Ra and Rz exhibited a decreasing trend as the grinding speed increased. Specifically, as the grinding speed increased from 60 to 250 m/s, Ra and Rz decreased by 36% and 39% respectively.

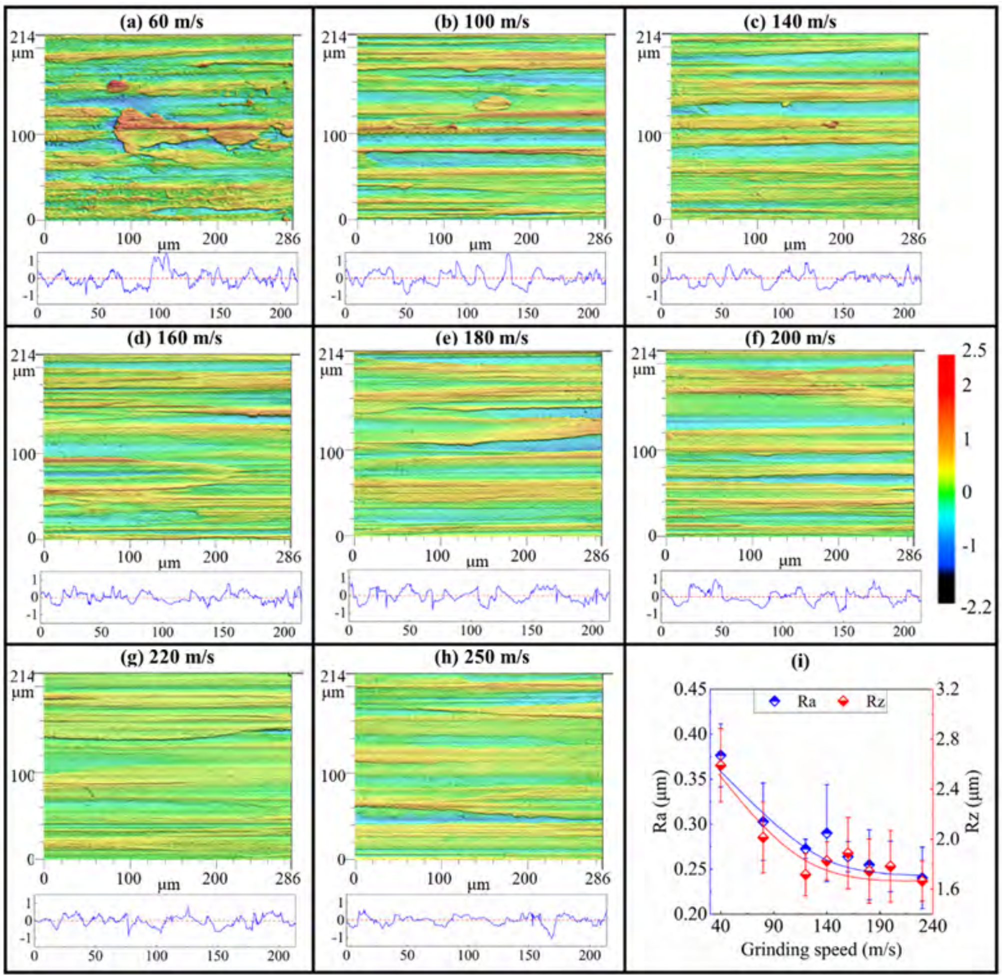

Fig. 7.6 3D surface topography and surface roughness of the wrought Ti6Al4V samples machined at various grinding speeds. (a-h) 3D surface topography and the aveage profile perpendicular to grinding direction; (i) The quantitative statistics of roughnees (Ra and Rz) at various grinding speeds.

7.3.2 SLM-ed Ti6Al4V

Figure 7.7 shows the SEM surface morphologies of the SLM-ed Ti6Al4V samples machined at grinding speeds from 20 to 220 m/s. Similar to the wrought Ti6Al4V, it is evident that surface smearings and furrows were also the primary surface defects at the SLM-ed Ti6Al4V samples machined at 60 m/s, and the occurrence of surface defects is significantly mitigated at higher grinding speeds. Notably, the smearing effect is less pronounced in the SLM-ed Ti6Al4V samples compared to the wrought Ti6Al4V samples. This disparity can be attributed to the higher hardness and reduced ductility of the SLM-ed Ti6Al4V, which limits the lateral plastic flow of the surface peaks during the machining process.

Additionally, the ground SLM-ed Ti6Al4V exhibited more prominent grinding streaks compared to the ground wrought Ti6Al4V samples under an identical grinding condition. This distinction is also evident in the 3D surface topographies and their corresponding average profiles (**Figs. 7.8, a-h**). According to the quantitative statistics of roughness (**Fig. 7.8i**), the roughness of the ground surface of SLM-ed Ti6Al4V samples was slightly higher in comparison to their wrought counterparts. This discrepancy in roughness can primarily be attributed to the differing material properties of the two materials. The SLM-ed Ti6Al4V possessed higher hardness and lower plasticity, endowing it with an enhanced ability to withstand plastic deformation. Conversely, the softer wrought Ti6Al4V was more prone to deformation when subjected to the impact of abrasive grits during the grinding process. Consequently, a greater extent of surface smearing occured on the ground surface of the wrought Ti6Al4V, leading to the formation of smooth smearing areas that conceal the grinding streaks. As a result, the overall surface roughness was reduced.

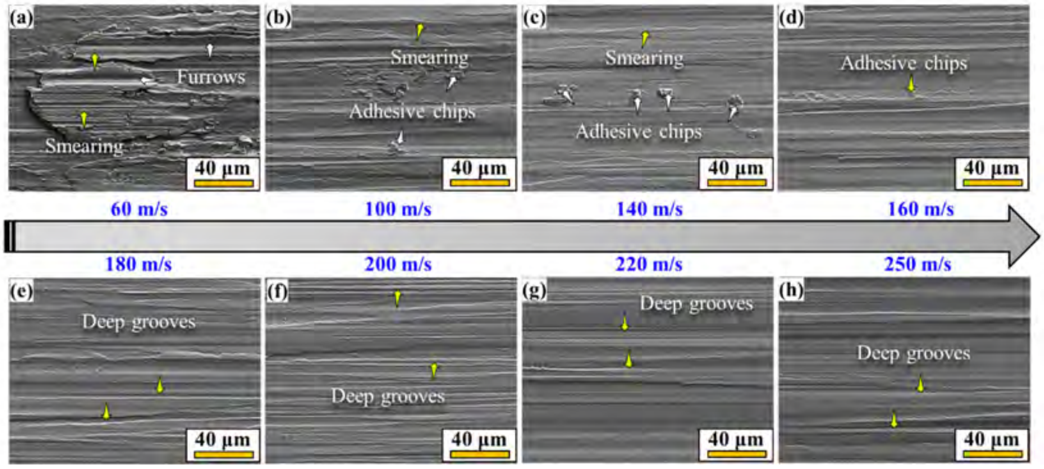

Fig. 7.7 SEM morphology of the SLM-ed Ti6Al4V samples machined at various grinding speeds.

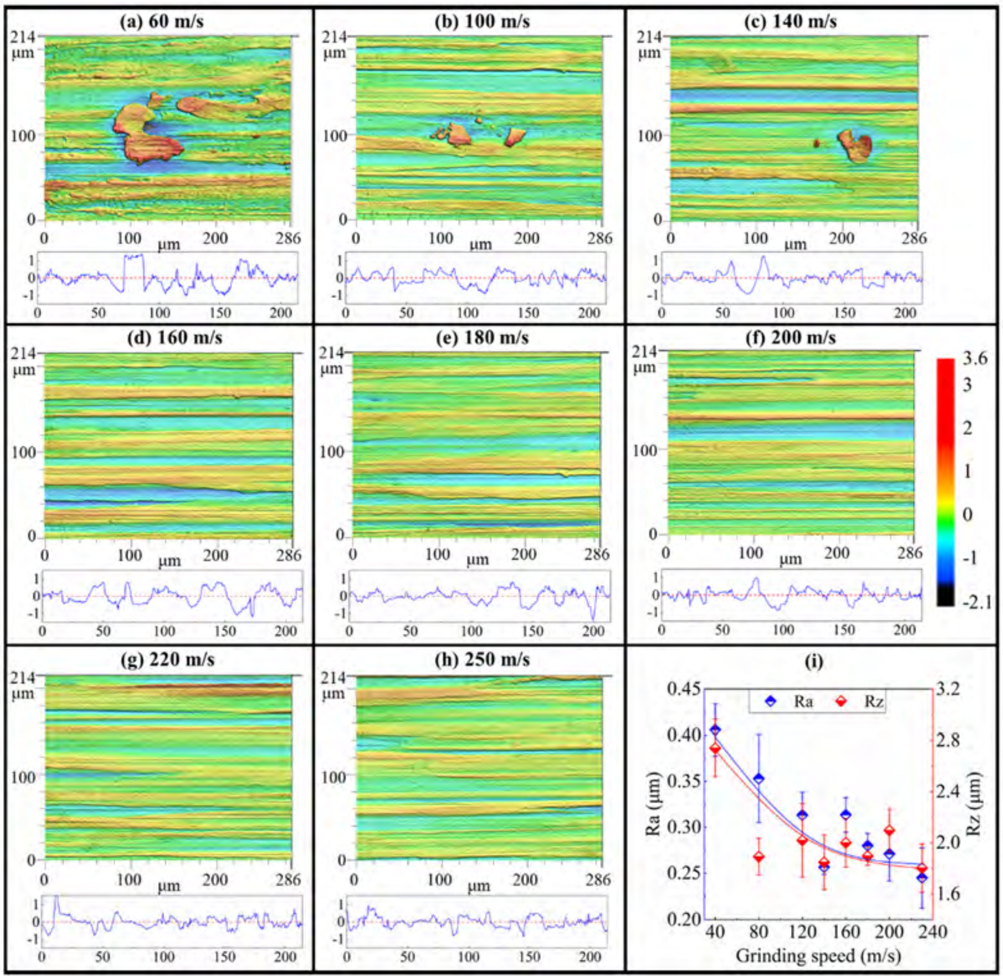

Fig. 7.8 3D surface topography and surface roughness of the SLM-ed Ti6Al4V samples machined at various grinding speeds. (a-h) 3D surface topography and the aveage profile perpendicular to grinding direction; (i) The quantitative statistics of roughnees

(Ra and Rz) at various grinding speeds.

7.4 Effects of Grinding Speed on the Microstructure Distribution of Ti-alloys

7.4.1 Wrought Ti6Al4V

To determine the effects of grinding speed on the distribution of subsurface microstructures, the cross-sections of samples ground at different speeds were meticulously cut, polished, and analyzed using the BSE mode in an SEM. The results clearly indicate that the microstructures within the near-surface layer underwent significant deformation, leading to the formation of an MDZ. Although it is difficult to directly discern the highly refined grain structure from the BSE images, the boundary between the MDZ and the matrix was discernible through the presence of deformed laminar β phases. As depicted in **Fig. 7.9**, the wrought Ti6Al4V samples ground at lower machining speed exhibited deeper MDZ, accompanied by observed surface cracks resulting from smearing defects on the ground surface. Notably, the depth of the MDZ exhibited a significant decrease as the grinding speed increased. Specifically, the depth decreased from ~6.9 μm at 60 m/s to about ~3.5 μm at 250 m/s, indicating a reduction of 49.3%.

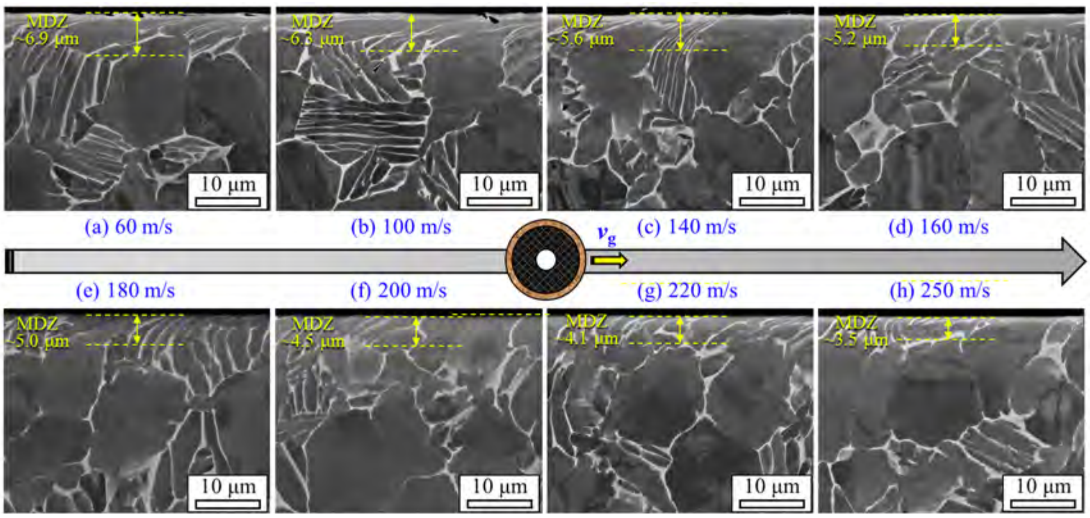

Fig. 7.9 BSE images of subsurface microstructure distribution in wrought Ti6Al4V ground at different speeds.

The Electron Backscatter Diffraction (EBSD) technique was utilized to enhance our understanding of the microstructure modification at the grain scale. The inverse pole figure (IPF) map provides valuable information about the grain structure and orientation. The phase map and grain boundary map reveal the distribution of different phases and grain boundaries, respectively. The kernel average misorientation (KAM) map computed from the EBSD data can determine the average misorientation angle between each measured point and its nearest neighbors (Bracke *et al.* 2009). This map serves as a significant indicator of the strain induced by geometrically necessary dislocation within the sample.

As depicted in **Fig. 7.10a**, the IPF reveals compelling evidence of deformation in wrought Ti6Al4V ground at 60 m/s. The grains in the upper region of MDZ experienced severe refinement to a nano-scale level, making it challenging to discern clear grain boundaries using EBSD (**Fig. 7.10d**). Nevertheless, this region exhibited high KAM values (**Fig. 7.10b)**, indicating a higher strain level was generated by extensive plastic deformation. In the lower region in MDZ, the grain structures were elongated (**Fig. 7.10a**). It is evident that the larger elongated grains were surrounded by HAGBs, while extensive LAGBs were identified within the larger grains, implying the presence of numerous substructures (**Fig. 7.10d**). The phase map further indicates that the β-Ti phase underwent substantial deformation, and the high strain level was also evident in the α/β interfaces. Additionally, the β-Ti acted as a barrier to the elongation of the α-Ti phase.

As the sample ground at 250 m/s, the deformation region was confined to a superficial layer (~4.0 μm), which is consistent with the observation in the BSE images. The microstructure within the MDZ also underwent severe refinement, but grains in the deeper depth showed an undeformed state. Particularly, no distinctive elongated grains like those observed in the sample ground at low grinding speed were observed, suggesting that plastic deformation was effectively suppressed under ultra-high strain rate conditions.

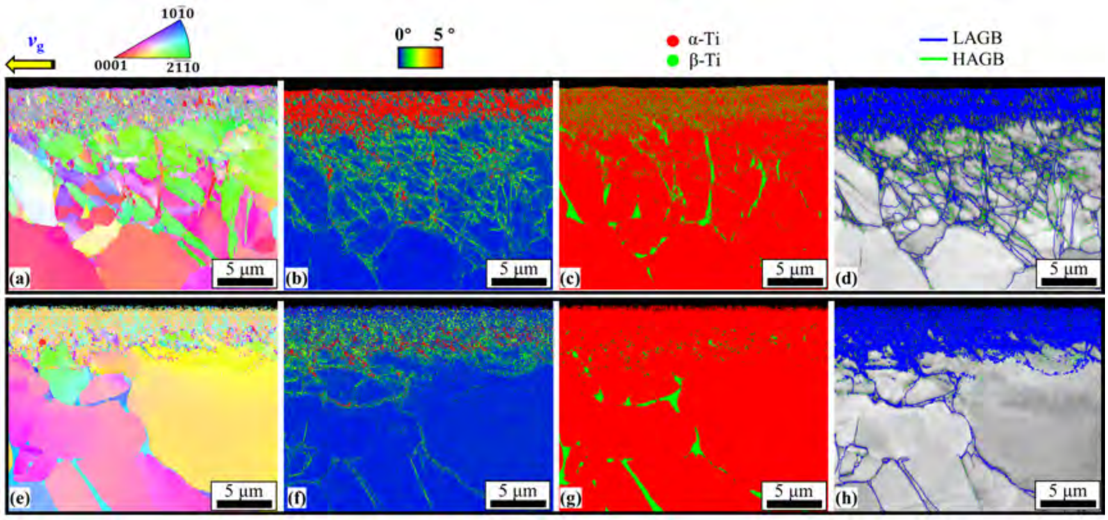

Fig. 7.10 EBSD characterization of subsurface microstructure in wrought Ti6Al4V: 60 m/s (a) IPF map; (b) KAM map; (c) Phase map; (d) Grain boundary map; 250 m/s (e) IPF map; (f) KAM map; (g) Phase map; (h) Grain boundary map.

7.4.2 SLM-ed Ti6Al4V

Figure 7.11 reveals the BSE images of the subsurface microstructure distribution of SLM-ed Ti6Al4V ground at different speeds. The images clearly demonstrate a distinct contrast between the MDZ and the matrix, facilitating the identification of the boundary between these two regions. As shown in **Fig. 7.11a**, the depth of MDZ in the sample ground at 60 m/s was ~6.3 μm. Two distinct zones can be identified in the MDZ, the uppermost zone is defined as the grain refinement zone (GRZ) in which the grains were too small to discern the grain morphology. Beneath the GRZ was the PDZ, characterized by the deformed and elongated lamellar α+β structures along the grinding direction. As the speed increases to 140 m/s, a significant reduction in the depth of the MDZ was observed. Notably, the depth of the GRZ remained almost unchanged, while the PDZ depth decreased to 2.1 μm (**Fig. 7.11c**). Interestingly, the PDZ vanished with further increases in grinding speed, but the depth of MDZ still exhibited a persistent decline (**Figs. 7.11, d-h**).

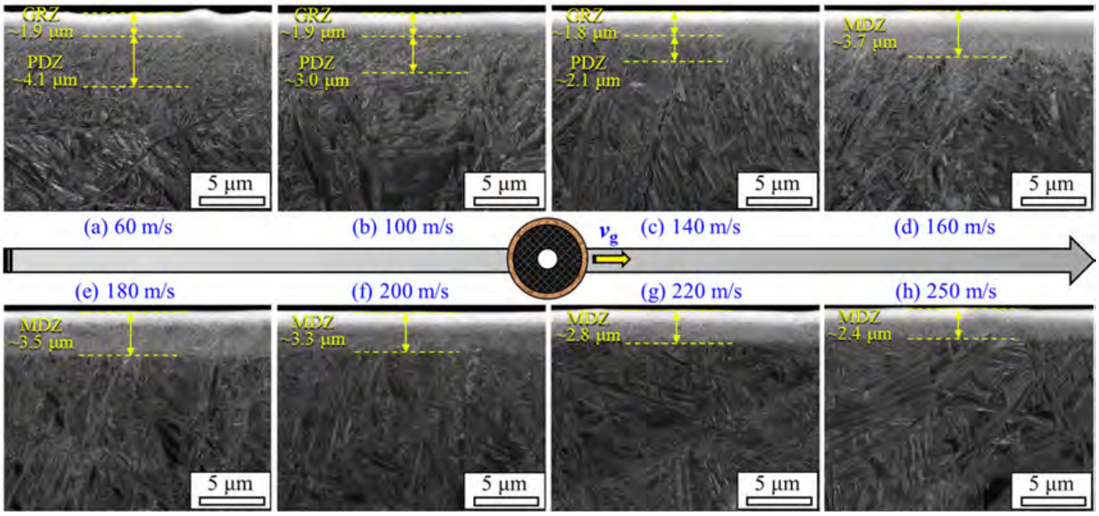

Fig. 7.11 BSE images of subsurface microstructure distribution in SLM-ed Ti6Al4V ground at different speeds.

Figure 7.12 presents the EBSD characterization of subsurface microstructure in SLM-ed Ti6Al4V. Unlike the coarse and equiaxed grains observed in wrought Ti6Al4V, SLM-ed Ti6Al4V displays a remarkably fine laminar grain structure. The KAM map reveals the presence of higher pre-strain in the α/β interfaces within the matrix material of SLM-ed Ti6Al4V. This phenomenon is commonly encountered in SLM-ed Ti-alloys due to the rapid cooling rate during the solidification process (Yao *et al.* 2022).

At a grinding speed of 60 m/s, the MDZ measures approximately 6.2 μm. The grain structure in the top layer was also significantly refined, displaying a higher strain level compared to that of wrought Ti6Al4V (**Figs. 7.12, a** and **b**). Furthermore, deformed and twisted grain structures were identified in the bottom region of MDZ, and a higher strain than the matrix material was identified in this region, which is associated with the induced high-density substructures. **Figs. 7.12, e-h** present the corresponding EBSD results of SLM-ed Ti6Al4V ground at 250 m/s. The MDZ was separated from the matrix material by a distinctive boundary. Similar to the sample ground at low speed, high strain and refined microstructures were evident within the MDZ. However, it is noteworthy that the grain structure beneath the boundary remained completely undeformed, even for the grains with half of their distribution located above the boundary. This observation suggests that the stress field is strictly confined to the superficial layer under ultra-high strain rate conditions.

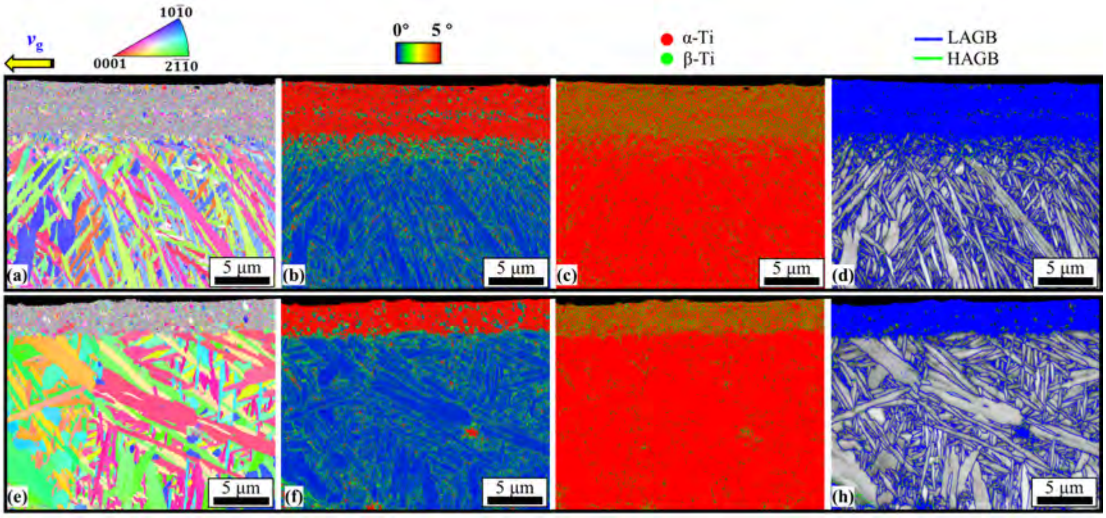

Fig. 7.12 EBSD characterization of subsurface microstructure in SLM-ed Ti6Al4V: 60 m/s (a) IPF map; (b) KAM map; (c) Phase map; (d) Grain boundary map; 250 m/s (e) IPF map; (f) KAM map; (g) Phase map; (h) Grain boundary map.

In order to quantitatively compare the depth of MDZ in both wrought and SLM-ed Ti6Al4V, multiple cross-sections of each sample were examined to determine the average values. As depicted in **Fig. 7.13**, both the wrought and SLM-ed Ti6Al4V show a consistent downward trend in MDZ depth, exhibiting a distinct skin effect of MDZ as the machining speed increases. Nevertheless, the SLM-ed Ti6Al4V demonstrates a smaller MDZ depth compared to the wrought Ti6Al4V under identical machining conditions. Additionally, the analysis of the fitting function indicates that the MDZ depth of wrought Ti6Al4V exhibits higher sensitivity to the machining speed, as evidenced by its steeper negative slope in comparison to that of SLM-ed Ti6Al4V.

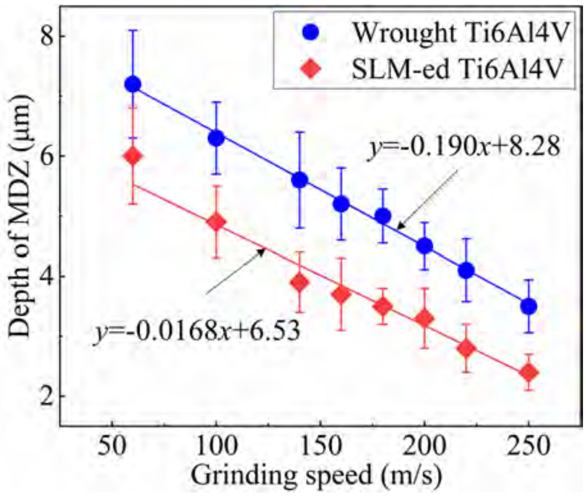

Fig. 7.13 Comparison of the MDZ depth in wrought and SLM-ed Ti6Al4V ground at differernt speeds.

7.5 Effects of Grinding Speed on Microstructure Evolution of Ti-alloys

7.5.1 Wrought Ti6Al4V

TEM samples were prepared by the FIB technique to investigate the underlying deformation mechanism at various grinding speeds. **Fig. 7.14** shows the STEM characterization of wrought Ti6Al4V ground at 60 m/s. As depicted in **Fig. 7.14a**, the machining deformation zone (MDZ) extended to a depth of 7 μm in the subsurface, and the MDZ can be divided into three zones regarding the distinct microstructures. The uppermost layer was defined as the DRXZ, possessing a thickness of approximately 700 nm. This zone was predominantly composed of DRX grains with an average diameter of ~90 nm that were produced by the thermomechanical effect (**Figs. 7.14, c** and **d**).

The second layer downward to the subsurface was the transition zone (TSZ), in which the mixed microstructures of nanoscale DRX grains and elongated grains were observed (**Fig. 7.14e**). Notably, the equiaxed DRX grains in the TSZ (average diameter: ~43 nm) were much smaller than those observed in the DRXZ. This discrepancy can be attributed to the higher temperatures generated on the top surface by the intense surface smearing, which promoted the grain growth of DRX grains in DRXZ.

Additionally, a crack was observed along the boundary of TSZ and PDZ, this was the trace of the surface smearing. Furthermore, according to the EDS map of V element (**Fig. 7.14b**), both DRXZ and TSZ possessed a higher concentration of V element than that in the beneath zone, and nanoscale β precipitations were identified in **Fig. 7.14e**. These pieces of evidence suggest that the deformation-induced α→β transformation occurred due to the severe thermomechanical effect.

The third zone corresponds to the PDZ, characterized as heavily deformed grains possessing inside substructures including high-density dislocations (HDDs), LAGBs, and deformation twins. As revealed in **Fig. 7.14g**, the nanoscale $\{0\bar{1}11\}$ deformation twins were identified in PDZ. It is worth noting that, the decrease in strain rate in the direction of grinding depth is not conducive to the induction of deformation twinning in the subsurface layer, this is also demonstrated in the SPS of wrought Ti6Al4V at lower machining speed. However, the applied coolant efficiently dispersed thermal energy in the grinding process, consequently, the temperature rise in the subsurface was inhibited, which facilitated the initiation of deformation twinning. Meanwhile, the matrix grains beneath the PDZ exhibited a high density of dislocations due to the applied stress.

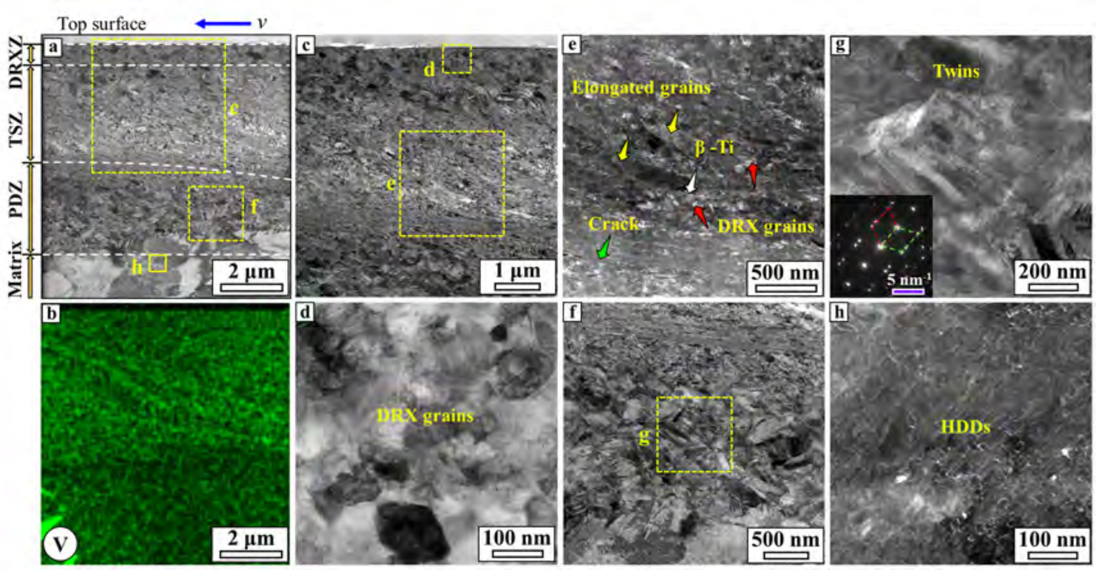

Fig. 7.14 STEM of wrought Ti6Al4V ground at 60 m/s. (a) Subsurface microstructure; (b) EDS map of V element; (c) Enlarge view of c in (a) shows the DRXZ and TSZ in the near-surface; (d) Nanoscale DRX grains in the DRXZ; (e) Enlarge view of e in (c) shows the microstructures in TSZ; (f) Enlarge view of f in (a) shows the microstructures

in the PDZ; (g) Deformation twins in the PDZ (the inset is the SAED pattern); (h) Dislocation structures in the matrix.

As the grinding speed increased to 180 m/s, the MDZ decreased to 4.6 μm (**Fig. 7.15a**), and the deformation mechanism also changes. Although the nanoscale DRX grains still existed in the topmost layer, their distribution is limited to a depth of 100 nm from the top surface (**Fig. 7.15c**). In the deeper zone, deformation twinning becomes the dominant deformation mechanism. **Fig. 7.15d** displays a typical fine grain with internal parallel twins distributed in the upper region of DITZ, the average thickness of deformation twins is around 13 nm.

In the region of PDZ, with increased strain rate and decreased deformation strain, coarser twins with an average thickness of around 33 nm are formed (**Fig. 7.15g**). Meanwhile, the bulky β-Ti within the DITZ underwent significant deformation, with high-density dislocations and substructures formed within the β laminas (**Fig. 7.15e**). Additionally, the deformation twins were confined in the DITZ, and a distinctive boundary between the DITZ and the matrix can be identified (**Fig. 7.15f**). Although no grain-scale deformation occurred in the matrix grains, high-density dislocations were generated in the matrix near the PDZ, and the LAGB structure was also induced as the pile-up of dislocations ((**Fig. 7.15h**).

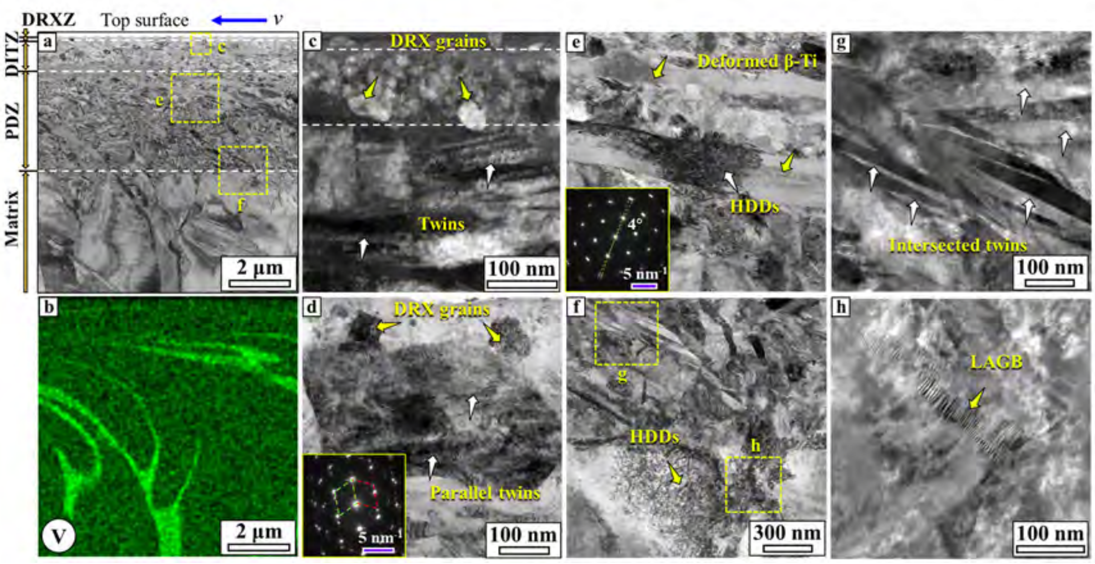

Fig. 7.15 STEM of wrought Ti6Al4V ground at 180 m/s. (a) Subsurface microstructure; (b) EDS map of V element; (c) Enlarge view of c in (a) shows the DRX grains and twins

in the near-surface; (d) Refined grain with internal parallel twins; (e) Deformed β-Ti; (f) Transformation-zone between PDZ and matrix; (g) Intersected twins in the PDZ; (h) LAGB structures in the matrix.

Figure 7.16 displays the STEM microstructure in the subsurface of wrought Ti6Al4V after grinding at a speed of 250 m/s. It is noteworthy that the MDZ is further decreased to ~3.2 μm. Notably, no DRXZ was observed in the subsurface. Instead, a DITZ was directly induced in the topmost region in the subsurface, in which the UGENTs was the dominant structure. A representative UGENTs grain is revealed in **Fig. 7.16d**, with its corresponding dark field image and SAED pattern depicted in **Fig. 7.16e**. Additionally, unidirectional parallel twins or multi-directional intersected twins were generated within the UGENTs grains dependent on the local stress/strain and orientation (**Fig. 7.16, f** and **g**). Beneath the DITZ, a PDZ with a depth of ~ 1.6 μm was observed, in which HDDs and dislocation tangles were produced within the deformed grains (**Fig. 7.16h**).

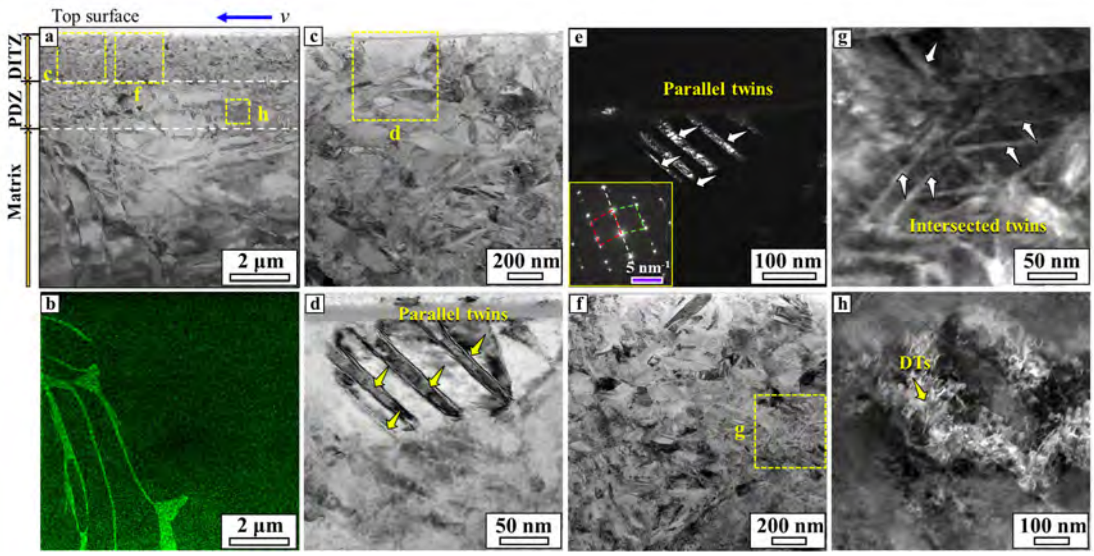

Fig. 7.16 STEM of wrought Ti6Al4V ground at 250 m/s. (a) Subsurface microstructure; (b) EDS map of V element; (c) Enlarge view of c in (a) shows the nanoscale deformation twins in the DITZ; (d) A typical ultrafine grain embedding nanotwins (UGENTs) structure; (e) The dark field image corresponding to d (the inset is the SAED pattern); (f) Enlarge view of f in (a); (g) Intersecting twins; (h) Dislocation structures in the matrix.

7.5.2 SLM-ed Ti6Al4V

Figure 7.17 displays the STEM observation of SLM-ed Ti6Al4V ground at 60 m/s, the machining influence zone can be divided into three regimes (**Fig. 7.17a**). The first region from the top surface, referred to as the DRXZ, was characterized by a dominant microstructure of DRX grains (**Fig. 7.17b**). Noticeably, within the DRXZ, the DRX grains displayed a sandwich-like distribution, with coarser DRX grains (averaging diameter size: ~125 nm) filling the middle part, while two thin layers consisting of nano-scale DRX grains sandwich the middle part. The chain-like DRX grain in nano-scale (**Fig. 7.17c**) suggests that these grains were generated through the discontinuous DRX (DDRX) mechanism. In contrast, the DRX in wrought Ti6Al4V followed the CDRX mechanism, this discrepancy may be ascribe to the different initial microstructures.

In SLM-ed Ti6Al4V, the refined microstructure possessed a large number of grain boundaries that promote the nucleation of DDRX grains during the rapid deformation process (Huang and Logé 2016). Meanwhile, as the DDRX has a higher temperature requirement, the microstructure distribution implies that both the top and bottom surfaces of the DRXZ experienced higher temperatures due to the smearing effect. The severe smearing effect resulted in a distinct crack that separated the DRXZ from the underlying TSZ at a depth of ~1.3 μm (**Fig. 7.17d**).

In the TSZ, the DRX grains in the upper region transited to deformation twins as the temperature declined, and the intersected twins were identified as $\{0\bar{1}11\}$ deformation twins (**Fig. 7.17e**). Moving further down to a depth of ~3.3 μm, the microstructure transformed into elongated laminar grains (**Fig. 7.17f**). The grains within PDZ exhibited a gradient feature size, with greater thickness along the depth direction due to less plastic deformation (**Fig. 7.17f**). Additionally, The microstructure in the matrix maintained a regular α+β laminar configuration without deformation (**Fig. 7.17h**).

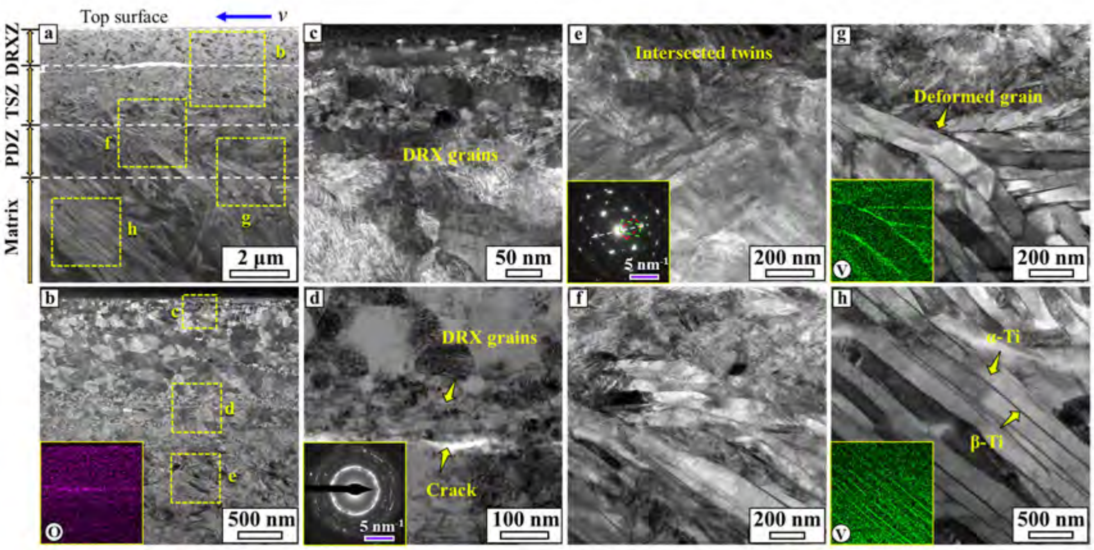

Fig. 7.17 STEM of SLM-ed Ti6Al4V ground at 60 m/s. (a) Subsurface microstructure; (b) Enlarge view of b in (a) showing the mincrostructure in the uppermost layer; (c) Enlarge view of c in (b); (d) Enlarge view of d in (b); (e) Enlarge view of e in (a) showing the intersected twins; (f) Enlarge view of f in (a); (g) Enlarge view of g in (a); (h) Enlarge view of h in (a).

As shown in **Fig. 7.18a**, the MDZ decreased to ~3.3 μm as the machining speed was raised to 180 m/s. Although a DRXZ still existed in the uppermost layer of MDZ, its thickness was reduced to 400 nm. Notably, the average diameter size of DRX grains was refined to ~15 nm as the high strain rate significantly limited the grain growth. The nano-twin was the primary microstructure in the upper region of TSZ. **Fig. 7.18d** reveals the presence of high-density twin clusters, and the dark-field image and SAED pattern confirm the twins are $\{01\bar{1}1\}$ twins. Furthermore, refined grains with internal nano-scale twins were also identified (**Fig. 7.18f**). In the deeper region of TSZ, the twin structure gradually transformed into severely refined elongated grains, containing internal substructures such as dislocations and sub-grain boundaries (**Fig. 7.18g**). The region with a depth range of 2.1 to 3.3 μm is identified as the PDZ, characterized by deformed grains with high-density dislocations (HDDs).

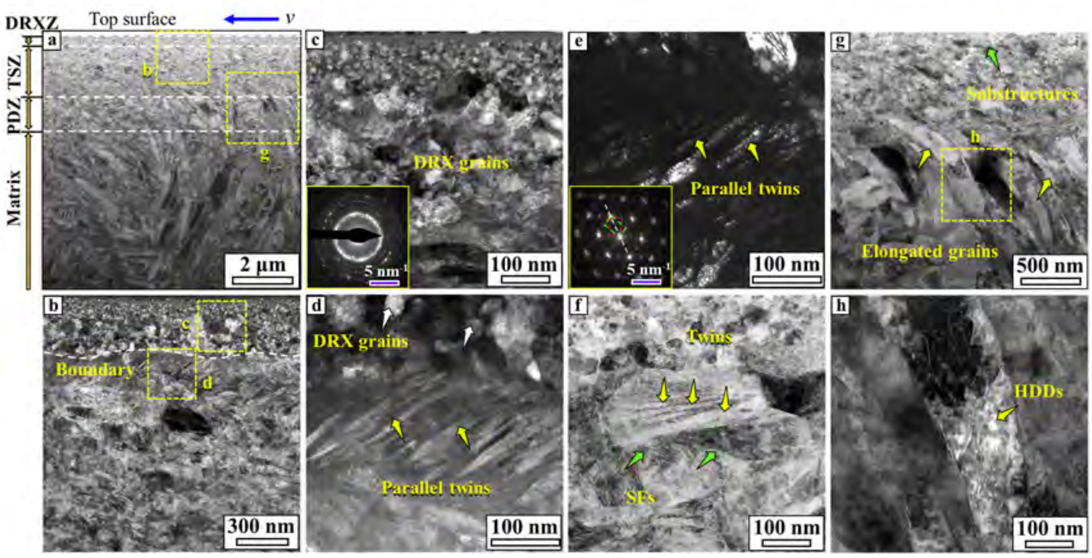

Fig. 7.18 STEM of SLM-ed Ti6Al4V ground at 180 m/s. (a) Subsurface microstructure; (b) Enlarge view of b in (a) showing the mincrostructure in the uppermost layer; (c) Enlarge view of c in (b); (d) Enlarge view of d in (b); (e) Dark-field image of (d) and the SAED pattern; (f) Refined grain with internal parallel twins; (g) Enlarge view of g in (a); (h) Enlarge view of h in (g).

The MDZ further decreased to ~2.3 μm as the grinding speed increased to 250 m/s (**Fig. 7.19a**). Similar to wrought Ti6Al4V, the DRX phenomenon was absent. Instead, a distinct DITZ was generated in the uppermost region. As revealed in **Fig. 7.19b**, the primary microstructure observed in the DITZ was the UGENTs, and the average diameter of the ploygonal grains was ~175 nm. Upon closer examination (**Fig. 7.19c**), a high density of nano-twins was found within the typical UGENTs grains. Additionally, a PDZ with a thickness of ~760 nm was distributed beneath the DITZ. **Fig. 7.19b** shows the STEM image of a UGENTs grain viewed along $[2\bar{1}\bar{1}0]$ zone axis, The intense contrast with adjacent grains indicates the presence of HAGB, which can be identified by the HRTEM image and FFT pattern (**Figs. 7.19, g** and **h**). Inside the UGENTs grain, multiple twinning systems along $\{0\bar{1}11\}$ planes were activated, and three-fold twins were observed at the intersected site of two twin boundaries. Meanwhile, multiple kinks were observed in the twin boundaries near the intersected site, which were demonstrated to facilitate the formation of hierarchical nano-twins (Zhu *et al.* 2022).

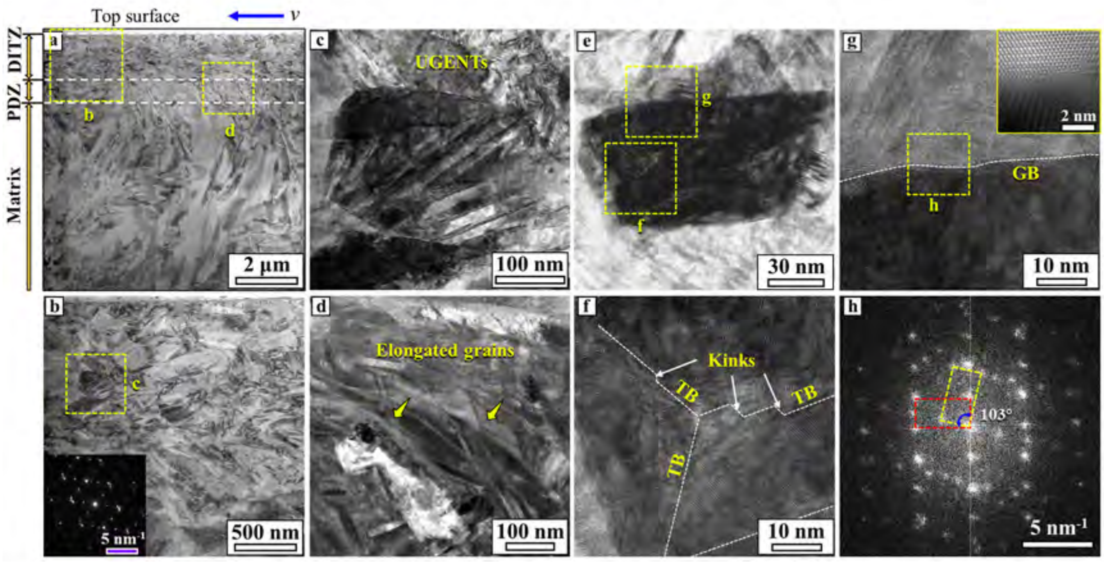

Fig. 7.19 STEM of SLM-ed Ti6Al4V ground at 250 m/s. (a) Subsurface microstructure; (b) Enlarge view showing the mincrostructure in DITZ; (c) A typical UGENTs; (d) Elongated grains; (e) STEM image of a UGENTs viewed along $[2\bar{1}\bar{1}0]$ zone axis; (f) HRTEM image of intersected twins; (g); HRTEM image of GB of UGENTs (h) FFT pattern of h.

7.6 Grinding force test

7.6.1 Wrought Ti6Al4V

The v_g/v_f ratio was fixed to examine the strain rate effect during ultra-high-speed grinding. The grinding force is an important indicator to describe the machining characteristics of a material. As illustrated in **Fig. 7.20a**, both the normal grinding force F_y and the tangential grinding force F_x exhibited an initial upward followed by a subsequent decrease. The maximum grinding force was attained at a grinding speed of 100 m/s. Three speed regions can be identified according to the variation of grinding force. The first region corresponded to grinding speeds ≤100 m/s, the grinding force remained at a low level, and grinding force waveform was relatively stable due to the low feed rate and the grinding speed. However, as the grinding speed increased, both the F_y and F_x grinding forces experienced a rapid increase attributable to the strain rate hardening effect. Meanwhile, the grinding force ratio F_y/F_x also showed an upward trend, which indicates that the abrasive particles encountered greater resistance while cutting into the workpiece, thereby resulting in a fluctuation of grinding force when the grinding wheel cut in and out of the workpiece.

The second speed region was 100~180 m/s, in which the predominant factor shifted from strain hardening to the thermal softening effect, resulting in a notable reduction in grinding forces. Additionally, the force ratio in this region also diminished, demonstrating that the material underwent softening, making it easier to cut into the workpiece. As the machining speed exceeded 180 m/s, the MDZ was significantly reduced as the strain-rate field and temperature field were confined to a superficial layer. Consequently, the influence of both strain rate hardening and thermal softening effects on the machined material diminished, leading to a tendency towards an equilibrium state in the grinding force.

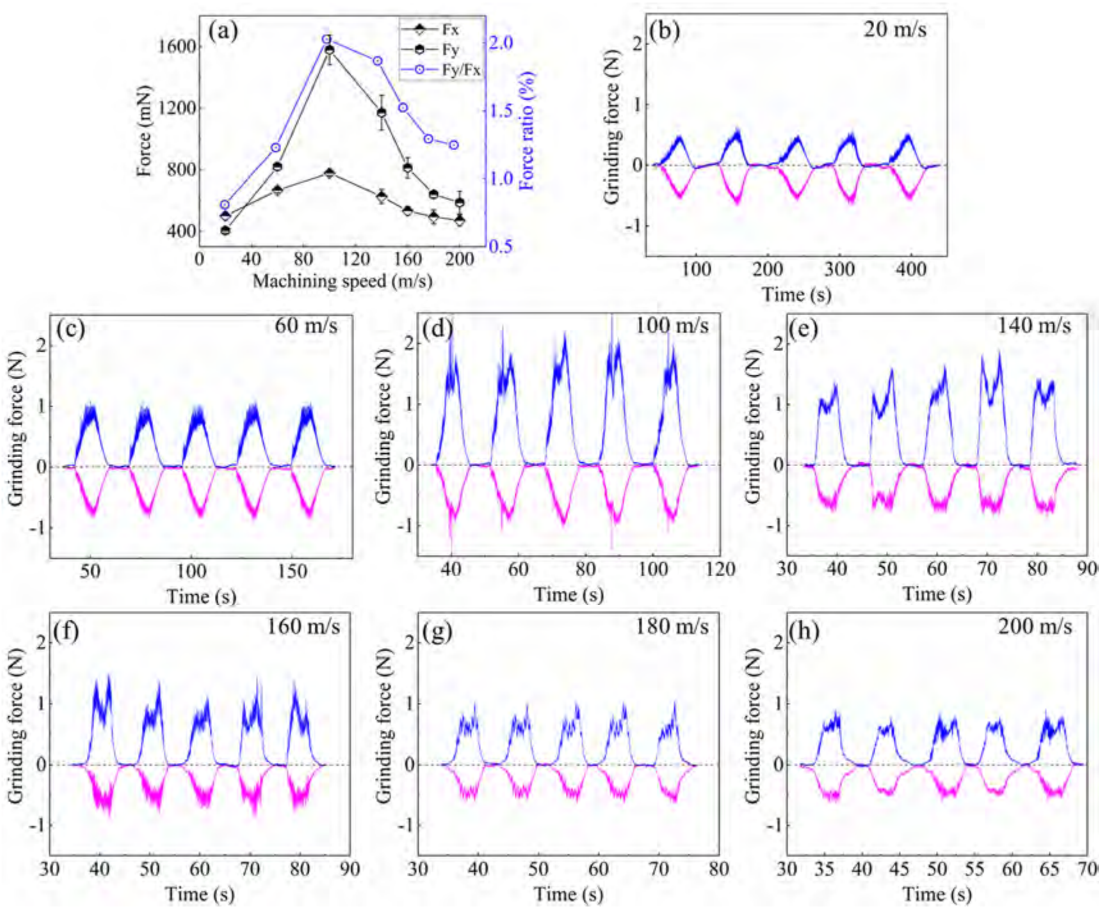

Fig. 7.20 Grinding force test of wrought Ti6Al4V at fixed v_g / v_f: (a) Grinding forces at different grinding speed; (b)-(f) Grinding force measurement results at grinding force from 20-200 m/s.

To explore the size effect, the feed rate (v_f) was maintained at a constant value of 100 mm/min, while the grinding speed was varied. Interestingly, the grinding force exhibited a similar variation trend compared to the fixed v_g/v_f ratio grinding. However, at lower machining speeds (<100 m/s) in the fixed v_f grinding, the grinding force was greater than that observed in the fixed v_g/v_f ratio grinding at the same grinding speed. This disparity arises because the material removal per individual abrasive particle is larger in the fixed v_f grinding as the feed rate is higher, indicating the presence of a size effect.

The material removal per individual abrasive particle decreased at higher grinding speed in fixed v_f grinding due to the size effect, which tended to decrease the grinding force. Nevertheless, the grinding force still showed an upward trend when the grinding speed ≤ 100 m/s, indicating the predominant influence of strain rate hardening. As the grinding speed exceeded 100 m/s, a more pronounced decline in the grinding force was observed, which can be attributed to the combined effects of thermal softening and the size effect.

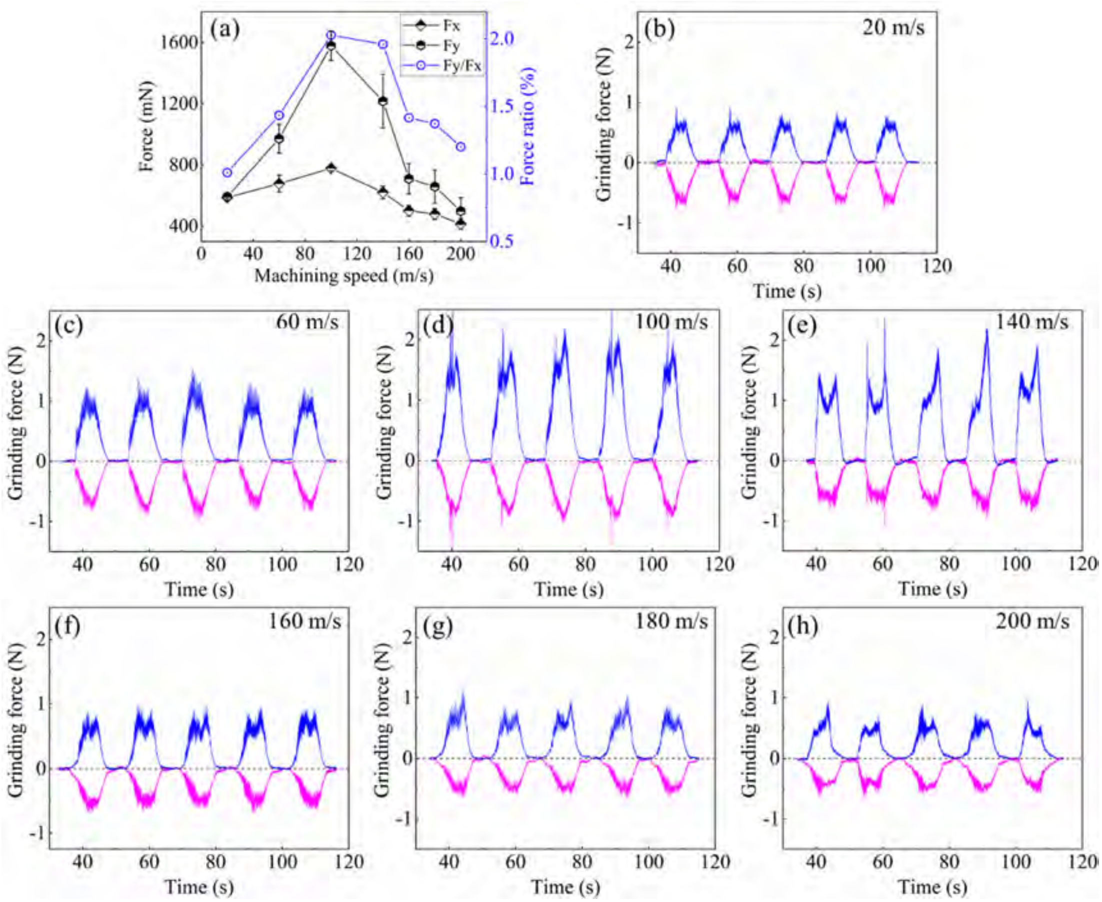

Fig. 7.21 Grinding force test of wrought Ti6Al4V at fixed v_f (100 mm/min): (a) Grinding forces at different grinding speed; (b)-(f) Grinding force measurement results at grinding force from 20-200 m/s.

7.6.2 SLM-ed Ti6Al4V

Figure 7.22 illustrates the variation in grinding forces during fixed v_g /v_f ratio grinding of SLM-ed Ti6Al4V. Despite the microstructural and mechanical property distinctions between SLM-ed Ti6Al4V and wrought Ti6Al4V, it is evident that the trend of the grinding force variation was similar. The strain rate hardening effect was the dominant factor at the speed region of 20~100 m/s, which governed the increase of grinding forces. Notably, the signal of the grinding force demonstrated a pronounced bimodal curve, particularly evidenced at the velocity of 100 m/s. This signified the occurrence of vigorous grinding force fluctuations as the grinding wheel engaged and disengaged with the workpiece. The thermal softening effect became the leading role, resulting in the rapid decline of grinding force in the high-speed region. In the UHSG region, the MDZ in the subsurface revealed a skin effect, resulting in a negligible variation in the grinding force when the grinding speed exceeds 180 m/s.

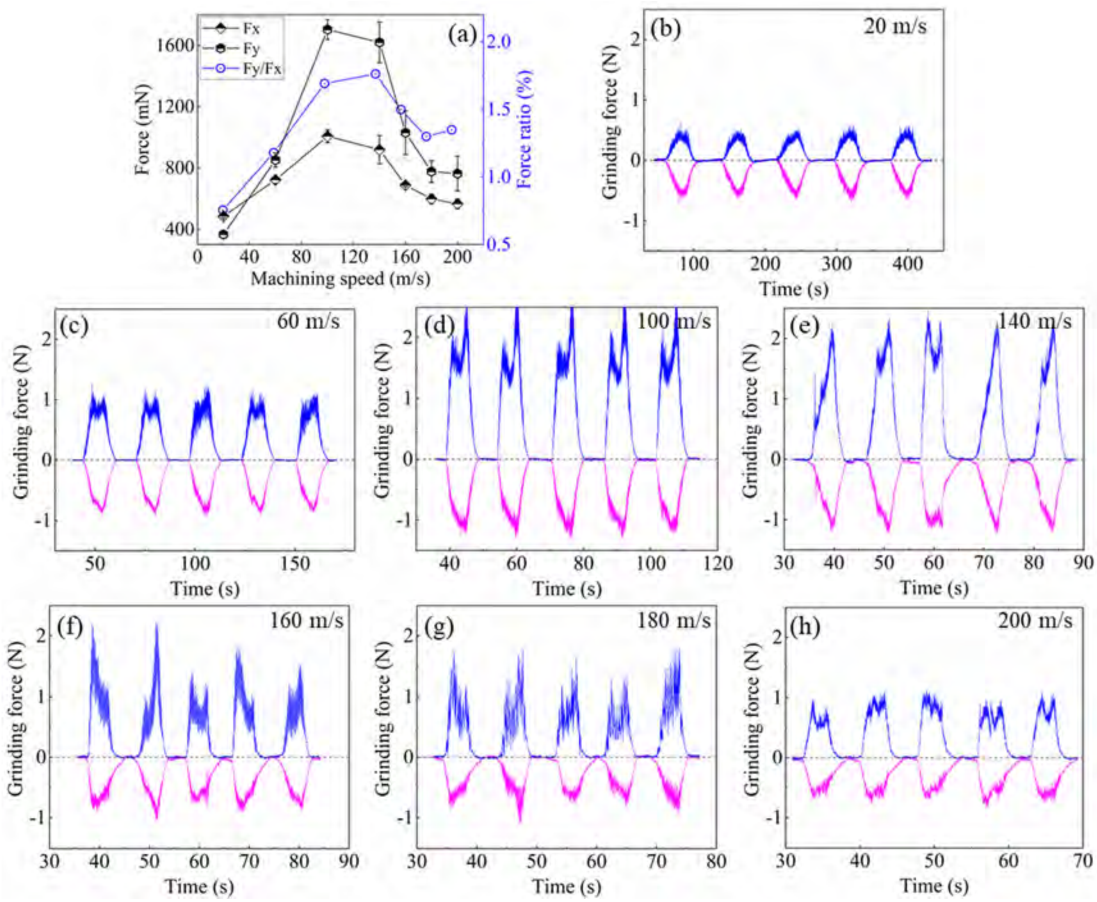

Fig. 7.22 Grinding force test of SLM-ed Ti6Al4V at fixed v_g/v_f: (a) Grinding forces at different grinding speed; (b)-(f) Grinding force measurement results at grinding force from 20-200 m/s.

Figure 7.23 illustrates the measured results of grinding forces during fixed v_f ratio grinding of SLM-ed Ti6Al4V. it is evident that the grinding force exhibited a similar variation trend with that of wrought Ti6Al4V since both materials have similar material characteristics. However, the grinding force of SLM-ed Ti6Al4V was always larger than that of wrought Ti6Al4V at similar machining conditions due to the higher strength and hardness.

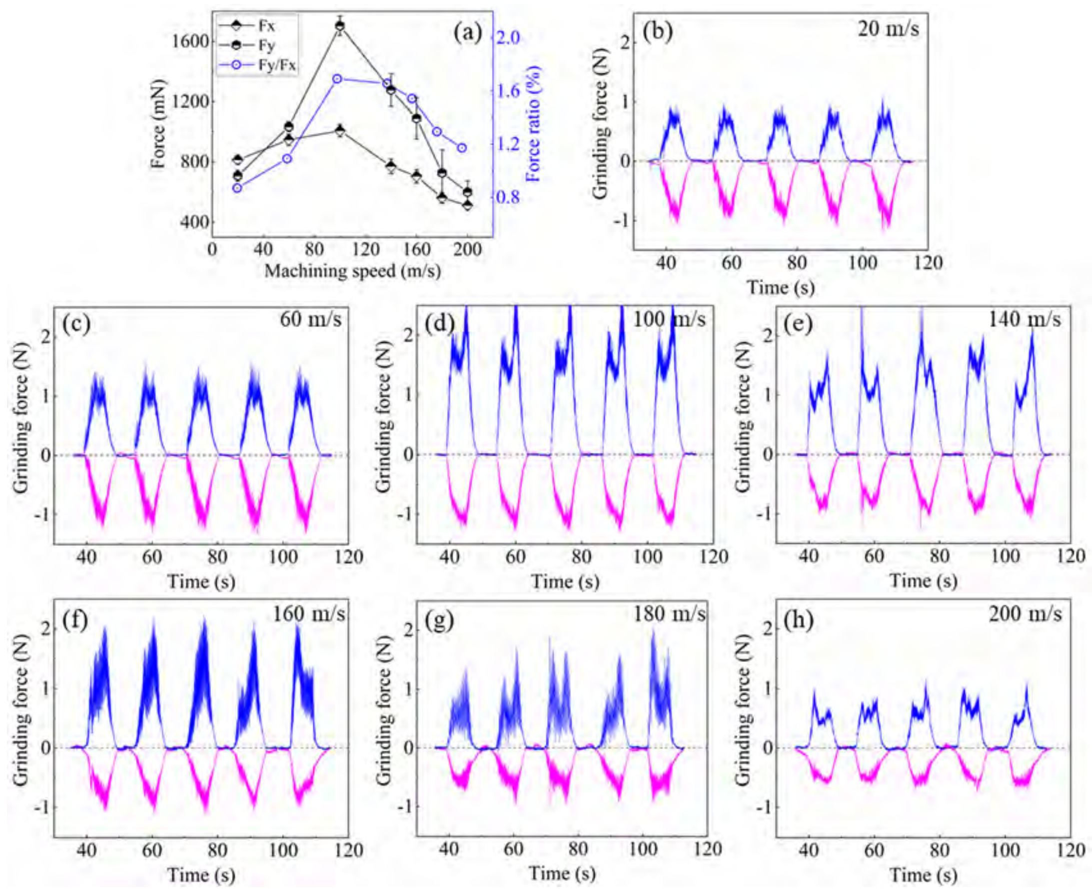

Fig. 7.23 Grinding force test of SLM-ed Ti6Al4V at fixed v_f (100 mm/min): (a) Grinding forces at different grinding speed; (b)-(f) Grinding force measurement results at grinding force from 20-200 m/s.

7.7 Discussion

UHSG is a complex process that involves simultaneously cutting of a large number of abrasive particles at extremely high speeds, and this process couples many effects, including thermal effect, size effect, strain and strain-rate effect (Guo *et al.* 2022). The preceding two chapters revealed the material removal mechanisms of Ti-alloys under ultra-high speeds in SPS. Building upon this foundation, the present chapter delves into the application of UHSG in the machining of Ti-alloys, and focuses on the investigation of surface integrity, attempting to achieve high-quality and high-efficiency machining of Ti-alloys.

7.7.1 Speed Dependence of Surface Integrity in Grinding of Ti-alloys

The dynamic properties of materials exhibit a strong dependence on the strain rate, leading to distinct dynamic responses (Salvado *et al.* 2017; Tang *et al.* 2023). Consequently, as machining speeds increase, the material removal behaviors and mechanisms may undergo significant variations, leading to differences in surface integrity. Based on the surface and subsurface detection and analysis, the alteration of surface integrity and the transition of dominant deformation mechanisms with grinding speed in grinding of Ti-alloy are discussed and illustrated in **Fig. 7.24**.

At low grinding speeds, the Ti-alloy material maintained its high plasticity, which enhanced the plowing effect of abrasive particles, thereby leading to the formation of severe material smearing on the ground surfaces. Such surface defects not only significantly correlated with the high surface roughness in low-speed region but also gave rise to the development of subsurface cracks. Meanwhile, a deeper machining deformation zone tended to be induced by the severe plastic deformation in low-speed machining. As the grinding speed increased within the low-speed region, the deformation process was predominantly influenced by the strain rate hardening effect. This effect led to a rapid increment in grinding force and, simultaneously, resulted in a considerable reduction in both surface smearing and the depth of the subsurface deformation layer.

The grinding force of both wrought and SLM-ed Ti6Al4V reached a turning point at 100 m/s, which implies that the thermal softening effect took over in the competition with strain rate hardening, and the machining speed entered the high-speed machining region. The thermal softening effect under high-speed conditions facilitated the shearing localization, which effectively inhibited the plastic deformation in the subsurface of ground samples. Notably, the side-flow was the primary defect observed on the ground surface in the high-speed region.

According to Salomon's cutting temperature curve, the cutting temperature experienced a rapid increase in the high-speed region as cutting speeds escalated. However, once the machining speed surpassed a critical value, the temperature began to decrease with further increases in machining speed (Longbottom and Lanham 2006). This phenomenon gives rise to what is commonly referred to as a "Death Valley" in the high-speed region. In this region, the elevated temperature can lead to severe tool wear and inferior surface quality, rendering it unsuitable for practical applications.

Nevertheless, the temperature turning point in Salomon's temperature curve has been a topic of ongoing debate. Some research studies have suggested that the temperature steadily increased with machining speed and does not exhibit a declining trend with further increases in speed (Dewes *et al.* 1999; Kitagawa *et al.* 1997). However, it is essential to note that the speed ranges explored in previous research have not yet reached the realm of high-speed or ultra-high-speed machining conditions, because conducting temperature tests under such extreme machining conditions remains a well-acknowledged challenge due to the limitations of the available detection methods (Gao and Iwamoto 2021).

It is indeed that a substantial portion of cutting heat is dissipated by the fast-moving chips. Particularly when fragmented chips are produced at very high machining speeds, their high specific surface area is favorable to heat dissipation. Therefore, the heat transfer to the machined surface may be effectively constrained. In the ultra-high-speed region, the strain rate evoked embrittlement effect became the predominant deformation mechanism. As a positive outcome, the surface finish was improved due to the diminish of surface defects. Additionally, the machining-induced stress, strain, and temperature tended to be confined in a very superficial layer, leading to the "skin effect" of MDZ. Accordingly, higher surface integrity was achieved under ultra-high strain rate conditions.

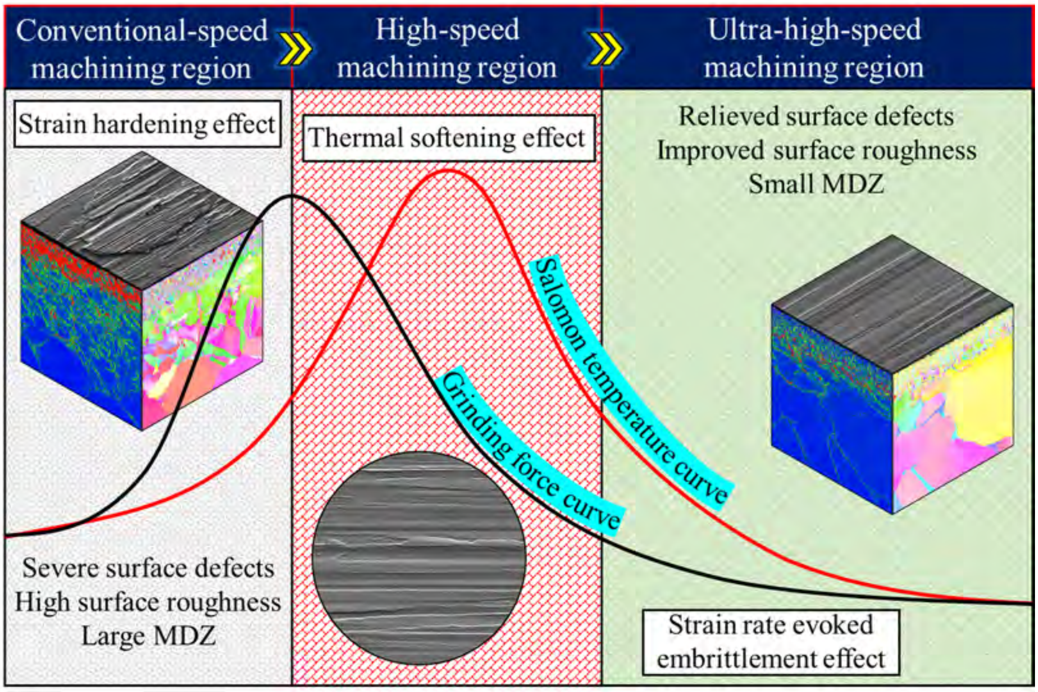

Fig. 7.24 Summary of the surface integrity characteristics and the underlying deformation mechanisms of Ti-alloy at different machining speed regions.

7.7.2 Material Machinability of Wrought and SLM-ed Ti-alloy

The exceptional combination of properties exhibited by Ti-alloys is a double-edged sword. On one hand, it makes Ti-alloys the most advantageous and versatile metal. On the other hand, it also renders them difficult-to-cut materials with lower machinability (Habrat *et al.* 2019). The machinability of a material is influenced by various factors, encompassing both intrinsic and extrinsic elements. Intrinsic factors involve microstructural characteristics (grain size and distribution, texture, presence of inclusions) and material properties (hardness, toughness, and thermal conductivity). The extrinsic factors include machining parameters, the utilization of machining fluids, and the selection of machining tools (Venkata Rao 2006; Zhang *et al.* 2022). Notably, the machinability of a material is a relative concept, as the assessment may vary depending on the criteria adopted for evaluation.

Accordingly, the machinability of wrought and SLM-ed Ti6Al4V was systematically analyzed and compared in terms of surface characteristics, subsurface deformation, and cutting force. Regarding the aspect of ground surfaces, wrought

Ti6Al4V demonstrated lower surface roughness compared to SLM-ed Ti6Al4V. However, it is essential to note that lower surface roughness does not necessarily imply a higher surface quality. In fact, this reduction in roughness was the consequence of severe material smearing. Such smearing defects tended to induce cracks in the subsurface layer, thus adversely affecting the overall service performance of the machined parts. As the machining speed increased, the disparity of surface roughness between wrought and SLM-ed Ti6Al4V diminished due to the relieving of surface defects induced by plastic deformation.

From the aspect of subsurface deformation, it is evident that the depth of MDZ in SLM-ed Ti6Al4V was smaller compared to that in wrought Ti6Al4V under the same conditions. The plastic deformation of a metal material relies on dislocation slip, SLM-ed Ti6Al4V with refined microstructure usually has higher dislocation slip resistance and shorter dislocation mean free path compared to the coarse-grained wrought Ti6Al4V (Cheng *et al.* 2022; Lian *et al.* 2023). Consequently, SLM-ed Ti6Al4V displayed higher brittleness, resulting in a reduced plastic deformation depth in the subsurface region.

Additionally, both wrought and SLM-ed Ti6Al4V exhibited a notably diminished plastic deformation layer when subjected to ultra-high strain rate conditions, primarily attributed to the phenomenon of strain rate evoked embrittlement. During a machining process, plastic deformation consumes a substantial amount of energy from the external loading by tools, with a major portion of this plastic energy being converted into heat, thereby resulting in temperature escalation (Zhou *et al.* 2003). Hence, the reduction of the plastic deformation layer at high grinding speeds contributes to the improvement of surface integrity, but also holds the potential to mitigate the temperature rise during machining. Additionally, the subsurface microstructure evolution is determined by the temperature and mechanical loading history. Inversely, the induced subsurface microstructures influence the subsequent processing (Pan *et al.* 2017). In both wrought and SLM-ed Ti6Al4V, the MDZ underwent significant work-hardening. However, wrought Ti6Al4V exhibited deeper MDZ, which required higher cutting forces and increased energy consumption for its removal in subsequent machining steps, consequently leading to a more pronounced decrease in its machinability.

In terms of grinding forces, due to the commonality of the machining process, both wrought and SLM-ed Ti6Al4V exhibited comparable tendencies in variations of grinding forces as the dominant deformation mechanisms shift. However, distinctions raised due to disparities between the two materials. Primarily, the grinding force of SLM-ed Ti6Al4V was slightly larger than wrought Ti6Al4V when subjected to identical conditions. This disparity was attributed to the higher material strength and hardness inherent to the SLM-ed Ti6Al4V. Meanwhile, the higher material strength and hardness of SLM-ed Ti6Al4V contributed to the severe drastic fluctuations of grinding force as the grinding wheel engaged and disengaged with the workpiece, particularly evident under conditions of severe strain rate hardening. Nevertheless, the wrought Ti6Al4V displayed a higher force ratio, as its enhanced plasticity intensified the plowing effect, consequently resulting in elevated normal grinding forces.

7.8 Conclusions

To achieve high-efficiency and high-quality machining of Ti-alloys, this study conducted systematic investigations on the UHSG of both wrought and SLM-ed Ti6Al4V. The UHSG was carried out at speeds of up to 250 m/s. The surface quality was examined and compared by considering both surface characteristics and subsurface microstructures. The alteration of surface roughness, surface defects, subsurface microstructure distribution and evolution were investigated as the grinding speed increased from conventional levels to the ultra-high-speed regime. Meanwhile, the influence of strain rate and size on UHSG was explored through the examination of variations in grinding force. The major conclusions are summarized as follows:

(1) Elevated grinding speeds led to improved surface quality, characterized by reduced surface roughness and a decrease in surface defects. Surface smearing was the primary defect at low-speed grinding, which tended to induce subsurface cracks. SLM-ed Ti6Al4V exhibited higher surface roughness but fewer surface smearing defects compared to wrought Ti6Al4V;

(2) The MDZ depth in both wrought and SLM-ed Ti6Al4V displayed a consistent downward trend, exhibiting a distinct skin effect as the machining speed increased. Notably, under identical machining conditions, SLM-ed Ti6Al4V demonstrated a smaller MDZ depth compared to the wrought Ti6Al4V due to its higher brittleness;

(3) The subsurface microstructure evolution and distribution were highly dependent on grinding speeds. Under conventional speed conditions, three distinct regions, including DRXZ, TSZ, and PDZ, were observed from the uppermost to the subsurface layer. Notably, the DRX in coarse-grained wrought Ti6Al4V followed the CDRX mechanism, while the DDRX mechanism was evident in SLM-ed Ti6Al4V;

(4) As the grinding speed increased, the plastic deformation was significantly suppressed. The twinning-mediated deformation became the dominant mode as the dislocation slip was inhibited under ultra-high strain rate conditions. And UGENTs structure was produced in the subsurface of both wrought and SLM-ed Ti6Al4V;

(5) Higher material strength and hardness inherent to the SLM-ed Ti6Al4V resulted in a higher grinding force compared to its wrought counterpart. However, the enhanced plasticity of wrought Ti6Al4V intensified the plowing effect, thereby leading to a higher grinding force ratio;

(6) Three speed regions can be classified according to the alteration of surface integrity and the transition of dominant deformation mechanisms. Within the conventional-speed region, the prevailing effect was strain hardening, severe surface defects and deep MDZ tended to be induced. The thermal softening effect took over in the high-speed region, which facilitated the shearing localization and resulted in grinding force reduction. Advancing further to the ultra-high-speed region, strain rate evoking embrittlement became the dominant effect, leading to enhanced surface integrity characterized by relieved surface defects, improved surface roughness, and small MDZ.

Chapter 8 Conclusions and Future Research

8.1 Overall Discussion and Conclusions

The manufacturing and processing of high-performance parts are a longstanding aspiration within the realm of engineering. This thesis commences with a comprehensive investigation of SLM manufacturing of Ti6Al4V alloy to achieve the production of strong and ductile Ti6Al4V parts. Subsequently, UHSM was applied to achieve high-efficiency and high-quality processing of both wrought and SLM-ed Ti6Al4V alloys. The material removal and deformation mechanisms across various speed regions were revealed by systematic SPS experiments. Furthermore, an extensive investigation was conducted to study the surface integrity and machining characteristics of Ti6Al4V alloys in UHSG.

The fundamental origin of strength-ductility trade-off dilemma in SLM-ed Ti6Al4V can be attributed to the presence of defects and non-equilibrium microstructure, which are highly correlated with input energy density. Therefore, to address the strength-ductility trade-off dilemma in SLM-ed Ti6Al4V, this study conducted systematic investigations in terms of process, structure, and property to reveal densification behaviors, defect formation mechanism, microstructure evolution mechanism, and mechanical properties variation of SLM-ed Ti6Al4V at different energy densities.

The densification map and process map were developed through systematic process optimizations. It is demonstrated that defect-free Ti6Al4V parts can be manufactured within the optimized process window around 65 J/mm^3. The microstructure showed a transition from lamellar α+β to fully martensitic α' with the decrease of E_d. An ultrafine lamellar α+β microstructure, characterized by an average α-lath thickness of 282 nm, was generated at the E_d of 76 J/mm^3. Both the high relative density and the advanced microstructure contributed to the exceptional performance of SLM-ed Ti6Al4V, resulting in a remarkable tensile strength of 1,390 MPa and an elongation of 9.66%.

Ti-alloy is a typical difficult-to-machine material with a low machinability associated with its inherent material properties such as high specific strength, low thermal conductivity, high chemical reactivity, and low elastic modulus. Severe surface defects and subsurface damage tend to be induced in conventional machining methods due to high machining force, elevated machining temperature, and rapid tool wear. Therefore, in the present study, UHSM was applied to address the machining problems in the machining of Ti-alloy.

In the UHSM of coarse-grained wrought Ti6Al4V, the material removal and deformation mechanisms were revealed by combining SPS experiments and FEM simulations. The surface creation, subsurface deformation, and chip formation of wrought Ti6Al4V under speeds ranging from 20 to 220 m/s were systematically investigated. The results indicated that the pile-up induced by material accumulation can be effectively inhibited at elevated machining speeds. Meanwhile, the MDZ showed a distinctive “skin effect” with the increase of machining speed. At conventional machining speeds, the MDZ consisted of DRXZ and PDZ from the top surface to subsurface. The dominant deformation mechanism transited from dislocation-mediated deformation to twinning-mediated deformation under UHSM conditions, with only a DITZ being produced in the subsurface. A novel microstructure referred to as UGENTs was generated under ultra-high strain rate conditions, and a new microstructure evolution mechanism was proposed to describe its evolution. Additionally, the chip formation process also exhibits a dependency on machining speed, as evidenced by the transformation from segmented chips to fragmented chips with the increasing machining speed, which also indicates the shift of material removal mechanisms.

Based on the theoretical basis and research methods developed in the UHSM of coarse-grained wrought Ti6Al4V, the material removal and deformation mechanisms of SLM-ed Ti6Al4V were also comprehensively investigated. Similar to wrought Ti6Al4V, SLM-ed Ti6Al4V also demonstrated a decrease in the pile-up ratio as machining speed increases, but less material accumulation was observed due to the higher brittleness of SLM-ed Ti6Al4V. Moreover, the MDZ was shallower in SLM-ed Ti6Al4V compared with wrought Ti6Al4V under similar condition. The transition from dislocation slip to twinning also existed in SLM-ed Ti6Al4V at very high strain rate conditions, which governs the microstructure evolution at different machining conditions. Significant distinctions were evident in chip formation between wrought and SLM-ed Ti6Al4V. The critical speed of segmented chips was higher in SLM-ed Ti6Al4V due to different chip formation mechanisms. In wrought Ti6Al4V, the initiation of segmented chips was triggered by phase transformations, whereas in SLM-ed Ti6Al4V, the primary driving force was the relative slip along the lath boundaries.

After clarifying the material removal mechanisms of Ti-alloys, the corresponding theories were employed to the UHSG process. A UHSG system was devised to realize UHSG machining with a maximum linear speed up to 250 m/s. A comprehensive analysis was carried out to evaluate the surface integrity considering both surface and subsurface characteristics. The results indicate that enhanced surface quality can be achieved at higher grinding speeds due to the reduction in surface defects. In comparison to wrought Ti6Al4V, SLM-ed Ti6Al4V displayed higher surface roughness but fewer surface smearing defects. The skin effect of MDZ was observed in both wrought and SLM-ed Ti6Al4V. Notably, SLM-ed Ti6Al4V exhibited a smaller MDZ depth owing to its increased brittleness.

Compared with SPS, the microstructure evolution in a grinding process showed visible alterations. For instance, the MDZ was relatively deeper in the grinding process due to the induced surface defects. The MDZ was divided into three zones under conventional speed conditions, namely DRXZ, TSZ, and PDZ. Additionally, the PDZ disappeared in SPS at 220 m/s. However, a small PDZ still existed in UHSG as the grinding speed was elevated to 250 m/s. This phenomenon can be ascribed to the successive cutting effects by numerous abrasive particles during a grinding process.

From the aspect of grinding force, both wrought and SLM-ed Ti6Al4V exhibited an initial upward followed by a subsequent decrease in grinding force. Compared with wrought Ti6Al4V, SLM-ed Ti6Al4V showed higher grinding forces but a lower grinding force ratio due to its higher material strength and hardness. Overall, based on the surface integrity and machining characteristics of Ti-alloys, the speed regions can be categorized into three distinct regions. In the realm of conventional speeds, strain hardening served as the dominant factor, leading to severe surface defects and deep MDZ. As the speed entered the high-speed range, the thermal softening effect played the leading role, facilitating shear localization and rapid reduction in grinding force. In the ultra-high-speed region, the dominant factor shifted to strain rate evoked embrittlement, which enhanced the surface integrity by reducing surface defects and MDZ.

In conclusion, this thesis conducted original research on SLM manufacturing and UHSM processing of high-performance Ti-alloy parts. It addressed the strength-ductility trade-off dilemma by in-situ tailoring of process parameters and microstructure, achieving the manufacturing of strong and ductile Ti6Al4V by SLM technique; The study revealed and compared the material removal and deformation mechanisms of both wrought and SLM-ed Ti6Al4V in various speed regions; Additionally, it established the interrelationship between surface integrity/machinability and grinding speeds. These findings provide a scientific theoretical foundation and valuable guidance for the manufacturing and processing of high-performance parts.

8.2 Suggestions for Future Research

This thesis focuses on the SLM manufacturing of Ti6Al4V and the UHSM of both wrought and SLM-ed Ti6Al4V. The process-structure-property relationship of SLM-ed Ti6Al4V, material removal/deformation mechanisms and surface integrity of both Ti6Al4V alloys are systematically revealed. Nevertheless, there are still significant concerns that require in-depth exploration to facilitate the industrial application of SLM-ed Ti6Al4V and to enhance our comprehensive understanding of the machining mechanisms underlying UHSM, particularly for difficult-to-machine materials. The summarized suggestions for potential research topics in related areas are as follows:

(1) Molecular dynamics (MD) simulation of high strain rate deformation: Current

experimental methods cannot directly observe the micro/nano-scale material responses under high strain rate conditions. Fortunately, the MD simulation can offer a powerful tool to investigate high-strain rate deformation due to its ability to provide atomic-level insights and access extreme conditions. It will enhance our understanding of the effect of strain rate on the material deformation and removal mechanism by systematically investigating material dynamics such as dislocation motion, dislocation–lattice interaction, dislocation/twin transition through MD simulations;

(2) Establishing material constitutive model suitable for UHSM: An accurate material constitutive model is a prerequisite for numerical simulation of the machining process. However, conventional material constitutive models are usually suitable for material deformation under a strain rate smaller than 10^6 s^{-1}. Therefore, new material constitutive model and constitutive parameters suitable for UHSM are urgent to be established;

(3) Tool wear comparison at different machining speeds: Severe tool wear is a critical issue in the conventional machining of Ti-alloys. Under UHSM conditions, the reduced machining force and the material embrittlement effect have the potential effect to mitigate the tool wear. Systematic evaluations are needed to compare the tool wear mechanism and state across conventional speed to ultra-high-speed conditions;

(4) Temperature measurement in UHSM: The temperature analysis within the machining zone is critical for the in-depth investigation of microstructure evolution and material deformation during a machining process. Nevertheless, the duration time scale and machining scale in UHSM are very small, and the conventional methods such as thermocouples or infrared thermal imager are difficult to accurately measure the temperature in the machining zone. Therefore, reliable and accurate methods for measuring the machining temperature are urgently required for future research;

(5) The material property detection of MDZ composing UGENTs microstructure: A

novel microstructure referred to as UGENTs is generated in the MDZ in Ti6Al4V alloy under ultra-high strain rate machining. This hierarchical microstructure is of great interest to enhance the material strength and ductility by combining the grain refinement strengthening and twinning-induced plasticity. However, direct property test is difficult as the thickness of MDZ is very small, therefore advanced test approach like micropillar compression is recommended to accurately detect the material property of MDZ composing UGENTs microstructure;

(6) Evaluating the service performance of parts after UHSM: Although the surface integrity and subsurface damage of Ti6Al4V alloys have been improved after UHSM, the service performance of machined parts, such as reliability and durability, needs to be tested to verify the advantages of UHSM.

References

Abukhshim N. A., Mativenga P. T. and Sheikh M. A. (2006). "Heat generation and temperature prediction in metal cutting: A review and implications for high speed machining." International Journal of Machine Tools and Manufacture **46**(7): 782-800.

Agrawal C., Wadhwa J., Pitroda A., Pruncu C. I., Sarikaya M. and Khanna N. (2021). "Comprehensive analysis of tool wear, tool life, surface roughness, costing and carbon emissions in turning Ti–6Al–4V titanium alloy: Cryogenic versus wet machining." Tribology International **153**: 106597.

Akcan S., Shah W. S., Moylan S. P., Chandrasekar S., Chhabra P. N. and Yang H. T. Y. (2002). "Formation of white layers in steels by machining and their characteristics." Metallurgical and Materials Transactions A **33**(4): 1245-1254.

Al-Rubaie K. S., Melotti S., Rabelo A., Paiva J. M., Elbestawi M. A. and Veldhuis S. C. (2020). "Machinability of SLM-produced Ti6Al4V titanium alloy parts." Journal of Manufacturing Processes **57**: 768-786.

Antonysamy A., Meyer J. and Prangnell P. (2013). "Effect of build geometry on the β-grain structure and texture in additive manufacture of Ti6Al4V by selective electron beam melting." Materials Characterization **84**: 153–168.

Aramcharoen A., Mativenga P. T., Group M. and Technology L. P. J. I. J. o. A. M. (2008). "White layer formation and hardening effects in hard turning of H13 tool steel with CrTiAlN and CrTiAlN/MoST-coated carbide tools." **36**(7-8): 650-657.

Armstrong M., Mehrabi H. and Naveed N. (2022). "An overview of modern metal additive manufacturing technology." Journal of Manufacturing Processes **84**: 1001-1029.

Arndt G. (1973). "Ultra-High-Speed Machining: A Review and an Analysis of Cutting Forces." ARCHIVE Proceedings of the Institution of Mechanical Engineers **187**(1973): 625-634.

Backer W., Marshall E. and Shaw M. (1952). "The size effect in metal cutting." Transactions of the American Society of Mechanical Engineers **74**(1): 61-71.

Bayat M., Thanki A., Mohanty S., Witvrouw A., Yang S., Thorborg J., Tiedje N. S. and

Hattel J. H. (2019). "Keyhole-induced porosities in Laser-based Powder Bed Fusion (L-PBF) of Ti6Al4V: High-fidelity modelling and experimental validation." Additive Manufacturing **30**: 100835.

Bertrand E., Castany P., Péron I. and Gloriant T. (2011). "Twinning system selection in a metastable β-titanium alloy by Schmid factor analysis." Scripta Materialia **64**(12): 1110-1113.

Bi Z., Tokura H. and Yoshikawa M. J. J. o. M. S. (1988). "Study on surface cracking of alumina scratched by single-point diamonds." **23**(9): 3214-3224.

Bourell D., Kruth J. P., Leu M., Levy G., Rosen D., Beese A. M. and Clare A. J. C. a. (2017). "Materials for additive manufacturing." **66**(2): 659-681.

Bracke L., Verbeken K., Kestens L. and Penning J. (2009). "Microstructure and texture evolution during cold rolling and annealing of a high Mn TWIP steel." Acta Materialia **57**(5): 1512-1524.

Brown M., Crawforth P., M'Saoubi R., Larsson T., Wynne B., Mantle A. and Ghadbeigi H. (2019). "Quantitative characterization of machining-induced white layers in Ti–6Al–4V." Materials Science and Engineering: A **764**: 138220.

Brown M., M’Saoubi R., Crawforth P., Mantle A., McGourlay J. and Ghadbeigi H. (2022). "On deformation characterisation of machined surfaces and machining-induced white layers in a milled titanium alloy." Journal of Materials Processing Technology **299**: 117378.

Cai T., Zhang Z., Zhang P., Yang J. B. and Zhang Z. (2014). "Competition between slip and twinning in face-centered cubic metals." Journal of Applied Physics **116**: 163512.

Cain V., Thijs L., Humbeeck J. V. and Hooreweder B. V. (2015). "Crack propagation and fracture toughness of Ti6Al4V alloy produced by selective laser melting." Additive Manufacturing **5**: 68-76.

Calamaz M., Coupard D. and Girot F. (2008). "A new material model for 2D numerical simulation of serrated chip formation when machining titanium alloy Ti–6Al–4V." International Journal of Machine Tools and Manufacture **48**(3): 275-288.

Cao S., Chen Z., Lim C. V. S., Yang K., Jia Q., Jarvis T., Tomus D. and Wu X. (2017).

"Defect, microstructure, and mechanical property of Ti-6Al-4V alloy fabricated by high-power selective laser melting." The Journal of The Minerals, Metals & Materials Society **69**(12): 2684-2692.

Cao Y., Li N., Luo Y., Tang H., Xie Q. and Fu A. (2022). "A novel ultra-high strength titanium alloy via hierarchical α/α′ precipitation strengthening." Materials Science and Engineering: A **840**: 142878.

Chen C., Yin J., Zhu H., Xiao Z., Zhang L. and Zeng X. (2019). "Effect of overlap rate and pattern on residual stress in selective laser melting." International Journal of Machine Tools and Manufacture **145**: 103433.

Chen J., Fang Q. and Li P. (2015). "Effect of grinding wheel spindle vibration on surface roughness and subsurface damage in brittle material grinding." International Journal of Machine Tools and Manufacture **91**: 12-23.

Chen M., Ma E., Hemker K. J., Sheng H., Wang Y. and Cheng X. J. S. (2003). "Deformation twinning in nanocrystalline aluminum." **300**(5623): 1275-1277.

Chen Z., Wu X., Tomus D. and Davies C. H. J. (2018). "Surface roughness of Selective Laser Melted Ti-6Al-4V alloy components." Additive Manufacturing **21**: 91-103.

Cheng J., Fernandez-Zelaia P., Hu X. and Kirka M. (2022). "Effect of microstructure on fatigue crack propagation in additive manufactured nickel-based superalloy Haynes 282: an experiment and crystal plasticity study." Journal of Materials Science **57**(21): 9741-9768.

Chou Y. K. and Evans C. J. (1999). "White layers and thermal modeling of hard turned surfaces." International Journal of Machine Tools and Manufacture **39**(12): 1863-1881.

Coghe F., Tirry W., Rabet L., Schryvers D. and Van Houtte P. (2012). "Importance of twinning in static and dynamic compression of a Ti–6Al–4V titanium alloy with an equiaxed microstructure." Materials Science and Engineering: A **537**: 1-10.

Crocker A. G. and Bevis M. (1970). "The crystallography of deformation twinning in titanium". In R. I. Jaffee and Promisel N. E. (Eds.), The Science, Technology and Application of Titanium (pp. 453-458): Pergamon.

Cui C., Hu B., Zhao L. and Liu S. (2011). "Titanium alloy production technology, market prospects and industry development." Materials & Design **32**(3): 1684-1691.

Dai L. and Song W. (2022). "A strain rate and temperature-dependent crystal plasticity model for hexagonal close-packed (HCP) materials: Application to α-titanium." International Journal of Plasticity **154**: 103281.

Darnbrough J. E., Roebuck B. and Flewitt P. E. J. J. J. o. A. P. (2015). "The influence of temperature and grain boundary volume on the resistivity of nanocrystalline nickel." **118**(18): 675-620.

Denkena B., Ben Amor R., De Leon-Garcia L. and Dege J. (2007). "Material specific definition of the high speed cutting range." International Journal of Machining Machinability of Materials **2**(2): 176-185.

Dewes R. C., Ng E., Chua K. S., Newton P. G. and Aspinwall D. K. (1999). "Temperature measurement when high speed machining hardened mould/die steel." Journal of Materials Processing Technology **92-93**: 293-301.

Dilberoglu U. M., Gharehpapagh B., Yaman U. and Dolen M. (2017). "The role of additive manufacturing in the era of industry 4.0." Procedia Manufacturing **11**: 545-554.

Dong Y., Ning J., Dong P., Ren Y. and Zhao S. (2020). "Investigation of Fracture Behavior and Mechanism in High-Speed Precise Shearing for Metal Bars with Prefabricated Fracture-Start Kerfs." Materials **13**(18).

Du J., Zhang Z., Liu Y., Shao Q., Zhang A., Xiong S. and Liu F. (2023). "Strength-ductility trade-off modulated by thermo-kinetic synergy of heat-treatable aluminum alloys." Journal of Materials Research and Technology **24**: 7876-7895.

Durai Murugan P., Vijayananth S., Natarajan M. P., Jayabalakrishnan D., Arul K., Jayaseelan V. and Elanchezhian J. (2022). "A current state of metal additive manufacturing methods: A review." Materials Today: Proceedings **59**: 1277-1283.

Edwards M. (2006). "Properties of metals at high rates of strain." Materials scienceand technology **22**(4): 453-462.

Facchini L., Magalini E., Robotti P., Molinari A., Höges S. and Wissenbach K. (2010). "Ductility of a Ti-6Al-4V alloy produced by selective laser melting of prealloyed powders." Rapid Prototyping Journal **16**(6): 450-459.

Fang Z. C., Wu Z. L., Huang C. G. and Wu C. W. (2020). "Review on residual stress in selective laser melting additive manufacturing of alloy parts." Optics & Laser Technology **129**: 106283.

Fu J., Hu Z., Song X., Zhai W., Long Y., Li H. and Fu M. (2020). "Micro selective laser melting of NiTi shape memory alloy: Defects, microstructures and thermal/mechanical properties." Optics & Laser Technology **131**: 106374.

Gao C. and Iwamoto T. (2021). "Measurement of transient temperature at super-high-speed deformation." International Journal of Mechanical Sciences **206**: 106626.

Gao Y. F., Zhang W., Shi P. J., Ren W. L. and Zhong Y. B. (2020). "A mechanistic interpretation of the strength-ductility trade-off and synergy in lamellar microstructures." Materials Today Advances **8**: 100103.

George J., Philip J. T., Mathew J. and Manu R. (2022). "Prediction and analysis of material removal rate and white layer thickness during wire electrical discharge turning (WEDT) process." CIRP Journal of Manufacturing Science and Technology **39**: 210-222.

George T. G. I. (2012). "High-Strain-Rate Deformation: Mechanical Behavior and Deformation Substructures Induced." Annual Review of Materials Research **42**(1): 285-303.

Gibson I., Rosen D. and Stucker B. (2015). "Additive Manufacturing Technologies." Additive Manufacturing Technologies.

Gong H., Rafi K., Gu H., Starr T. and Stucker B. (2014). "Analysis of defect generation in Ti–6Al–4V parts made using powder bed fusion additive manufacturing processes." Additive Manufacturing **1-4**: 87-98.

Gray G. T. (1988). "Deformation twinning in Al-4.8 wt% Mg." Acta Metallurgica **36**(7): 1745-1754.

Greitemeier D., Dalle Donne C., Syassen F., Eufinger J. and Melz T. (2016). "Effect of surface roughness on fatigue performance of additive manufactured Ti–6Al–4V." Materials Science and Technology **32**(7): 629-634.

Griffiths B. J. (1987). "Mechanisms of White Layer Generation With Reference to

Machining and Deformation Processes." Journal of Tribology **109**(3): 525-530.

Gu L., Kang G., Chen H. and Wang M. (2016). "On adiabatic shear fracture in high-speed machining of martensitic precipitation-hardening stainless steel." Journal of Materials Processing Technology **234**: 208-216.

Guerra-Yánez H., Florido-Suárez N. R., Voiculescu I. and Mirza-Rosca J. C. (2023). "Corrosion behavior of new titanium alloys for medical applications." Materials Today: Proceedings **72**: 533-537.

Guo S., Lu S., Zhang B. and Cheung C. F. (2022). "Surface integrity and material removal mechanisms in high-speed grinding of Al/SiCp metal matrix composites." International Journal of Machine Tools and Manufacture **178**: 103906.

Guo S., Zhang J., Jiang Q. and Zhang B. (2022). "Surface integrity in high-speed grinding of Al6061T6 alloy." CIRP Annals **71**(1): 281-284.

Guo W., Su J., Lu W., Liebscher C. H., Kirchlechner C., Ikeda Y., Körmann F., Liu X., Xue Y. and Dehm G. (2020). "Dislocation-induced breakthrough of strength and ductility trade-off in a non-equiatomic high-entropy alloy." Acta Materialia **185**: 45-54.

Gurrutxaga-Lerma B., Balint D. S., Dini D. and Sutton A. P. (2015). "The mechanisms governing the activation of dislocation sources in aluminum at different strain rates." Journal of the Mechanics and Physics of Solids **84**: 273-292.

Gurrutxaga–Lerma B., Verschueren J., Sutton A. P. and Dini D. (2021). "The mechanics and physics of high-speed dislocations: a critical review." International Materials Reviews **66**(4): 215-255.

Guy S. and Gary L. (2013). "Very high speed cutting of Ti-6Al-4V titanium alloy - Change in morphology and mechanism of chip formation." International Journal of Machine Tools and Manufacture **66**: 37–43.

Habrat W., Markopoulos A. P., Motyka M. and Sieniawski J. (2019). "Chapter 11 - Machinability". In H. Garbacz, Semenova I. P., Zherebtsov S. and Motyka M. (Eds.), Nanocrystalline Titanium (pp. 209-236): Elsevier.

Han J., Yang J., Yu H., Yin J., Gao M., Wang Z. and Zeng X. (2017). "Microstructure and mechanical property of selective laser melted Ti6Al4V dependence on laser energy density." Rapid Prototyping Journal **23**(2): 217-226.

Han Q., Li J. and Yi X. (2023). "Overcoming strength–ductility trade-off of nanocrystalline metals by engineering grain boundary, texture, and gradient microstructure." Journal of the Mechanics and Physics of Solids **173**: 105200.

He B., Wu W., Zhang L., Lu L., Yang Q., Long Q. and Kun C. (2018). "Microstructural characteristic and mechanical property of Ti6Al4V alloy fabricated by selective laser melting." Vacuum **150**: 79-83.

He J., Li D., Jiang W., Ke L., Qin G., Ye Y., Qin Q. and Qiu D. (2019). "The Martensitic Transformation and Mechanical Properties of Ti6Al4V Prepared via Selective Laser Melting." Materials **12**(2): 321.

Hiratani M. and Nadgorny E. M. (2001). "Combined model of dislocation motion with thermally activated and drag-dependent stages." Acta Materialia **49**(20): 4337-4346.

Hollander D. A., Walter M. V., Wirtz T., Sellei R., Schmidt-Rohlfing B., Paar O. and Erli H. J. (2006). "Structural, mechanical and in vitro characterization of individually structured Ti-6Al-4V produced by direct laser forming." Biomaterials **27**(7): 955-963.

Hopkinson N. and Mumtaz K. "Top surface and side roughness of Inconel 625 parts processed using selective laser melting." Rapid Prototyping Journal **2009**(15): 96-103.

Hu H., Xu Z., Dou W. and Huang F. (2020). "Effects of strain rate and stress state on mechanical properties of Ti-6Al-4V alloy." International Journal of Impact Engineering **145**: 103689.

Huang K. and Logé R. E. (2016). "A review of dynamic recrystallization phenomena in metallic materials." Materials & Design **111**: 548-574.

Jamil M., He N., Gupta M. K., Zhao W. and Khan A. M. (2022). "Tool wear mechanisms and its influence on machining tribology of face milled titanium alloy under sustainable hybrid lubri-cooling." Tribology International **170**: 107497.

Javidi A., Rieger U. and Eichlseder W. (2008). "The effect of machining on the surface integrity and fatigue life." International Journal of Fatigue **30**(10): 2050-2055.

Jiang Q., Li S., Guo S., Fu M. and Zhang B. (2023). "Comparative study on process-structure-property relationships of TiC/Ti6Al4V and Ti6Al4V by selective laser melting." International Journal of Mechanical Sciences **241**: 107963.

Johnson G. R. and Cook W. H. (1985). "Fracture characteristics of three metals subjected to various strains, strain rates, temperatures and pressures." Engineering Fracture Mechanics **21**(1): 31-48.

Jung H., Hayasaka T., Shamoto E. and Xu L. (2020). "Suppression of forced vibration due to chip segmentation in ultrasonic elliptical vibration cutting of titanium alloy Ti–6Al–4V." Precision Engineering **64**: 98-107.

Kalantari O., Jafarian F. and Fallah M. M. (2021). "Comparative investigation of surface integrity in laser assisted and conventional machining of Ti-6Al-4 V alloy." Journal of Manufacturing Processes **62**: 90-98.

Karimi J., Suryanarayana C., Okulov I. and Prashanth K. G. (2021). "Selective laser melting of Ti6Al4V: Effect of laser re-melting." Materials Science and Engineering: A **805**: 140558.

Khairallah S. A., Martin A. A., Lee J. R., Guss G., Calta N. P., Hammons J. A., Nielsen M. H., Chaput K., Schwalbach E. and Shah M. N. (2020). "Controlling interdependent meso-nanosecond dynamics and defect generation in metal 3D printing." Science **368**(6491): 660-665.

Khaliq W., Zhang C., Jamil M. and Khan A. M. (2020). "Tool wear, surface quality, and residual stresses analysis of micro-machined additive manufactured Ti–6Al–4V under dry and MQL conditions." Tribology International **151**: 106408.

Khanna N., Zadafiya K., Patel T., Kaynak Y., Rahman Rashid R. A. and Vafadar A. (2021). "Review on machining of additively manufactured nickel and titanium alloys." Journal of Materials Research and Technology **15**: 3192-3221.

Kim S., Kim H., Kang K. and Kim S. Y. (2020). "Relativistic effect inducing drag on fast-moving dislocation in discrete system." International Journal of Plasticity **126**: 102629.

Kishawy H. and Elbestawi M. (2001). "Tool wear and surface integrity during high-speed turning of hardened steel with polycrystalline cubic boron nitride tools." Proceedings of the Institution of Mechanical Engineers, Part B: Journal of Engineering

Manufacture **215**(6): 755-767.

Kishawy H. A., Nguyen N., Hosseini A. and Elbestawi M. (2023). "Machining characteristics of additively manufactured titanium, cutting mechanics and chip morphology." CIRP Annals **72**(1): 49-52.

Kitagawa T., Kubo A. and Maekawa K. (1997). "Temperature and wear of cutting tools in high-speed machining of Inconel 718 and Ti 6Al 6V 2Sn." Wear **202**(2): 142-148.

Kobryn P. A. and Semiatin S. L. (2001). "The laser additive manufacture of Ti-6Al-4V." JOM Journal of the Minerals Metals and Materials Society **53**(9): 40-42.

Komanduri R. and Reed Jr W. (1983). "Evaluation of carbide grades and a new cutting geometry for machining titanium alloys." Wear **92**(1): 113-123.

Kumar P., Prakash O. and Ramamurty U. (2018). "Micro-and meso-structures and their influence on mechanical properties of selectively laser melted Ti-6Al-4V." Acta Materialia **154**: 246-260.

Kuntoğlu M., Salur E., Canli E., Aslan A., Gupta M. K., Waqar S., Krolczyk G. M. and Xu J. (2023). "A state of the art on surface morphology of selective laser-melted metallic alloys." The International Journal of Advanced Manufacturing Technology **127**(3): 1103-1142.

Kuruc M., Vopát T., Peterka J., Necpal M., Šimna V., Milde J. and Jurina F. (2022). "The influence of cutting parameters on plastic deformation and chip compression during the turning of C45 medium carbon steel and 62SiMnCr4 tool steel." Materials **15**(2): 585.

la Monaca A., Axinte D. A., Liao Z., M'Saoubi R. and Hardy M. C. (2022). "Temperature-dependent shear localisation and microstructural evolution in machining of nickel-base superalloys." Materials & Design **219**: 110792.

la Monaca A., Murray J. W., Liao Z., Speidel A., Robles-Linares J. A., Axinte D. A., Hardy M. C. and Clare A. T. (2021). "Surface integrity in metal machining - Part II: Functional performance." International Journal of Machine Tools and Manufacture **164**: 103718.

Le Coz G., Piquard R., D'Acunto A., Bouscaud D., Fischer M. and Laheurte P. (2020). "Precision turning analysis of Ti-6Al-4V skin produced by selective laser melting using a design of experiment approach." The International Journal of Advanced Manufacturing Technology **110**: 1615-1625.

Lee W.-S., Lin C.-F. and Liu T.-J. (2007). "Impact and fracture response of sintered 316L stainless steel subjected to high strain rate loading." Materials Characterization **58**(4): 363-370.

Lewandowski J. J. and Seifi M. (2016). "Metal Additive Manufacturing: A Review of Mechanical Properties." Annual Review of Materials Research **46**: 151–186.

Li B., Zhang S., Du J. and Sun Y. (2022). "State-of-the-art in cutting performance and surface integrity considering tool edge micro-geometry in metal cutting process." Journal of Manufacturing Processes **77**: 380-411.

Li G., Chandra S., Rahman Rashid R. A., Palanisamy S. and Ding S. (2022). "Machinability of additively manufactured titanium alloys: A comprehensive review." Journal of Manufacturing Processes **75**: 72-99.

Li G., Ma F., Liu P., Qi S., Li W., Zhang K. and Chen X. (2023). "Review of micro-arc oxidation of titanium alloys: Mechanism, properties and applications." Journal of Alloys and Compounds **948**: 169773.

Li G., Xu W., Jin X., Liu L., Ding S. and Li C. (2023). "The machinability of stainless steel 316 L fabricated by selective laser melting: Typical cutting responses, white layer and evolution of chip morphology." Journal of Materials Processing Technology **315**: 117926.

Li J., Xie D. Y., Xue S., Fan C., Chen Y., Wang H., Wang J. and Zhang X. (2018). "Superior twin stability and radiation resistance of nanotwinned Ag solid solution alloy." Acta Materialia **151**: 395-405.

Li K., Yang T., Gong N., Wu J., Wu X., Zhang D. Z. and Murr L. E. (2023). "Additive manufacturing of ultra-high strength steels: A review." Journal of Alloys and Compounds **965**: 171390.

Li L., Zhang Z., Zhang P. and Zhang Z. (2023). "A review on the fatigue cracking of twin boundaries: Crystallographic orientation and stacking fault energy." Progress in Materials Science **131**: 101011.

Li M., Karpuschewski B., Ohmori H., Riemer O., Wang Y. and Dong T. (2021). "Adaptive shearing-gradient thickening polishing (AS-GTP) and subsurface damage inhibition." International Journal of Machine Tools and Manufacture **160**: 103651.

Li X., Zhang Z. and Wang J. (2023). "Deformation twinning in body-centered cubic metals and alloys." Progress in Materials Science: 101160.

Lian F., Chen L., Wu C., Zhao Z., Tang J. and Zhu J. (2023). "Selective Laser Melting Additive Manufactured Tantalum: Effect of Microstructure and Impurities on the Strengthening-Toughing Mechanism." Materials **16**(8): 3161.

Liang X. and Liu Z. (2017). "Experimental investigations on effects of tool flank wear on surface integrity during orthogonal dry cutting of Ti-6Al-4V." The International Journal of Advanced Manufacturing Technology **93**(5): 1617-1626.

Liang X., Liu Z. and Wang B. (2020). "Dynamic recrystallization characterization in Ti-6Al-4V machined surface layer with process-microstructure-property correlations." Applied Surface Science **530**: 147184.

Liang X., Liu Z. and Wang B. (2019). "State-of-the-art of surface integrity induced by tool wear effects in machining process of titanium and nickel alloys: A review." Measurement **132**: 150-181.

Liao Z., la Monaca A., Murray J., Speidel A., Ushmaev D., Clare A., Axinte D. and M'Saoubi R. (2021). "Surface integrity in metal machining - Part I: Fundamentals of surface characteristics and formation mechanisms." International Journal of Machine Tools and Manufacture **162**: 103687.

Liao Z., Polyakov M., Diaz O. G., Axinte D., Mohanty G., Maeder X., Michler J. and Hardy M. (2019). "Grain refinement mechanism of nickel-based superalloy by severe plastic deformation - Mechanical machining case." Acta Materialia **180**: 2-14.

Liu C. and Ahrens T. (1997). "Stress wave attenuation in shock-damaged rock." Journal of Geophysical Research: Solid Earth **102**(B3): 5243-5250.

Liu J., Sun Q., Zhou C. A., Wang X., Li H., Guo K. and Sun J. (2019). "Achieving

Ti6Al4V alloys with both high strength and ductility via selective laser melting." Materials Science and Engineering: A **766**: 138319.

Liu M., Wang P., Lu G., Huang C.-Y., You Z., Wang C.-H. and Yen H.-W. (2022). "Deformation-activated recrystallization twin: New twinning path in pure aluminum enabled by cryogenic and rapid compression." iScience **25**(5): 104248.

Liu Y., Lu C., Wang H., Tieu A. K. and Liu B. (2020). "Microstructure evolution, lattice rotation retardation and grain orientation fragmentation in commercial purity aluminium deformed by high pressure torsion." Journal of Materials Research and Technology **9**(3): 6642-6654.

Liu Y., Yang Y. and Wang D. (2016). "A study on the residual stress during selective laser melting (SLM) of metallic powder." International Journal of Advanced Manufacturing Technology **87**(1-4): 1-10.

Liu Z., Xu J., Han S. and Chen M. (2013). "A coupling method of response surfaces (CRSM) for cutting parameters optimization in machining titanium alloy under minimum quantity lubrication (MQL) condition." International Journal of Precision Engineering Manufacturing **14**: 693-702.

Longbottom J. M. and Lanham J. D. (2006). "A review of research related to Salomon's hypothesis on cutting speeds and temperatures." International Journal of Machine Tools and Manufacture **46**(14): 1740-1747.

Lu J. and Zhuo L. (2023). "Additive manufacturing of titanium alloys via selective laser melting: Fabrication, microstructure, post-processing, performance and prospect." International Journal of Refractory Metals and Hard Materials **111**: 106110.

Luqman M., Ali Y., Zaghloul M. M. Y., Sheikh F. A., Chan V. and Abdal-hay A. (2023). "Grain refinement mechanism and its effect on mechanical properties and biodegradation behaviors of Zn alloys – A review." Journal of Materials Research and Technology **24**: 7338-7365.

Ma W., Chen X. and Shuang F. (2017). "The chip-flow behaviors and formation mechanisms in the orthogonal cutting process of Ti6Al4V alloy." Journal of the Mechanics and Physics of Solids **98**: 245-270.

Malakizadi A., Mallipeddi D., Dadbakhsh S., M'Saoubi R. and Krajnik P. (2022). "Post-processing of additively manufactured metallic alloys – A review." International Journal of Machine Tools and Manufacture **179**: 103908.

Mele M., Bergmann A., Campana G. and Pilz T. (2021). "Experimental investigation into the effect of supports and overhangs on accuracy and roughness in laser powder bed fusion." Optics & Laser Technology **140**: 107024.

Meng L. X., Yang H. J., Ben D. D., Ji H. B., Lian D. L., Ren D. C., Li Y., Bai T. S., Cai Y. S., Chen J., Yi J. L., Wang L., Yang J. B. and Zhang Z. F. (2022). "Effects of defects and microstructures on tensile properties of selective laser melted Ti6Al4V alloys fabricated in the optimal process zone." Materials Science and Engineering: A **830**: 142294.

Meyers M. A., Vöhringer O. and Lubarda V. A. (2001). "The onset of twinning in metals: a constitutive description." Acta Materialia **49**(19): 4025-4039.

Mills M. J. and Neeraj T. (2001). "Dislocations in Metals and Metallic Alloys". In K. H. J. Buschow, Cahn R. W., Flemings M. C., Ilschner B., Kramer E. J., Mahajan S. and Veyssière P. (Eds.), Encyclopedia of Materials: Science and Technology (pp. 2278-2291). Oxford: Elsevier.

Ming W., Chen J., An Q. and Chen M. (2019). "Dynamic mechanical properties and machinability characteristics of selective laser melted and forged Ti6Al4V." Journal of Materials Processing Technology **271**: 284-292.

Mishra S. K., Talwar D., Singh K., Chopra A., Ghosh S. and Aravindan S. (2021). "Micromechanical characterization and dynamic wear study of DC-Arc coated cemented carbide cutting tools for dry titanium turning." Ceramics International **47**(22): 31798-31810.

Mogilevsky M. and Newman P. (1983). "Mechanisms of deformation under shock loading." Physics Reports **97**(6): 357-393.

Moridi A., Demir A. G., Caprio L., Hart A. J., Previtali B. and Colosimo B. M. (2019). "Deformation and failure mechanisms of Ti–6Al–4V as built by selective laser melting." Materials Science and Engineering: A **768**: 138456.

Motoyama Y., Tokunaga H., Kajino S. and Okane T. (2021). "Stress–strain behavior of a selective laser melted Ti-6Al-4V at strain rates of 0.001–1/s and temperatures 20–1000 °C." Journal of Materials Processing Technology **294**: 117141.

Muthuramalingam T., Akash R., Krishnan S., Phan N. H., Pi V. N. and Elsheikh A. H. (2021). "Surface quality measures analysis and optimization on machining titanium alloy using CO2 based laser beam drilling process." Journal of Manufacturing Processes **62**: 1-6.

Naskar A., Choudhary A. and Paul S. (2020). "Wear mechanism in high-speed superabrasive grinding of titanium alloy and its effect on surface integrity." Wear **462-463**: 203475.

Nguyen H. D., Pramanik A., Basak A. K., Dong Y., Prakash C., Debnath S., Shankar S., Jawahir I. S., Dixit S. and Buddhi D. (2022). "A critical review on additive manufacturing of Ti-6Al-4V alloy: microstructure and mechanical properties." Journal of Materials Research and Technology **18**: 4641-4661.

Ni C., Zhu L., Zheng Z., Zhang J., Yang Y., Hong R., Bai Y., Lu W. F. and Wang H. (2020). "Effects of machining surface and laser beam scanning strategy on machinability of selective laser melted Ti6Al4V alloy in milling." Materials & Design **194**: 108880.

Nicolò Maria d. V., Peter S., Amit S., Manish J. and Cinzia P. (2023). "Micromechanical response of pure magnesium at different strain rate and temperature conditions: twin to slip and slip to twin transitions." Acta Materialia **243**: 118528.

Niinomi M. (2019). "Titanium Alloys". In R. Narayan (Ed.), Encyclopedia of Biomedical Engineering (pp. 213-224). Oxford: Elsevier.

Niknam S. A., Khettabi R. and Songmene V. (2014). "Machinability and Machining of Titanium Alloys: A Review". In J. P. Davim (Ed.), Machining of Titanium Alloys (pp. E1-E1). Berlin, Heidelberg: Springer Berlin Heidelberg.

Niu Q., Rong J., Jing L., Gao H., Tang S., Qiu X., Liu L., Wang X. and Dai F. (2023). "Study on force-thermal characteristics and cutting performance of titanium alloy milled by ultrasonic vibration and minimum quantity lubrication." Journal of

Manufacturing Processes **95**: 115-130.

Oda H., Nishizawa O., Kusunose K. i. and Hirata T. (1990). "Frequency-dependence of velocity and attenuation of elastic waves in granite under uniaxial compression." Pure and Applied Geophysics **133**(1): 73-85.

Oke S. R., Ogunwande G. S., Onifade M., Aikulola E., Adewale E. D., Olawale O. E., Ayodele B. E., Mwema F., Obiko J. and Bodunrin M. O. (2020). "An overview of conventional and non-conventional techniques for machining of titanium alloys." Manufacturing Review **7**: 34.

Olakanmi E. O., Cochrane R. F. and Dalgarno K. W. (2015). "A review on selective laser sintering/melting (SLS/SLM) of aluminium alloy powders: Processing, microstructure, and properties." Progress in Materials Science **74**: 401-477.

Opoz T. and Chen X. (2016). "Chip Formation Mechanism Using Finite Element Simulation." Journal of Mechanical Engineering **62**: 636-646.

Pal S., Lojen G., Hudak R., Rajtukova V., Brajlih T., Kokol V. and Drstvenšek I. (2020). "As-fabricated surface morphologies of Ti-6Al-4V samples fabricated by different laser processing parameters in selective laser melting." Additive Manufacturing **33**: 101147.

Pan H., He Y. and Zhang X. (2021). "Interactions between dislocations and boundaries during deformation." Materials **14**(4): 1012.

Pan Z., Feng Y. and Liang S. Y. (2017). "Material microstructure affected machining: a review." Manufacturing Review **4**: 5.

Pantawane M. V., Sharma S., Sharma A., Dasari S., Banerjee S., Banerjee R. and Dahotre N. B. (2021). "Coarsening of martensite with multiple generations of twins in laser additively manufactured Ti6Al4V." Acta Materialia **213**: 116954.

Parameswaran V. R., Urabe N. and Weertman J. (2003). "Dislocation Mobility in Aluminum." Journal of Applied Physics **43**(7): 2982-2986.

Paton N. E. and Backofen W. A. (1970). "Plastic deformation of titanium at elevated temperatures." Metallurgical Transactions **1**(10): 2839-2847.

Pawade R. S., Joshi S. S., Brahmankar P. K. (2008). "Effect of machining parameters and cutting edge geometry on surface integrity of high-speed turned Inconel 718."

International Journal of Machine Tools and Manufacture **48**(1): 15-28.

Polishetty A., Shunmugavel M., Goldberg M., Littlefair G. and Singh R. K. (2017). "Cutting Force and Surface Finish Analysis of Machining Additive Manufactured Titanium Alloy Ti-6Al-4V." Procedia Manufacturing **7**: 284-289.

Pramanik A. (2014). "Problems and solutions in machining of titanium alloys." The International Journal of Advanced Manufacturing Technology **70**(5): 919-928.

Pramanik A. and Littlefair G. (2015). "Machining of Titanium Alloy (Ti-6Al-4V)-Theory to Application." Machining Science and Technology **19**(1/2): 1-49.

Pushp P., Dasharath S. M. and Arati C. (2022). "Classification and applications of titanium and its alloys." Materials Today: Proceedings **54**: 537-542.

Qi Y. W., Luo Z. P., Li X. Y. and Lu K. (2022). "Transition of deformation mechanisms from twinning to dislocation slip in nanograined pure cobalt." Journal of Materials Science & Technology **121**: 124-129.

Qiao K., Wang K., Wang J., Hao Z., Xiang Y., Han P., Cai J., Yang Q. and Wang W. (2024). "Microstructural evolution and deformation behavior of friction stir welded twin-induced plasticity steel." Journal of Materials Science & Technology **169**: 68-81.

Rafi H. K., Karthik N. V., Gong H., Starr T. L. and Stucker B. E. (2013). "Microstructures and Mechanical Properties of Ti6Al4V Parts Fabricated by Selective Laser Melting and Electron Beam Melting." Journal of Materials Engineering and Performance **22**(12): 3872-3883.

Rasmussen C. J., Fæster S., Dhar S., Quaade J. V., Bini M. and Danielsen H. K. (2017). "Surface crack formation on rails at grinding induced martensite white etching layers." Wear **384-385**: 8-14.

Regazzoni G., Kocks U. F. and Follansbee P. S. (1987). "Dislocation kinetics at high strain rates." Acta Metallurgica **35**(12): 2865-2875.

Ren-Guo Guan D. T. (2017). "A Review on Grain Refinement of Aluminum Alloys: Progresses, Challenges and Prospects." Acta Metallurgica Sinica (English Letters) **30**(5): 409-432.

Rida A., Micoulaut M., Rouhaud E. and Makke A. (2020). "Understanding the strain rate sensitivity of nanocrystalline copper using molecular dynamics simulations." Computational Materials Science **172**: 109294.

Rosi F. D. (1957). "Twin intersections in titanium." Acta Metallurgica **5**(6): 337-339.

Rotella G., Imbrogno S., Candamano S. and Umbrello D. (2018). "Surface integrity of machined additively manufactured Ti alloys." Journal of Materials Processing Technology **259**: 180-185.

Salvado F. C., Teixeira-Dias F., Walley S. M., Lea L. J. and Cardoso J. B. (2017). "A review on the strain rate dependency of the dynamic viscoplastic response of FCC metals." Progress in Materials Science **88**: 186-231.

Schulz H. and Moriwaki T. (1992). "High-speed Machining." CIRP Annals **41**(2): 637-643.

Sefene E. M. (2022). "State-of-the-art of selective laser melting process: A comprehensive review." Journal of Manufacturing Systems **63**: 250-274.

Shi K., Ren J., Zhang D., Zhai Z. and Huang X. (2017). "Tool wear behaviors and its effect on machinability in dry high-speed milling of magnesium alloy." The International Journal of Advanced Manufacturing Technology **90**: 3265-3273.

Shunmugavel M., Goldberg M., Polishetty A., Nomani J., Sun S. and Littlefair G. (2019). "Chip formation characteristics of selective laser melted Ti–6Al–4V." Australian Journal of Mechanical Engineering **17**(2): 109-126.

Siju A. S., Jose S. and Waigaonkar S. D. (2022). "Experimental analysis and characterisation of chip segmentation in dry machining of Ti-6Al-4V alloy using inserts with hybrid textures." CIRP Journal of Manufacturing Science and Technology **36**: 213-226.

Singla A. K., Banerjee M., Sharma A., Singh J., Bansal A., Gupta M. K., Khanna N., Shahi A. S. and Goyal D. K. (2021). "Selective laser melting of Ti6Al4V alloy: Process parameters, defects and post-treatments." Journal of Manufacturing Processes **64**: 161-187.

Srivastava M., Rathee S., Patel V., Kumar A. and Koppad P. (2022). "A review of various materials for additive manufacturing: Recent trends and processing issues."

Journal of Materials Research and Technology **21**: 2612-2641.

Stef J., Poulon-Quintin A., Redjaimia A., Ghanbaja J., Ferry O., De Sousa M. and Gouné M. (2018). "Mechanism of porosity formation and influence on mechanical properties in selective laser melting of Ti-6Al-4V parts." Materials & Design **156**: 480-493.

Stepanov N., Tikhonovsky M., Yurchenko N., Zyabkin D. and Salishchev G. J. I. (2015). "Effect of cryo-deformation on structure and properties of CoCrFeNiMn high-entropy alloy." **59**: 8-17.

Sun C., Guo N., Fu M. and Wang S. (2016). "Modeling of slip, twinning and transformation induced plastic deformation for TWIP steel based on crystal plasticity." International Journal of Plasticity **76**: 186-212.

Sun J. and Guo Y. B. (2009). "Material flow stress and failure in multiscale machining titanium alloy Ti-6Al-4V." The International Journal of Advanced Manufacturing Technology **41**(7): 651-659.

Sun J. L., Trimby P. W., Yan F. K., Liao X. Z., Tao N. R. and Wang J. T. (2013). "Grain size effect on deformation twinning propensity in ultrafine-grained hexagonal close-packed titanium." Scripta Materialia **69**(5): 428-431.

Sun K., Yu X., Tan C., Ma H., Wang F. and Cai H. (2014). "Effect of microstructure on adiabatic shear band bifurcation in Ti–6Al–4V alloys under ballistic impact." Materials Science and Engineering: A **595**: 247-256.

Sun S., Brandt M. and Dargusch M. S. (2009). "Characteristics of cutting forces and chip formation in machining of titanium alloys." International Journal of Machine Tools and Manufacture **49**(7): 561-568.

Sun Z., To S. and Yu K. (2019). "An investigation in the ultra-precision fly cutting of freeform surfaces on brittle materials with high machining efficiency and low tool wear." The International Journal of Advanced Manufacturing Technology **101**: 1583-1593.

Sutter G. and List G. (2013). "Very high speed cutting of Ti-6A1-4V titanium alloy - change in morphology and mechanism of chip formation." International Journal of

Machine Tools and Manufacture **66**: 37-43.

Sutter G. and List G. (2013). "Very high speed cutting of Ti–6Al–4V titanium alloy – change in morphology and mechanism of chip formation." International Journal of Machine Tools and Manufacture **66**: 37-43.

Tang M. X., Li C., Cai Y. and Luo S. N. (2022). "Deformation twinning to dislocation slip transition in single-crystal tantalum under dynamic compression." Journal of Materials Science **57**(10): 6026-6038.

Tang Y., Wang R., Xiao B., Zhang Z., Li S., Qiao J., Bai S., Zhang Y. and Liaw P. K. (2023). "A review on the dynamic-mechanical behaviors of high-entropy alloys." Progress in Materials Science **135**: 101090.

Thijs L., Verhaeghe F., Craeghs T., Humbeeck J. V. and Kruth J.-P. (2010). "A study of the microstructural evolution during selective laser melting of Ti–6Al–4V." Acta Materialia **58**(9): 3303-3312.

Tiamiyu A. A., Pang E. L., Chen X., LeBeau J. M., Nelson K. A. and Schuh C. A. (2022). "Nanotwinning-assisted dynamic recrystallization at high strains and strain rates." Nature Materials **21**(7): 786-794.

Tian Y., Ren F. and Chen F. (2022). "Twin-boundary-spacing-dependent strength in gradient nano-grained copper." Materials Today Communications **33**: 104836.

Tofail S. A., Koumoulos E. P., Bandyopadhyay A., Bose S., O'Donoghue L. and Charitidis C. (2018). "Additive manufacturing: scientific and technological challenges, market uptake and opportunities." Materials Today **21**(1): 22-37.

Tönshoff H., Karpuschewski B., Lapp C. and Andrae P. (1998). *New machine techniques for high-speed machining.* Paper presented at the International Seminar on improving Machine Tool Performance.

Trent E. M. and Wright P. K. (2000). "Metal cutting." Butterworth-Heinemann.

Tuffentsammer K. and Icks G. (1982). *Lathe criteria for the turning at ultra-high cutting speeds.* Paper presented at the Proc. 10th NAMRC.

Van Belle L., Vansteenkiste G. and Boyer J. C. (2013). "Investigation of Residual Stresses Induced during the Selective Laser Melting Process." Key Engineering

Materials **554-557**: 1828-1834.

Velásquez J. D. P., Tidu A., Bolle B., Chevrier P. and Fundenberger J. J. (2010). "Sub-surface and surface analysis of high speed machined Ti–6Al–4V alloy." Materials Science and Engineering: A **527**(10): 2572-2578.

Veldhuis S. C., Dosbaeva G. K., Elfizy A., Fox-Rabinovich G. S., Wagg T. and Performance (2010). "Investigations of White Layer Formation During Machining of Powder Metallurgical Ni-Based ME 16 Superalloy." Journal of Materials Engineering & Performance **19**(7): 1031-1036.

Venkata Rao R. (2006). "Machinability evaluation of work materials using a combined multiple attribute decision-making method." The International Journal of Advanced Manufacturing Technology **28**(3): 221-227.

Vinogradov A., Vasilev E., Linderov M. and Merson D. (2016). "In situ observations of the kinetics of twinning–detwinning and dislocation slip in magnesium." Materials Science and Engineering: A **676**: 351-360.

Vrancken B., Thijs L., Kruth J. P. and Humbeeck J. V. (2012). "Heat treatment of Ti6Al4V produced by Selective Laser Melting: Microstructure and mechanical properties." Journal of Alloys and Compounds **541**: 177-185.

Wan Z. P., Zhu Y. E., Liu H. W. and Tang Y. (2012). "Microstructure evolution of adiabatic shear bands and mechanisms of saw-tooth chip formation in machining Ti6Al4V." Materials Science and Engineering: A **531**: 155-163.

Wang B. and Liu Z. (2015). "Shear localization sensitivity analysis for Johnson–Cook constitutive parameters on serrated chips in high speed machining of Ti6Al4V." Simulation Modelling Practice and Theory **55**: 63-76.

Wang B., Liu Z., Cai Y., Luo X., Ma H., Song Q. and Xiong Z. (2021). "Advancements in material removal mechanism and surface integrity of high speed metal cutting: A review." International Journal of Machine Tools and Manufacture **166**: 103744.

Wang B., Liu Z., Su G. and Ai X. (2015). "Brittle removal mechanism of ductile materials with ultrahigh-speed machining." Journal of Manufacturing Science and Engineering **137**(6): 061002.

Wang B., Liu Z., Su G., Song Q. and Ai X. (2015). "Investigations of critical cutting speed and ductile-to-brittle transition mechanism for workpiece material in ultra-high speed machining." International Journal of Mechanical Sciences **104**: 44-59.

Wang C, Fang Q, Chen J and Y L. (2016). "Subsurface damage in high-speed grinding of brittle materials considering kinematic characteristics of the grinding process %J International Journal of Advanced Manufacturing Technology." **83**(5-8): 937-948.

Wang Q. and Liu Z. (2016). "Plastic deformation induced nano-scale twins in Ti-6Al-4V machined surface with high speed machining." Materials Science and Engineering: A **675**: 271-279.

Wang T., Li B., Li M., Li Y., Wang Z. and Nie Z. (2015). "Effects of strain rates on deformation twinning behavior in α-titanium." Materials Characterization **106**: 218-225.

Wang X. and Chou K. (2018). "EBSD study of beam speed effects on Ti-6Al-4V alloy by powder bed electron beam additive manufacturing." Journal of Alloys and Compounds **748**: 236-244.

Wang X. X., Zhan M., Gao P. F., Ma P. Y., Yang K., Lei Y. D. and Li Z. X. (2020). "Deformation mode dependent mechanism and kinetics of dynamic recrystallization in hot working of titanium alloy." Materials Science and Engineering: A **772**: 138804.

Waqar S., Guo K. and Sun J. (2022). "Evolution of residual stress behavior in selective laser melting (SLM) of 316L stainless steel through preheating and in-situ re-scanning techniques." Optics & Laser Technology **149**: 107806.

Wei Y., Chen G., Li W., Li M., Zhou Y., Nie Z. and Xu J. (2022). "Process optimization of micro selective laser melting and comparison of different laser diameter for forming different powder." Optics & Laser Technology **150**: 107953.

Wu T., Liu C., Chang L., Wang H., Zhang L. and Zhou X. (2023). "Understanding the surface grain refinement mechanisms for type 316L stainless steel during machining process via advanced microstructure characterization." Materialia **31**: 101866.

Wu X., Li L., Liu W., Li S., Zhang L. and He H. (2018). "Development of adiabatic shearing bands in 7003-T4 aluminum alloy under high strain rate impacting." Materials Science and Engineering: A **732**: 91-98.

Xiao Z., Chen C., Zhu H., Hu Z., Nagarajan B., Guo L. and Zeng X. (2020). "Study of residual stress in selective laser melting of Ti6Al4V." Materials & Design **193**: 108846.

Xing X., Yu M., Chen W. and Zhang H. J. C. M. S. (2017). "Atomistic simulation of hydrogen-assisted ductile-to-brittle transition in α-iron." **127**: 211-221.

Xu W., Brandt M., Sun S., Elambasseril J., Liu Q., Latham K., Xia K. and Qian M. (2015). "Additive manufacturing of strong and ductile Ti–6Al–4V by selective laser melting via in situ martensite decomposition." Acta Materialia **85**: 74-84.

Xu W., Lui E. W., Pateras A., Qian M. and Brandt M. (2017). "In situ tailoring microstructure in additively manufactured Ti-6Al-4V for superior mechanical performance." Acta Materialia **125**: 390-400.

Xu W., Sun S., Elambasseril J., Liu Q., Brandt M. and Qian M. (2015). "Ti-6Al-4V Additively Manufactured by Selective Laser Melting with Superior Mechanical Properties." JOM **67**(3): 668-673.

Xu X., Zhang J., Liu H., He Y. and Zhao W. (2019). "Grain refinement mechanism under high strain-rate deformation in machined surface during high speed machining Ti6Al4V." Materials Science and Engineering: A **752**: 167-179.

Xuan C. (2023). "A study of microstructural factors governing strength and ductility of titanium alloys fabricated by powder bed fusion additive manufacturing." Journal of Alloys and Compounds **952**: 170094.

Yadroitsev I. and Yadroitsava I. (2015). "Evaluation of residual stress in stainless steel 316L and Ti6Al4V samples produced by selective laser melting." Virtual Physical Prototyping **10**(2): 67-76.

Yan N., Li Z., Xu Y. and Meyers M. A. (2021). "Shear localization in metallic materials at high strain rates." Progress in Materials Science **119**: 100755.

Yang D. and Liu Z. (2015). "Surface topography analysis and cutting parameters optimization for peripheral milling titanium alloy Ti–6Al–4V." International Journal of Refractory Metals and Hard Materials **51**: 192-200.

Yang X. and Zhang B. (2019). "Material embrittlement in high strain-rate loading." International Journal of Extreme Manufacturing **1**(2): 022003.

Yang Z., Yang M., Ma Y., Zhou L., Cheng W., Yuan F. and Wu X. (2020). "Strain rate dependent shear localization and deformation mechanisms in the CrMnFeCoNi high-entropy alloy with various microstructures." Materials Science and Engineering: A **793**: 139854.

Yao Z., Yang T., Yang M., Jia X., Wang C., Yu J., Li Z., Han H., Liu W., Xie G., Yang S., Zhang Q., Wang C., Wang S. and Liu X. (2022). "Martensite colony engineering: A novel solution to realize the high ductility in full martensitic 3D-printed Ti alloys." Materials & Design **215**: 110445.

Ye G. G., Xue S. F., Jiang M. Q., Tong X. H. and Dai L. H. (2013). "Modeling periodic adiabatic shear band evolution during high speed machining Ti-6Al-4V alloy." International Journal of Plasticity **40**: 39-55.

Ye G. G., Xue S. F., Ma W. and Dai L. H. (2017). "Onset and evolution of discontinuously segmented chip flow in ultra-high-speed cutting Ti-6Al-4V." The International Journal of Advanced Manufacturing Technology **88**(1): 1161-1174.

Ye T., Zhao F., Chen L., Jiang K., Deng Q., Chen Y., Wang Q. and Suo T. (2021). "Effect of strain rate and low temperature on mechanical behaviour and microstructure evolution in twinning-induced plasticity steel." Materials Science and Engineering: A **823**: 141734.

Zafari A., Barati M. R. and Xia K. (2018). "Controlling martensitic decomposition during selective laser melting to achieve best ductility in high strength Ti-6Al-4V." Materials Science and Engineering: A **744**: 445-455.

Zepeda-Ruiz L. A., Stukowski A., Oppelstrup T. and Bulatov V. V. (2017). "Probing the limits of metal plasticity with molecular dynamics simulations." Nature **550**(7677): 492-495.

Zhang B. and Howes T. D. J. C. A.-M. T. (1994). "Material-Removal Mechanisms in Grinding Ceramics." **43**(1): 305-308.

Zhang B., Li Y. and Bai Q. (2017). "Defect Formation Mechanisms in Selective Laser Melting: A Review." Chinese Journal of Mechanical Engineering **30**(3): 515-527.

Zhang B. and Yin J. F. (2019). "The ‘skin effect’ of subsurface damage distribution in materials subjected to high-speed machining." International Journal of Extreme Manufacturing **1**(1).

Zhang C., Zou D., Mazur M., Mo J. P. T., Li G. and Ding S. (2023). "The State of the Art in Machining Additively Manufactured Titanium Alloy Ti-6Al-4V." Materials **16**(7): 2583.

Zhang M., Ng C.-H., Dehghan-Manshadi A., Hall C., Bermingham M. J. and Dargusch M. S. (2023). "Towards isotropic behaviour in Ti–6Al–4V fabricated with laser powder bed fusion and super transus hot isostatic pressing." Materials Science and Engineering: A **874**: 145094.

Zhang P., Liu Z., Du J., Su G., Zhang J. and Xu C. (2020). "On machinability and surface integrity in subsequent machining of additively-manufactured thick coatings: A review." Journal of Manufacturing Processes **53**: 123-143.

Zhang S., Liu Z., Wang B., Ren X., Khan A. M. and Zhao M. (2021). "Phase transition and dynamic recrystallization mechanisms of white layer formation during turning superalloy Inconel 718." Journal of Materials Research and Technology **15**: 5288-5296.

Zhang X., Peng Z., Li Z., Sui H. and Zhang D. (2020). "Influences of machining parameters on tool performance when high-speed ultrasonic vibration cutting titanium alloys." Journal of Manufacturing Processes **60**: 188-199.

Zhang X. P., Shivpuri R. and Srivastava A. K. (2014). "Role of phase transformation in chip segmentation during high speed machining of dual phase titanium alloys." Journal of Materials Processing Technology **214**(12): 3048-3066.

Zhang Y., Lee Y. J., Chang S., Chen Y., Bai Y., Zhang J. and Wang H. (2022). "Microstructural modulation of TiAl alloys for controlling ultra-precision machinability." International Journal of Machine Tools and Manufacture **174**: 103851.

Zhang Z., Huang S., Chen L., Zhu Z. and Guo D. (2017). "Formation mechanism of fivefold deformation twins in a face-centered cubic alloy." Scientific Reports **7**(1): 45405.

Zhao C., Parab N. D., Li X., Fezzaa K., Tan W., Rollett A. D. and Sun T. (2020). "Critical instability at moving keyhole tip generates porosity in laser melting." Science

370(6520): 1080-1086.

Zhao Q., Sun Q., Xin S., Chen Y., Wu C., Wang H., Xu J., Wan M., Zeng W. and Zhao Y. (2022). "High-strength titanium alloys for aerospace engineering applications: A review on melting-forging process." Materials Science and Engineering: A **845**: 143260.

Zhong H. Z., Zhang X. Y., Wang S. X. and Gu J. F. (2018). "Examination of the twinning activity in additively manufactured Ti-6Al-4V." Materials & Design **144**: 14-24.

Zhong X., Huang L. and Liu F. (2020). "Discontinuous Dynamic Recrystallization Mechanism and Twinning Evolution during Hot Deformation of Incoloy 825." Journal of Materials Engineering and Performance **29**(9): 6155-6169.

Zhou L., Shimizu J., Muroya A. and Eda H. (2003). "Material removal mechanism beyond plastic wave propagation rate." Precision Engineering **27**(2): 109-116.

Zhou N., Lin Peng R. and Pettersson R. (2017). "Surface characterization of austenitic stainless steel 304L after different grinding operations." International Journal of Mechanical and Materials Engineering **12**(1): 6.

Zhu Q., Huang Q., Tian Y., Zhao S., Chen Y., Cao G., Song K., Zhou Y., Yang W., Zhang Z., An X., Zhou H. and Wang J. (2022). "Hierarchical twinning governed by defective twin boundary in metallic materials." Science Advances **8**(20): eabn8299.

Zhu Y., Zhang K., Meng Z., Zhang K., Hodgson P., Birbilis N., Weyland M., Fraser H. L., Lim S. C. V., Peng H., Yang R., Wang H. and Huang A. (2022). "Ultrastrong nanotwinned titanium alloys through additive manufacturing." Nature Materials **21**(11): 1258-1262.

Zhu Y. T., Liao X. Z. and Wu X. L. (2012). "Deformation twinning in nanocrystalline materials." Progress in Materials Science **57**(1): 1-62.

Zhu Y. T., Liao X. Z., Wu X. L. and Narayan J. (2013). "Grain size effect on deformation twinning and detwinning." Journal of Materials Science **48**(13): 4467-4475.